INFORMATION TO USERS

This manuscript has been reproduced from the microfilm master. UMI films the text directly from the original or copy submitted. Thus, some thesis and dissertation copies are in typewriter face, while others may be from any type of computer printer.

The quality of this reproduction is dependent upon the quality of the copy submitted. Broken or indistinct print, colored or poor quality illustrations and photographs, print bleedthrough, substandard margins, and improper alignment can adversely affect reproduction.

In the unlikely event that the author did not send UMI a complete manuscript and there are missing pages, these will be noted. Also, if unauthorized copyright material had to be removed, a note will indicate the deletion.

Oversize materials (e.g., maps, drawings, charts) are reproduced by sectioning the original, beginning at the upper left-hand corner and continuing from left to right in equal sections with small overlaps. Each original is also photographed in one exposure and is included in reduced form at the back of the book.

Photographs included in the original manuscript have been reproduced xerographically in this copy. Higher quality 6" x 9" black and white photographic prints are available for any photographs or illustrations appearing in this copy for an additional charge. Contact UMI directly to order.

UMI

A Bell & Howell Information Company
300 North Zeeb Road, Ann Arbor MI 48106-1346 USA
313/761-4700 800/521-0600

MODELING OF THE POLAR IONOSPHERE IN THE INERTIAL COROTATING FRAME

A

THESIS

Presented to the Faculty of the University of Alaska
in Partial Fulfillment of the Requirements
for the Degree of

DOCTOR OF PHILOSOPHY

By

Sergei A. Maurits, M.S. Physics

Fairbanks, Alaska
August 1996

MODELING OF THE POLAR IONOSPHERE

IN THE INERTIAL COROTATING FRAME

BY

SERGEI A. MAURITS

RECOMMENDED:

Advisory Committee Chair

Department Head

APPROVED:

Dean, College of Natural Sciences

Dean of the Graduate School

5-10-96

Date

ABSTRACT

The ionospheric model presented in this thesis is developed from first principles. It is a three-dimensional and time-dependent model that covers the region poleward from 50 degrees of geographic latitude and extends to the height range of 80-500 *km*. In this model, equations of continuity, motion, and energy balance are self-consistently solved for the densities of 7 ion species [$O^+(^4S, ^2D, ^2P)$, NO^+, O_2^+, N_2^+, N^+] and electrons. The model accounts for 40 photochemical processes, the neutral wind drag with its shear, electromagnetic E×B-drift, and field-aligned ambipolar diffusion. The background thermospheric parameters here are derived from the VSH/MSIS models. Minor species *NO*, $N(^4S, ^2D)$ and their molecular and eddy diffusion transfer in the lower ionosphere are considered in this model. Energy balance equations for isotropic electron and ion temperatures are are solved, including electron thermal conduction and Joule heating. The model is applicable to a limited polar region (hence the curvature is neglected) and the equations are solved in the corotating Cartesian frame with an azimuthal equidistant projection of all parameters and point-by-point transformation of the inputs specified in the geomagnetic frame. The regular grid has a scaleable resolution; the workstation version of the code presented in this thesis has achieved 100×100 *km* horizontal resolution. The algorithm maintains numerical stability for variable time steps in the range from 10-15 minutes to 1-2 minutes, allowing a flexible time coverage. This effective algorithm and even spatial coverage of the regular grid saves significant computational resources.

The model output realistically represents seasonal changes and other large-scale polar ionospheric features such as the abundant dayside ionization, the polar cap tongue of ionization, the auroral oval, the polar hole, and ionospheric troughs of different origins. Ionospheric simulations developed in response to different IMF variations demonstrate destruction of continuous polar cap structures and the creation of "patches" of ionized plasma. Several model simulations have shown good overall agreement with observed ionospheric events.

TABLE OF CONTENTS

L I S T O F F I G U R E S

L I S T O F T A B L E S

A C K N O W L E D G M E N T S

I would like to thank my academic advisor and the Committee Chair Professor Brenton Watkins for his help and guidance and especially for his interest in the implementation of the pivotal idea of this thesis: the development of a high-resolution polar ionospheric model in the earth's corotating frame. Having allowed me the time and freedom to find my own direction, he then helped me to follow it to completion of the work. His leadership, firm support, encouragement, and daily involvement helped this project tremendously on its long road to success. I should also acknowledge the best computing resources available, which were provided for this work, as well as resources for extensive travel, which allowed me to present the scientific results and to follow the current trends in this field.

I also wish to express my gratitude to Professor Fred Rees who initially invited me to the UAF graduate school and who was my advisor in the earlier stages of this project. His ideas were of much help for me in choosing the field of research. His help and recommendations in final preparation of this thesis were the most useful.

The contribution of the Committee member Dr. Dirk Lummerzheim to this work was very significant. In addition to useful discussions and countless practical advice during the entire term of this project, Dr. Lummerzheim undertook a thorough editing of the thesis manuscript, helping tremendously to improve its style, consistency, and content.

I would like to thank all other members of my Advisory Committee for their help and attention to this work: John Olson, Mitchell Roth, and Daniel Swift. Discussions with Dr. Swift about scientific goals of this project helped me to think over and formulate a strategy of using this model for ionospheric simulations and to develop a better understanding of its place in the variety of the space physics approaches. The vast experience of Dr. Roth was most helpful in preparation of the post-processing visualization and animation package for this model and, together with Richard Guritz, in video production of the computer ani-

mated feature about polar ionosphere dynamics based on the model runs. The permanent support and encouragement from Dr. Olson were very valuable for me.

In the computational part of this thesis, it would be difficult to overestimate the contribution from Geophysical Institute System Analyst Don Rice. Besides his excellent network technical support, Don's encyclopedic computer knowledge and his readiness to share it were the most valuable resource for this project.

Last but not least, the creative atmosphere at UAF and the Geophysical Institute and the constant interaction with faculty and other graduate students were of the utmost help for this work. I really appreciated the warm welcome and help in gaining an everyday experience in a new country from Dr. Roger Smith, the graduate school Administrative Assistant Sue Poling, and my fellow graduate students Geoff McHarg, Joe Minow, Jim Conner, and many others.

Going back in time, I wish to thank my parents for their care and their permanent interest in my education at all of its stages. I am most grateful to them for the opportunities they provided.

Finally, I wish to thank my wife Alla and son Kirill for their love, understanding, and support throughout all these years. Without them this work would not be possible.

"We cannot help but be interested in the atmosphere: It affects our attitudes, it limits our endeavors, it causes tragedies, it provides spectacular scenery. The atmosphere cannot be ignored, it is our environment. We are curious and want to know the how's and why's of atmospheric processes. We are practical and want to control, or at least make good use of, the vital processes we observe. We are also artistic, poetic, philosophical and religious: we are awed by phenomena that affect all our senses and constantly remind us of the crudeness of our knowledge, the vulnerabilities of our lives and endeavors, the infinite complexities of nature, and the sheer beauty of our world. It is no wonder, then, that the study of the atmosphere should be one of the oldest intellectual pursuits and, in the same time, perhaps the most disorganized."

R.C.Whitten, I.G.Poppoff
Fundamentals of Aeronomy

CHAPTER 1

I N T R O D U C T I O N

1.1. Overview

The efforts of two last decades in modeling of the terrestrial ionosphere have substantially improved our understanding of the physical mechanisms that govern its behavior [e.g., see recent review by *Maurits and Ivanov-Kholodny*, 1993]. In conjunction with an expanded experimental data base and theoretical findings, the field of ionospheric modeling is evolving rapidly with continuing model refinements and additions. Recent global models solve the governing equations simultaneously for the ionized and neutral components of the thermosphere. Despite relatively low spatial resolutions and numerous parameterizations, these models are nearing the limits of currently available computer technology. Also, topical ionospheric tasks require much higher spatial resolution. Therefore, the pragmatic approach adopted in this thesis includes justifiable simplifications for the purposes of gaining higher resolution. Further, this work only applies to the polar latitudes.

As far as the different regional peculiarities of the terrestrial ionosphere are concerned, modeling of the high-latitude ionosphere is complicated by a combination of factors. Some of these important considerations are:

- Uneven exposure to ionizing solar EUV irradiance due to the polar-day and polar-night phenomena;
- High spatial and temporal variations of auroral precipitation;
- Time-varying intensive horizontal advective plasma motion in the ionospheric F-region caused by **ExB**-drift;
- Highly inhomogeneous local energy sources, due to auroral precipitation and to Joule heating;
- Strong chemical coupling with minor neutral species such as atomic nitrogen and nitric oxide, which are abundant in the polar iono-

spheric E-region due to auroral production; and

- Thermospheric-ionospheric dynamic coupling and the mutual effect on the neutral wind and ion drift patterns and temperature values.

This regional polar ionospheric model must include all appropriate physical and chemical processes in order to the user to achieve a realistic description of the medium. However, some simplifications can be made.

For example, consider the following system: for the heights of the ionospheric F-region (200-600 *km*) at high-latitudes, the prevailing type of horizontal ion motion is convection-like **ExB** drift in a two-cell vortex pattern with strong anti-sunward flow between the cells. Ion drifts in this region can exceed velocities as high as 1 *km/sec*. The drag forcing by convecting ions is sufficiently strong to drive the neutral wind in a similar two-cell circulation pattern, which follows but temporally lags the pattern of ion convection. The lag time varies from tens to hundreds of minutes due to the dependency of the time constant for momentum transfer upon the highly variable ion density [*Roble*, 1992]. The practically non-achievable steady-state situation is the co-incidence of both ion drift and neutral wind patterns.

One possible simplification for describing this system is the adoption of the Lagrangian approach of fluid dynamics. Using this approach, the reference frame convects together with the ionospheric plasma, and Earth's rotation is described by the introduction of a co-rotating potential. In the framework of this approach, the time stepping is equivalent to displacement of magnetic flux tubes to the next position along the plasma convection trajectory. The transition to this moving frame significantly simplifies the governing equations and reduces a 3-D problem to a quasi 1-D case.

The basic assumption for the Lagrangian approach is the concept of a flux tube that convects as a whole. In other words, in the Lagrangian frame the absence of any vertical shear in the drift velocities is assumed. Otherwise, in a general 3-D case the height-variable advection pattern would destroy the vertical continuity of the flux tube.

In the terrestrial thermosphere, the assumption of absence of the vertical shears in the ion motion is valid only for the *F2* region heights, where the ion motion is dominated by the height-independent **ExB**-drift. In the lower ionospheric regions, starting from the lower *F1* region and especially in the *E* region, there is a considerable vertical shear since the transition from **ExB**-driven ion motion to the collisionally dominated drag by neutral winds takes place in this altitude range (100-200 *km*) [*Roble*, 1992]. The role of the neutral wind and its own height-dependence is quite important there (for instance, formation of sporadic *E* layers). The Lagrangian approach cannot easily account for these effects, and it has therefore become common practice in Lagrangian models to ignore them by assuming the *F*-region plasma drifts map down uniformly through the entire ionosphere.

Historically, Lagrangian models were the first polar ionospheric models that simulated the large-scale and mesoscale features of the polar ionosphere [e.g., *Sojka et al.*, 1993, and references therein] and for a long time the Lagrangian frame was the only approach implemented in polar ionospheric modeling. Among these modeling efforts, a Lagrangian polar ionosphere model was developed with participation of the author of this thesis [*Shirochkov, Makarova, and Maurits*, 1993].

However, due to limitations of the Lagrangian approach for the description of systems with vertical shear, the neutral thermosphere models were developed in the Eulerian corotating frame. Recently, the Eulerian description of the global thermosphere-ionosphere system in the inertial corotating frame in the NCAR TIGCM model [*Roble and Ridley*, 1987] revived interest in the Eulerian approach and to its application in ionospheric models.

The inertial corotating frame is the most suitable frame for the computational treatment of a multi-dimensional plasma since its implementation requires a minimum of limiting assumptions. The corotating frame rests in Earth's geographic coordinate system. The frame therefore accounts explicitly for all types of plasma motion, including the effects of vertical wind shear. The corotating frame also preserves the regularity and the even coverage of its grid. This latter advanta-

ge is especially important for high-resolution modeling.

The disadvantage of the corotating frame approach is the additional mathematical complexities that are introduced, plus the corresponding numerical challenge in solving the mixed diffusive-advective partial differential equations in 3-D. Applied to a limited region, the method essentially requires a specification of the time-dependent boundary conditions on the domain sides. Another potential disadvantage is the considerably greater demand for computer memory. However, this is no longer a limitation with modern computing resources.

As noted previously, the Lagrangian frame is not applicable to the description of the neutral thermosphere because of significant vertical wind-shear effects that occur there. Therefore, a self-consistent model of the coupled ionosphere-thermosphere system should adopt the corotating frame for the description either of its thermospheric part or for description of both thermosphere and ionosphere. The latter approach - an entirely corotating framework - is implemented in the NCAR Thermospheric and Ionospheric Global Circulation Model (NCAR TIGCM), which solves both sets of thermospheric and ionospheric equations at each time step. The combination of the Lagrangian and corotating frames in one model is realized, for example, in the University College London Three-Dimensional Thermospheric Model (UCL-TDTM), in which the thermosphere description in the corotating frame is combined with the Lagrangian "Sheffield" ionosphere model. In this combined approach the code executes both ionospheric and thermospheric models separately, while information is exchanged between the frames, and all parameters are adjusted at every model hour.

The use of fully self-consistent ionosphere-thermosphere approach has demonstrated that while the polar winter ionosphere substantially affects the thermospheric wind system and temperatures in certain regions [*Roble and Ridley*, 1987], this influence is not dominant. The separated and not fully self-consistent treatment of the thermosphere and ionosphere is still a reasonable and practical approach. Comparison of the high-latitude responses of the UCL-TDTM model (a fully self-consistent approach) with the Utah State University Time-Dependent

Ionosphere model (USU TDIM, which uses the empirical MSIS-86 as a thermospheric input and is not a fully self-consistent model concerning the thermospheric coupling) has shown that there are certain regions that displayed significant differences, while the overall agreement is mostly within a surprisingly good range of 10-30% for the *F2*-region peak electron density parameter (*NmF2*) [*Sojka et al.*, 1992]. Differences as high as a factor of two were found equatorward from the boundary of the auroral oval in the morning sector, and in the polar cap tongue of ionization. These differences result from the neutral temperature and composition changes due to Joule heating and the corresponding perturbations in the ion composition.

Although the auroral sources of ionization included in polar models are important, the appropriate particle precipitation characteristics are difficult to model. Different approaches and parameterizations were compared by *Rees and Fuller-Rowell* [1992]. They found that the NOAA/TIROS Power Indices [*Fuller-Rowell and Evans*, 1987], which are basically characteristics of integral precipitation intensity, are the best choice from physical considerations, but these indices are not available on a regular basis. A practical, and at the same time physically reasonable approach, is a parameterization by the Auroral Electrojet (AE) index, which is usually available with high temporal resolution. However, a compilation of this index requires substantial effort and time, which makes it applicable only for past geophysical situations. The third choice is Kp, or the closely related Ap, indices, but their poor time resolution (3-hour sampling) usually is not sufficient for the modeling of an individual event. On the other hand, this is the most convenient choice in terms of availability, because these indices are quickly available. Several statistical models of precipitation patterns have been developed that use Kp or Ap as an input parameters [e.g., *Hardy at al.*, 1987 and references therein]. The establishment of quantitative connection between Kp, Ap and AE indices by *Rostoker* [1991] has made the index choice interchangeable.

The most recent approach is *in situ* aurora spectral imaging, which can be recalculated into the parameters of precipitation (energy

flux and characteristic energy) with the highest available temporal and spatial resolution [*Lummerzheim et al.*, 1991; *Rees*, 1992]. Resolutions as high as several tens to one hundred kilometers, and with image recurrence of 12 minutes, are currently available (*Dynamic Explorer* 1). Imagers with even better characteristics are included in several upcoming space missions, e.g. *ISTP/GGS* [*Rees*, 1992].

Existing global models covering the polar ionosphere have poor spatial resolution and therefore can not accommodate highly resolved auroral inputs. The TIGCM model has $5 \times 5^{\circ}$ geographic latitude-longitude resolution. The resolution of the UCL-TDTM model is $2 \times 18^{\circ}$, and the resolution of the USU-TDIM model in its global version is $3 \times 15^{\circ}$ in magnetic coordinates. These models include parameterized auroral sources of ionization and simulate only the large scale (thousands of kilometers) ionospheric structures. Mesoscale phenomena (several hundred kilometers in size) such as patch-like electron density enhancements that occur in the polar cap in ionospheric *F*-region, sun-aligned polar cap arcs, plasma vortices, or aurorally generated inhomogeneous odd nitrogen production in E-region, are beyond the scope of such resolutions. The current approach for investigation of the mesoscale effects are the regional polar high-resolution models [*Decker et al*, 1994] or the models that are applicable to a limited spatial domain for simulation of specific phenomena such as polar cap ionospheric patches [*Sojka et al.*, 1993, 1994] and sun-aligned arcs [*Crain et al.*, 1994; *Zhu et al.*, 1994].

Significant progress has been made recently in the studies and simulations of magnetospheric electric field patterns [*Rich and Hairston*, 1994; *Weimer*, 1995]. This input plays a crucial role in polar ionosphere modeling since it determines both the governing dynamic processes in the upper ionosphere and the major Joule heating source. However, only statistically averaged E-field patterns without mesoscale variability are currently available.

The electric field pattern is strongly dependent has a strong dependence on the IMF orientation. The IMF B_y-component variability may change the configuration of the polar cap flow by asymmetric distorting

of convection structures to the down or dusk directions. The southward orientation of B_z-component ($B_z < 0$) generates a two-cell, vortex-like pattern with an intensive anti-sunward flow in the polar cap, while northward B_z ($B_z > 0$) corresponds to the situation of suppressed convection of irregular configuration with numerous vortices and stagnation zones.

Early electric field models have been formulated predominantly for the southward orientation of B_z [e.g., *Heelis*, 1982, 1984; *Heppner and Maynard*, 1987; *Rich and Maynard*, 1989]. Recent publications [*Rich and Hairston*, 1994; *Weimer*, 1995] have introduced the most comprehensive electric field models to date, which generate patterns for a general orientation of B_z and B_y IMF components, including $B_z > 0$. This approach allows the user to realistically describe time-dependent convection processes for real periods when the history of B_z and B_y variations are known. The electric field model by *Weimer* [1995] has a numerical representation of convection patterns that makes it immediately available for implementation in ionospheric modeling studies. Another recent statistical electric field model is based on data collected with ground-based radar (Goose Bay HF radar) that provides a point of comparison with satellite-based models [*Ruohoniemi and Greenwald*, 1995].

Significant progress in the simulation of individual electric field patterns for the case studies has been achieved using the Assimilative Mapping of Ionospheric Electrodynamics (AMIE) technique [*Richmond and Kamide*, 1988]. Several reconstructions of electric field variations by the AMIE method have been made for periods as long as two days with the temporal resolution of 10 and 5 minutes [*CEDAR data base catalogue*, 1995]. Although still very sparse, these data allow a comparison of ionospheric parameters performed with the statistical models of electric field against the results obtained with independent realizations of convection patterns. The AMIE technique permits simulation of ionospheric responses for large-scale disturbances, which are out of the scope of the statistical models. Examples of studies using these techniques are reconstructions of the electric fields for the large magnetic storm of March 20-21, 1990 [*Knipp et al.*, 1994] and the Space

Weather Event Campaign covering the period of November 1-4, 1993 [*Knipp*, 1995].

In conclusion of this overview section, the recent establishment of the United States National Space Weather Program must be mentioned. Among the other goals, this program includes global forecast of ionospheric parameters available in real time. This task emphasizes the importance of the accuracy and adequate temporal and spatial resolution of ionospheric models, and also their computational effectiveness and convenience for operative running. In this connection, the important features of the forecasting model are the real-time availability of the model's direct inputs (or, for that matter, the geophysical indices for the index-driven inputs) and the possibility of adequate forecast of these parameters.

1.2. This work

In the previous section it was demonstrated that the current tendencies in ionospheric modeling are either a comprehensive self-consistent treatment of the coupled thermosphere-ionosphere system on a rather sparse grid, or high-resolution modeling with a somewhat simplified physical approach, particularly specification of the neutral thermosphere through an empirical (MSIS) or hybrid model (VSH). In this context, the model developed in this thesis belongs to the second class — it is a high-resolution regional polar ionosphere model.

The motivation for the development of a new model with a high-resolution capability was the availability of high-resolution inputs (such as precipitation characteristics derived from the auroral images), new electric field models formulated for an arbitrary orientation of Interplanetary Magnetic Field (IMF) (including northward orientation), and an availability of updated values of kinematic coefficients, chemical reaction rates, various parameterizations, models, and approximations of aeronomy interest. The implementation of such a model has potential in several topical tasks of ionospheric physics. In the framework of this thesis, we have focused on the upper ionosphere ap-

plications, including the high-resolution simulation of polar plasma structures, such as ionospheric patches, their generation mechanisms and their effect on ionospheric parameters, including situations with northward orientation of the IMF B_z component.

The model is developed in the corotating frame. The motivation for such a choice is to avoid computational difficulties associated with run-time distortions of the Lagrangian moving mesh. A better description of the lower part of the ionosphere in the corotating frame permits a study of vertical shear effects. The following scientific goals guided the creation of this model:

- development of a polar ionospheric model in an inertial corotating frame exploring potential computational advantages of the corotating frame approach for high-resolution simulations;
- development of the numerical algorithm for a computationally effective solution of the mixed diffusive-advective partial differential equations and testing its feasibility against the traditional Lagrangian schemes;
- comparison of different approaches for the simulation of electric fields in terms of generated ionospheric response, including AMIE-reconstructions;
- detailed studies of convection corresponding to northward orientation of the IMF ($B_z > 0$);
- development of the modeling capability for real geophysical events and periods with detailed reconstructions of their time history through appropriate variation of the model inputs and/or geophysical indexes;
- model application to a high-resolution simulation of patch-like mesoscale ionospheric structures in the polar cap F region using different scenarios of IMF variability including realistic reconstruction of the time-history of individual events with subsequent comparisons with data; and
- model application to storm periods, particularly to study the limitations of the statistical model inputs, such as the elec-

tric field model.

The model described in this thesis is a 3-D time-dependent model that covers the ionospheric region poleward from 50 degrees of geographic latitude. The model height range is 80-500 kilometers. It self-consistently solves the equations of continuity, equations of motion, and the equation of energy balance to establish the 3-D distribution of electrons, seven ion species ($O^+(^4S)$, $O^+(^2D)$, $O^+(^2P)$, NO^+, O_2^+, N_2^+, N^+), and the minor neutral species NO and $N(^4S)$, $N(^2D)$, which are important for the ionization balance in the lower ionosphere. The VSH/MSIS neutral thermosphere models are used to derive densities of the major neutral thermospheric components and the neutral winds. The ionospheric model includes about 40 photochemical processes. A number of parameterizations and input-generating models account for night sources of ionization and auroral precipitation, variations of EUV radiation over the course of the solar activity cycle, solar activity associated neutral composition changes, sheared drag of neutral thermospheric winds, electromagnetic drifts in the crossed electric and magnetic fields, and field-aligned ambipolar diffusion. The vertical transport mechanism for the long-living neutral species NO and $N(^4S)$ is molecular and eddy diffusion. The model also solves the equation of energy balance for isotropic electron and ion temperatures, including thermal conduction by electrons, and Joule heating effects. As with any newly created model, this effort takes full advantage of recent developments in ionospheric studies, including neutral thermosphere modeling, EUV measurements and parameterizations, magnetospheric electric field studies, auroral input representations, improvements of the kinetic coefficients values, the chemical reaction rates, and cooling and heating rates parameterizations for different ion species and electrons.

The model uses a quasi-hydrodynamic approach that results in a system of the first five velocity moments of the Boltzmann equation. Empirical relations are used for the stress tensor and the heat flow vector that truncates the chain of equations and makes the system mathematically closed. Since the model is applicable to a limited po-

lar region of Earth, the curvature is neglected and the system of equations is solved on a Cartesian grid with azimuthal equidistant projection of all geographic coordinates. All inputs which are defined in the geomagnetic frame are included with point-by-point transformations that account for the offset of the geographic and geomagnetic poles.

The model frame co-rotates with Earth. It consists of a regular grid, which has a scaleable horizontal resolution. The range of available resolutions is rather broad. The workstation version of the model is tested with resolutions in a range from $2\times2^{\circ}$ (220x220 *km*) to $1\times1^{\circ}$ (110x110 *km*) for the cell horizontal dimensions. The resolution can be significantly improved on a supercomputer, especially on a parallel architecture machine, up to a few tens of kilometers. Further increasing of the horizontal resolution to a scale of kilometers requires an investigation of meso- and micro-scale effects that need to be accounted for at smaller distances, particularly the horizontal pressure gradient drifts and the horizontal components of the field-aligned ambipolar diffusion (more detailed discussion of these effects are in Chapter 3 of this thesis on pp. 76-77 and p. 81).

The numerical algorithm maintains stability for variable time steps in the range from about a hundred seconds up to 10-15 minutes; this allows a flexible time coverage of the processes with different time scales. This highly effective algorithm together with the uniformly even spatial coverage of the regular model grid significantly saves computational resources and the model can be run on a low-cost workstation platform with a useful resolution.

The model output realistically represents the seasonal changes and the large-scale features of the polar ionosphere such as the sunlit region ionization that is extended into the dusk sector due to a co-rotation of the long-living O^{+} ions, the polar cap tongue of ionization, the auroral oval, the polar hole, and ionospheric troughs of different origins. Numerical experiments with a fast-changing convection field (variation of B_y-component of IMF) successfully demonstrate the destruction of homogeneous polar cap structures and creation of separated "patches" of ionized plasma of several hundred kilometers in

characteristic diameter. Simulations of real geophysical periods are in a good agreement with ionospheric data.

The thesis structure is as follows. This chapter is an introductory description of the field, and offers an outline of this model placed amongst other research efforts.

In Chapter 2, the scope of the developed model as well as its inputs and outputs are considered. The choice of the corotating inertial frame approach and overall model philosophy, e.g. the adoption of the neutral thermosphere parameters, the model resolution, its vertical and regional scope, are substantiated. The model geometry and coordinate system is also discussed.

Chapter 3 introduces the system of governing equations which includes the equations of continuity, motion, and energy balance in the framework of quasi-hydrodynamics approach. Simplifications of corresponding equations based on valid physical assumptions are made and the remaining terms are discussed in detail. 3-D and 1-D (vertical) approaches are compared and the importance of horizontal advection terms are outlined in the 3-D case.

Chapter 4 discusses the processes of production and loss. The ionization sources in the polar region and the numerical procedures to obtain the production rate developed in the model are described. Through the adopted parameterizations, the variation of solar EUV during the course of a solar cycle and the spatial and temporal variations of auroral precipitation are taken into account. The precipitating pattern perturbations in several auroral models related to the geomagnetic activity and IMF control are discussed. The photochemical scheme adopted in the model is also described in this chapter.

Chapter 5 is devoted to the numerical treatment of the system of governing equations. 3-D algorithms and their connection to the 1-D solution for the ion vertical profiles are described. The model temporal and spatial resolution, different initial and boundary conditions, and the influence of these choices to the solution are also considered in this chapter.

Chapter 6 describes the model implementation to the ionospheric

simulations. Both simplified scenarios of the IMF variations and case studies with reproduction of the time-history of IMF variations for real periods are considered. Simulation-to-data comparisons are performed. A case study of an extended period of northward IMF orientation and the ionospheric dynamic regime corresponding to northward IMF is presented. A study of a magnetically disturbed period with a consequent intensive magnetic storm of March 20, 21, 1990 is discussed. A comparison of ionospheric responses using an implementation of a statistical electric field model and an AMIE-reconstruction for this case is presented.

Chapter 7 provides the summary if this work, formulates the thesis conclusions, and specifies the recommendations for future work.

CHAPTER 2

MODEL SCOPE, INPUTS, AND OUTPUTS

2.1. General structure of the model

A detailed model of the polar ionosphere should provide a description of all ionospheric parameters, such as height profiles of ion densities for the major species, electron and ion temperatures, and ion drift velocities. To achieve this goal it is necessary to include in the model all important inputs, preferably time variable in accordance with the current geophysical situation. The problem is complicated since the polar upper atmosphere, both its ionized and neutral parts, is driven not only by the production and loss mechanisms common for the whole terrestrial thermosphere, but is significantly affected by specifically polar phenomena such as large-scale convective electric fields, auroral precipitation, and polar-night and polar-day phenomena.

Figure 2.1a shows a flow chart of the time-dependent ionospheric model showing inputs at the top and outputs at the bottom. Figure 2.1b describes in more detail the major index-driven inputs, their interaction with the governing processes, and the mutual dependence and parameters exchanged between the the model equations. Mathematically, the ionosphere-thermosphere system can be described (see Chapter 3 for details) by the quasi-hydrodynamic system of equations that includes the equations of continuity (mass conservation), equations of motion (momentum conservation), and equations of energy balance (energy conservation). Generally speaking, each system component must be described by the full set of equations. However, substantial simplifications can be applied to reduce the complexity of the problem.

The most rigorous approach for the mutually dependent ionosphere-thermosphere system is the self-consistent description using a coupled system of equations for both neutral and ionized components. This approach is implemented in the NCAR TIGCM and partially in the UCL TDTM global models. Both ionosphere and thermosphere are treated in the same

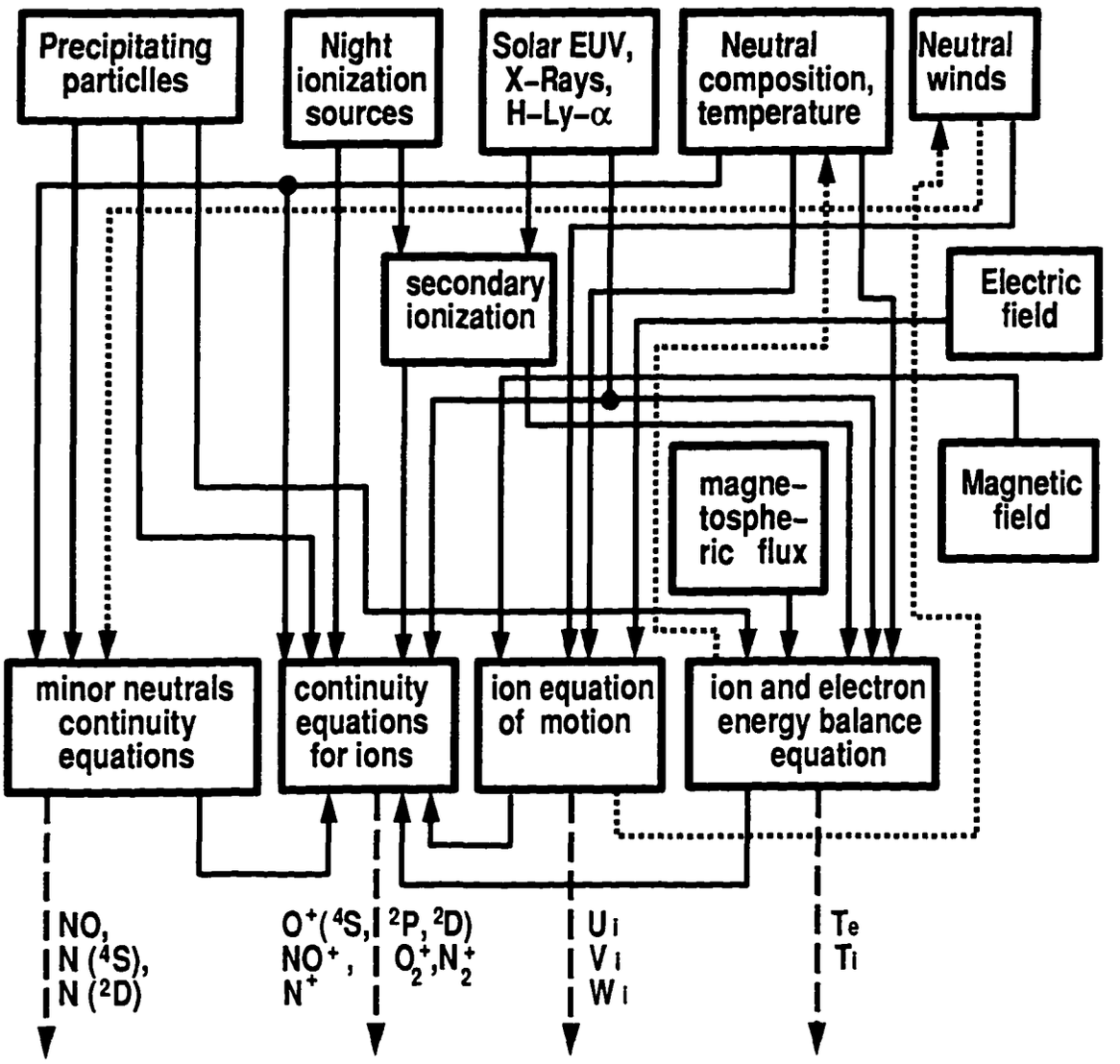

Figure 2.1a. Flow chart of the polar ionospheric model from its inputs (top rows) to the governing processes (middle row) and outputs (bottom row). Dotted arrows correspond to the coupling that physically exists but is not accounted for in the model version. Dashed arrows represent the model outputs (see next diagram for more details).

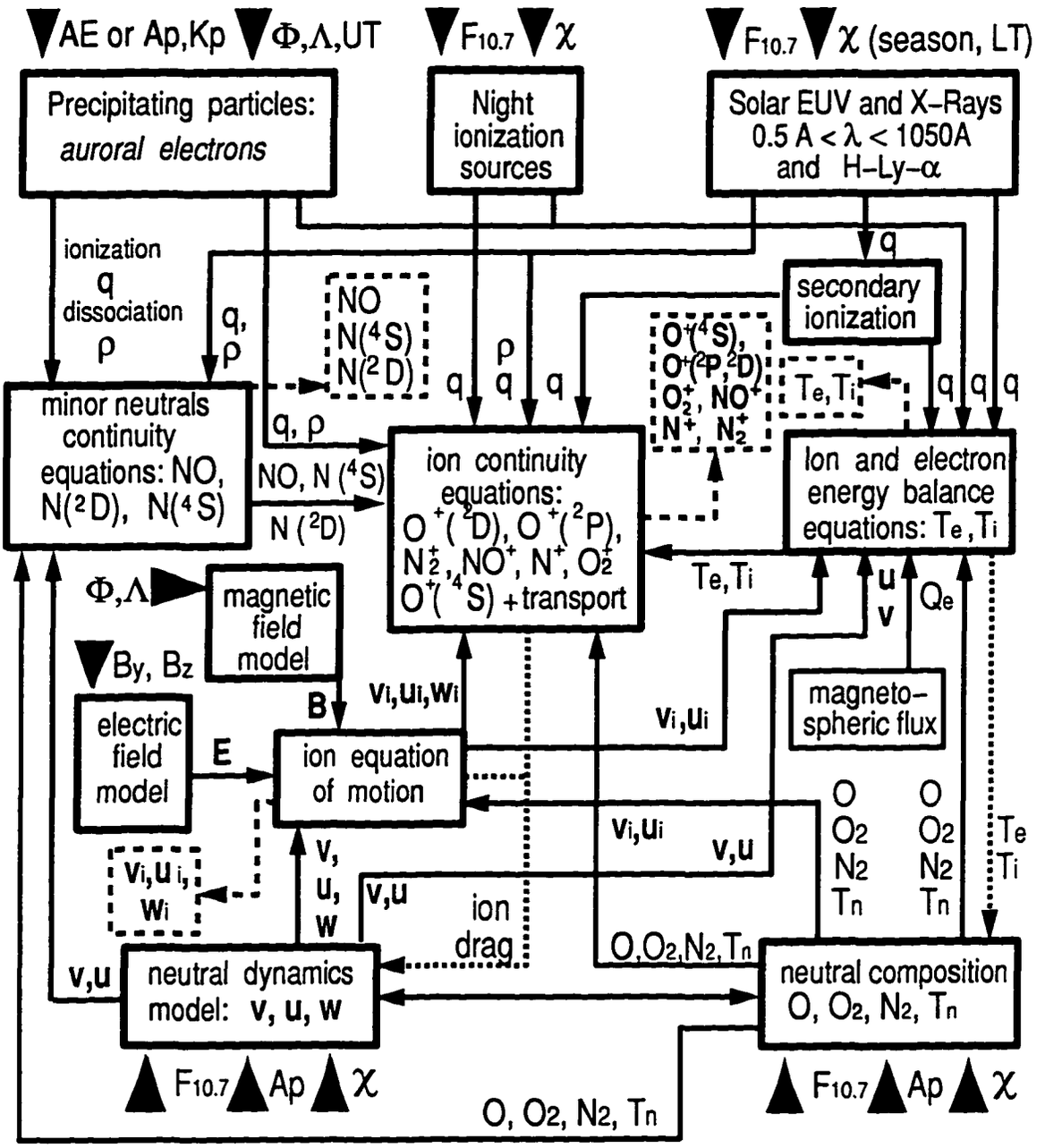

Figure 2.1b. Schematic diagram of the polar ionospheric model. The inputs are represented by solid black triangles: season; Universal Time (UT); local time (LT) for the every location; the level of solar activity (F10.7); the level of geomagnetic activity (AE, Kp, Ap indices inter-changeably); and the IMF components *By*, *Bz*. Characteristic of the particle precipitation depend upon geomagnetic location Φ, Λ and the UT-dependent auroral oval configuration. Dotted arrows correspond to the coupling that physically exists but is not accounted for in the model version. Dashed arrows represent the model outputs.

frame in NCAR TIGCM, and the model solves the coupled equations simultaneously at each time step. In the UCL TDTM model, the ionosphere and thermosphere are treated in different frames and the corresponding parameters are exchanged each model hour. However, reasonable accuracy can generally be achieved without resorting to an entirely self-consistent approach [*Sojka et al.*, 1992]. Thermospheric models (e.g. MSIS, HWM, VSH) can be used for descriptions of various thermospheric parameters — major neutral gas densities $[O, O_2, N_2]$, neutral temperature, and winds — apparently without a significant loss of accuracy for standard geophysical situations. This approach is illustrated in figure 2.1, which shows separation of the neutral thermospheric parameters (major neutral densities, neutral temperature and neutral wind field) from the equation-governed part of the scheme. These thermospheric values are considered as inputs and are variable in accordance with the current geophysical situation through the input set of geophysical indices in the respective models. The minor neutral components of the odd nitrogen chemical family (in the thermosphere and the upper mesosphere it is $N(^4S)$, $N(^2D)$, NO) are treated self-consistently by the coupled continuity equations.

Other physical inputs for the model are the large-scale convective electric fields, the polar auroral spatial precipitation pattern and quantitative characteristics such as number flux and characteristic energy, and the ionizing solar EUV radiation spectrum (direct radiation during daytime, and EUV fluxes scattered from the geocorona as the night ionization sources). These values in turn are produced by respective parameterization driven by geophysical indices. Hence, the direct input of the entire model is the set of geophysical indices describing the levels of solar and geomagnetic activity, location of the point of interest, time, and season. In addition to this traditional set of parameters, the electric field model by *Weimer* [1995] requires IMF (Interplanetary Magnetic Field) B_y and B_z components.

The following is a more detailed description of inputs and outputs of the ionospheric model, including intermediate values to be used in the system of governing equation and respective models for deriva-

tion of these intermediate parameters.

2.1.1. General inputs of the ionospheric model

The following direct inputs of the ionospheric model are chosen to describe the geophysical situation inside the entire polar region:

- season (Julian day) and Universal Time (UT)
- solar activity index $F_{10.7}$
- geomagnetic activity, interchangeable indices Kp, Ap, and AE
- IMF B_y and B_z components

This choice represents minimal requirements of input information for the ionospheric model. These geophysical indices are generally available for past periods, although significant gaps in B_z and B_y data are rather common, especially for geomagnetically disturbed periods. The solar activity index $F_{10.7}$ is measured daily, and the current value is available in real time. Its day-to-day variations usually are not large and the short-term (days) and long-term forecast (months and years) of this index is the most reliable among parameters of interest.

Geomagnetic activity indices Kp and Ap have 3-hour sampling and cannot represent faster geomagnetic variations. Auroral AE (Auroral Electrojet) index is more representative of short time variations in the polar regions and is available with 1 minute and 5 minutes temporal resolution. The established relationship between AE and Kp/Ap [*Rostoker*, 1991] allows us to use an "effective" Kp/Ap index that corresponds to the current AE as an input to Kp/Ap-driven models. However, the AE index is available with only a significant delay, which currently is several years. Short-time forecasts (12-24 hours) of geomagnetic activity are available in terms of Kp/Ap values, but the forecasts are unreliable and generally poor.

2.1.2. Neutral thermospheric models

We use a combination of two models to determine background thermo-

spheric parameters MSIS [*Hedin*, 1991] and VSH [*Killeen et al.*, 1987]. The MSIS model is a Legendre polynomial fit to a large data set of thermospheric measurements of different kinds. The VSH (Vector Spherical Harmonics) model is also a polynomial fit, but instead of data the archives of NCAR TIGCM runs performed for a variety of geophysical conditions are fitted. This model is combined with the MSIS model to generate the output for altitudes which are out of the height range of the TIGCM (100-500 *km*). The VSH model has been tuned to the climatological values of winds and densities that have been accumulated over many satellite passes [*Killeen et al.*, 1987]. Hence, the model combines the measurements' validity with a smaller scale variability of the parameters which a first principles model can provide. The horizontal resolution of the TIGCM is 5x5° and, thus, the resolution of VSH is not better. In the ionospheric model, the neutral thermosphere parameters are derived at a 445x445 *km* grid (approximately 4x4°) with subsequent interpolation for smaller scales.

The MSIS and VSH inputs, outputs, and connections to the ionospheric model are specified as follows:

input	season (Julian day), F10.7, Ap, UT, and the location
output	time-variable 3-D fields of $\mathbf{v}_n$, T_n, $[O]$, $[O_2]$, $[N_2]$
used for	- continuity equations (photochemical sinks and sources, diffusion coefficients, collision frequencies) - energy balance equation (heating parameterization, cooling rates due to various processes, thermal conduction coefficient) - equation of ion motion (collision frequencies, neutral wind drag) - initial condition (initial distribution of $[N(^4S)]$, and $[\bar{e}\,]$ from VSH model

The models generate time-varying 3-D fields of thermospheric

data, including the major component densities, neutral winds and temperatures. The parameters correspond to the geophysical situation specified from the set of basic geophysical indices. In addition to the neutral thermospheric data, the VSH model yields some ionospheric parameters that can be used as the boundary and the initial conditions. Although these values do not represent the polar ionospheric fine structures in their dynamics, these parameters are useful as an initial condition. Starting the calculations from a realistic ionization distribution considerably reduces the model run time and, consequently, reduces CPU resources that are necessary to achieve convergence of the numerical simulation to diurnally reproducible solutions.

2.1.3. Magnetospheric electric field models

Since the electric field input determines both the governing dynamic processes in the upper ionosphere and the major Joule heating source, it plays a crucial role in polar ionospheric modeling. However, only statistically averaged patterns are currently available and the meso-scale variability is not well known at this time. The breakthrough to the individual realization of the electric field pattern is the technique known as AMIE (Assimilative Mapping of the Ionospheric Electrodynamics) reconstruction (e.g., *Knipp at al.* [1994]). The CEDAR data base contains only a few periods, not exceeding 10 days altogether [*CEDAR Data Base Catalogue*, 1995], while the extended period of AMIE-reconstruction for the November 1993 Space Weather Event is under preparation. A promising approach is a program of remote measurements of ionospheric drifts by the chain of Doppler radars (SuperDARN) and recalculation to the electric fields values that will be available to the users in real time. As this thesis was written (late 1995), the program was in its initial stages. A statistical electric field model has been published recently that is based on data collected with ground-based radar (Goose Bay HF radar) that provides a point of comparison with satellite-based models [*Ruohoniemi and Greenwald*, 1995].

The following chart illustrates the inputs of different E-field

models, outputs, and the electric field used in the ionospheric model:

input	IMF components B_y, B_z ; cross-cap potential Φ
output	electric potential distribution or **E**-field components
used in	- equation of ion motion (Lorentz force components) - equation of ion energy balance, Joule heating term

Inputs are varying for different electric field models that were tested in the ionospheric model. For instance, the *Heelis* [1982] model requires as input the IMF B_y-component (with the limitation of $B_z \leq 0$) and the cross-cap potential (Φ) as the measure of geomagnetic activity. There are several parameterizations of the cross-cap potential in terms of geomagnetic activity. As an example of such a parameterization, a relation $\Phi\ [kV] = 17 + 17K_p$ is suggested by *Heppner and Maynard* [1987]. Electric potential patterns by *Heppner and Maynard* [1987] are specified only for two IMF configurations, for $B_z < 0$, $B_y < 0$ and for $B_z < 0$, $B_y << 0$ without quantitative characterization.

AMIE-reconstructions are period-specific and are available as arrays of potential data with several minutes temporal resolution. The most recent reconstruction for the magnetic storm period March 20-21, 1990 is performed with 5-minute sampling, while 10 minutes resolution was used for the earlier studies. Finally, the electric field model by *Weimer* [1995] is applicable to arbitrary IMF configurations and uses the IMF B_z, B_y - components as inputs.

The electric field pattern has a strong dependence on the IMF orientation. The effect of the IMF B_y-component is the asymmetric distortion of convection structures that may change the configuration of the polar cap flow. A southward orientation of B_z-component $(B_z < 0)$ generates a two cell vortex-like pattern with the anti-sunward flow in the polar cap. Several electric field models have been formulated predominantly for southward orientation of B_z [e.g., *Heelis*, 1982, 1984; *Heppner and Maynard*, 1987; *Rich and Maynard*, 1989].

Several parameterizations of the electric field were tested in

the ionospheric model. Earlier investigations [e.g., *Heelis et al.*, 1986; *Knipp et al.*, 1991] have demonstrated that positive or northward orientation of B_z ($B_z > 0$) significantly decreases the cross-cap potential and the intensity of convection and yields either an irregular pattern or multi-cell convection structure with combination of sunward and anti-sunward flows in the polar cap. Recent publications [*Rich and Hairston*, 1994; *Weimer*, 1995] have introduced the most comprehensive electric field models to date, including patterns for any orientation of the IMF B_z and B_y components (including northward B_z, $B_z > 0$). The model patterns are represented on figures 2.2a - 2.2d.

The ionospheric model was tested with "two-cell" electric field models that correspond to the numerical representation of potential patterns for $B_z < 0$ [*Heelis*, 1982; *Heppner and Maynard*, 1987; *Rich and Maynard*, 1989]. The current model version uses convection patterns derived by *Weimer* [1995]. This electric field model can be readily used for numerical simulations since it provides a digital representation of the potential for arbitrary orientation of IMF. This model is constructed from spherical harmonic coefficients that vary with different values of the tangential component of the IMF ($B_T = (B_z^2 + B_y^2)^{1/2}$), or in another version with the value of magnetic dipole tilt. The latter variable represents large-scale seasonal changes, while the former (B_T) causes geomagnetic activity [*Shue and Weimer*, 1994]. In the ionospheric model the B_T representation is chosen for the simulations of the ionospheric response to the real B_z and B_y variations. Bilinear interpolation between sixteen angular sectors of IMF orientation and four B_T ranges provides a continuous transition between the potential patterns for different values and orientations of IMF.

2.1.4. Solar EUV spectrum model

The solar EUV spectrum model derived by *Barth and Tobiska* [1990] is the most recent compilation of all up-to-date measurements of the solar EUV that takes into account numerous published corrections and calibrations. The approach of this model is the separation of solar

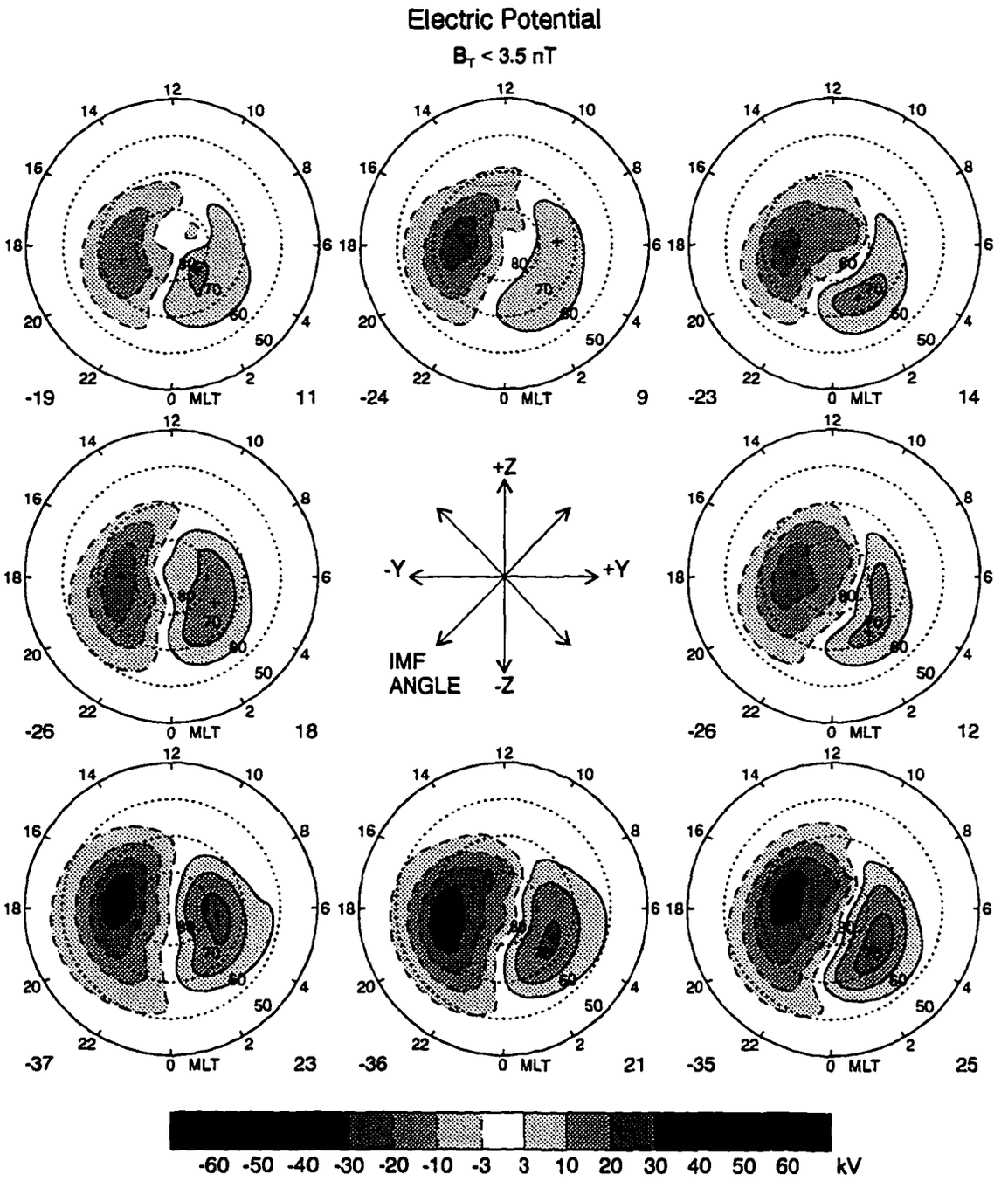

Figure 2.2a. Contour graphs of electric potential for tangential IMF component $B_T < 3.5\ \gamma$. The positive and negative potentials are indicated by solid and dashed lines, respectively. The numbers at the lower left and lower-right corners of each graph show the values of the smallest and largest potentials in each pattern, while the plus symbols mark the location of these points (from *Weimer* [1995]).

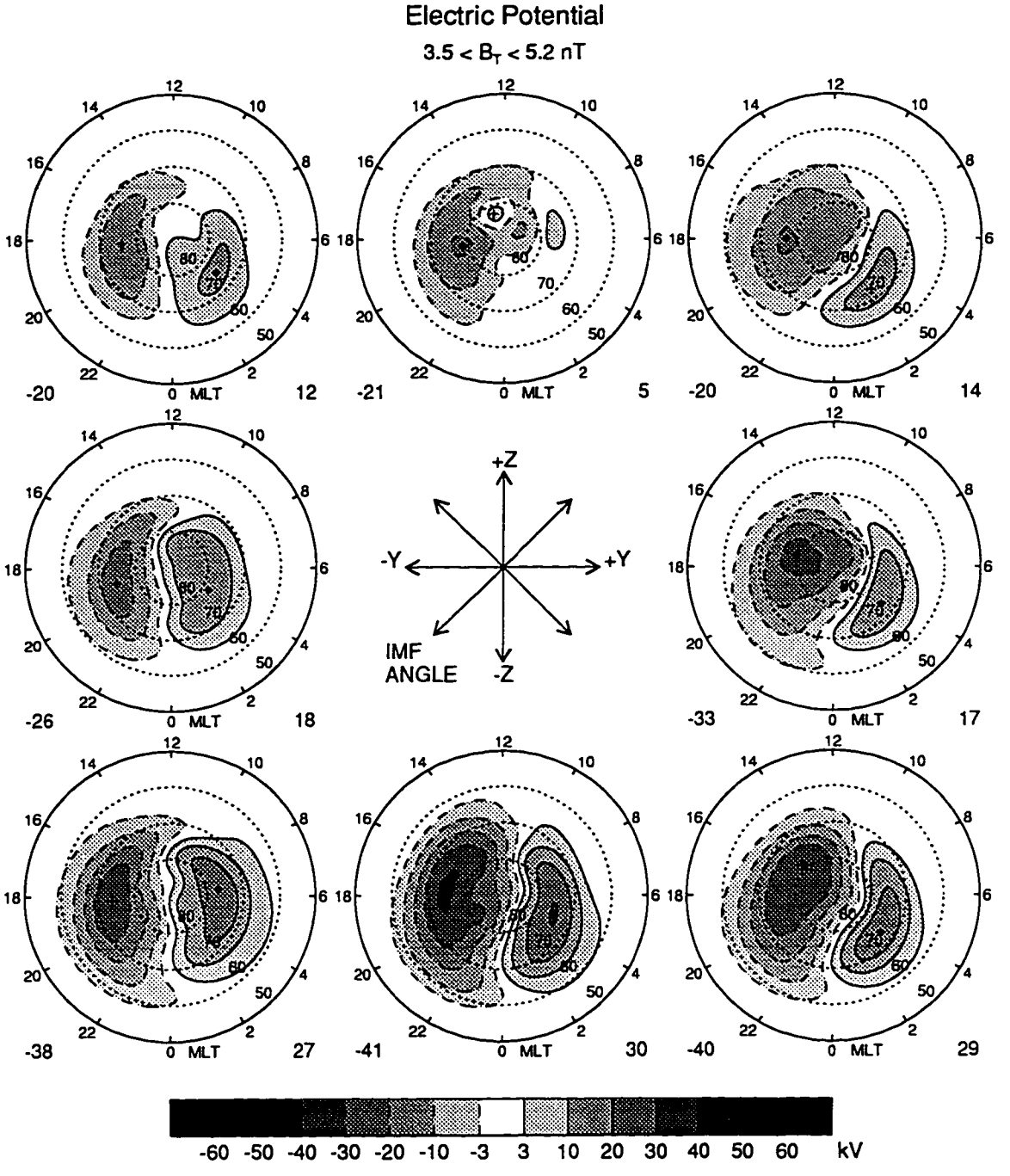

Figure 2.2b. Contour graphs of electric potential for $3.5\gamma < B_T < 5.2\gamma$ (from *Weimer* [1995]).

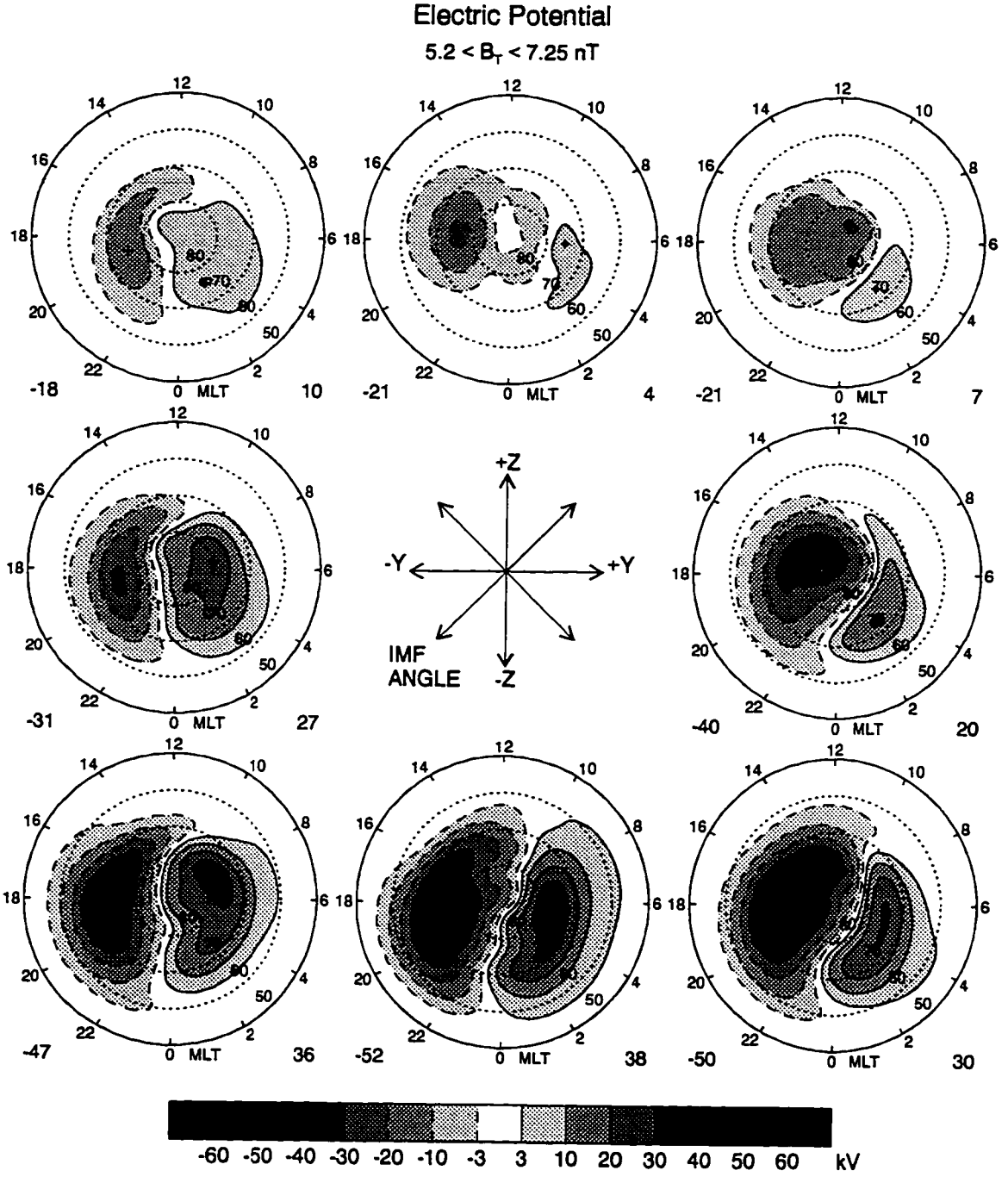

Figure 2.2c. Contour graphs of electric potential for $5.2\gamma < B_T < 7.25\gamma$ (from *Weimer* [1995]).

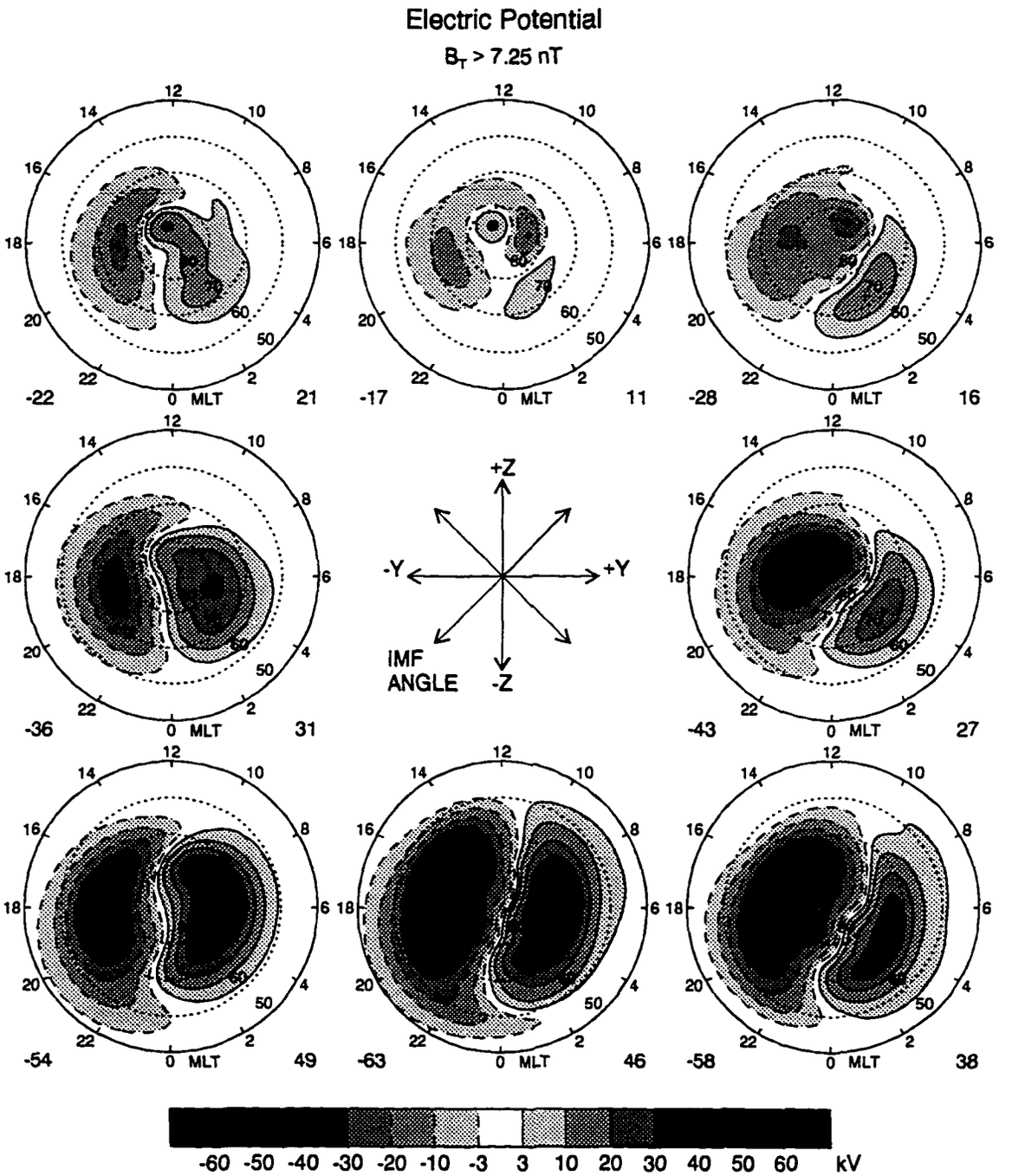

Figure 2.2d. Contour graphs of electric potential for $B_T > 7.25\gamma$ (from *Weimer* [1995]).

lines and continua in accordance to their origin at the Sun, with the subsequent double parameterization by two indices, $F_{10.7}$ (for irradiance from the solar corona and transitional regions) and the daily measured solar emission in the *H Lyman-α* line (for chromospheric irradiance).

The *H Lyman-α* line shows a quantitatively studied correlation with solar activity. Several parameterizations of the H Lyman-α irradiance as a function of the $F_{10.7}$ index are known from the literature (e.g., *Bossy* [1983]). Thus, for climatic-scale studies, when the EUV spectra accuracy is not the highest priority, the EUV model inputs can be simplified to only the $F_{10.7}$ index by introduction of corresponding parameterization of its second input, H Lyman-α line irradiance, in accordance with the $F_{10.7}$ index. The following chart represents EUV model inputs, outputs, and their use in the ionospheric model:

input	solar activity index $F_{10.7}$ (radio flux at λ=10.7 cm), (optional input: *H-Ly-α* line (1216Å) emission)
output	solar EUV spectrum intensity in 50Å ≤ λ ≤ 1050Å range
used in	ionization rate calculations

2.1.5. Secondary ionization by photoelectrons

Secondary ionization by photoelectrons is a significant addition to the primary processes. Simplified estimations give the efficiency of secondary ionization as one third of the primary ionization rate. Similarly, the efficiency level of 30% is adopted in the NCAR TIGCM global model.

However, in the ionospheric applications, especially those involving the lower ionospheric regions, a more rigorous approach can be adopted to account for a pronounced solar zenith angle dependence of the secondary ionization. A full-scale solution to the transport equation for photoelectrons is not a feasible approach for 3-D ionospheric modeling, and parameterization is necessary. An analytical parameteri-

zation of the solution of the photoelectron transport equation is derived by *Lilensten et al.* [1989]. The secondary ionization efficiency, defined as the ratio of the secondary ionization rate to the rate of the primary ionization by EUV photons, is parameterized by the solar zenith angle, altitude, thermospheric composition (through the latitudinal dependence of the parameterization), and the solar activity. The following chart illustrates the inputs and outputs of this parameterization, and their use in the ionospheric model:

input	$F_{10.7}$, solar zenith angle, latitude
output	altitude profile of the efficiency of the secondary ionization by photoelectrons
used in	ionization rate calculations

2.1.6. Auroral precipitation patterns

The statistical model of auroral precipitation characteristics by *Hardy et al.* [1987] is chosen as the basic input in the ionospheric model. The precipitation model is formulated with the geomagnetic activity index K_P as an input. It derives the following parameters for the given location:

input	geomagnetic activity level and geomagnetic coordinates of the location
output	number flux, energy flux, and characteristic energy of precipitation particles
used in	auroral ionization rate calculation

The model also derives the parameters of the auroral oval configuration, such as an average radius to the peak of precipitation at the given geomagnetic latitude, and the equatorward and polarward slopes of the radial cross-section of the precipitation intensity. The precipi-

tation model is formulated regardless of the IMF orientation and is driven only by the *Kp* index.

The precipitation model input, the *Kp* index, has inadequate time sampling (3 hours) to be used to describe rapid geomagnetic disturbances. However, the established quantitative relationship between AE and *Kp* indices [*Rostoker*, 1991] solves the problem, since the AE time resolution is adequate for our modeling purposes. Statistical auroral models such as that provided by *Hardy et al.* [1987] give only the averaged pattern of precipitation, corresponding to a given level of geomagnetic activity. These models cannot be expected to have a detailed accuracy sufficient for high resolution case studies or individual event modeling. A technique of re-calculating measured auroral spectral brightness images into time-dependent precipitation characteristics [*Rees*, 1992; *Rees at al.*, 1995] is the most suitable approach for that kind of model application.

2.1.7. Magnetic field model

A realistic main magnetic field is used in the model. The magnetic inclination, declination, and radial components are calculated by the NASA MAGSAT Fortran package in accordance with the spherical harmonics representation of the International Magnetic Field Reference Model (IGRF80) for a specified magnetic epoch.

2.1.8. Outputs of the ionospheric model

As shown on figure 2.1, the set of governing equations of the model includes the equation of motion for ions, continuity equations for ionized and minor neutral components, and energy the balance equation for ions and electrons (Chapter 3 in this thesis). The coefficients of these equations include the ionization and dissociation rates and photochemical sinks and sources (Chapter 4). Numerical algorithms (Chapter 5) are implemented to solve the equations in time on the 3-D spatial grid. The ionospheric model output is time-dependent 3-D fields of ion drift velocities $\mathbf{v}_i$; ion and electron temperatures T_i and

T_e; and concentrations of $[e^-]$, $[O^+(^4S)]$, $[O^+(^2D)]$, $[O^+(^2P)]$, $[NO^+]$, $[O_2^+]$, $[N_2^+]$, $[NO]$, $[N(^4S)]$, $[N(^2D)]$.

2.2. The model coordinates

The inertial model frame co-rotates with the Earth and the basic coordinates of the model are therefore geographic coordinates. Since the model covers only a limited polar region of the Earth, the curvature can be neglected and simple Cartesian geometry is applicable. An azimuthal equidistant projection is used to map the geographic longitude and latitude to the Cartesian frame, while the spherical radial distance is mapped as the vertical coordinate (see figure 2.3, upper panel). The primary region of interest for the model coverage is poleward of 50 degrees of geographic latitude. However, calculations are performed in a broader domain (figure 2.3, lower panel) to account for boundary effects, particularly when strong electric fields penetrate below 50 degree of latitude. *X*- and *Y*-axis are directed along meridians $90^\circ E$ and $180^\circ E$, respectively.

The azimuthal equidistant projection preserves the azimuth angles and meridional distances. However, it introduces linear distortions in the zonal direction. Although the distortions are negligible in the auroral zone and in the polar cap — the regions of the most interest for this model — the distortions can reach up to 10% near the equatorward edges of the computational domain.

Let us assume that the projection is to be made to the Cartesian plane, which has its origin at the Earth's pole and is tangential to the Earth at the pole. Then the azimuthal equidistant projection maps a point with co-latitude α on the Earth to the model plane at the distance r from the Cartesian system origin

$$r = \alpha R_E \qquad (2.1)$$

where α is measured in radians and R_E is the radius of the Earth.

The procedure is invariant for longitude λ, which is preserved

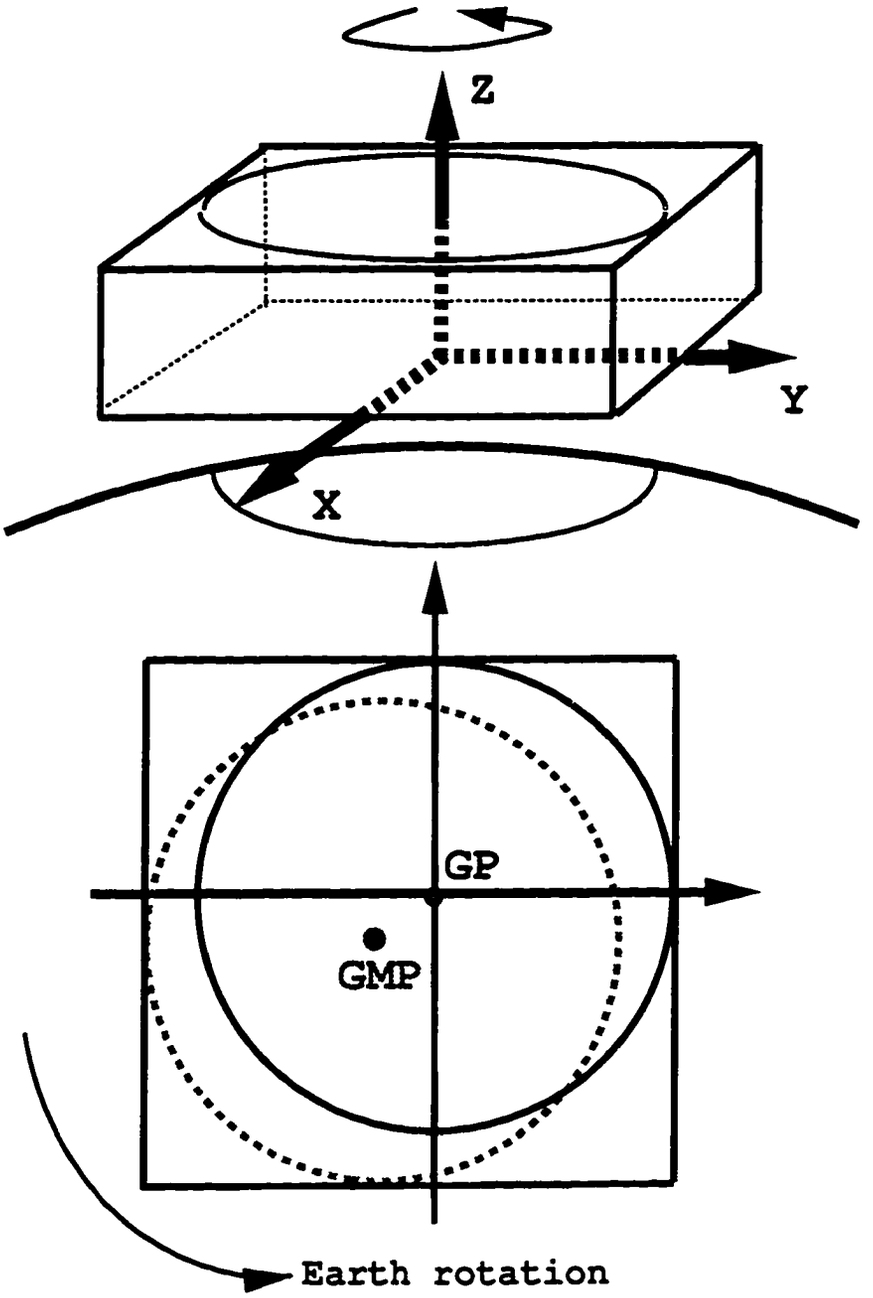

Figure 2.3. Corotating Cartesian coordinate frame of the ionospheric model (upper panel) and its horizontal cross-section (lower panel). To demonstrate the limits of the computational domain and the frame positioning, both geographic (GP, at the coordinates center) and geomagnetic poles (GMP) together with latitudes of 50° in both systems are schematically specified on the plot.

intact by the projection. This projection also preserves the distances in the meridional directions that become the radial directions in the Cartesian system. However, the zonal distances are increased by a factor of $\alpha/sin\alpha$. This can be seen by comparing expressions for the circumference of the latitudinal circle on the sphere $(2\pi R_E sin\alpha)$ and in the Cartesian plane $(2\pi R_E \alpha)$. The relative distortion factors are given in Table 2.1.

Table 2.1. Relative zonal distortion factor for azimuthal equidistant projection for the limited latitudinal region of interest

latitude, degr.	90	80	70	60	50	45	40
distortion factor, %	0.0	0.5	2.0	4.5	7.0	10.0	12.2

The distortion does not exceed a few percent in the region of primary interest of the model. However, the distortion can appear as an artificial deceleration of the zonal motion near the low latitude edge of the model. If the velocities are transformed from the spherical coordinate system to the model coordinate system, an introduction of the small correction coefficient of $sin\alpha/\alpha$ for the zonal velocity component can solve this problem.

This approach is applicable in this ionospheric model, since the involved velocities are found either as output of external models (neutral winds from MSIS/VSH models) in the geographic coordinate system or as an analytical solution of algebraic equations for ion drift velocity (section 3.3.1). The components of electric fields are found by the application of the numerical gradient procedure in the spherical system that excludes an appearance of the distorted Cartesian spatial steps.

Once the Cartesian coordinates of the regular mesh are established as $x_i = i\Delta x$, $y_j = j\Delta y$, their spherical equivalents are available from

$$\alpha_{ij} = \sqrt{x_i^2 + y_j^2} \;/\; \sqrt{\Delta x^2 + \Delta y^2} \tag{2.2}$$

$$\lambda_{ij} = \begin{cases} \tan^{-1}(y_j/x_i) & , \quad y_j \geq 0,\ x_i \neq 0 \\ 90 & , \quad y_j > 0,\ x_i = 0 \\ 180 + \tan^{-1}(y_j/x_i) & , \quad y_j \geq 0,\ x_i < 0 \\ -90 & , \quad y_j < 0,\ x_i = 0 \\ -180 + \tan^{-1}(y_j/x_i) & , \quad y_j \leq 0,\ x_i < 0 \\ o & , \quad y_j = 0,\ x_i = 0 \end{cases} \tag{2.3}$$

where α_{ij} is the co-latitude and λ_{ij} is the longitude of the ij-th point on the Cartesian plane, and Δx and Δy are the spatial steps in x- and y-directions, respectively. Expressions (2.2) and (2.3) establish relations between two sets of coordinates, Cartesian $\{x_i, y_j\}$ and geographic $\{\alpha_{ij}, \lambda_{ij}\}$.

Several inputs of the ionospheric model, such as the thermospheric models MSIS/VSH, the magnetic field model, and others, generate their output in the spherical geographic system. In this case the inputs calculated at $\{\alpha_{ij}, \lambda_{ij}\}$ are projected to $\{x_i, y_j\}$. Other inputs of the ionospheric model are specified in the geomagnetic system, namely, the potential pattern of the magnetospheric electric field and auroral precipitations. Point by point transformation is used to convert the scalar fields specified in the geomagnetic system to the spherical geographic [*Baker and Wing*, 1989], and finally to the model Cartesian frame. The intermediate values, such as the zonal and meridional components of the electric field vector, are calculated by the numerical application of the gradient procedure in the distortionless spherical frame. The vector values specified in terms of the geographic zonal u and meridional v components are converted to Cartesian x,y-components by applying the following procedure

$$\begin{aligned} v_x &= Sign(v)\ \cos(\lambda+\beta)\ \sqrt{v^2 + u^2} \\ v_y &= Sign(v)\ \sin(\lambda+\beta)\ \sqrt{v^2 + u^2} \end{aligned} \tag{2.4}$$

where angle β defines a vector direction with regard to the local meridian

$$\beta = \begin{cases} -\tan^{-1}(u/v), & v \neq 0 \\ \frac{\pi}{2} Sign(u), & v = 0 \end{cases} \tag{2.5}$$

and function $Sign(x)$ is defined as

$$Sign(x) = \begin{cases} -1, & x \leq 0 \\ +1, & x > 0 \end{cases} \tag{2.6}$$

and λ is the geographic longitude, v is the meridional and u is the zonal components of an arbitrary vector, and v_x, v_y are the x- and y-components of this vector in the Cartesian frame.

2.3. The model spatial and temporal resolution

During the last few years, high resolution polar ionospheric modeling has emerged as a field of intensive development. Research interests have shifted to mesoscale and, even further, to microscale phenomena, accounting for realistic variability of ionospheric parameters. Better inputs, such as new comprehensive models of electric fields and auroral images that provide precipitation characteristics for individual events with resolutions as good as tens of kilometers [*Rees*, 1992], have become available. On the "climate-weather" scale, this stage is comparable to the "space weather" studies, the term which has become widespread and is used in the title of the National Space Weather Program.

At high latitudes the mesoscale ionospheric structures are of prime interest. These are known as "patches" and "blobs" that have characteristic horizontal sizes from 1000 to 100 *km*. Consequently, the development of the models with horizontal resolutions of at least 100 *km* is necessary to study these phenomena. The model developed in this thesis aims to achieve this resolution.

One of the model's features is its scaleable resolution in the

horizontal plane. The horizontal resolution is one of the inputs for the particular model run and resolutions of $2x2^{\circ}$, $1.5x1.5^{\circ}$, and $1x1^{\circ}$ were tested in the model current version based on a workstation computational platform with limited memory resources.

The temporal resolution of the model is also flexible. The algorithm (see Chapter 5 for details) is numerically stable in a wide range of time steps. Typically, the calculations for this thesis were performed with 5-minute time steps, while other time steps from 1 to 30 minutes were tested.

The vertical coverage of the ionospheric model has been chosen from both physical and numerical considerations. The lower height boundary of the model is chosen at 80 km, at the lowest level where the heavy cluster ions and negative ions are negligible. The upper boundary is 500 *km*, a level where the convenient boundary condition of diffusive equilibrium is applicable and many simplifications are still valid. For instance, H^+, He^+ ion densities are negligible compared to O^+, ion thermal conductivity is negligible, the the relaxation time for ion heating does not exceed a few tens of seconds, making steady state assumptions valid for the ion temperature.

The densities and diffusion coefficients vary exponentially with the height in the thermosphere. Conditions for accuracy of the numerical algorithms require that the height resolution is less than the scale height. A height step of 10 *km* appears to be a good compromise between the computational limitations and accuracy considerations. This resolution is quite sufficient to describe the parameters of interest on *F2* region heights, including height of main ionospheric maximum. On the other hand, it is a reasonable approximation for the lower heights of *F1* and *E* regions.

2.4. Corotating frame of the model

The model frame is the corotating regular frame with even coverage of the region of interest that is preserved throughout the run to sustain the specified resolution. Another frame option, the Lagrangian frame moving with the advective velocity in the horizontal direction,

is not effective for this application due to the following reasons:

- initially even coverage of the region of interest gets severely distorted during the run of a moving frame model that requires additional efforts to sustain the specified resolution throughout the computational domain (figure 2.4);
- maintaining high spatial resolution would require decreasing of the model time steps significantly, since for the moving frame its horizontal displacement (and, thus, resolution) is determined by the time step through the kinematic relation ($\Delta x = v\Delta t$); and
- limitations of the Lagrangian approach require a uniform vertical profile of the horizontal velocity. This excludes the lower ionosphere effects of the vertical drift shear from consideration and precludes a wide class of possible applications in the lower ionosphere (sporadic *E* layer, the height-dependent perpendicular ion currents, self-consistent treatment of minor neutrals with account of the horizontal dynamics, and others).

The corotating frame is more advantageous for multi-grid applications, when some limited domain requires a higher resolution compared to other regions with coarser coverage (for instance, modeling in the vicinity of an Incoherent Scatter Radar). A Lagrangian trajectory must be followed even if it leaves the region of interest because that trajectory may re-enter the high-resolution domain at later times. Thus, the true separation of the high-resolution domain in the Lagrangian frame is only conditional, calculations of the same resolution must be performed in a much broader region.

A likely development in computer technology of massively parallel architectures with distributed memory necessitates an analysis of how a particular computational approach is suitable for the parallel implementations. The corotating frame operates with a fixed in time 3-D computational domain. This approach allocates neighboring sub-domains in the mesh-space to neighboring processors in partition. Hence, the possibility of local representation of finite differences and the local

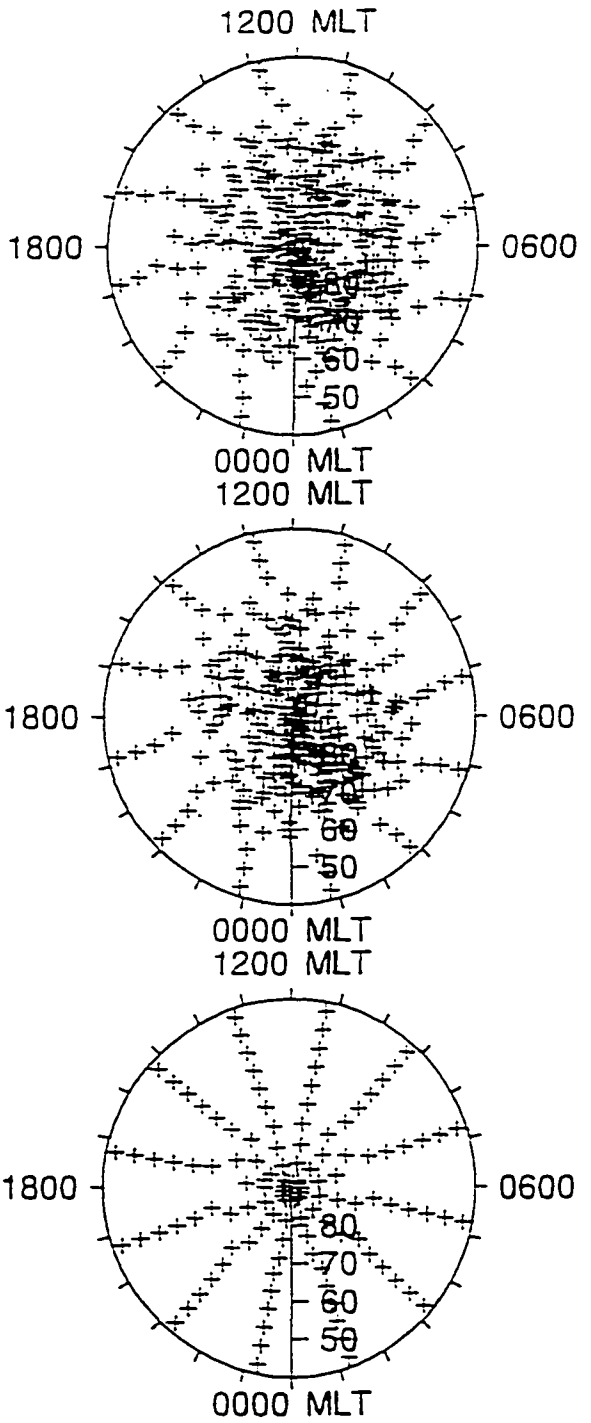

Figure 2.4. Initial spacing of the trajectories in the Lagrangian frame (bottom panel) and their positions after one (middle panel) and three (top panel) model days (from *Schunk and Sojka*, 1995). Even coverage of initial spacing gets distorted during the model run and the zones of rarefied and excessively tight coverage are created.

computation and allocation of coefficients of the equations in the distributed memory simplifies an effective partition of the problem and provides a high parallelism for the algorithm by minimization of interprocessor overhead. Thus, the predictability and regularity of the 3-D computational domain becomes an advantage for implementation in massively parallel architectures.

A corotating frame has its own disadvantages. The numerical solution of the mixed diffusive-advective PDE in 3-D is mathematically more complex when compared to the case of a one-dimensional parabolic equation to which the problem is reduced by adoption of a moving frame. The corotating frame introduces the problem of the proper choice for the low-latitude boundary condition; a problem that is avoided in the moving frame.

These issues are addressed in Chapter 5 of the thesis. Several options for the low-latitude boundary conditions are tested and the domain limits are chosen to minimize their possible interference. An effective numerical algorithm is developed by splitting the vertical (diffusion) and the horizontal (advection) directions into separated finite-difference representation.

CHAPTER 3

SYSTEM OF GOVERNING EQUATIONS

3.1. Quasi-hydrodynamic approach

The terrestrial atmosphere can be characterized as a non-equilibrium mixture of different gases in partially ionized and excited states. It can be described in terms of a general kinetic approach with the Boltzmann equation for corresponding distribution functions. Under some physical restrictions on the spatial scales and characteristic relaxation times, the general kinetic Boltzmann equation can be approximated by the equations for the first velocity moments of the distribution functions, i.e. concentration, velocity, and energy [*Schunk*, 1975]. These limitations, both on spatial and temporal scales, generally hold true throughout the entire height range of interest (80-500 km). Thus, the transition to the system of equations for moments is physically justified for the thermosphere.

However, these simplifications are mathematically insufficient for the system solution. Since the unknown $(i+1)$-th moment is involved in the equation for i-th moment, the chain of equations must be truncated to be solved. It is possible to apply physical considerations to express a high moment in terms of lower order moments to effectively truncate the system. At present, 5-moments and 13-moments approaches are generally used. Use of the 13-moments approach is mostly limited to the theoretical analysis and modeling of aeronomical situations in one vertical dimension. The 5-moments approach is known as the quasi-hydrodynamics approach and is widely used for modeling in practice, including 3-D global circulation models.

The present model is formulated in the framework of the quasi-hydrodynamic assumption. The governing model equations are the equation of continuity, equation of motion, and equation of energy balance for each considered species. The higher moments of the distribution function, stress tensor and heat flow vector, are not included in this

equation set. To close the system these parameters are expressed in terms of already defined physical quantities. In addition to these equations, the equation of state for an ideal gas is included to relate the temperature *(T)* and concentration *(n)* of a particular component with its partial pressure *($p = nkT$)*.

Since the characteristics of major thermospheric components are derived from empirical thermospheric models, the approach is not completely self-consistent. Throughout this work we assume that temperature, velocity, and concentrations of major thermospheric components *[O, O_2, and N_2]* are fully determined by background thermospheric models and are varied in accordance with the thermospheric model input (through the set of geophysical indices). Hence, the governing equations are derived for ionized and minor neutral species only.

This simplification is common in ionospheric modeling and is based on the fact that the charged component typically represents only one thousandth part of the thermospheric density at *F*-region heights and one millionth part in the *E* region. Nonetheless, the ionosphere is a considerable source of the heat and momentum to the neutral thermosphere. To investigate whether the separate treatment of neutral and charged components is quantitatively justified, comparisons of both coupled and uncoupled approaches were performed.

A fully self-consistent ionosphere-thermosphere approach has demonstrated that while the polar winter ionosphere substantially affects the thermospheric wind system and temperatures in certain regions [*Roble and Ridley*, 1987], this influence is not dominant. The separated and, rigorously speaking, not fully self-consistent treatment of the thermosphere and ionosphere is still a reasonable and practical approach. Comparison of high-latitude responses of the UCL-TDTM model (a fully self-consistent approach) and Utah State University Time-Dependent Ionosphere model (USU TDIM, which uses empirical MSIS-86 as a thermospheric input and is hence not self-consistent model with respect to the thermospheric coupling) has shown that there are some regions that displayed significant differences, while the overall agreement is mostly within a surprisingly good range of 10-30% for the *F2* region

peak electron density parameter (*NmF2*) [*Sojka et al.*, 1992]. The differences as high as a factor of two were found equatorward from the boundary of auroral oval in the morning sector, and in the tongue of ionization, which were explained by the neutral temperature and composition changes due to the Joule heating and the corresponding perturbations in the ion composition.

For the heights of the ionospheric *F* region (200-600 *km*) at high-latitudes, the horizontal **ExB** ion drift has mainly a two-cell vortex pattern with anti-sunward flow between the cells that can be very intensive for periods of negative orientation of IMF. In these situations ion drifts can exceed velocities as high as 1 *km/sec*. The drag forcing by convecting ions is sufficiently strong to drive the neutral wind in a similar two-cell circulation pattern, which follows but temporally lags the pattern of ion convection. The lag time varies from tens to hundreds of minutes due to the dependency of the time constant for momentum transfer upon the highly variable ion density [*Roble*, 1992]. The steady-state situation that is never achieved is the coincidence of ion drift and neutral-wind patterns. However, the influence in the opposite direction (viz ion drifts affected by neutral wind) is not as significant at *F*-region altitudes since the collision frequency is small compared to gyrofrequency.

3.2. Energy balance equations

The general form for the energy balance equation in terms of the heat flow vector $\mathbf{q}$ and stress tensor $\mathbb{P}$ in the presence of local energy sources (Q) and sinks (L) can be written as follows

$$\frac{N}{2} k \frac{D(nT)}{Dt} = - \frac{5}{2} nkT \nabla\cdot\mathbf{v} - \nabla\cdot\mathbf{q} - \mathbb{P}:\nabla\mathbf{v} + Q - L \qquad (3.1)$$

where $D(nT)/Dt \equiv \partial(nT)/\partial t + \mathbf{v}\cdot\nabla(nT)$ is the derivative taken along the trajectory of motion of the gas parcel moving with the velocity $\mathbf{v}$, N is the number of degrees of freedom ($N=3$ for mono-atomic gas, $N=5$ for di-

atomic molecules), k is the Boltzmann constant, n is the density, and T is the gas kinetic temperature. The processes of heat advection, $\mathbf{v}\cdot\nabla(nkT)$, cooling due to expansion or heating due to compression under the effect of scalar pressure variations $(-5/2nkT\nabla\cdot\mathbf{v})$, divergence of the heat flow vector $(-\nabla\cdot\mathbf{q})$, viscous heating due to stress in the fluid $(-\mathbb{P}:\nabla\mathbf{v})$, and local energy sources (Q) and sinks (L) are included in the general equation of energy balance.

Two higher velocity moments of the distribution function are presented in the energy balance equation, the heat flow vector $\mathbf{q}$ and the pressure tensor $\mathbb{P}$. To close the system of moments equations, these quantities must be expressed in terms of temperature, velocity components, and pressure, combined with coefficients of thermal conductivity, viscosity, and the thermoelectric coefficient. The heat flow vector $(\mathbf{q})$ is a sum of thermal conductive heat flux due to temperature gradients and the heat carried by electrical currents in case of charged species. It is expressed as

$$\mathbf{q} = -\lambda\ \nabla T - \beta\ \mathbf{J} \tag{3.2}$$

where λ is the thermal conductivity and β is the thermoelectric coefficient.

The pressure tensor components will be discussed in detail in the Section 3.3, which is devoted to the momentum equation. Here we assume that viscous heating can be neglected for the charged components.

Equation (3.1) is written in the most general form and is applicable to neutrals, ions, and electrons. It is assumed that the temperature is the same for all species inside the multi-species group such as ions (and, for that matter, neutrals). Therefore, only ion and electron temperatures (T_i and T_e) are subject to determination from the equations of energy balance in the model, while the neutral temperature (T_n) is an input taken from the background thermospheric model.

3.2.1 Energy balance equation for electrons

The equation of electron gas energy balance can be derived [*Rees*, 1989] in the framework of certain assumptions:

- the dominance of local sources compared to energy transport;
- negligible heat transport across the field by advection, by adiabatic heating and cooling, and by conduction, compared to the field-aligned transport;
- viscous heating or cooling is negligible;
- heating from exothermic chemical reactions is small.

Neglecting viscous heating one can rewrite the general equation of energy balance for electrons as follows

$$\frac{3}{2}k\left[\frac{\partial(n_e T_e)}{\partial t} + \mathbf{v}_e\cdot\nabla(n_e T_e)\right] = -\frac{5}{2}kT_e n_e \nabla\cdot\mathbf{v}_e - \nabla\cdot\mathbf{q} + Q_e - L_e \qquad (3.3)$$

where Q_e is the electron heat sources (mainly heating by Coulomb collisions with suprathermal electrons) and L_e is the electron heat sinks (cooling by elastic and inelastic collisions with neutrals).

Since for electrons the energy transfer across the field is negligible, the only important direction is field-aligned. Height profiles of electron temperature can be determined in every latitude-longitude grid cell without accounting for energy transport across the field. Therefore, the task of determination of the electron temperature field is essentially a 1-D problem to be solved on a 2-D grid, which is a much simpler approach compared to the direct 3-D consideration.

In the field-aligned direction, the ambipolar diffusion velocity is dominant. It can be expressed in terms of the polarization electric field **E** and the sum of collision frequencies with the major neutral components $\nu_e = \sum_n \nu_{en}$ as

$$\mathbf{v}_e = -\frac{1}{n_e m_e \nu_e}\left[k\,\nabla(n_e T_e) + n_e e\,\mathbf{E}\right] \qquad (3.4)$$

where the gravitational force on electrons is neglected and the the drift velocity is dominated by field-aligned electron ambipolar diffusion. Due to the greater electron mobility compared to ions, the parallel current can be expressed in terms of electron flow only, as follows,

$$\mathbf{J}_e = - n_e e \mathbf{v}_e = \frac{e}{m_e \nu_e} \left(k n_e \nabla T_e + k T_e \nabla n_e + n_e e \mathbf{E} \right). \qquad (3.5)$$

The heat flow vector $\mathbf{q}$ from equations (3.1, 3.2, 3.3) is the next higher velocity moment of the distribution function. It can be expressed as $\frac{1}{2} mn\overline{C^2 \mathbf{C}}$, where $\mathbf{C}$ is the random velocity of the gas particles. For a Maxwell distribution one can obtain, after averaging,

$$\mathbf{q}_e = - \frac{5kT_e}{2m_e \nu_e} \left(2kn_e \nabla T_e + k T_e \nabla n_e + n_e e \mathbf{E} \right). \qquad (3.6)$$

The polarization field $\mathbf{E}$ due to gravitational separation of heavy ions and light electrons can be eliminated between equations (3.5) and (3.6). The heat flow vector can be expressed explicitly in terms of current and electron temperature gradients, which defines the coefficients of thermal conductivity and the thermoelectric coefficient as a combination of known parameters

$$\mathbf{q}_e = - \lambda_e \nabla T_e - \beta_e \mathbf{J} = - \frac{5k^2 T_e n_e}{2 m_e \nu_e} \nabla T_e - \frac{5kT_e}{2|e|} \mathbf{J}_e \qquad (3.7)$$

where the thermoelectric term contribution is negligible compared to the thermal conduction. This is justified by the condition of electrical neutrality that results in a reverse field-aligned current in response to the current carried by the incoming flux of bombarding electrons. The net current is small and this assumption is valid at all altitudes [*Rees et al.*, 1971; *Rees and Roble*, 1975; *Schunk and Nagy*,

1978]. Thus, all current related terms in (3.3) are negligible.

The thermal conductivity coefficient λ_e is a tensor quantity due to the terrestrial ionospheric anisotropy caused by the Earth's magnetic field

$$\lambda_e = \begin{vmatrix} \lambda_\perp & -\lambda_H & 0 \\ \lambda_H & \lambda_\perp & 0 \\ 0 & 0 & \lambda_{oe} \end{vmatrix} \tag{3.8}$$

where $\lambda_{oe} = \frac{5}{2}(k^2 T_e n_e)/(m_e \nu_e)$ is the field-aligned thermal conductivity, $\lambda_\perp = (\lambda_{oe}\nu_e^2)/(\omega_e^2 + \nu_e^2)$ is the thermal conductivity in the direction perpendicular to **B** and parallel to **E**, and $\lambda_H = (\lambda_{oe}\nu_e\omega_e)/(\omega_e^2 + \nu_e^2)$ is the thermal conductivity in the direction perpendicular to both **B** and **E**, and $\omega_e = eB/cm_e$ is the electron gyrofrequency).

The electron gyrofrequency ω_e is much larger than the collision frequency ν_e throughout almost the whole height range of interest (80-500 *km*), except for its lowest part (where a local equilibrium condition is applicable to the electron temperature and differences) between T_e and T_n are negligible). Therefore, the coefficients $\lambda_\perp$ and λ_H are small and anisotropic effects can be neglected. The scalar value of thermal conductivity coefficient $\lambda_e \cong \lambda_{oe}$ is a good approximation in the ionosphere.

The terrestrial ionosphere is only partially ionized. The electron-neutral collisions reduce the electron mean free path and consequently the thermal conductivity properties of the electron gas. The effect can be taken into account by introducing an effective thermal conductivity coefficient

$$\lambda_e = \frac{\lambda_{ei}}{1 + \lambda_{ei} / \sum_n \lambda_{en}} \tag{3.9}$$

where λ_{ei} is electron-ion thermal conductivity coefficient, and the λ_{en} are thermal conductivity coefficients due to electron-neutral colli-

sions [*Banks*, 1966a] (summation over all major neutral components, *n*, is implied here).

A theoretical expression for the electron-ion thermal conductivity coefficient λ_{ei} was derived for the case of a Maxwellian velocity distribution in a singly charged fully ionized plasma [*Spitzer*, 1956]

$$\lambda_{ei} = 7.7 \times 10^{5} \; T_e^{5/2} \qquad [eV \; cm^{-1} sec^{-1} K^{-1}]. \tag{3.10}$$

Expressions for λ_{en} are derived by *Banks* [1966a]

$$\lambda_{en} = \frac{2}{3} \frac{n_e}{n_n} k \left(\frac{8kT_e}{\pi m_e} \right)^{1/2} \left(\sum_n \overline{Q}_{Dn} \right)^{-1} \tag{3.11}$$

where $\overline{Q}_{Dn}$ are velocity-averaged momentum transfer cross-section and the summation is implied over all neutral species.

$$\overline{Q}_{Dn} = \left(\frac{m_e}{2kT_e} \right)^3 \int_0^\infty V_e^5 \, \sigma_{Dn}(V_e) \, exp \left[- \frac{m_e V_e^2}{2kT_e} \right] dV_e \tag{3.12}$$

$\overline{Q}_{Dn}$ can be calculated for a particular neutral species if the collision cross sections $\sigma_{Dn}(V_e)$ are available [*Banks*, 1966b; *Itikawa*, 1971, 1973]. Parameterizations (in units of cm^2) of momentum transfer cross-sections for different species are given below:

$$\begin{aligned}
\overline{Q}_{D\text{-}N_2} &= 2.82 \times 10^{-17} \; T_e^{1/2} - 3.41 \times 10^{-21} \; T_e^{3/2} \\
\overline{Q}_{D\text{-}O_2} &= 2.20 \times 10^{-16} + 7.92 \times 10^{-18} \; T_e^{1/2} \\
\overline{Q}_{D\text{-}O} &= 1.10 \times 10^{-16} + 6.27 \times 10^{-20} \; T_e
\end{aligned} \tag{3.13}$$

$$\overline{Q}_{D\text{-}He} = 5.69\times10^{-16}$$
$$\overline{Q}_{D\text{-}H} = 5.47\times10^{-15} - 7.45\times10^{-19}\, T_e \,. \qquad (3.13)$$

Substitution of equations (3.10-3.13) into an expression (3.9) gives the parameterized result for the thermal conductivity coefficient in units of $eV\ cm^{-1} sec^{-1} K^{-1}$

$$\lambda_e = 7.7\times10^5\ T_e^{5/2}\left(1 + 3.22\times10^4 \frac{T_e^2}{n_e} \sum_{j=1}^{5} n_j\ \overline{Q}_{Dj}\right)^{-1}. \qquad (3.14)$$

It has been shown by *Schunk and Walker* [1970] that the approximate expression (3.14), based on the simple free-path consideration, is accurate to within 20% at all altitudes throughout the ionospheric *E* and *F* regions. Note that for the limiting case of the diluted upper thermosphere at the altitudes above approximately 300 km the expression (3.14) reduces to the fully ionized gas conductivity λ_{ei}. For the lower thermosphere at altitudes below about 100 *km*, the electron-neutral collisions dominate.

Having derived the parameterized expression for thermal conductivity coefficient, we can proceed with the equation for electron temperature (3.3). We have already neglected all current-related terms compared to the thermal conduction. The time-dependency of equation (3.3) is also negligible since the time required for auroral electrons to penetrate the thermosphere and heat the ambient electrons is of the order of several seconds, which is short compared to the time scale of changes in the medium and the model time step (a few hundred seconds). A steady state assumption for the electron temperature equation results in substantial simplification of the mathematical procedures for its solution, since it permits the transition from partial differential equation to ordinary differential form. The final form of the electron energy balance equation with the account of magnetic field inclination by dip angle *I* is

$$\sin^2 I \ \frac{\partial}{\partial z}\left(\lambda_e \ \frac{\partial T_e}{\partial z} \right) + Q_e - L_e = 0 \ . \qquad (3.15)$$

This is an ordinary differential equation of second order that may be solved by a standard numerical procedure, the method of relaxation. The next section is devoted to parameterization of the terms Q_e (electron heat sources) and L_e (electron heat sinks).

3.2.2. Electron energy sources and sinks

Local sources (Q_e) and sinks (L_e) of electron energy are very important terms of equation (3.15). At low altitudes the electron temperature is dominated by the balance between local heating and cooling rates. Only above 150-200 *km* does the heat transport start to play a significant role, and it becomes dominant above 500-600 *km* [*Rees et al.*, 1971]. Heating of electrons may result from collisions with suprathermal electrons of different origin. Among them are photoelectrons created by solar EUV ($Q_{e\text{-}ph}$), secondary electrons created by precipitating particles ($Q_{e\text{-}p}$), and energetic electrons originating from the quenching reactions ($Q_{e\text{-}q}$). A noticeable source is heating due to the sink of electron population from predominantly the "cold tail" of the energy distribution function in dissociative recombination reactions ($Q_{e\text{-}dr}$). Another possible source of electron heating is heating due to perpendicular and parallel electric fields ($Q_{e\perp}$ and $Q_{e\parallel}$ respectively). The total electron heating (Q_e) must be determined as follows:

$$Q_e = Q_{e\perp} + Q_{e\parallel} + Q_{e\text{-}p} + Q_{e\text{-}ph} + Q_{e\text{-}q} + Q_{e\text{-}dr} \ . \qquad (3.16)$$

The electric field heating involves collisions of electrons with slower ions and neutrals. In other words, this is a Joule current dissipation and a simple expression for $Q_{e\parallel}$ is [*Rees et al.*, 1971]

$$Q_{e\parallel} = \frac{J_\parallel^{\,2}}{\sigma_\parallel} = \frac{e^2 F^2}{\sigma_\parallel \sin^2 I} = \frac{F^2 m_e (\nu_{en} + \nu_{ei})}{\sin^2 I \ n_e} \qquad (3.17)$$

where the parallel conductivity $\sigma_{\parallel}$ is determined by the electron mobility at the altitudes of interest. *Rees et al.* [1971] showed that this source is small at all altitudes under consideration, even in the case of strong auroral precipitation with strong flux *F*.

The electron heat source due to perpendicular electric ($Q_{e\perp}$) field is much more important, due to the considerably larger perpendicular field. The total source (including both ions and electrons) is $J^2/\sigma_{\perp}$ or $\sigma_{\perp}E_{\perp}^2$. To separate the contributions from ion and electron currents, the electron part of this source can be expressed in terms of energy transfer by the ion-electron and the neutral-electron collisions

$$Q_{e\perp} = \sum_i n_i \mu_{ei} \nu_{ei} (\mathbf{v}_e - \mathbf{v}_i)^2 + \sum_n n_n \mu_{en} \nu_{en} (\mathbf{v}_e - \mathbf{v}_n)^2 \qquad (3.18)$$

where summation over all species of ions *(i)* and neutrals *(n)* applies, μ_{et} is the reduced mass ($\mu_{et} = m_e m_t/(m_e + m_t)$, and ν_{et} is the momentum transfer collision frequencies, where subscript *t* stands for *i* for ions and *n* for neutrals. *Rees and Walker* [1968] have shown that in the presence of even a weak electric field with magnitude as low as 10 *mV/m*, this heating source is comparable with heating by secondary photoelectrons. Since the Joule dissipation is proportional to E^2 while other collisional sources are proportional to *E*, an increasing field can make this the dominant source.

Use of equation (3.18) requires knowledge of all drift and wind velocities. Momentum transfer collision frequencies (in units of sec^{-1}) are given by *Rees and Walker* [1968] and *Rees and Roble* [1975]

$$\nu_{ei} = \frac{4}{3}(2\pi)^{1/2} n_e \left(\frac{e^2}{4\pi\varepsilon_0 k T_e}\right)\left(\frac{kT_e}{m_e}\right)^{1/2} \ln\Lambda \cong 3.63 n_e \ln\Lambda \; T_e^{-3/2} \qquad (3.19)$$

where

$$\Lambda \cong \frac{3kT_e^2}{e}\lambda_D \qquad \text{and} \qquad \lambda_D = \left(\frac{kT_e}{4\pi e^2 n_e}\right)^{1/2} \qquad (3.20)$$

and for electron-neutral collisions

$$\begin{aligned}
\nu_{e\text{-}N_2} &= n(N_2)\ [3.07\times10^{-23}\ v^2 - 3.23\times10^{-39}\ v^4] \\
\nu_{e\text{-}O_2} &= n(O_2)\ [2.20\times10^{-16}\ v - 8.57\times10^{-24}\ v^2] \\
\nu_{e\text{-}O} &= n(O)\ [3.40\times10^{-16}\ v] \\
\nu_{e\text{-}H} &= n(H)\ [5.47\times10^{-15}\ v - 8.10\times10^{-31}\ v^3] \\
\nu_{e\text{-}He} &= n(He)\ [3.07\times10^{-23}\ v^2 - 3.23\times10^{-39}\ v^4]
\end{aligned} \tag{3.21}$$

where $$v = 2(kT_e/m_e)^{1/2}. \tag{3.22}$$

An exact expression for the Coulomb logarithm $ln\Lambda$ has been derived by *Itikawa* [1971]

$$ln\Lambda = ln\left(\frac{4kT_e}{\gamma^2 e^2 k_e}\right) - \left[\left(\frac{k_e}{k_i}\right)^2 + 1\right] ln\left\{\left[\left(\frac{k_e}{k_i}\right)^2 + 1\right]^{\frac{1}{2}}\right\} \tag{3.23}$$

where $ln\gamma = 0.577$ is Euler's constant and $k^2_{e,i} = 4\pi n_{e,i} e^2/kT_{e,i}$. The value of Coulomb logarithm varies insignificantly at the thermospheric heights and a constant value can be used (in the model we adopted the value of $ln\Lambda = 15.0$).

To evaluate the heating rate, it is possible to circumvent the explicit determination of the relative velocities. This expression for the heating rate has been derived by *Rees and Walker* [1968] in the reference frame of the neutral gas (here $\omega_i = \frac{eB}{cm_i}$ is gyrofrequency of ion species i)

$$Q_{e\perp} = \frac{E'^2_\perp}{B^2} m_e\left\{n_e \sum_n \nu_{en} + \sum_i n_i \nu_{ei}\left[1 + \left(\sum_n \frac{\omega_i}{\nu_{in}}\right)^2\right]^{-1}\right\} \tag{3.24}$$

where $E'_{\perp}$ is an effective electric field determined in the reference frame of the neutral gas. When the neutral gas velocity, $\mathbf{v}_n$, and electric field, $\mathbf{E}_{\perp}$, in the model reference frame are specified, the effective electric field, $\mathbf{E}'_{\perp}$, is

$$\mathbf{E}'_{\perp} = \mathbf{E}_{\perp} + \frac{1}{c}\mathbf{v}_n \times \mathbf{B} \tag{3.25}$$

or, introducing the meridional and zonal neutral velocity components v_n and u_n, respectively, and assuming that only the vertical magnetic field component ($B_z = B\ sinI$) contributes to $\mathbf{v}_n \times \mathbf{B}$ and neglecting the vertical neutral velocity component, we obtain

$$E'_{\perp} = [(E_{\perp}^{mer} - B\ sinI\ u_n/c)^2 + (E_{\perp}^{zon} + B\ sinI\ v_n/c)^2]^{1/2} . \tag{3.25a}$$

The principal auroral and/or day-time source of electron heating is due to Coulomb collisions of EUV photoelectrons and/or suprathermal electrons of auroral origin [*Stamnes and Rees*, 1983a] with ambipolar thermal electrons. This source was defined as $Q_{e\text{-}st} = Q_{e\text{-}ph} + Q_{e\text{-}p}$). If the flux $I(E,z)$ of suprathermal electrons integrated over all pitch angles is known for all altitudes z, the heating rate can be expressed (in units of $eV\ cm^{-3}\ sec^{-1}$)

$$Q_{e\text{-}st} = Q_{e\text{-}p} + Q_{e\text{-}ph} = n_e(z) \int_{E_c}^{\infty} I(E,z)\ L_e(E,z)\ dE \tag{3.26}$$

where E_c is the crossover energy at which the thermal electron and the photoelectron flux are equal. The upper limit of the integration can be reduced to about *10 eV* for all practical purposes. $L_e(E,z)$ is the stopping cross section or, in other terms, the amount of energy per electron which will be lost per unit distance $L_e(E,z) = [n_e(z)]^{-1} dE/dx$. A parameterization of the stopping cross-section offered by *Swartz et al.*, 1971 is valid for electrons above the thermal energy range (in

units of $eV\ cm^2$)

$$L_e(E,z) = \frac{3.37\times10^{-12}}{E^{0.94}\, n_e(z)^{0.03}} \left[\frac{E - E_e}{E - 0.53\, E_e}\right]^{2.36} \tag{3.27}$$

where $E_e = 3/2kT_e = 8.618\times10^{-5} T_e(z)$ is the electron temperature, and the suprathermal electron energy (E), are both expressed in eV units.

Hoegy [1977], solving the Boltzmann equation with kinetic approach, describes additional terms for the heating rate (in units of $eV\ cm^{-3}\ sec^{-1}$)

$$Q_{e\text{-}st} = n_e \left\{ \int_0^{E_c} I(E,z)\ L_e(E,z) P_e\, dE + \int_{E_c}^{\infty} I(E,z) L_e(E,z)\, dE + \right.$$
$$\left. + (E_c - 3kT_e/2) L_e(E,z) I(E,z) \right\} \tag{3.28}$$

where the first term corresponds to the heating by precipitating electrons that are degraded into the thermal energy regime. This term is negligible compared to the other two terms. The second term has already been introduced in (3.26). It describes the heating of ambient electrons by Coulomb collisions with precipitating or photoelectrons and contributes about half of the total heating. The third term, called the "surface" term [*Hoegy*, 1977], contributes as much as the remaining 50% of the total heating. Evaluation of the heating rate from precipitating electrons $(Q_{e\text{-}p})$ is very similar to the photoelectron case. Only the low energy distribution tail of primary and secondary particles below an energy of about 5 eV are effective in heating the ambient electron gas [*Schunk and Nagy*, 1978].

Both equations (3.26, 3.28) require knowledge of the flux of suprathermal electrons $I(E,z)$ to be used in the heating rate evaluation. Calculations of this flux are costly in terms of computer resources and this approach is not feasible for a 3-D model. A parameterized source of heating by suprathermal electrons that is used in the

global thermospheric-ionospheric model NCAR TIGCM [*Roble*, 1989] is expressed in terms of ionization rates q_i of different ion species (in units of $cm^{-3}sec^{-1}$) and the electron density and the densities of the major neutrals n_e, $n[O]$, $n[O_2]$, $n[N_2]$ (in units of cm^{-3}), respectively,

$$Q_{e-st} = \varepsilon \left[q[O^+] + q[NO^+] + q[O_2^+] + q[N_2^+] + q[N^+] \right] \qquad (3.29)$$

where $q[i]$ is the production rate of ion of species i, and the parameter ε is $\varepsilon = exp[-(12.75 + 6.941R + 1.166R^2 + 0.08034R^3 + 0.001996R^4)]$ with $R = ln\ [n_e/(n[O_2] + n[N_2] + 0.1\ n[O])]$. This parameterization is accurate within 15-20% compared with the solution of electron transport equation for the range of altitudes of interest [*Lummerzheim*, 1993, *private communication*].

The heating rate Q_{e-q} due to electron quenching of excited component, e.g. $N(^2D)$, $O^+(^2D)$, $O^+(^2D)$, is a small daytime source, noticeable only above 300 *km* [*Rohrbaugh et al.*, 1973].

The last term contributing to the heating rate in equation (3.16) is the heat source (Q_{e-dr}), due to selective removal of colder electrons by dissociative recombination of O^+ and NO^+ ions. It is also not very important since its effectiveness is only a few percent of suprathermal electron heating.

Several cooling processes are effective for the ambient electrons in the thermosphere (typical energy range *0.05-0.25 eV or 500-3000K*)

$$L_e = L_{e-rot} + L_{e-vib} + L_{e-fst} + L_{e-eex} + L_{e-n} + L_{e-i} \qquad (3.30)$$

where L_{e-rot} is the cooling from rotational excitation of N_2 and O_2; L_{e-vib} is due to vibrational excitation of N_2 and O_2; L_{e-fst} is due to atomic oxygen fine structure excitation; L_{e-eex} is electronic excitation of O, N, N_2 and O_2; and L_{e-n} and L_{e-i} are cooling due to elastic electron-neutral interactions and elastic collisions with positive ions, respectively. Each process has a different relative importance which depends on altitude and geophysical conditions. Generally the

most important contributions in the polar latitudes in the presence of aurora are vibrational excitation of N_2 and O_2, electronic excitation of atomic oxygen fine structure, and low-lying metastable states of O by electrons in the high-energy tail of the thermal distribution. Parameterized formulas for these processes are reviewed by *Schunk and Nagy* [1978] and the physical mechanisms of interaction are described in details by *Rees* [1989] and *Min* [1993].

a). Cooling due to rotational excitation of O_2 and N_2

Rotational excitation of O_2 and N_2 by electrons was analyzed by *Dalgarno* [1969]. The approach was based on the Born approximation, in which it is assumed that rotational excitation is caused by the long-range interaction of the electron and the quadrupole moment of the molecule. In the framework of the Born approximation, the general expression for the cooling rate of an electron gas due to rotational excitation of a molecular species with specified rotational constant and quadrupole moment was derived by *Mentsoni and Rao* [1963]. The following parameterizations for the process rates were provided by *Dalgarno* [1969] for the molecules of O_2 and N_2 (all loss rates are in units of $eV\ cm^{-3}\ sec^{-1}$)

$$L_{e\text{-}rot}(N_2) = 2.9\times10^{-14}\ n_e n(N_2) T_e^{-1/2} (T_e - T_n) \tag{3.31}$$

$$L_{e\text{-}rot}(O_2) = 6.9\times10^{-14}\ n_e n(O_2) T_e^{-1/2} (T_e - T_n)\ . \tag{3.32}$$

b). Cooling due to vibrational excitation of O_2 and N_2

Parameterized cooling rates due to vibrational excitation of O_2 and N_2 were introduced by *Stubbe and Varnum* [1972] and by *Prasad and Furman* [1973], respectively:

$$L_{e\text{-}vib}(N_2) = 2.99\times10^{-12}\ n_e n(N_2)\ \exp\left(f\frac{T_e - 2000}{2000\ T_e}\right)\cdot \cdot\left[\exp\left(-g\frac{T_e - T_n}{T_e T_n}\right) - 1\right] \tag{3.33}$$

$$L_{e\text{-}vib}(O_2) = 5.196\times10^{-13}\; n_e n(O_2)\; exp\left(h\frac{T_e - 700}{700\; T_e}\right)\cdot$$
$$\cdot\left[exp\left(-2770\;\frac{T_e - T_n}{T_e T_n}\right) - 1\right] \qquad (3.34)$$

where $f = 1.06\times10^{4} + 7.51\times10^{3}\; tanh\; [1.10\times10^{-3}\; (T_e - 1800)]$

$g = 3300 + 1.233\; (T_e - 1000) - 2.056\times10^{-4}(T_e - 1000)(T_e - 4000)$

$h = 3300 - 839\; sin[1.91\times10^{-4}(T_e - 2700)]$.

c). Cooling due to fine structure excitation of O

Electron gas cooling due to excitation of the fine structure of atomic oxygen is one of the most important cooling processes in the lower ionosphere. It was found to be a dominant electron energy sink below *220km* for day-time conditions [*Perkins and Roble*, 1978] and a noticeable sink in typical auroral conditions at the same altitudes [*Rees and Roble*, 1975]. The process $e + O(^3P_J) \longrightarrow e + O(^3P_{J'})$ affects the triplet ground state of $O(^3P_{0,1,2})$ and results in the loss of electron energy in amounts of *0.020eV*, *0.028eV*, and *0.008eV* for transitions *1-2*, *0-2*, and *0-1*, respectively. In terms of Kelvin degrees, the energy losses are *228K*, *326K*, *and 98K*, respectively. The process rate parameterized by *Hoegy* [1976] is

$$L_{e\text{-}fst} = 8.629\times10^{-6}\;\frac{n_e n(O)}{Z}\sum_j A_j B_1 B_2 B_3 T_e^{[B_j - 1/2]}\{\varepsilon_j (D_j - E_j^x)$$
$$+ 5.91\times10^{-9}(T_e - T_n)[(1 + B_j)D_j + (E_j/T_e + 1 + B_j)E_j^x]\} \qquad (3.35)$$

where T_o and T_1 are temperatures of the J=0 and J=1 levels respectively and $Z = 5 + 3\; exp(-228/T_1) + exp(-326/T_o)$. Summation over all tree transitions *(1-2, 0-2, 0-1)* applies, and in respective order, all other parameters in the expression (3.35) are

$$\varepsilon_j = 0.02,\; 0.028,\; 0.008;\quad D_j = exp\left(-\frac{228}{T}\right),\; exp\left(-\frac{326}{T}\right),\; exp\left(-\frac{98}{T}\right);$$

$$E_j^x = exp\left(-\frac{228}{T_e}\right),\ exp\left(-\frac{326}{T_e}\right),\ exp\left[-\left(\frac{98}{T_e} + \frac{228}{T_1}\right)\right];\ E_j = 228,\ 326,\ 98;$$

$$B_j = 1.019,\ 0.8998,\ 1.268;\ A_j = 8.58\times10^{-6},\ 7.201\times10^{-6},\ 2.463\times10^{-7}\ .$$

d). Cooling due to electronic excitation of O, N, O_2, and N_2

Electron energy losses due to electronic excitation of *O, N,* O_2, and N_2 at low-lying levels have different rates since the processes have different cross sections. For the case of atomic oxygen, only the excitation of $O(^1D)$ metastable state with the excitational threshold of *1.96 eV* is important. The next level $O(^1S)$ has the threshold of *4.17 eV,* which is too high to be an important sink for thermal energy. For electron temperatures as high as *3000K (0.25 eV)* there is a sufficient number of electrons in the high-energy tail of the Maxwellian distribution to result in the noticeable excitation of the $O(^1D)$ state. The energy sink is found to be a dominant one above *400 km* in auroral conditions [*Rees and Roble,* 1975]. The electron gas cooling rate by this process has been calculated by *Stubbe and Varnum* [1972]

$$L_{e\text{-}eex}[O(^1D)] = 1.57\times10^{-12} n_e\, n(O)\ exp\left(d\,\frac{T_e - 3000}{3000\ T_e}\right) \cdot\left[exp\left(-22713\ \frac{T_e - T_n}{T_e T_e}\right) - 1\right] \qquad (3.36)$$

where parameter $d = 2.4\times10^4 + 0.3(T_e - 1500) - 1.947\times10^{-5}(T_e - 1500)(T_e - 4000)$ and T_e and T_i are specified in units of *K.*

Only one low-lying electron state of atomic nitrogen, $N(^2D)$, with a threshold *2.37 eV,* is low enough to be excited by thermal electrons. Analytical expression offered for the cooling rate by *Rees and Roble* [1975] is as follows

$$L_{e\text{-}eex}[N(^2D)] = 3.4\times10^{-18} n_e\, n(N)\ \Omega(T_e)\ exp\left(-\frac{2.74\times10^4}{T_e}\right) T_e^{-1/2} \qquad (3.37)$$

where the effective collision strength $\Omega(T_e)$ is derived by *Henry and Williams* [1968]

$$\Omega(T_e) = 1.0\times10^{-4}T_e \ , \qquad T_e \leq 1000K$$

$$\Omega(T_e) = 0.1 + 8.5\times10^{-5}T_e \ , \qquad 1000K \leq T_e \leq 5000K$$

$$\Omega(T_e) = 0.44 + 5.8\times10^{-5}T_e \ , \qquad T_e \leq 10000K \ .$$

Molecular oxygen has two low-lying metastable levels that can be excited by thermal electrons; these are $O_2(a^1\Delta g)$ with an excitational threshold of *0.98 eV*, and $O_2(b^1\Sigma g^+)$ with threshold of *1.63* eV. However, the cooling rate for molecular oxygen is negligible since the molecular oxygen is abundant only in the lower thermosphere, and the electron temperature at those altitudes is not sufficient to excite the mentioned electronic states. This loss process needs to be considered only for intense auroral precipitation. Expressions for the cooling rates of the process are derived by *Prasad and Furman* [1973].

Although molecular nitrogen is abundant throughout the entire thermosphere, the energy threshold of the lowest electronic state $A^3\Sigma g^+$ is *6.5eV*. It is too high to make the process a noticeable sink for thermal electron energy.

e). Cooling due to elastic electron-neutral interactions

The rate of exchange of energy due to elastic collisions between two gases with different temperatures has been derived by *Desloge* [1962] under the assumption that the velocity distribution of both gases are Maxwellian. The small electron mass makes the relation particularly simple for the case of an electron-neutral pair

$$L_{e\text{-}n} = \frac{3k(T_e - T_n)}{m_n} n_e m_e \nu_{en} \qquad (3.38)$$

where ν_{en} is the Maxwellian averaged collision frequency

$$\nu_{en} = \frac{8n_n}{3\pi^{1/2}} \overline{Q_{Dn}} \left(\frac{2kT_e}{m_e} \right)^{1/2} \tag{3.39}$$

and $\overline{Q_{Dn}}$ are velocity-averaged momentum transfer cross section (equation 3.12) with the collisional cross sections obtained from integration of the differential scattering cross sections $\sigma_{en}(V_e,\theta)$ over the angle θ

$$\sigma_{eD}(V_e) = 2\pi \int_0^{\pi} (1 - \cos\theta)\, \sigma_{en}(V_e,\theta)\, \sin\theta\, d\theta \ . \tag{3.40}$$

Parameterizations for collision frequencies and momentum transfer cross sections of neutral species of thermospheric interest have been introduced in (3.12) and (3.13), respectively. Using these relationships, the cooling rates for different species can be expressed as follows [*Schunk and Nagy*, 1978]

$$\begin{aligned}
L_{e\text{-}N2} &= 1.77\times10^{-19} n_e\, n(N_2)\, [1-1.21\times10^{-4} T_e]\, T_e\, (T_e - T_n) \\
L_{e\text{-}O2} &= 1.22\times10^{-18} n_e\, n(O_2)\, [1+3.6\times10^{-2} T_e^{1/2}]\, T_e^{1/2}\, (T_e - T_n) \\
L_{e\text{-}O} &= 7.9\times10^{-19} n_e\, n(O)\, [1+5.7\times10^{-4} T_e]\, T_e^{1/2}\, (T_e - T_n) \\
L_{e\text{-}H} &= 9.63\times10^{-16} n_e\, n(H)\, [1-1.35\times10^{-4} T_e]\, T_e^{1/2}\, (T_e - T_e) \\
L_{e\text{-}He} &= 2.46\times10^{-17} n_e\, n(He)\, T_e^{1/2}\, (T_e - T_n) \ .
\end{aligned} \tag{3.41}$$

The total cooling rate due to electron-neutral elastic collisions is the sum of all rates with the account for particular ratio of the species concentration in the total distribution.

f). Cooling due to elastic collisions with positive ions

The differential scattering cross section for elastic electron-ion Coulomb interactions is given by the Rutherford formula. For singly charged ions it is

$$\sigma_{ei}(V_e,\theta) = \left(\frac{e^2}{2m_e V_e^2}\right)^2 \sin^{-4}\frac{\theta}{2} \qquad (3.42)$$

Substitution of an explicit expression for $\sigma_{ei}(V_e,\theta)$ into equation (3.40) gives the following relationship for the ion electron momentum transfer cross-section

$$\overline{Q_{Di}} = 16\pi \left(\frac{e^2}{2m_e V_e^2}\right)^2 ln\Lambda \qquad (3.43)$$

where $ln\Lambda$ is the Coulomb logarithm defined previously (equation 3.23). Combining expressions (3.38), (3.39), and (3.43) one can obtain an expression for velocity averaged electron-ion collision frequency (equation 3.19) and electron gas cooling rate due to electron elastic interactions with the single charged ion species i

$$L_{e-i}(i) = \frac{4(2\pi)^{1/2}}{m_i} n_e n_i e^4 \frac{k(T_e - T_i)}{(kT_e)^{3/2}} ln\Lambda \ . \qquad (3.44)$$

For a mixture of the major ions, the parameterized expression for the cooling rate of electron gas will be

$$L_{e-i} = 3.2\times10^{-8} n_e \frac{(T_e - T_i)}{T_e^{3/2}} ln\ \Lambda\cdot \qquad (3.45)$$

$$\cdot[n(O^+) + 0.5\, n(O_2^+) + 0.53\, n(NO^+ + 4\, n(He^+) + 16\, n(H^+))] \ .$$

An assumption that all ions have the same temperature Ti is implied in derivation of expression (3.45). Although there are some differences in the temperatures of different ion species, this effect is negligible on the electron temperature in the region of interest.

The relative importance of the various electron cooling rates is dependent upon the geophysical conditions. Figure 3.1 shows a comparison of the cooling rates for typical daytime conditions.

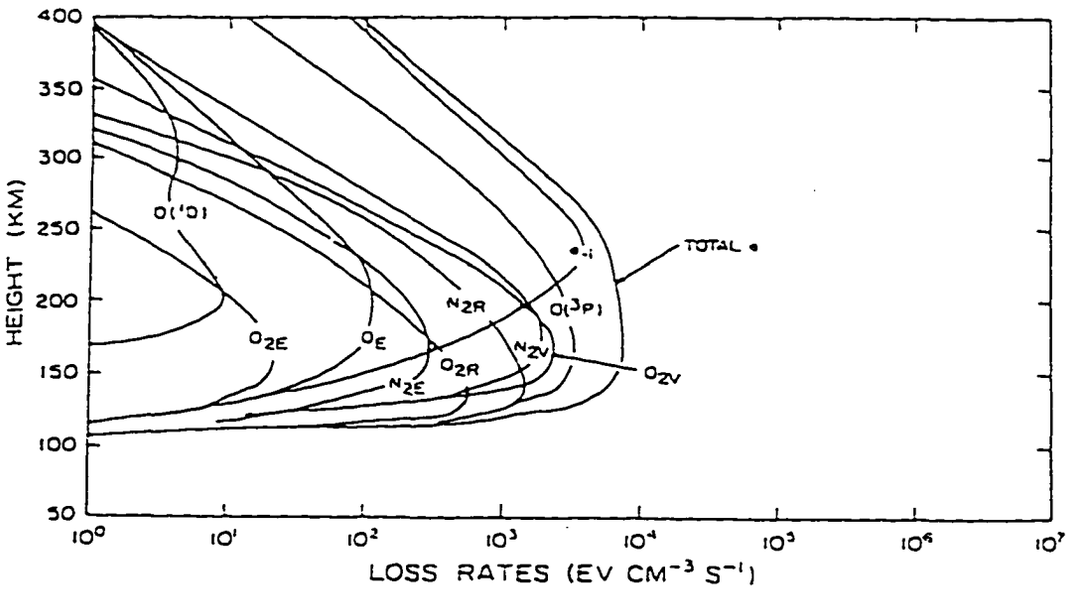

Figure 3.1. Electron energy loss rates profiles in the daytime ionosphere. The curves labeled N_2V and O_2V represent losses due to the excitation of the vibrational states, N_2R and O_2R represent losses in the excitation of rotational levels, for molecular nitrogen and oxygen, respectively. N_2E, O_2E, OE represent losses due to elastic collisions between electrons and the neutral species. The curve labeled $O(^1D)$ represents the losses in the excitation of the corresponding electronic state of atomic oxygen O, and that labeled $O(^3P)$ the losses due to the excitation of fine structure levels in O. The curve labeled e-i represents the losses in Coulomb collisions between electrons and ions (from *Perkins and Roble* [1978]).

3.2.3. Energy balance equation for ions

The ion energy balance equation is applied to the ion gas as a whole, despite the small temperature differences between different ion species. In the upper thermosphere, the largest difference is between O^+ and H^+ temperatures, which does not exceed *200K*, while the temperature difference of O^+ and He^+ does not exceed *50K*. Thus, the largest difference is less than 10% and the single temperature approach is valid for more collisionally coupled ions in the *F* and *E* regions.

The ion energy balance equation can be derived from the Boltzmann equation

$$\frac{3}{2}k\left[\frac{\partial(n_i T_i)}{\partial t} + \mathbf{v}_i\cdot\nabla(n_i T_i)\right] = -\frac{5}{2}kT_i n_i \nabla\cdot\mathbf{v}_i - \nabla\cdot\mathbf{q}_i + Q_i - L_i \qquad (3.46)$$

where Q_i is the local ion heating sources (exothermic chemical reactions, frictional heating by external electric field drift, Coulomb collisions with electrons), L_i is the local ion heat sinks (elastic non-resonant ion-neutral collisions, resonant charge transfer with parent neutral, e.g. $O^+ + O \longrightarrow O + O^+$) and other terms are similar to the terms in equation (3.3) with the substitution of subscript *i* for ions.

Similar to the case of the electron temperature balance, the major transfer of ion energy takes place in the vertical direction due to vertical ion temperature gradients and diffusion. The latter usually has a smaller contribution. Consequently, we can write for the ion heat flow vector

$$\mathbf{q}_i = -\lambda_i \nabla T_i + \frac{5}{2}kn_i T_i \mathbf{v}_i \qquad (3.47)$$

where λ_i is ion thermal conductivity coefficient, which is approximately equal to the product of the electron thermal conductivity coefficient λ_e, and the square root of electron to ion mass ratio, i.e. it is smaller than λ_e by a factor of *0.004*.

For the case of several ion species of comparable concentrations, the effect of different conductivities must be taken into account. *Banks* [1967] offered an approximation for the ion thermal conductivity coefficient λ_i (in units of $eV\ cm^{-1}\ sec^{-1}\ K^{-1}$), which is valid within several percent of accuracy

$$\lambda_i = 1.2 \times 10^4 \left[n(O^+) + 2n(He^+) + 4n(H^+) \right] T_i^{5/2} n_e^{-1} . \qquad (3.48)$$

By applying equation (3.14), rewritten for ions to the equation 3.46, and implying height-dependence of all variables, one can obtain an ion energy balance equation [*Banks*, 1967; *Rees and Roble*, 1975]

$$\frac{3}{2} n_i k \frac{\partial T_i}{\partial t} = -Sin^2 I \left[\frac{3}{2} n_i k v_i \frac{\partial T_i}{\partial z} + n_i k T_i \frac{\partial v_i}{\partial z} - \frac{\partial}{\partial z} \left(\lambda_i \frac{\partial T_i}{\partial z} \right) \right] + Q_i - L_i \qquad (3.49)$$

where v_i is the ambipolar diffusion velocity (all other notations have been introduced earlier). Note that it is necessary to know the ambipolar diffusion velocity v_i for the equation (3.49) to be solved.

As in the case of electrons, substantial simplifications are applicable to equation (3.49). First, the relaxation times for the ion temperature approaches a value of a few tens of seconds only near the upper boundary of the model at 500 *km*, being considerably smaller at the lower heights of the main ionospheric maximum (in the range 280-400 *km* the relaxation time varies from 3 to 15 *sec)* [*Banks and Kockarts*, 1973]. Thus, the ion temperature relaxation time, although higher than the electron temperature relaxation times (seconds), is nevertheless smaller than the model time step (hundreds of seconds) throughout the altitude range of interest. Consequently, a steady state approximation for the equation of ion temperature balance is assumed.

Second, the heat transfer terms due to ambipolar diffusion are smaller than the terms due to thermal conductivity in the height range of interest. Third, the ion thermal conduction coefficient is only a

small fraction of electron conduction coefficient, $\lambda_i \approx 0.004\ \lambda_e$. Hence, contrary to the case of electron energy balance, the conductance term in the ion equation is smaller than the local sinks and sources at least up to 600 *km*. Thus, the ion energy equation balance reduces to the algebraic relation

$$Q_i - L_i = 0 \ . \tag{3.50}$$

The major heating sources for ions (Q_i) are Joule heating or frictional heating by perpendicular electric fields $(Q_{i\perp})$, ion heating by exothermic chemical reactions $(Q_{i\text{-}ch})$, and heating due to Coulomb collisions with electrons $(Q_{i\text{-}e})$.

$$Q_i = Q_{i\perp} + Q_{i\text{-}ch} + Q_{i\text{-}e} \ . \tag{3.51}$$

The ion-electron Coulomb collisions are a sink of energy for hotter electrons and, at the same time, the source of energy for ions

$$Q_{i\text{-}e} = L_{e\text{-}i} \ . \tag{3.52}$$

The parameterized expression for this source from *Rees and Roble* [1975] is already given in equation (3.45).

For all practical cases, heating of ions by perpendicular electric fields is the main source of energy. This electric field heating involves collisions with neutrals, while collisions with electrons are usually negligible. The Joule dissipation is given by

$$Q_{i\perp} = \sum_i n_i \sum_n \mu_{in} \nu_{in} (\mathbf{v}_i - \mathbf{v}_n)^2 \tag{3.53}$$

where $\mu_{in} = m_i m_n / (m_i + m_n)$ is the reduced mass, and the ion-neutral momentum transfer collision frequency ν_{in} is given by

$$\nu_{in} = \frac{4}{3}\frac{\mu_{in}}{m_i} n_n \left(\frac{8k}{\pi}\right)^{1/2} \left(\frac{T_i}{m_i} + \frac{T_n}{m_n}\right)^{1/2} \overline{\overline{Q_{in}}} \qquad (3.54)$$

or, in units of sec^{-1},

$$\nu_{in} \cong 1.55 \times 10^{-10} \frac{\mu_{in}}{m_i} n_n \left(\frac{T_i}{m_i} + \frac{T_n}{m_n}\right)^{1/2} \overline{\overline{Q_{in}}} \qquad (3.54a)$$

where summation over all ion *(i)* and neutral *(n)* species is implied.

Similar to the case of electrons, equations (3.53, 3.54) can be used for the source evaluation if all drift and wind velocities involved are known. An expression for the ion heating rate in the reference frame of the neutrals derived by *Rees and Walker* [1968] is

$$Q_{i\perp} = \frac{E_\perp'^2}{B^2} \sum_i \left\{ n_i \left[\sum_n \mu_{in} \nu_{in} \right] \left[1 + \left(\sum_n \frac{\nu_{in}}{\omega_i} \right)^2 \right]^{-1} \right\} \qquad (3.55)$$

where $E_\perp'$ is the effective electric field defined by equation (3.25). Expression (3.55) has close resemblance with the analogous equations for the electron heating (3.24).

Exothermic chemical reactions also contribute to ion heating, but this energy source ($Q_{i\text{-}ch}$) is small in the polar region compared to the collisions with electrons and especially with electric field heating.

The major ion cooling processes are due to ion-neutral elastic non-resonant collisions with polarization interactions ($L_{i\text{-}n}$); and sinks due to charge exchange reactions or resonant charge transfer ($L_{i\text{-}ex}$) usually with the parent neutral species, e.g. such processes as $O^+ + O \longrightarrow O + O^+$

$$L_i = L_{i\text{-}n} + L_{i\text{-}ex} \; . \qquad (3.56)$$

Polarization interaction energy losses can be expressed in terms

of atomic polarizability α_o [*Banks*, 1966c] (in units of $eV\ cm^{-3} sec^{-1}$)

$$L_{i-n} = 6.8 \times 10^{-13}\ n_i\ n_n \frac{(\mu_{in} \alpha_o)^{1/2}}{\mu_i + \mu_n}\ (T_i - T_n) \tag{3.57}$$

where μ_{in} is the ion-neutral reduced mass and μ_i, μ_n are the ion and neutral mass in atomic mass units, respectively.

The rate of energy transfer due to resonant charge exchange for gases with Maxwellian velocity distribution from *Banks* [1966c]

$$L_{i-ex} = 2k \left(\frac{8k}{\pi m} \right)^{1/2} n_i\ n_n (T_i - T_n)(T_i + T_n)^{1/2}\ \overline{Q_E} \tag{3.58}$$

where $\overline{Q_E}$ is the charge exchange cross section. Using experimentally established cross-sections, *Banks* [1966b] derived the energy loss rates for each thermospheric ion-neutral pair. Combined results for charge exchange, and for ion-neutral collisions are summarized in Table 3.1.

A good approximation for ion temperature in the polar F-region can be obtained by simply equating the Joule heating to the ion-neutral collisional cooling, i.e. by simplification of equation (3.50) to

$$Q_{i\perp} - L_{i-n} = 0\ . \tag{3.50a}$$

Neglecting all interactions except collisions of the dominating ion (O^+) with the dominating neutral species (atomic oxygen O) the ion temperature for F-region is

$$T_i = T_n + \frac{m_n}{3k} (\mathbf{v}_i - \mathbf{v}_n)^2\ . \tag{3.59}$$

The contribution from the field-aligned velocity is negligible compared to the contribution from the perpendicular direction. As it will be demonstrated in section 3.3, ExB-drift dominates the ion motion in the ionospheric F-region. Thus, the difference of velocities can be

Table 3.1. Energy loss rates due to ion-neutral collisions

Ion mixture	Energy loss rate, in 10^{-14} $eV\ cm^{-3}s^{-1}$
O^+ - N2	$6.6\ n(O^+)n(N2)(Ti - Tn)$
O^+ - O2	$5.8\ n(O^+)n(O2)(Ti - Tn)$
O^+ - He	$2.8\ n(O^+)n(He)(Ti - Tn)$
O^+ - O	$0.21\ n(O^+)n(O)(Ti - Tn)(Ti + Tn)^{1/2}$
O^+ - H	$0.36\ n(O^+)n(H)(Ti - Tn)\ Tn^{1/2}$
He^+ - N2	$5.3\ n(He^+)n(N2)(Ti - Tn)$
He^+ - O2	$4.5\ n(He^+)n(O2)(Ti - Tn)$
He^+ - O	$5.8\ n(He^+)n(O)(Ti - Tn)$
He^+ - H	$10.0\ n(He^+)n(H)(Ti - Tn)$
He^+ - He	$0.4\ n(He^+)n(He)(Ti - Tn)(Ti + Tn)^{1/2}$
H^+ - N2	$3.1\ n(H^+)n(N2)(Ti - Tn)$
H^+ - O2	$2.8\ n(H^+)n(O2)(Ti - Tn)$
H^+ - He	$5.5\ n(H^+)n(He)(Ti - Tn)$
H^+ - O	$0.4\ n(H^+)n(O)(Ti - Tn)Tn^{1/2}$
H^+ - H	$1.4\ n(H^+)n(H)(Ti - Tn)(Ti + Tn)^{1/2}$
NO^+ - N2	$5.91\ n(NO^+)n(N2)(Ti - Tn)$
NO^+ - O2	$5.45\ n(NO^+)n(O2)(Ti - Tn)$
NO^+ - O	$4.5\ n(NO^+)n(O)(Ti - Tn)$
$O2^+$ - N2	$5.807\ n(O2^+)n(N2)(Ti - Tn)$
$O2^+$ - O2	$0.14\ n(O2^+)n(O2)(Ti - Tn)(Ti + Tn)^{1/2}$
$O2^+$ - O	$4.358\ n(O2^+)n(O)(Ti - Tn)$

expressed explicitly with the meridional and zonal components of the neutral wind, while the ion drift velocity is expressed by **E**x**B**-drift components in terms of electric and magnetic fields $v_i^{mer} = - E_{zon}/ B_z$; $v_i^{zon} = E_{mer}/ B_z$, where sub- and superscripts *mer* and *zon* corresponds to meridional and zonal components, respectively. Thus, the expression for ion temperature becomes

$$T_i = T_n + \frac{m_n}{3k}\left[\left(\frac{E_{mer}}{B_z} - v_n^{zon}\right)^2 + \left(\frac{E_{zon}}{B_z} + v_n^{mer}\right)^2\right] . \qquad (3.60)$$

Another expression for T_i can be derived in the frame of moving neutrals in which $\mathbf{v}_n$ vanishes and the drift velocity is $(cE'/B)^2$

$$T_i = T_n + \frac{m_n}{3k}(cE'/B)^2 \qquad (3.61)$$

where E' is effective electric field in the moving neutrals frame (equations 3.25 and 3.25a). A simple parameterization for stationary neutral thermosphere is $T_i[K] = T_n[K] + 1217\ (E_\perp[mV/m]\ /55)^2$ [*Banks and Kockarts*, 1973].

3.3 Equations of motion

All three basic governing equations of the model -- the equation of continuity, the equation of motion, and the equation of energy balance -- are coupled. The velocity $\mathbf{v}_j$ of the j-th species is needed for solving the equation of continuity. The velocity $\mathbf{v}_j$ itself is governed by the equation of motion (or equation of momentum conservation) which equates the acceleration of a unit mass parcel, in the corotating Earth coordinate system, to the sum of all affecting forces

$$\frac{\partial \mathbf{v}_j}{\partial t} + \mathbf{v}_j\cdot\nabla\mathbf{v}_j + 2\Omega\times\mathbf{v} + \frac{1}{\rho_j}\nabla\cdot\mathbb{P} = \mathbf{g} + \frac{1}{\rho_j}(\mathbf{J}\times\mathbf{B}) + \frac{\mathbf{A}_j}{\rho_j} \qquad (3.62)$$

where the two first terms represent the convective derivative along the trajectory of a unit mass parcel ($D\mathbf{v}_j/Dt \equiv \partial \mathbf{v}_j/\partial t + \mathbf{v}_j \cdot \nabla \mathbf{v}_j$), the third term is the Coriolis acceleration (centripetal acceleration term is negligible at the heights of interest), the divergence of pressure tensor $\mathbb{P}$ gives the pressure gradient and viscous forces, $\mathbf{g}$ is the acceleration of gravity, $\mathbf{J}$ is the current density and the term $(\mathbf{J}\times\mathbf{B})/\rho_j$ is acceleration due to ion drag. The last term is the collision term ($\mathbf{A}_j = \sum_k \mathbf{A}_{jk}$) that describes the dynamic effects of friction between gases of different relative velocity [*Banks and Kockarts*, 1973].

An explicit expression for $\mathbf{A}_{ik}$ can be derived if two species have displaced Maxwellian distributions with the parameters T_k, v_k and T_j, v_j, respectively, and when the flow velocities are much smaller than the speed of sound. Both assumption are realistic in the height range of interest

$$\mathbf{A}_{jk} = \left[m_j m_k/(m_j + m_k)\right] n_j \bar{\nu}_{jk} (\mathbf{v}_k - \mathbf{v}_j) \tag{3.63}$$

where $\bar{\nu}_{jk}$ is the momentum transfer collision frequency, which can be calculated for the known collision cross-section σ_D as

$$\bar{\nu}_{jk} = \frac{4}{3} n_k \left(\frac{8k}{\pi}\right)^{1/2} \left(\frac{T_j}{m_j} + \frac{T_k}{m_k}\right)^{1/2} \bar{\mathbb{Q}}_D \tag{3.64}$$

and

$$\overline{\mathbb{Q}_D} = \left(\frac{1}{c}\right)^6 \int_0^\infty v_{jk}^5 \sigma_D(v_{jk}) \exp[-v_{jk}^2/c^2]\, dv_{jk} \tag{3.65}$$

where v_{jk} is the relative velocity and $c^2 = 2k(T_j/m_j + T_k/m_k)$.

Using equations (3.63-3.65) and the relevant cross-section data, the average momentum transfer collision frequency of specific types of collisions, viz electron-neutral, ion-neutral, ion-electron, neutral-neutral, ion-ion, electron-electron collisions can be derived [*Banks and Kockarts*, 1973], and their relative contributions can be estimated.

For the major neutral thermospheric species only ion-neutral collisions are significant.

In the spherical coordinate system, the vertical, zonal, and meridional components of the equation of motion (3.62) are respectively [*Rees*, 1989]

$$\frac{dw}{dt} - 2u\cos\phi + \frac{1}{\rho}\frac{\partial p}{\partial z} = g + (wi - w) \tag{3.66}$$

$$\frac{du}{dt} - \frac{uv\tan\phi}{r} + \frac{uw}{r} - 2v\sin\phi + \frac{1}{\rho}\left[\frac{1}{r\sin\phi}\frac{\partial p}{\partial\lambda} - \frac{\partial}{\partial z}\left(\eta\frac{\partial u}{\partial z}\right)\right] = \frac{B^2}{c\rho}\left[\sigma_\perp(u_i - u) + \sigma_H \sin I\,(v_i - v)\right] \tag{3.67}$$

$$\frac{dv}{dt} - \frac{u^2\tan\phi}{r} + \frac{vw}{r} + 2u\sin\phi + \frac{1}{\rho}\left[\frac{1}{r}\frac{\partial p}{\partial\phi} - \frac{\partial}{\partial z}\left(\eta\frac{\partial v}{\partial z}\right)\right] = \frac{B^2}{c\rho}\left[\sigma_\perp \sin^2 I\,(v_i - v) + \sigma_H \sin I\,(u_i - u)\right] \tag{3.68}$$

where the full derivative $\frac{d}{dt} = \frac{\partial}{\partial t} + \frac{u}{r\cos\phi}\frac{\partial}{\partial\lambda} + \frac{v}{r}\frac{\partial}{\partial\phi} + w\frac{\partial}{\partial z}$, ϕ is latitude, λ is longitude; $r = (R_E + z)$ is the radius from the Earth center, p is pressure, η is viscosity, ρ is density, subscript i corresponds to the ion drift components, and expressions for the Pedersen conductivity $\sigma_\perp$ (3.66) and Hall conductivity σ_H (3.67) are, respectively

$$\sigma_\perp = \sum_i \sigma_o \frac{\nu_{in}^2}{\omega_{ci}^2 + \nu_{in}^2} \tag{3.69}$$

$$\sigma_H = \sum_i \sigma_o \frac{\nu_{in}\,\omega_{ci}}{\omega_{ci}^2 + \nu_{in}^2} \tag{3.70}$$

where the ion gyrofrequency is $\omega_{ci} = eB/m_i c$ and $\sigma_o = \sum_i n_i e/m_i \nu_{in}^2$.

The system of equations (3.66, 3.67, 3.68) has been solved in the

NCAR TIGCM global thermospheric-ionospheric model. Results of model runs for a variety of geophysical conditions have been parameterized in the VSH (Vector Spherical Harmonics) model [*Killeen et al.*, 1987]. The VSH model is one of inputs of the ionospheric model developed in this thesis. The VSH model generates input-driven fields of neutral winds for the solution of the ion equations of motion.

3.3.1. Equation of motion for ions

In writing the basic equation of motion (3.62) for ions, we must include the electromagnetic forcing. Introducing a force due to electric field **E** results in an expression for the Lorentz force $e(\mathbf{E}+\mathbf{v}_i \times \mathbf{B}/c)$ to be included into the equation of ion motion. Further, the Coriolis force and viscosity can be neglected. An ionized component represents a small portion of the neutral atmosphere, from a thousandth in the *F*-region to a millionth part in the *E* region, and its own viscosity is negligible throughout the heights of interest. As will be shown later, in the ionospheric *F* region the ion motion is dominated by the ExB-drift and in the lower *E* region it is collisionally dominated by neutral wind. In this system the Coriolis force is negligible in the upper ionosphere and is implicitly accounted for through the motion of neutrals in the lower ionosphere, where the solution for the motion of neutrals is obtained in the TIGCM/VSH models with the Coriolis force contribution.

Taking into account these considerations, the equation of motion for ions is

$$\frac{\partial \mathbf{v}_i}{\partial t} + \mathbf{v}\cdot\nabla\mathbf{v} + \frac{1}{\rho_i}\nabla p_i - \mathbf{g} - \frac{e}{m_i}\left(\mathbf{E} + \frac{1}{c}\mathbf{v}_i \times \mathbf{B}\right) = \sum_k \nu_{in}^k (\mathbf{v}_n - \mathbf{v}_i) \quad . \qquad (3.71)$$

The non-linear second term represents inertial effects. Let us compare the inertia term with the pressure gradient in the vertical direction. Assuming that gradient procedure in the vertical direction in the exponential thermosphere can be scaled as $\nabla_{\parallel} \sim 1/L$, where L is a

characteristic height scale. The ratio of these two terms is

$$n_i m_i (\mathbf{v}_{i\parallel} \cdot \nabla_\parallel) v_{i\parallel} / \nabla_\parallel (n_i kT_i) \sim v_{i\parallel}^2 / (kT_i/m_i) = M_i^2$$

where $kT_i/m_i = C_i^2$ is the definition of isothermal speed of sound, and M_i is the Mach number of the ion flow. Estimations for the ratio $v_{i\parallel}^2 / (kT_i/m_i)$ suggest that at realistic $T_i = 1500K$ the O^+ flow is still subsonic if the vertical velocities do not exceed about 750 *m/sec*, a condition that holds true in the *E* and *F* regions of the ionosphere. Thus, the subsonic condition allows us to neglect the nonlinear inertia term in the derivation for vertical velocity.

In the horizontal direction, ion motion is dominated by electromagnetic drift. Relaxation times (tens of seconds) for ion response to the variations of electric field configuration [*Rees*, 1989] are much smaller than the typical model time step (hundreds of seconds) that leaves the relaxation processes beyond the model scope. The model considers electric field as a magnetospheric input determined by external effects and assumes the variations are instantaneous. The ion inertia is neglected and steady-state is also assumed for ion motion in horizontal direction.

For the derivation of expressions for ion velocities it is instructive to consider two directions, perpendicular and parallel to the magnetic field **B**, and combine the results vectorially to obtain the solution for the components of full vector of the ion velocity.

a) Across the field direction

The steady state condition for the ion motion perpendicular to **B** is the equality of the Lorentz force and the neutral wind drag force. We neglect the horizontal partial pressure force for ions and introduce the total ion-neutral collision frequency ν_{in} ($\nu_{in} = \sum_k \nu_{in}^k$)

$$\mathbf{v}_{i\perp} = \mathbf{v}_n + \frac{e}{\nu_{in} m_i} \left(\mathbf{E}_\perp + \frac{1}{c} \mathbf{v}_{i\perp} \times \mathbf{B}\right) . \qquad (3.72)$$

Note that the second term in equation (3.72) is small in the *E*-region (up to about 130 *km*); this corresponds to strong collisional coupling where $\mathbf{v}_{i\perp} \cong \mathbf{v}_n$. By contrast, at *F2* region heights the second term dominates and the ion motion is predominantly determined by the Lorentz force. Given the neutral wind velocity and the electric and magnetic field components, the vector equation (3.72) gives rise to a system of three equations for three components of the ion drift velocity. Introducing the ratio of gyrofrequency to collisional frequency $\gamma_i = \omega_{ic} / \nu_{in}$ one can obtain a solution to the system (3.72) for an arbitrary orientation of the magnetic and electric field vectors in Cartesian coordinates $\mathbf{B} = B_x\mathbf{i} + B_y\mathbf{j} + B_z\mathbf{k}$ and $\mathbf{E} = E_x\mathbf{i} + E_y\mathbf{j} + E_z\mathbf{k}$, respectively. If the coordinate system at a given location is oriented with the *x*-axis directed eastward, the *y*-axis directed northward, and the *z*-axis directed upward, the expressions for the velocity components are as follows

$$u_i = \left(1 + \gamma_i^2\right)^{-1} \left[\left(u + \gamma_i \frac{E_x}{B}\right) + \left(v + \gamma_i \frac{E_y}{B}\right) \frac{\gamma_i B_z}{B} - \left(w + \gamma_i \frac{E_z}{B}\right) \frac{\gamma_i B_y}{B}\right] \quad (3.73)$$

$$v_i = \left(1 + \gamma_i^2\right)^{-1} \left[-\left(u + \gamma_i \frac{E_x}{B}\right) \frac{\gamma_i B_z}{B} + \left(v + \gamma_i \frac{E_y}{B}\right) - \left(w + \gamma_i \frac{E_z}{B}\right) \frac{\gamma_i B_x}{B}\right] \quad (3.74)$$

$$w_i = \left(1 + \gamma_i^2\right)^{-1} \left[\left(u + \gamma_i \frac{E_x}{B}\right) \frac{\gamma_i B_y}{B} - \left(v + \gamma_i \frac{E_y}{B}\right) \frac{\gamma_i B_x}{B} + \left(w + \gamma_i \frac{E_z}{B}\right)\right] \quad (3.75)$$

where u_i, v_i, w_i and u, v, w are *x*-, *y*-, and *z*-components of velocities of the ion drift and neutral wind (or zonal, meridional, and vertical components), and E_x, E_y, E_z and B_x, B_y, B_z are zonal, meridional, and vertical components of the electric and magnetic field respectively. Note that the relations $\mathbf{E}_\perp \cdot \mathbf{B} = 0$ and $\mathbf{v}_{i\perp} \cdot \mathbf{B} = 0$ were used in the derivation.

Expressions (3.73-3.75) have been derived for an arbitrarily located cartesian coordinate system oriented so that the y-axis coincides with meridional direction (positive northward), the x-axis coincides

with zonal direction (positive eastward), and the z-axis is directed upward. Thus, the transformations (2.1-2.3) are applied to obtain the drift velocity components in the model coordinate system defined in Chapter 2. Further, to separate these two systems we will use notations v, u, and w for meridional, zonal, and vertical components of the velocities, respectively, while after the transformation to the model system the velocity components will be v_x, v_y, v_z. Sub- or superscript i or n will be used for ion or neutral velocities, respectively.

The appearance of the vertical electric field component in equations 3.73-3.75 is solely due to the condition $\mathbf{E}_\perp \cdot \mathbf{B} = 0$ with an inclined magnetic field. Assuming the electric field E_x, E_y-components are measured or derived from the electric field model, to satisfy $\mathbf{E}_\perp \cdot \mathbf{B} = 0$ one must introduce a vertical component of the electric field E_z. For general orientation of the magnetic field:

$$E_z = - (E_x \sin D + E_y \cos D)/\tan I \qquad (3.76)$$

where I, D are the inclination and declination angles of the magnetic field vector $\mathbf{B}$, respectively. The inclination angle I is defined as the angle between $\mathbf{B}$ and the horizontal plane, and the declination angle D is the angle between the local northward direction and the horizontal component of magnetic field vector $\mathbf{B}$.

Expressions (3.73-3.75) can be simplified by neglecting the vertical wind velocity compared to the horizontal components and by assuming that E_z is small everywhere in the region of interest. In the polar cap region this is due to the $(\tan I)^{-1}$ factor, since the dip angle is close to 90°, near the domain mid-latitude boundary the E_x, E_y components themselves are small. It is instructive to consider the limiting cases for the drift velocity expressions near the lower and upper height boundaries. In the collisionally coupled lower thermosphere parameter $\gamma_i \ll 1$. Due to the contribution difference, the electric field terms of order of $o(\gamma_i^2)$ and the neutral velocity terms of order of $o(\gamma_i)$ are of about the same magnitude. Neglecting these terms, one can obtain for the drift components in the E-region

$$u_i = u + \gamma_i E_x/B \tag{3.73a}$$

$$v_i = v + \gamma_i E_y/B \tag{3.74a}$$

$$w_i = w + \gamma_i E_z/B \ . \tag{3.75a}$$

Expressions (3.73a-3.75a) state that $u_i \cong u$, $v_i \cong v$, $w_i \cong w$ holds true in the lower part of E-region where terms of order of $o(\gamma_i)$ are negligible, which reduces to a vector relation $\mathbf{v}_i \cong \mathbf{v}_n$. Small contributions from the corresponding components of the electric field are due to the Coulomb interaction with charged ions.

At higher altitudes the collision frequency decreases while the gyrofrequency remains approximately the same, which results in a reversal of the relation $\gamma_i \gg 1$. In this case an asymptotic approximation neglecting terms of order of $o(\gamma_i^{-1})$ for the ion drift velocities is

$$u_i = (E_y B_z - E_z B_y)/B^2 \cong \frac{E_y}{B} \sin I \tag{3.73b}$$

$$v_i = (E_z B_x - E_x B_z)/B^2 \cong -\frac{E_x}{B} \sin I \tag{3.74b}$$

$$w_i = (E_x B_y - E_y B_x)/B^2 \tag{3.75b}$$

which are components of the electromagnetic drift $\mathbf{v}_{ie} = c\mathbf{E}\times\mathbf{B}/B^2$. E_z is usually small and the drift horizontal components can be simplified to $u_i \cong (E_y/B) \sin I$; $v_i \cong -(E_x/B) \sin I$, where I is the dip angle.

Figure 3.2 represents the vertical profiles of the magnitudes of the ion and neutral velocities for dip angle 80° and a strong electric field 45 mV/m. The velocity of the ions closely follow the vertical profile of the velocity of neutrals in the collisionally dominant E region but is fully determined by the height-independent $\mathbf{E}\times\mathbf{B}$-drift at F region altitudes. At 100-200 km is a transitional region, where the competition of both mechanisms — neutral drag and electromagnetic

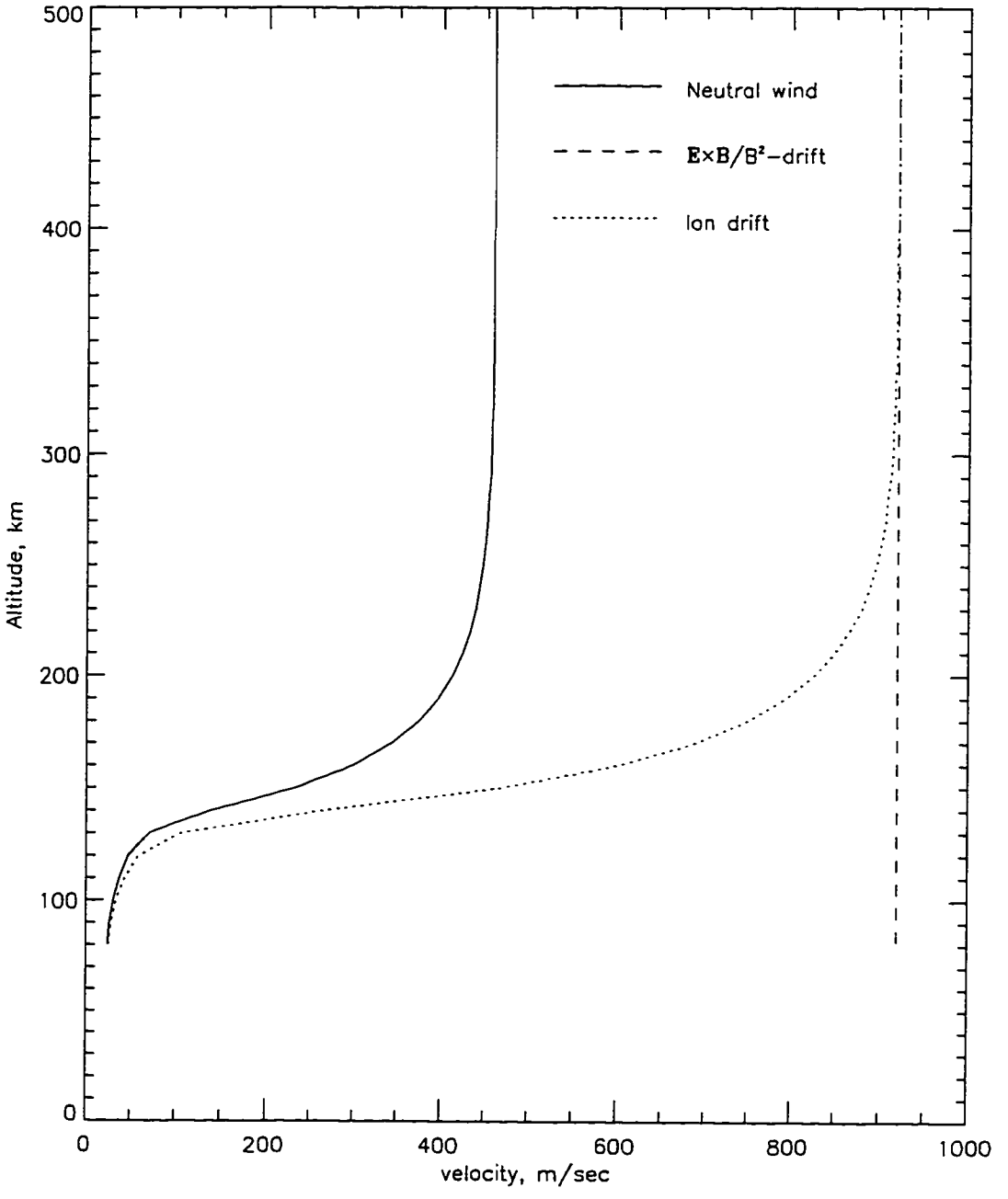

Figure 3.2 Typical vertical profiles of the ion drift and neutral wind velocities for a dip angle of 80° (the polar cap region) and an electric field of *45 mV/m*. Ion drift is collisionally dominated at the *E*-region heights and controlled by electromagnetic drift in the *F* region and above. At 130-200 *km* is transitional region with significant drift shear.

drift -- takes place. This region is characterized by considerable ion velocity vertical shear.

We consider here the direction perpendicular to the magnetic field **B**, which is inclined by the dip angle *I* measured between the vector **B** and the horizontal. In this geometry the horizontal magnetic field component, *BcosI*, is non-zero and, thus, there is a vertical component of **ExB**-drift, w_i, everywhere in the polar region except the vicinity of the magnetic pole, where the dip angle is close to 90°. The vertical drift is a noticeable feature of 3-D convection that is observed in the polar region [e.g., *Heelis*, 1992]. In the first approximation, the horizontal component of **B** is directed radially along geomagnetic meridians toward the geomagnetic pole, while the electric field inside the polar cap is directed from dusk to dawn. This orientation of the fields result in a predominantly upward vertical drift in the day-side sector of the geomagnetic pole, and a downward drift on the night-side. At the low-latitude boundary of the polar cap, the direction of the electric field has more structure and the vertical drift direction has a more complicated pattern. The vertical drift velocities can be several tens of *m/sec*, while the extremes reach up to 100 *m/sec*. This is sufficient to affect the vertical ion density profiles.

For the realistic terrestrial magnetic field the zonal component B_y is not zero. The declination angle *D* is introduced, defined as the angle between the local northward direction and horizontal component of the total vector **B**. Although these corrections are small, they are accounted for in the model.

For the derivation of equation (3.72) we neglected the cross-field ion partial pressure gradient terms $\nabla p_i/\rho_i = \nabla(n_i k T_i)/n_i m_i$. It has been shown by *Schunk* [1983, 1988] that the contribution of this term modifies the steady-state equation for ion velocity as follows

$$\mathbf{v}_i - \mathbf{v}_n = -\frac{D_{i\perp}}{n_i}\nabla n_i + \mu_{i\perp}\mathbf{E}_\perp + \left[1 + \left(\frac{\nu_{in}}{\omega_{ic}}\right)^2\right](\mathbf{v}_{ie} + \mathbf{v}_{iD}) \qquad (3.77)$$

where ion diffusion coefficient $D_{i\perp}$, ion mobility coefficient $\mu_{i\perp}$, and

diamagnetic drift $\mathbf{v}_{iD}$ are, respectively

$$D_{i\perp} = \left(1 + \frac{\omega_{ic}^2}{\nu_{in}^2}\right) \frac{kT_i}{m_i \nu_{in}} \tag{3.78}$$

$$\mu_{i\perp} = \left(1 + \frac{\omega_{ic}^2}{\nu_{in}^2}\right) \frac{e}{m_i \nu_{in}} \tag{3.79}$$

$$\mathbf{v}_{iD} = - c \, (\nabla (n_i kT_i) \times \mathbf{B}) / e_i n_i B^2 \tag{3.80}$$

and the expression for the electromagnetic drift velocity, $\mathbf{v}_{ie}$, has been already introduced ($\mathbf{v}_{ie} = c(\mathbf{E} \times \mathbf{B})/B^2$).

At *F*-region altitudes the ion gyrofrequency is much larger than the ion-neutral collision frequency and the relation $\omega_{ic}/\nu_{in} \gg 1$ holds true. Comparison of the contribution of different terms in expression (3.77) indicates that the electromagnetic drift dominates if the scale length for horizontal variations is greater than a few km. For high-resolution modeling of the ionospheric structures of characteristic sizes of order 10 *km*, the ion partial pressure gradient forces can be important. A significant horizontal gradient of ion density and temperature can occur inside islands of enhanced ion density (ionospheric "patches"), near stable auroral arcs, and inside the oval due to highly structured precipitation. In the current version of the model the diamagnetic drifts are not accounted for, since the model horizontal resolution currently does not exceed *100 km*. Transition to higher resolution will require this term. These studies are a topic for future investigation.

b) Field-aligned direction

In the direction parallel to the magnetic field, the conductivity is two orders of magnitude larger than in the perpendicular direction. Any external parallel electric field would induce a current, which in turn will create a charge separation and a corresponding polarization electric field directed to compensate the original external field.

Thus, any external electric field would immediately be eliminated. Only small polarization electric fields exist in the **B**-field direction that arise from gravitational separation of light electrons and heavier ions and acts to keep electron and ion gases together to maintain the plasma neutrality $n_e = \sum_i n_i$.

Considering equation (3.71) for charged component motion, and assuming steady state conditions prevail ($\partial/\partial t=0$), the flow speed is subsonic, and stress tensor effects are negligible, the equations of parallel motion for ions (with charge, velocity and mass e, $\mathbf{v}_i$, m_i, respectively) and electrons ($-e$, $\mathbf{v}_e$, m_e) with respect to the diffusion velocity of neutrals ($\mathbf{v}_n$) will be

$$(\mathbf{v}_e - \mathbf{v}_n)_{\parallel} = -\frac{1}{n_e m_e \nu_{en}} \left(\nabla p_e - n_e m_e \mathbf{g} + n_e e \mathbf{E} \right)_{\parallel} \tag{3.81}$$

$$(\mathbf{v}_i - \mathbf{v}_n)_{\parallel} = -\frac{1}{n_i m_i \nu_{in}} \left(\nabla p_i - n_i m_i \mathbf{g} - n_i e \mathbf{E} \right)_{\parallel} \tag{3.82}$$

where $\mathbf{E}_{\parallel}$ is the polarization electric field, p is the scalar partial pressure (equation of state $p = nkT$ holds true for both ions and electrons), and ν_{en}, ν_{in} are electron-neutral and ion-neutral collision frequencies, respectively (see next section 3.3.2 for details of derivation of equation of motion for electrons).

Ambipolar diffusion produces zero net current resulting in $\mathbf{v}_i = \mathbf{v}_e$. Solving equation (3.81) for $e\mathbf{E}_{\parallel}$ and substituting it into equation (3.82), after neglecting small terms in m_e/m_i the diffusion velocity is

$$(\mathbf{v}_i - \mathbf{v}_n)_{\parallel} = -\frac{1}{m_i \nu_{in}} \left(kT_i \frac{\nabla n_i}{n_i} + kT_e \frac{\nabla n_e}{n_e} + k\nabla(T_e + T_i) - m_i \mathbf{g} \right)_{\parallel} \tag{3.83}$$

where n_i is the dominant ion density.

The field-aligned component of the gradient, $\nabla_{\parallel}$, on the right hand side of equation (3.83) is $sinI \frac{\partial}{\partial z}$. A similar factor $sinI$ is necessary to express the field-aligned component of the vertical gravi-

tational acceleration g. Taking the vertical projection of the field-aligned components in equation (3.83) we obtain

$$w_d = - \sin^2 I \frac{k(T_e + T_i)}{m_i \nu_{in}} \left(\frac{\frac{\partial}{\partial z} n_i}{n_i} + \frac{\frac{\partial}{\partial z}(T_e + T_i)}{(T_e + T_i)} + \frac{m_i g}{k(T_e + T_i)} \right) \qquad (3.84)$$

Introducing the ambipolar diffusion coefficient D_a

$$D_a = \frac{k(T_e + T_i)}{m_i \nu_{in}} \qquad (3.85)$$

and the plasma temperature $T_p = (T_e + T_i)/2$, one can rewrite expression (3.84) in a compact form

$$w_d = -D_a \sin^2 I \left(\frac{\partial \ell n(n_i)}{\partial z} + \frac{\partial \ell n(T_p)}{\partial z} + \frac{m_i g}{2kT_p} \right) . \qquad (3.86)$$

The last unaccounted term for the vertical velocity is the neutral wind-related drag. In contrast to the direction across the field, where the neutral wind drag is controlled by the Lorentz force, in the field-aligned direction the **v**x**B**-force vanishes and **B**-field constraints are absent. Hence, a wind component in the field-aligned direction will result in the ion motion. In the polar regions the neutral wind drag in the field-aligned direction contributes mainly in the vertical motion due to near-vertical orientation of the magnetic field.

Both the horizontal and the vertical neutral wind components have a field-aligned projection onto the direction of the inclined field. Even though almost all vertical wind contribute into this motion, its contribution is small due to insignificant velocity magnitude. If we denote vertical wind as w, its $w \cdot \sin I$-component contributes to the field-aligned drag, that results in $w \cdot \sin^2 I$ for the vertical projection of this contribution. The field-aligned projection of the horizontal neutral wind components for a general orientation of the inclined magnetic field **B** with dip angle I and declination angle D is

$$\vartheta_{\parallel} = (\vartheta \cos D + u \sin D) \cos I \tag{3.88}$$

and its vertical and horizontal components respectively are

$$\vartheta^{z}_{\parallel} = (\vartheta \cos D + u \sin D) \cos I \sin I \tag{3.89}$$

$$\vartheta^{x}_{\parallel} = (\vartheta \cos D + u \sin D) \cos^2 I \sin D \tag{3.90}$$

$$\vartheta^{y}_{\parallel} = (\vartheta \cos D + u \sin D) \cos^2 I \sin D \; . \tag{3.91}$$

Under special circumstances all three terms can contribute to the ion motion. However, in a majority of cases only the vertical component contributes significantly, while the major contribution inside $\vartheta^{z}_{\parallel}$ usually comes from meridional wind ϑ.

The combined vertical ion velocity is the sum of the individual terms. Combining (3.89) with the field-aligned vertical neutral wind contribution $w \cdot \sin^2 I$, with the ambipolar diffusion velocity (3.86), with the vertical component of ExB-drift (3.75), and introducing the relations $B_x = B \cos I \sin D$, $B_y = B \cos I \cos D$, $B_z = B \sin I$, the following expression for the ion vertical velocity is obtained

$$w_i = w \sin^2 I + (\vartheta \cos D + u \sin D) \cos I \sin I +$$

$$- D_a \sin^2 I \left(\frac{\partial \ell n (n_i)}{\partial z} + \frac{\partial \ell n (T_p)}{\partial z} + \frac{m_i g}{2kT_p} \right) \tag{3.92}$$

$$\left(1 + \gamma_i^2\right)^{-1} \left[\left(u + \gamma_i \frac{E_x}{B} \right) \gamma_i \cos I \cos D - \left(\vartheta + \gamma_i \frac{E_y}{B} \right) \gamma_i \cos I \sin D + \left(w + \gamma_i \frac{E_z}{B} \right) \right].$$

The horizontal ion drift velocities are given by equations (3.73, 3.74). Neglecting small terms (terms including w and E_z) they become

$$u_i = \left(1 + \gamma_i^2\right)^{-1} \left[\left(u + \gamma_i \frac{E_x}{B}\right) + \left(w + \gamma_i \frac{E_y}{B}\right)\gamma_i \sin I\right] \qquad (3.93)$$

$$w_i = \left(1 + \gamma_i^2\right)^{-1} \left[-\left(u + \gamma_i \frac{E_x}{B}\right)\gamma_i \sin I + \left(w + \gamma_i \frac{E_y}{B}\right)\right] . \qquad (3.94)$$

Small contributions from the horizontal component of the ambipolar diffusion and the ion drag from the field-aligned neutral wind (expressions 3.90 and 3.91) have been neglected. Expressions 3.92 - 3.94 can be used to evaluate the ion velocity components given the magnetic and electric fields and the neutral wind.

For the current horizontal scales of this model (a hundred kilometers), neglecting the horizontal component of field-aligned ambipolar diffusion is perfectly justified. However, for transitions to higher horizontal resolution down to several kilometers it is necessary to remember that the ratio of the vertical to the horizontal fluxes due to ambipolar diffusion is proportional to $\tan I$. Contribution of the horizontal component is small near the geomagnetic pole, however it is comparable with the vertical flux near the low-latitude boundary of the model domain. Thus, the effects of transport due to ambipolar diffusion in the vertical and in the horizontal directions are comparable at these latitudes and must be accounted for at similar length scales. Similarly, the horizontal components of the field aligned neutral wind drag can be important.

3.3.2. Equation of motion for electrons

The equation of motion for electrons is not solved in the current version of the model. Instead, the electron density is derived as the sum of the ion densities applying the quasi-neutrality condition. However, having a goal to include a dynamic electro-magnetic coupling in the next versions of the model, it is instructive to present in this section of the thesis a discussion of induced currents in the lower ionosphere and arising polarization fields that map up along highly

conductive field lines and affect the *F* region convection.

The same approach as that taken for derivation of equations of horizontal ion motion (3.71-3.75) is applicable in the case of electrons with a corresponding sign reversal in the terms with the negative electron charge *(-e)*. Accounting for this sign reversal, the general form of the equation of electron motion will be

$$\frac{D\mathbf{v}_e}{Dt} + \frac{1}{\rho_e}\nabla p_e - \mathbf{g} + \frac{e}{m_e}(\mathbf{E} + \frac{1}{c}\mathbf{v}_e \times \mathbf{B}) = \sum_k \nu_{en}^k (\mathbf{v}_n - \mathbf{v}_e) \quad . \qquad (3.95)$$

Applying a simplifying assumption of the steady-state condition, we obtain from equation (3.95) the following expression for the horizontal components of electron motion

$$\mathbf{v}_{e\perp} = \mathbf{v}_n - \frac{e}{\nu_{en} m_e}(\mathbf{E}_\perp + \frac{1}{c}\mathbf{v}_{e\perp} \times \mathbf{B}) \quad . \qquad (3.96)$$

Solution of the vector equation (3.96) can be derived similarly to solution (3.73-3.74) of the equation of ion motion with account of the charge sign reversal. It is equivalent to the reversal of sign of all terms with factor γ_e. Neglecting the terms of secondary importance, we obtain the following expression for the horizontal components of the drift velocity

$$u_e = \left(1 + \gamma_e^2\right)^{-1}\left[\left(u - \gamma_e \frac{E_x}{B}\right) - \left(v - \gamma_e \frac{E_y}{B}\right)\gamma_e \sin I\right] \qquad (3.97)$$

$$v_e = \left(1 + \gamma_e^2\right)^{-1}\left[\left(u - \gamma_e \frac{E_x}{B}\right)\gamma_e \sin I + \left(v - \gamma_e \frac{E_y}{B}\right)\right] \quad . \qquad (3.98)$$

In the limiting case of the upper ionosphere, where electron gyrofrequency is much larger than electron collision frequency and $\gamma_e >> 1$ holds true, expressions (3.97) and (3.98) are reduced to the

corresponding components of electromagnetic drift

$$u_e = E_y \sin I / B \qquad (3.97b)$$

$$\upsilon_e = -E_x \sin I / B , \qquad (3.98b)$$

which is exactly the same as corresponding expressions for the ion motion (3.73*b*, 3.74*b*), which we will repeat here

$$u_i = E_y \sin I / B \qquad (3.73b)$$

$$\upsilon_i = -E_x \sin I / B . \qquad (3.74b)$$

Since electrons and ions move together, electromagnetic or ExB-drift does not produce any current.

However, this symmetry with the case of horizontal ion motion takes place only in the upper ionosphere. At the heights of *D* and *E* ionospheric regions electrons and ions move with different average speed that results in electrical currents and polarization fields. At the lowest altitudes below about 70 *km*, both the electron and ion gyrofrequency are much smaller than the collision frequency, and relations $\gamma_e << 1$ and $\gamma_i << 1$ hold true. In this case the systems (3.73, 3.74) and (3.97, 3.98) are reduced to (3.73a, 3.74a) and (3.97a, 3.98a)

$$u_e = u - \gamma_e E_x / B \qquad (3.97a)$$

$$\upsilon_e = \upsilon - \gamma_e E_y / B \qquad (3.98a)$$

$$u_i = u + \gamma_i E_x / B \qquad (3.73a)$$

$$\upsilon_i = \upsilon + \gamma_i E_y / B . \qquad (3.74a)$$

The velocity component induced by the electric field has diffe-

rent directions for ions (3.73a,3.74a) and electrons (3.97a, 3.98a), resulting in the net current $\mathbf{j} = e(\sum_i n_i \mathbf{v}_i - n_e \mathbf{v}_e)$. This current is carried predominantly by electrons, since $m_i \nu_i >> m_e \nu_e$. However, at these altitudes concentrations of the charged species are insignificant and effect is small.

There is a region above 70 *km* and below about 130 *km* where a different effect occurs. The electron gyrofrequency is more than three orders of magnitude (m_i/m_e-times) larger than the ion gyrofrequency, while the electron-neutral and ion-neutral collision frequencies differ to much smaller extent. This difference results in different heights of transition to ExB-drift (3.97b, 3.98b and 3.73b, 3.74b) from the motion induced by the neutral wind and electric field (3.97a, 3.97a and 3.73a, 3.74a). Consequently, in the region of about 70 - 130 *km* the motion of electrons is already governed by equations (3.97b, 3.98b), while ions still can move across magnetic field lines in response to the neutral winds and external electric field in accordance with equations (3.73b) and (3.74b). Ionospheric conductivity becomes anisotropic and the electric field, when applied to the *E*-region, will result in current flow. Similarly, the neutral wind drag will result in a net current. The currents lead to the establishment of a polarization electric field. These currents can be expressed explicitly as a vector difference between the ion flux, $ne\mathbf{v}_i$, and the electron flux, $ne\mathbf{v}_e$, where n is the concentration of charged species. The corresponding velocities, $\mathbf{v}_e$ and $\mathbf{v}_i$, are derived in (3.97, 3.98) and (3.73, 3.74, 3.75) and can be expressed in terms of the conductivity tensor, $\vec{\sigma}$, and the neutral wind drag as

$$\mathbf{j} = \vec{\sigma}\cdot\mathbf{E} + ne(\vec{\sigma}_i - \vec{\sigma}_e)\cdot\mathbf{v}_n = \vec{\sigma}\cdot(-\nabla\Phi) + ne(\vec{\sigma}_i - \vec{\sigma}_e)\cdot\mathbf{v}_n \qquad (3.99)$$

where $\mathbf{v}_n$ is the neutral wind velocity, $\vec{\sigma}$ is the conductivity tensor, $\mathbf{E}$ is the electric field, which can be considered as a field due to polarization potential Φ ($\mathbf{E}=-\nabla\Phi$). Tensors $\vec{\sigma}_{i,e}$ in the second term due to the neutral wind, $\mathbf{v}_n$, drag are defined as follows

$$\vec{\sigma}_{i,e} = \frac{B}{1+\gamma_{i,e}^2} \begin{pmatrix} 1 & -\gamma_{i,e} \\ \gamma_{i,e} & 1 \end{pmatrix} .$$

Assuming a steady-state and the quasi-neutrality condition, $\nabla \cdot \mathbf{j} = 0$, holds true, one can obtain an elliptic PDE to relate the electric field potential to the ion velocity and ionospheric conductivities (for simplicity magnetic field is assumed to be vertical in this derivation)

$$- \frac{\partial}{\partial x} \sigma_{\perp} \frac{\partial \Phi}{\partial x} + \frac{\partial}{\partial x} \sigma_{H} \frac{\partial \Phi}{\partial y} - \frac{\partial}{\partial y} \sigma_{\perp} \frac{\partial \Phi}{\partial x} - \frac{\partial}{\partial y} \sigma_{H} \frac{\partial \Phi}{\partial y} - \frac{\partial}{\partial z} \sigma_{o} \frac{\partial \Phi}{\partial z} - \nabla \cdot ne(\vec{\sigma}_{i} - \vec{\sigma}_{e}) \cdot \mathbf{v}_{n} = 0 \qquad (3.99a)$$

where $\sigma_{\perp}$, σ_{H}, and σ_{o} are the Pedersen, Hall, and parallel conductivities, respectively.

To simplify the 3-D consideration to 2-D, equation (3.99a) can be integrated over the heights with high conductivity (ionospheric *E* region). After integration, the terms with derivatives with respect to the vertical direction will result in the field-aligned current. The equation will then relate the height-integrated conductivities and drifts with the field-aligned current, coupling the ionospheric effects with field-aligned current driven from the magnetospheric sources

$$- \frac{\partial}{\partial x} \Sigma_{\perp} \frac{\partial \Phi}{\partial x} + \frac{\partial}{\partial x} \Sigma_{H} \frac{\partial \Phi}{\partial y} - \frac{\partial}{\partial y} \Sigma_{\perp} \frac{\partial \Phi}{\partial x} - \frac{\partial}{\partial y} \Sigma_{H} \frac{\partial \Phi}{\partial y} = j_{\parallel} + \nabla \cdot \vec{\Sigma} \cdot \mathbf{v}_{n} \qquad (3.99b)$$

where $j_{\parallel}$ in is the field-aligned current, $\vec{\Sigma}$ is the height-integrated tensor $ne(\vec{\sigma}_{i} - \vec{\sigma}_{e})$, and $\Sigma_{\perp}$ and Σ_{H} are the height-integrated Pedersen and Hall conductivities, respectively.

This derivation illustrates a coupling of ionospheric processes to the magnetosphere through the field-aligned currents. A rigorous treatment of this coupling requires a self-consistent approach combining the magnetosphere and ionosphere in the same model. In this coup-

led consideration the electric field can be calculated self-consistently with instantaneous values of conductivities and plasma drifts and with the magnetospheric-driven field-aligned current. This task is yet to be solved and is not attempted in this thesis. Currently the practical approach used in this work and by other researchers is to isolate the magnetospheric considerations, and use statistically averaged fixed electric field patterns as inputs. Thus the electric fields used in this model are not strictly self-consistent. The polarization electric fields induced by horizontal variations in ionospheric conductivities are not fed back to the statistical E-field inputs, or to any magnetosphere model via field-aligned currents.

A totally self-consistent treatment would ideally require coupling via field-aligned current to an appropriate magnetospheric model. This ambitious task is a possible future research direction.

3.4. Equations of continuity

The continuity equation or equation of mass conservation for a particular species is

$$\frac{\partial n}{\partial t} + \nabla\cdot(n\mathbf{v}) = -L + P \qquad (3.100)$$

where n is the concentration, $\mathbf{v}$ is the velocity, L is the sum of local sinks, and P is the sum of local sources. Physically, this equation expresses that the changes of concentration in time are equal to the difference of local sources and sinks, plus influx or outflow. This equation is coupled to the equation of motion, through the velocity field. Given the velocity together with the production and losses of species (which are described in Chapter 4) the continuity equation governs the density.

It is of interest to estimate the relative importance of the different terms in the continuity equation. Assuming an exponential height distribution, vertical derivatives can be replaced by the reciprocal of the scale height, $\partial/\partial z \propto 1/H$. Vertical flux is mainly of

diffusive origin, since effects of vertical winds are usually smaller than those due to molecular and eddy diffusion. It scales as $\phi_D \propto -n(D_m+K)/H$ and its divergence as $-(D_m+K)n/H^2$, where D_m and K are coefficients of molecular and eddy diffusion, respectively. For charged species this sum must be replaced by D_a, the ambipolar diffusion coefficient.

The divergence of the advective flux can be scaled as $v(n-n_1)/\Delta$, where v is the characteristic horizontal velocity, Δ is the grid size, and n and n_1 are concentrations at neighboring grid cells. Local sinks are determined by the chemical lifetime. With the loss frequency ℓ_j we have $L_j = \ell_j n_j$. The scaled equation becomes, after multiplication by n^{-1} and under the assumption that there is no production of species ($P_j = 0$)

$$\frac{1}{\tau} = \frac{D_m}{H^2} + \frac{K}{H^2} + \frac{v}{\Delta}\left(1 - \frac{n_1}{n}\right) + \ell_j = \frac{1}{\tau_D} + \frac{1}{\tau_K} + \frac{1}{\tau_A} + \frac{1}{\tau_{Ch}} . \qquad (3.101)$$

The τ_D, τ_K, τ_A, τ_{Ch} are the typical time scales for the respective processes. The process with the shortest time constant determines the species concentration. For comparable time constants several processes must be considered. Comparison of the time constants determines the model time step that must be adopted.

From all species included in the model, only three have chemical lifetimes long enough that the loss term is comparable with the transport term. These are $O^+(^4S)$, NO, and $N(^4S)$.

In figure 3.3, a comparison of the time scales for NO and $N(^4S)$ is presented. Chemical processes determine the $N(^4S)$ concentration at the lower boundary, justifying an adoption of the photo-chemical equilibrium concentration as the lower boundary condition. The transport due to molecular diffusion becomes important from approximately above 150 *km*. By contrast, NO concentrations are affected by eddy diffusion near the lower boundary and the photo-chemical equilibrium concentration is not suitable for the lower boundary condition. Chemical pro-

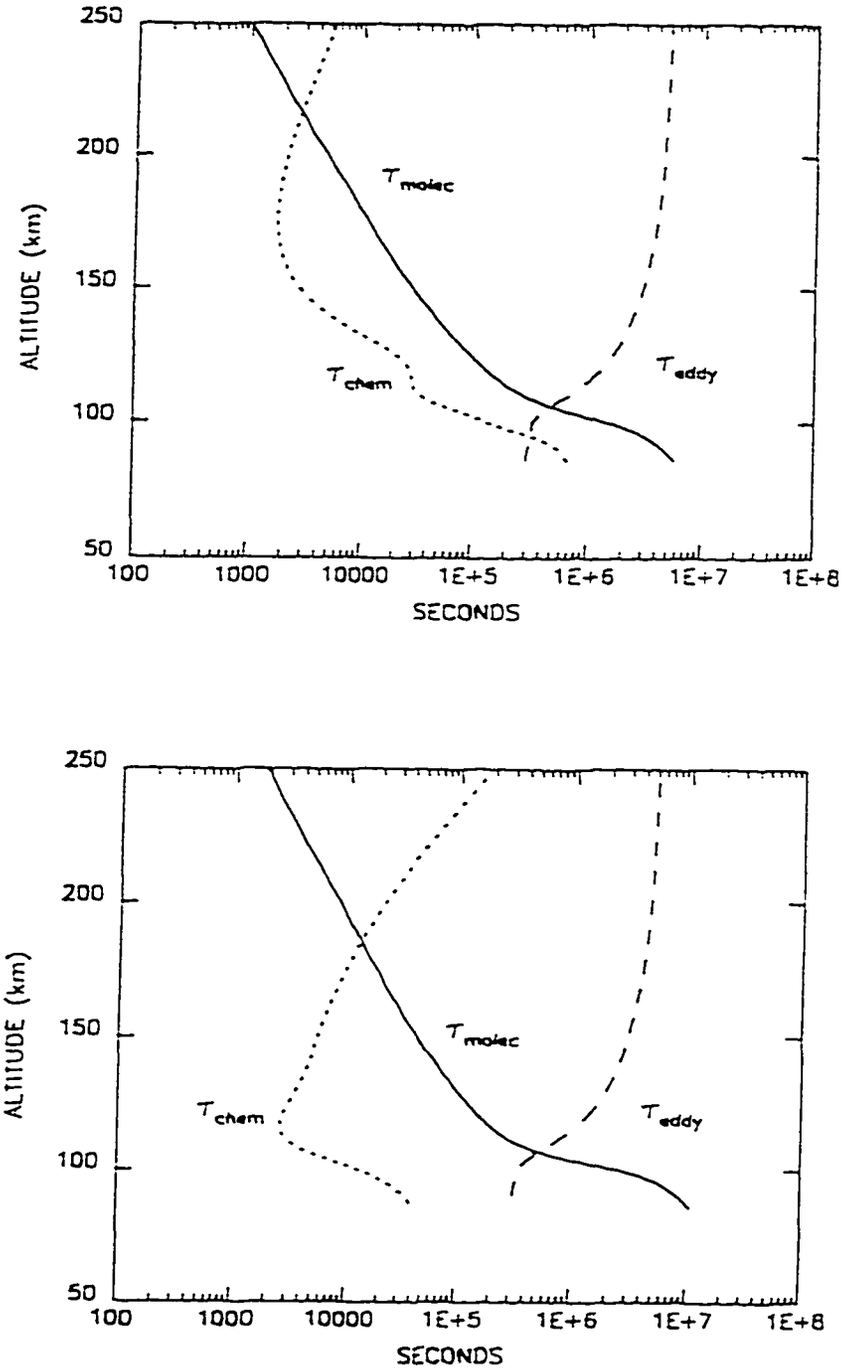

Figure 3.3. Comparison of the time scales due to different processes for *NO* (upper panel) and $N(^4S)$ (lower panel) (from *Siskind* [1988]).

cesses mainly determine the profile in a range from about 100 *km* to 200 *km* with the molecular diffusion dominant above that altitude.

The advective lifetime in equation (3.100) cannot be established without further assumptions about characteristic scales and the horizontal gradients of the concentration. For instance, for the grid size of *100x100 km* and for a convective velocity of O^+ ion of 1 *km/sec*, the time scale of advective processes is *100 sec* times $(1 + n/|n-n_1|)$, where n, n_1 are concentrations at the neighboring cells. If we assume that the concentrations differ by no more than a factor of 2, the advective time scale is 200 *sec*. This time is comparable with the model time step and therefore the advection must be included into consideration.

The same analysis for the odd nitrogen species requires a decrease in the wind velocity by a factor of 10 to 100 *m/sec* and it requires the assumption of much less variability in the concentrations. An upper limit estimate of the concentration difference at 10% level yields 10^4 *sec* for the advective time scale for *NO*. This is comparable with the chemical lifetime. However, a 10% difference in concentrations is a very high estimation, valid only for the local fluctuations. Although a rigorous account for all possible effects would require advection considerations, reasonable accuracy can be achieved by accounting only for the vertical transport [*Siskind et al.*, 1989a,b].

The lifetimes of molecular ions NO^+ and O_2^+ are defined by the highly effective processes of dissociative recombination with reaction rates valued at about $10^{-7} cm^{-3} sec^{-1}$. Their loss rate depends on the electron concentration and varies from a short lifetime of 10 *sec* at the *F* region day-side (maximum of electron concentration $n_e \sim 10^6 cm^3$) to 10^5 *sec* at the night-side *E* region ($n_e \sim 10^3\ sm^3$), having an intermediate value of 100 *sec* in the auroral *E* region ($n_e \sim 10^5 cm^3$). While the assumption of photo-chemical equilibrium is perfectly valid for the *F* region and remains a reasonable assumption for the auroral *E* region, the night-time *E* region requires appropriate accounting for transport.

In the current version of the model we focused mainly on the upper ionosphere, and the model has been tailored primarily for a compu-

tationally effective description of the *F* region and auroral *E* region. Molecular ions are assumed to be in photo-chemical equilibrium in the model, although this assumption is not valid for the night-side *E* region outside the auroral oval and in the polar cap.

All other species considered in the model have very short chemical lifetimes and the assumption of photochemical equilibrium is valid throughout the altitude range of interest for the entire variety of geophysical situations. There is no significant transport of these species and they are completely controlled by local processes. The concentration changes are fast compared to the model time step (5-10 minutes), hence relaxation processes are negligible. In photo-chemical equilibrium we obtain an algebraic equation for the concentration n_j for the species j

$$P_j - \ell_j n_j = 0 \ . \tag{3.102}$$

For species with long lifetimes the continuity equation (3.100) in the model Cartesian system becomes

$$\frac{\partial n}{\partial t} + \frac{\partial (\phi_n + nv_z)}{\partial z} + \frac{\partial (nv_y)}{\partial y} + \frac{\partial (nv_x)}{\partial x} = P - \ell n \tag{3.103}$$

where v_x, v_y, v_z are X-, Y-, Z-components of the velocity vector $\mathbf{v}$, respectively, and ϕ_n is the vertical flux by diffusion, either molecular diffusion and eddy diffusion in the lower *E* region in case of neutrals or ambipolar diffusion in case of ions.

As a reasonable approximation, following the approach implemented by *Siskind et al.* [1989a,b] for the long-living neutral species *NO* and $N(^4S)$, we neglected the horizontal advective fluxes. The vertical flux by molecular and eddy diffusion can be expressed as

$$\phi_n = - D_m \left(\frac{\partial n_n}{\partial z} + \frac{n_n}{T} \frac{\partial T}{\partial z} + \frac{n_n}{H} \right) - K \left(\frac{\partial n_n}{\partial z} + \frac{n_n}{T} \frac{\partial T}{\partial z} + \frac{n_n}{H} \right) \tag{3.104}$$

where D_m is the molecular diffusion coefficient, K is the eddy diffusion coefficient (this term is important up to 120 km), H_n is the scale height and n_n is the number density of n-th species, and H is the scale height of the background gas mixture.

After substitution of the explicit expression (3.104) into the continuity equation (3.103) and neglecting the advective horizontal transport terms, we obtain a second order partial differential equation of the parabolic type in the final form

$$\frac{\partial n_n}{\partial t} = A \frac{\partial^2 n_n}{\partial z^2} + B \frac{\partial n_n}{\partial z} + (\ell_n + C) n_n + P_n \qquad (3.105)$$

where all coefficients A, B, C, L_n, P_n are generally time- and height-dependent. Coefficients A, B, C are defined as follows

$$A = D_m + K \qquad (3.106)$$

$$B = \frac{\partial}{\partial z}\left(D_m + K\right) + \frac{D_m + K}{T}\frac{\partial T}{\partial z} + \left(\frac{D_m}{H_n} + \frac{K}{H}\right) - v_z^n \qquad (3.107)$$

$$C = \frac{\partial}{\partial z}\left(\frac{D_m + K}{T}\frac{\partial T}{\partial z}\right) + \frac{\partial}{\partial z}\left(\frac{D_m}{H_n} + \frac{K}{H}\right) . \qquad (3.108)$$

Equation (3.105) can be solved numerically. The methods of its solution are described in Chapter 5 of this thesis.

For the species of our primary interest in the model, the ion continuity equation is considered without simplifying assumptions. Contrary to the case of odd nitrogen neutrals, for major ion species such as O^+ the local ion production is very often smaller than transport terms and the advective horizontal fluxes cannot be excluded in any reasonable approximation. Expressions for the ion velocity components (3.92-3.94) have been derived in section 3.3, and their substitution into equation (3.103) will result in a mixed diffusive-advective

PDE of second order

$$\frac{\partial n_i}{\partial t} = A \frac{\partial^2 n_i}{\partial z^2} + B' \frac{\partial n_i}{\partial z} - \frac{\partial (n_i v_y^i)}{\partial y} - \frac{\partial (n_i v_x^i)}{\partial x} + (\ell_i + C) n_i + P_i \tag{3.109}$$

where coefficients A, B', C are as follows

$$A = D_a \sin^2 I \tag{3.110}$$

$$B' = \sin^2 I \left[\frac{\partial D_a}{\partial z} + \frac{D_a}{T_p} \frac{\partial T_p}{\partial z} + \frac{D_a}{2H_p} - w^n \right] - \cos I \left[\sin I \, (v^n \cos D + u^n \sin D) + (E_x \cos D - E_y \sin D)/B \right] \tag{3.111}$$

$$C = \sin^2 I \left[\frac{\partial}{\partial z} \left(\frac{D_a}{T_p} \frac{\partial T_p}{\partial z} \right) + \frac{\partial}{\partial z} \left(\frac{D_p}{2H_p} \right) \right] \tag{3.112}$$

where D_a is the ambipolar diffusion coefficient, T_p is the plasma temperature, H_p is the height scale corresponding to the plasma temperature, I and D are inclination and declination angle, respectively, v^n, u^n, and w^n are meridional, zonal, and vertical components of neutral wind, E_x and E_y are electric field components, and B is magnetic field.

The numerical approaches for solution of equations (3.105) and (3.109) are described in Chapter 5. Chapter 4 is devoted to the description of sink and source terms for both neutral and charged modeled species.

CHAPTER 4

PRODUCTION AND LOSS

In the previous chapter it was shown that production and loss terms are the major terms in the equation of continuity for the majority of species. These species are assumed to be in photo-chemical equilibrium. The three long-living species $O^+(^4S)$, NO, $N(^4S)$ that are accounted for in the model with consideration of their transport mechanisms are also affected by their respective production and loss processes.

The dayside production processes are dominated by solar extreme ultraviolet irradiance (EUV). In the auroral region the production processes of ionization and dissociation by energetic precipitating particles (mainly electrons) are superimposed. Primary ionization products, unless they are stable themselves, are transformed by chemical reactions into other stable products and recombine while advecting or diffusing out of the volume they were produced. Detailed analysis of these transformations will be made in this chapter together with a quantitative evaluation of production and loss terms for all modeling species.

4.1. Ionization and dissociative ionization

The ionization source q^i of the i-th ion species is the sum of the ionization rates by the primary ($q^i_{DP\text{-}EUV}$) and secondary ($q^i_{DS\text{-}EUV}$) ionization due to direct solar EUV, the night-time ionization source by the scattered solar UV in the *HeI (584 Å)*, *HeII (304 Å)* and *H Lyman-β (1026 Å)* and *H Lyman-α (1216 Å)* lines ($q^i_{SC\text{-}EUV}$), and by the precipitating energetic particles (q^i_{AUR}).

$$q^i = q^i_{DP\text{-}EUV} + q^i_{DS\text{-}EUV} + q^i_{SC\text{-}EUV} + q^i_{AUR} \quad . \tag{4.1}$$

4.1.1. Direct EUV ionization

The following primary photoionization processes for major thermospheric components are accounted for in the photochemical scheme of the model (wavelength and energy thresholds are shown in parenthesis)

$$N_2 + h\nu \ (\lambda \le 796\text{Å},\ E \ge 15.6eV) \longrightarrow N_2^+ + e \qquad (P1)$$

$$N_2 + h\nu \ (\lambda \le 504\text{Å},\ E \ge 24.6eV) \longrightarrow N^+ + N + e \qquad (P2)$$

$$O_2 + h\nu \ (\lambda \le 1027\text{Å},\ E \ge 11.6eV) \longrightarrow O_2^+ + e \qquad (P3)$$

$$O_2 + h\nu \ (310\text{Å} \le \lambda \le 796\text{Å},\ E \ge 15.6eV) \longrightarrow O^+ + O + e \qquad (P4)$$

$$O + h\nu \ (\lambda \le 910\text{Å},\ E \ge 13.6eV) \longrightarrow O^+ (^4S,\ ^2D,\ ^2P) + e\ . \qquad (P5)$$

The ionization rate, $q^i_{DP\text{-}EUV}$, of the i-th ion species by direct EUV absorption in the model is calculated as

$$q^i_{DP\text{-}EUV} = n_j(z) \int_{\lambda 1}^{\lambda 2} F_o(\lambda) \cdot \sigma_I^i(\lambda) \cdot exp\left[-\sum_{m=1}^{3} \sigma_T^m(\lambda) \cdot N_m(z) \right] d\lambda \qquad (4.2)$$

where n_j is the density of parent neutral species; $\lambda_{1,2}$ are the wavelength limits of the ionization process, $F_o(\lambda)$ is the incident solar photon flux at the top of the atmosphere, $\sigma_I^i(\lambda)$ is the cross-section for ionization, $\sigma_T^m(\lambda)$ is the absorption cross-section of major neutral components, $N_m(z)$ is the line-of-sight integrated density of the major thermospheric components (O, N_2, O_2) corresponding to the subscript m = 1, 2, 3, respectively.

To numerically calculate the values, it is necessary to know the vertical profiles of the major neutral components of the thermosphere, cross-sections of both total absorption and ionization, and the solar EUV flux at the top of the atmosphere. Dissociative ionization yields and branching ratios are necessary for an estimation of the production

rate for a particular electronic state. An extensive compilation of measured and theoretical cross-sections, the quantum yields, and branching ratios of aeronomic interest was made by *Kirby-Docken et al.* [1979].

Line-of-site integrated densities in a spherical exponential atmosphere can be approximated by

$$N_m(z) = n_m(z) \cdot H_m(z) \cdot Ch(\chi, X_m) \tag{4.3}$$

where $H_m(z)$ is the scale height of m-th major neutral component, ($H_m = kT/m_m g$) and $Ch(\chi, X_m)$ is the Chapman grazing incidence function. The parameter $X_m = (R_E + z)/H_m$, where R_E is the Earth's radius, and χ is the solar zenith angle.

An approximation for the Chapman function by *Smith III & Smith* [1972] was adopted in the model. The solar zenith angle is a function of the geographic location, season, and local time given by the following relation

$$\cos\chi = \sin\delta \sin\phi + \cos\delta \cos\phi \cos\left[\frac{2\pi}{24} \cdot (LT-12)\right] \tag{4.4}$$

where ϕ is the geographic latitude, LT is the local time in units of decimal hours, δ is the solar declination, $\delta = 23.5^{\circ} \sin[2\pi/365 \cdot (d-80)]$, where d is the day number in the calendar year.

The major source of uncertainties in the direct EUV ionization calculation is a strong spectral dependence of solar flux intensity $F_0(\lambda)$ on the solar activity level. Attempts to parameterize the solar output by solar activity index $F_{10.7}$ cannot take into account small scale and short time events on the sun. EUV irradiance output is generated at different regions of the sun, while $F_{10.7}$ index is a characteristic index for average coronal activity. The latest parameterization by *Tobiska and Barth* [1990] is based on the division of all solar lines in accordance to their origin at the sun. In this model the spectral intensities of the chromospheric irradiance are subject to parameteri-

zation by the daily measured solar emission in the *H Lyman-α* line, while the irradiance from the solar corona and from the transitional region is parameterized by traditional solar activity index $F_{10.7}$. All known up-to-date satellite and rocket measurements of EUV have been included in the model and its results satisfy the general constraints of the measurements for a wide range of solar activity levels.

Figure 4.1. shows the solar EUV output in strong lines (upper panel) and various continua (lower panel) for three evenly separated values of $F_{10.7}$ index (*75, 150,* and *225*). The dependencies are not linear, and have a complicated spectral character.

Figure 4.2 shows ionization rate profiles, calculated in accordance with expressions (4.2, 4.3, and 4.4) for summer noon conditions in high latitudes ($\phi = 65^{\circ}N$, $\chi = 61^{\circ}$) for the three solar activity levels in figure 4.1. The graphs demonstrate the nonlinear response and different behavior at different altitude ranges. At *F2*-region heights the respective peak ionization rates are about 1800, 2250, and 2500 $cm^{-3}sec^{-1}$ for low, moderate, and high solar activity. The heights of peaks vary in the range of *50 km* around an altitude level of 200 km. Below that level there is a minimum in the ionization rate and all three profiles almost coincide in the vicinity of this feature at *120* km altitude. At the height of 100 km there is a second peak, giving the rates (1700, 1950, and 2200 $cm^{-3}sec^{-1}$) in response to the three levels of solar activity.

An explanation for this complicated pattern is that the contribution of different ranges of solar EUV spectrum varies at different heights. At the *F2*-region heights, the main contribution is from the broad middle part of the EUV range with the complicated non-linear response to the solar activity modulation. The strong *H-Ly-β* line *(1026* Å) almost exclusively causes the lower peak. The response of this line to solar activity variation is almost linear. The short wavelength continuums below about *175* Å contribute to the ionization near the minimum; their dependence on the solar activity is insignificant.

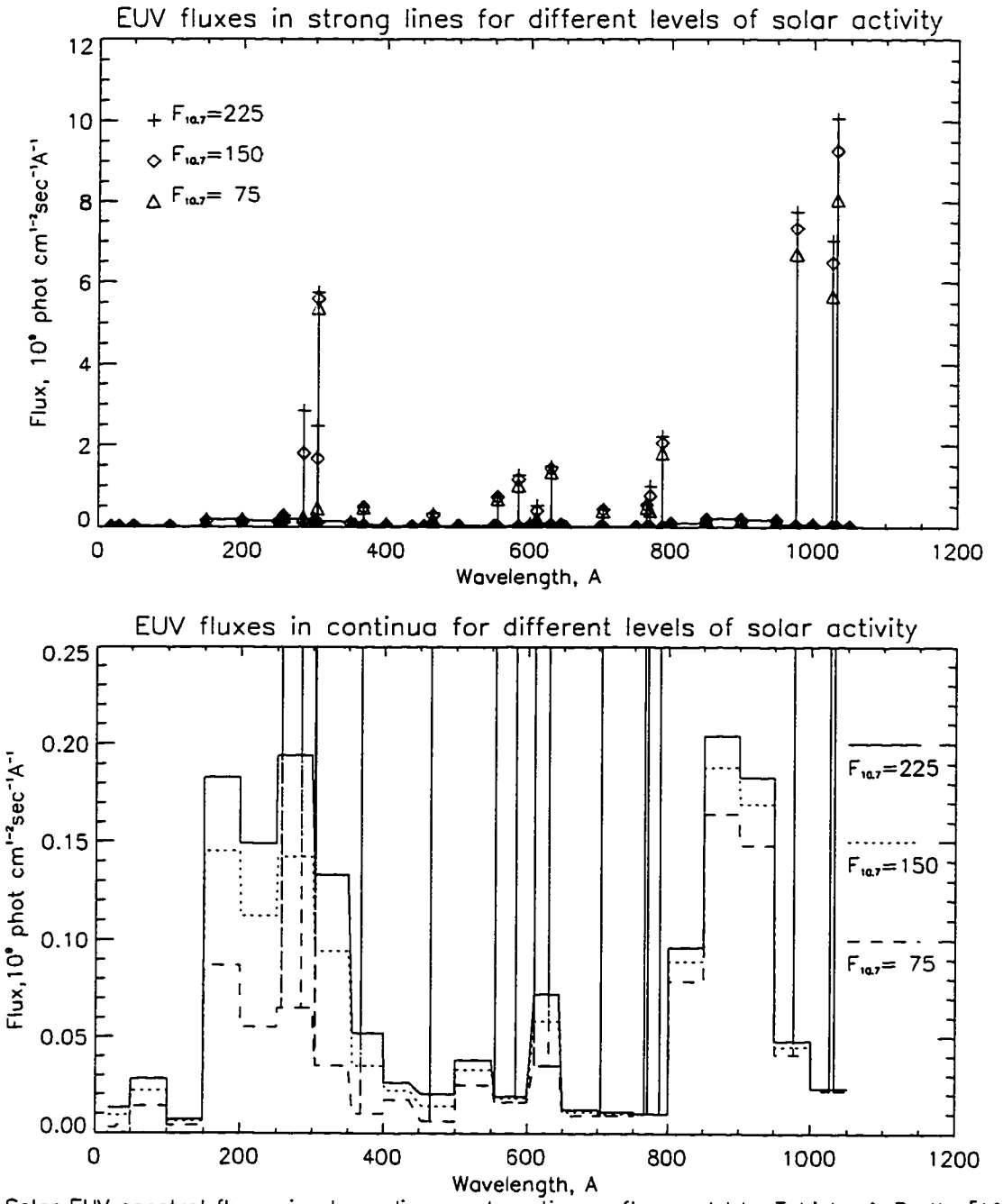

Solar EUV spectral fluxes in strong lines and continua, after model by Tobiska & Barth, [1990]

Figure 4.1. The solar EUV output in strong lines (upper panel) and various continua (lower panel) derived from the spectral model by *Tobiska and Barth* [1990]. Positions of strong spectral lines marked by the vertical lines. The dependencies are shown for three evenly separated levels of solar activity ($F_{10.7}$ = *75, 150, 225*), they are not linear and exhibit a complicated spectral behavior.

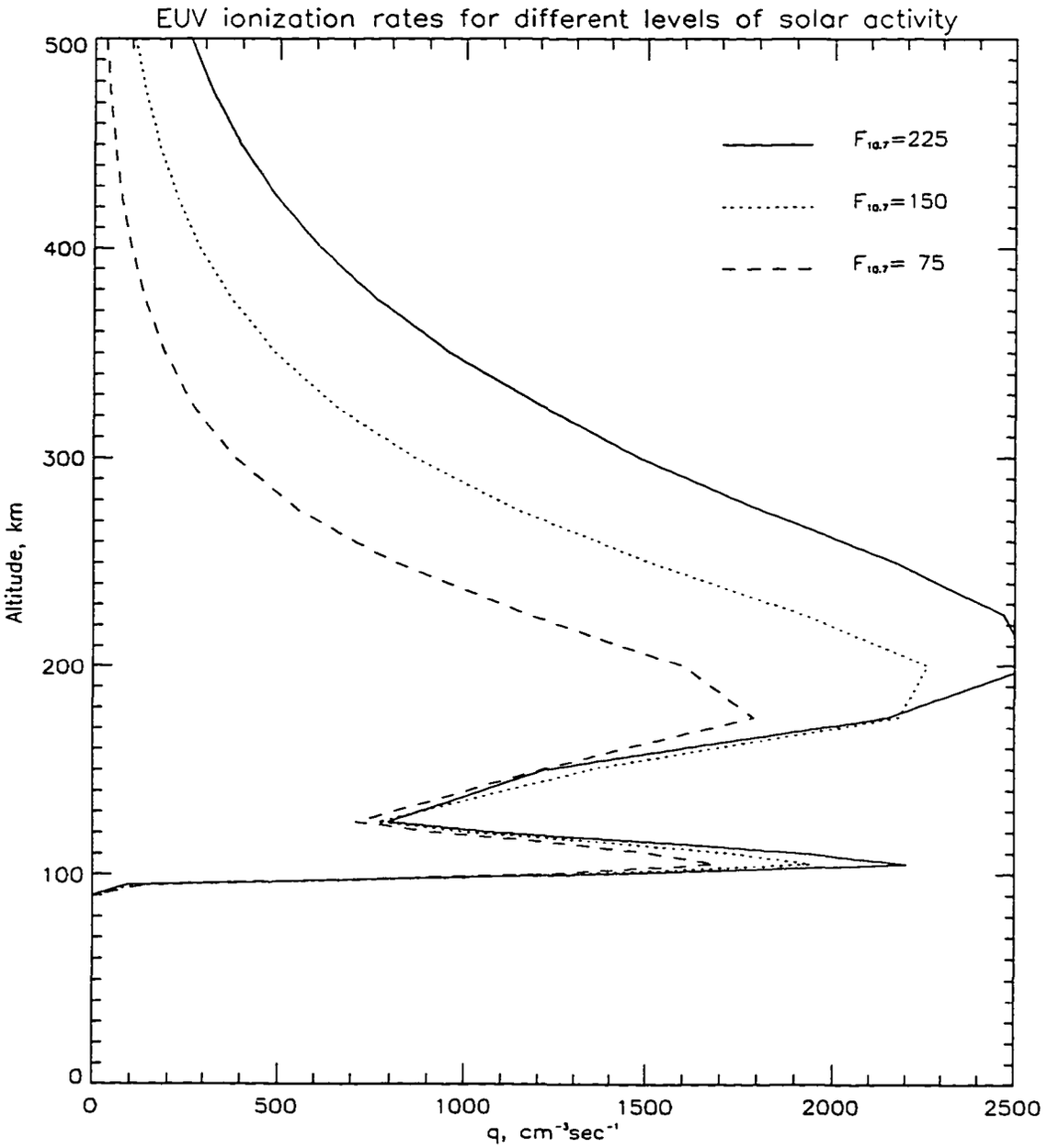

Figure 4.2. Vertical profiles of the ionization rate for three levels of solar activity ($F_{10.7}$ = 75, 150, 225) for high-latitude summer noon conditions.

4.1.2. Ionization by photoelectrons

To calculate ionization by photoelectrons, the most rigorous method involves a solution to the transport equation for photoelectron fluxes. This is a complicated computational task (e.g. *Stamnes* [1980]), and, therefore, this approach is not feasible for large 3-D models. Simplified parameterizations are necessary. As an example of such parameterization, the average efficiency of the secondary ionization adopted in NCAR TIGCM is 30% of the primary EUV ionization rate for all altitudes, zenith angles, solar activity levels, seasons, and locations [*Roble et al.*, 1987].

Such an approximation is roughly representative of values typical for the altitude range covering the ionospheric *F* region, while ignoring the weak but noticeable variations due to the solar activity level, solar zenith angle, and neutral thermospheric composition (which depends on the geographic location). However, at lower altitudes where the profile of the efficiency of secondary ionization has a sharp peak, this approximation fails to account for the drastic changes of secondary ionization efficiency. The efficiency of secondary ionization can double the primary ionization, and can peak up as high as a factor of 3 above the primary ionization in case of higher solar activity [*Lilensten et al.*, 1989]. An analytical parameterization of the secondary ionization efficiency by solar zenith angle, altitude, and geographic latitude for several solar activity levels by *Lilensten et al.*, 1989 was used in the ionization rate calculations. This is given by

$$K_L = \begin{cases} A(\chi)\cdot\exp\left[-\left(\dfrac{z-z_m(\chi)}{\sigma}\right)^{2\alpha_1}\right], & z \le z_m \\ (A(\chi)-C)\cdot\exp\left[-\left(\dfrac{z-z_m(\chi)}{\sigma}\right)^{2\alpha_2}\right] + C, & z > z_m \end{cases} \tag{4.5}$$

where K_L is the ratio of secondary to primary ionization, and the expressions for A and z_m are as follows

$$q^{i}_{DS\text{-}EUV} = K_L \, q^{i}_{DP\text{-}EUV} \tag{4.6}$$

$$A = \alpha_3 (cos\chi)^{-1} + \alpha_4 + \alpha_5 sin\phi \tag{4.7}$$

$$z_m = \alpha_6 (cos\chi)^{-1} + \alpha_7 + \alpha_8 sin\phi \tag{4.8}$$

where z is the altitude, χ is the solar zenith angle, and ϕ is the geographical latitude. Parameter z_m determines the altitude of the maximum efficiency, and A is the corresponding amplitude. Three coefficient sets (α_{i-7}, σ, and C, see Table 4.1) were calculated by *Lilensten et al.*, 1989 to fit the results of transport equation solutions performed for three levels of solar activity ($F_{10.7}$ = 68, 155, 248). The fitting error is found to be less 5%. The dependencies of these coefficients upon the solar activity index is roughly linear, and linear interpolation is applied in the model to calculate the corresponding coefficients for the intermediate values of $F_{10.7}$.

There is a dependence of parameter A (amplitude) and z_m (the height of maximum efficiency) upon the secant of the solar zenith angle ($1/cos\chi$). For zenith angles larger than 75°, the Chapman function should be used in place of the secant dependence

$$A = \alpha_3 Ch(\chi, X) + \alpha_4 + \alpha_5 sin\phi \tag{4.7a}$$

$$z_m = \alpha_6 Ch(\chi, X) + \alpha_7 + \alpha_8 sin\phi \; . \tag{4.8a}$$

The parameter C in the Table 4.1 makes the main contribution to the value of secondary ionization efficiency at the high altitudes. It has a constant profile at higher altitudes far from the efficiency peak. The value of C for moderate level of solar activity is close to that adopted in NCAR TIGCM model estimation of secondary ionization efficiency as 30% [*Roble et al.*, 1987].

The transport equations were solved by *Lilensten et al.* [1989] only for zenith angles less than 90°. For solar zenith angles larger

Table 4.1. Coefficients for computing the secondary electron production from model by *Lilensten et al.* 1989

Solar activity	Quiet	Mean	High
$F_{10.7}$	68	155	248
α_1	0.721	0.680	0.665
α_2	2.30	1.53	1.36
α_3	0.088	0.156	0.209
α_4	2.05	2.79	3.52
α_5	-0.43	-0.59	-0.86
α_6	4.61	5.73	6.28
α_7	118	116	120
α_8	-4.54	-2.71	-4.31
σ	21.1	21.6	22.1
C	0.223	0.303	0.364

than 90° we have adopted the secondary ionization efficiency profile correspondent to $\chi = 90^\circ$.

Several examples of the secondary ionization efficiency profiles obtained using the parameterization by *Lilensten et al.* [1989] are shown in figure 4.3. Variations of the parameter near its peak are from 2 to 3 for low solar activity and 3 to 4.5 for high solar activity levels. When the solar zenith angle approaches 90°, the peak height increases from *120 km* to *180 km* and its value rises.

4.1.3. Ionization by scattered EUV

An important night source of ionization at the heights of interest is EUV irradiance in the spectral lines *HeI, HeII* (584 Å, 304 Å), and *H Lyman-β* and *H Lyman-α* (1026 Å, 1216 Å) originating from resonant scattering from geocoronal *H* and *He* atoms. This process generates a

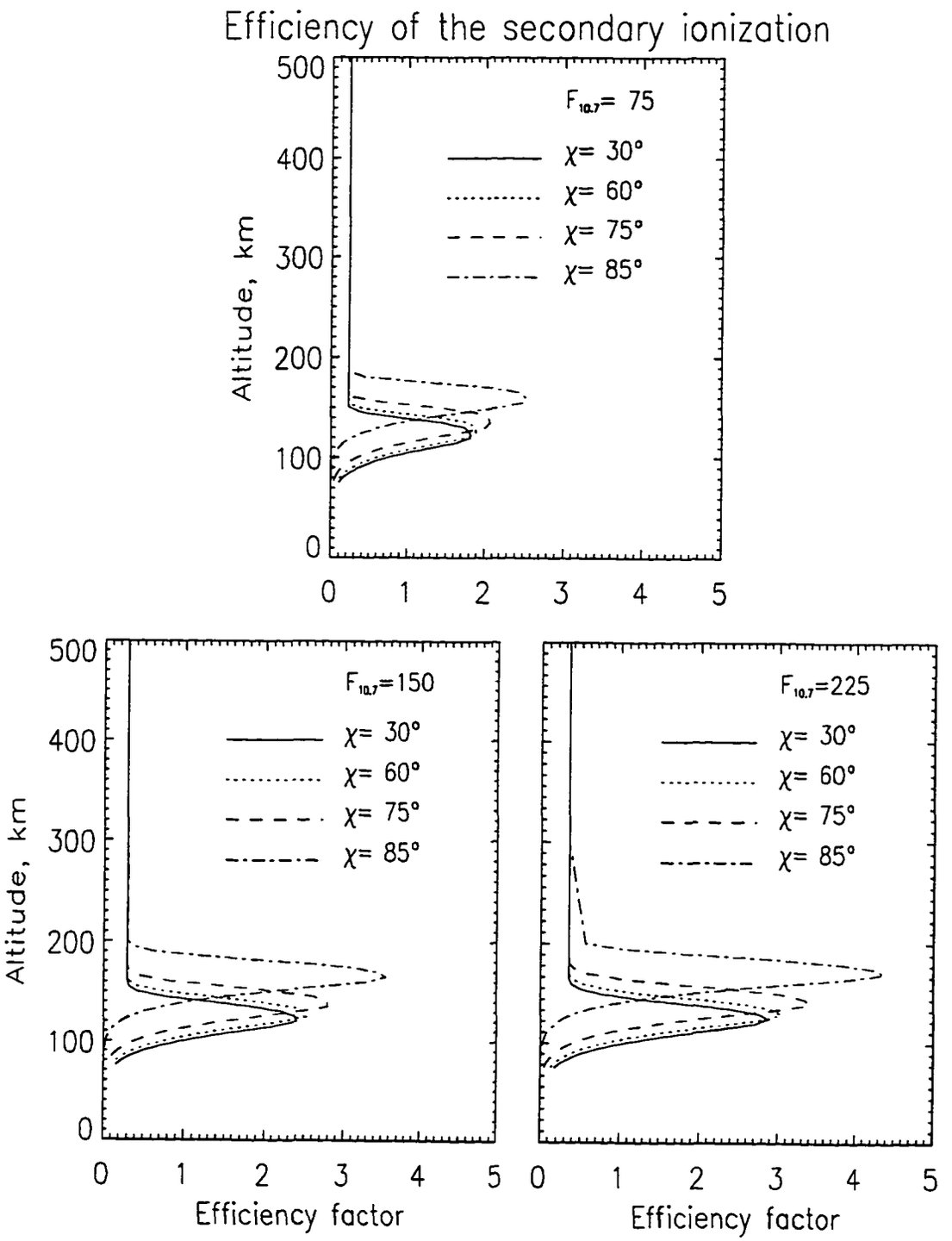

Figure 4.3. Several profiles of the secondary ionization efficiency according to parameterization by *Lilensten et al.* [1989].

photon flux which is approximately two orders of magnitude smaller than the direct solar flux in these spectral intervals. When the Sun's zenith angles are greater than about 95° the scattered fluxes are comparable to or bigger than direct fluxes (figure 4.4) and must be accounted for in the ionospheric *F* region (lines *HeI, HeII*) and *E* region (lines *H Lyman-α, H Lyman-β*) ionization rate. In the model these fluxes have been calculated by interpolation of detailed measurements by *Strobel et al.*, [1975]. The correction factors due to dependence of both direct solar EUV fluxes as well as scattered fluxes upon the solar activity level were used in the calculations in accordance with EUV parameterization model by *Tobiska and Barth*, [1990]. Efficiency factor for ionization by the secondary electrons is also applied for corrections.

4.1.4. Auroral ionization

Ionization by energetic precipitating particles, mainly by electrons, is a source comparable to EUV ionization near the regions of intensive precipitation (the auroral oval). During the winter at high latitudes it is the dominant source in the polar cap.

Compared to the spatially homogeneous ionization source from solar EUV, the determination of auroral ionization is considerably more difficult due to the spatial inhomogeneity of the precipitation pattern. The auroral oval is centered around the geomagnetic pole, which is not coincident with the geographic pole. This results in a UT-dependence of auroral effects. Superposition of auroral ionization and ionization by EUV results in a variable level of ionization during the course of a day. At about UT=17.00 the geomagnetic pole is closest to the local noon and the auroral ionization is masked by the abundant direct solar EUV source. At UT=05.00 most of the aurora precipitation is on the night side and ionization by energetic electrons is dominant.

Ionospheric models should include a detailed auroral source taking account of not only the value of precipitating fluxes, but also of the configuration of the precipitation pattern. Variations of both geomagnetic activity and IMF components lead to changes of the auroral oval size and to shifts and deformation of its configuration. The ef-

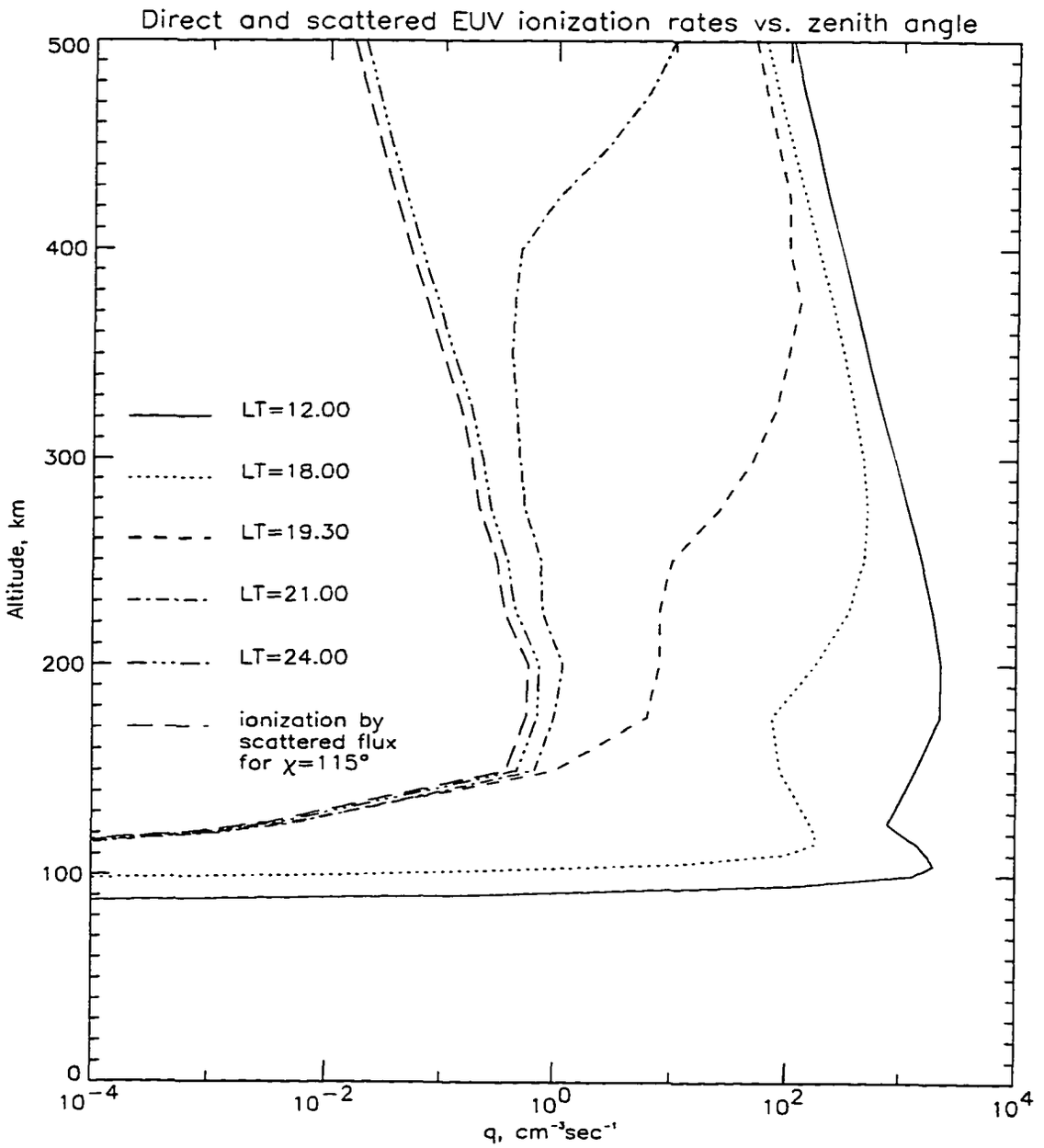

Figure 4.4. Total EUV ionization rate comprised of direct and scattered fluxes as a function of zenith angle for equinox conditions at high latitudes (65°N). Propagation of the Earth shadow upwards and transition to domination of the scattered fluxes is demonstrated in the plot. It is evident from comparison with the ionization profile due to scattered fluxes for χ=115°, the profile for χ = 111° (24.00 LT) is almost not affected by the direct irradiance. The profile for χ = 61° (14.00 LT) is produced mainly by the direct solar irradiance.

fects of IMF variations are more complicated, because of poorly understood interactions with the magnetosphere. The variations of IMF orientation produce dramatic changes even at the same level of geomagnetic activity. However, available detailed statistical models of precipitation characteristics [*Hardy et al.*, 1985, 1987, *Spiro et al.*, 1982] depend only on the level of geomagnetic activity, while IMF components are not included in the inputs. On the other hand, the models that describe the oval configuration and position depending upon IMF components, are not as detailed in the description of the precipitation characteristics inside the oval [*Akasofu and Roederer*, 1984].

A different approach to account for the auroral source in the polar ionosphere modeling was described by *Rees and Fuller-Rowell* [1992]. They found that the most practical and at the same time physically justified approach is a parameterization by the Auroral Electrojet (AE) index, routinely available with high temporal resolution. The NOAA/TIROS Power Indices [*Fuller-Rowell and Evans*, 1987], which are basically characteristics of intensity of precipitations, are a better choice because of the physical considerations, but they are not available as regularly as AE. An established correlation between the Power Index and AE solves this problem and allows the use of the AE-index as an input to the NOAA/TIROS model to generate the precipitation intensity and the oval configuration. The third choice is the K_p index, but its poor time resolution (3-hour sampling) is not sufficient for the individual event modeling. An advantage of K_p index is its availability, including its short-term forecasts. Similar to the combination of the AE index and NOAA/TIROS Power Index, a high correlation and quantitative relationship between AE and K_p indices are established by *Rostoker* [1991]. It is a very useful relationship, since it allows the user to apply the highly variable AE index as an input in the K_p-driven auroral statistical models.

One of the most widely used statistical auroral precipitations model by *Hardy at al.* [1987] is based on the fitting of analytic function to a large set of data. Fourier expansion in latitude and Epstein functions representation in longitude are used in the model to repre-

sent the results in functional form. The dependencies of the number flux and energy flux are represented as functions of the geomagnetic location and are derived for seven levels of Kp index from Kp = 0o to Kp ≥ 6o. The model gives the number flux patterns with 1° geomagnetic latitude resolution, including the soft component of the day-side precipitation that is important for *F* region modeling. However, the model does not account for variability of the polar cap precipitations, specifying a constant energy and number fluxes outside the oval poleward boundary of 10^7 *keV* $cm^{-2}sec^{-1}sr^{-1}$ and 10^7 *electrons* $cm^{-2}sec^{-1}sr^{-1}$, respectively. Thus, the polar cap precipitations, which produce the sun-aligned stable arcs during the IMF positive orientation, are not accounted for in the auroral model. As we shall see in Chapter 6 of this thesis, this is a major simplification which results in the discrepancies of the ionospheric simulation from polar cap data.

It would be desirable to replace statistical representation by measurements like aurora spectral imaging, which can be interpreted in terms of precipitation (energy flux and characteristic energy) [*Lummerzheim et al.*, 1991; *Rees*, 1992]. This approach is most applicable for individual event modeling, since statistical precipitation models provide only averaged characteristics, inevitably oversimplifying reality. The current spatial resolution of the method is several tens to a hundred kilometers, while the temporal resolution is 10-12 minutes (*Dynamic Explorer I*). Imagers with much better resolution are included in the POLAR satellite, launched February 1996 [*Rees*, 1992, *Rees at al.*, 1995].

Auroral models supply precipitation characteristics such as particle number fluxes and either energy flux or characteristic energy for the given geomagnetic location. These parameters are not sufficient to reconstruct an exact form of differential spectrum of precipitation. However, the adoption of a Maxwellian spectrum is usually justified and the ionization rate by electrons can be calculated with some simplifying assumptions [e.g. *Rees*, 1989].

$$q^{i}_{AUR}(z) = 1/\Delta\varepsilon_{ion} \sum_{p} \varepsilon(z, E_p) \qquad (4.9)$$

where $\Delta\varepsilon_{ion}$ is the mean energy loss per ionization (35 *eV*); $\varepsilon(z,E_p)$ is the energy deposition function for monoenergetic electrons with initial energy E_p

$$\varepsilon(z,E_p) = F_o E_p \Lambda(s/R) \frac{\rho(z)}{R(E_p)} \tag{4.10}$$

where F_o is the electron number flux (in units of $cm^{-2}sec^{-1}$), $\rho(z)$ is the mass density. The atmospheric scattering depth (in units of $g \cdot cm^{-2}$) is introduced as $s = \int_z^\infty \rho(z)dz$. $R(E_p)$ is the effective range (the path of an electron with initial energy E_p until it will be stopped), and $\Lambda(s/R)$ is the energy dissipation function which is a function of the fractional range s/R. The range R is an experimentally derived parameter and its most recent determination by *Barret and Hays* [1976] is valid up to characteristic energies as high as 5 *keV*; it is given by

$$R(E_p) = 4.3\times10^{-7} + 5.36\times10^{-6}E_p^{1.67} - 3.8\times10^{-9}E_p^{-0.7} \tag{4.11}$$

where E_p is expressed in units of *keV*.

Because of the requirement of energy conservation, the energy dissipation function must be normalized. The function $\Lambda(s/R)$ is calculated for different angular distributions of incident electrons by *Rees* [1963]

$$\int_{-1}^{+1} \Lambda(s/R)d(s/R) \equiv 1 \ . \tag{4.12}$$

This approach was implemented in the model for energies above 0.6 *keV*. It is not valid for softer electrons, since the energy loss per ionization drastically increases for lower energies. To properly account for the ionization by soft electrons, which is especially important in the *F* region in the day-side auroral sector, the results of the two-stream electron transport model by *Banks et al.* [1974] were used. Calculated ionization rates by a unit flux of monoenergetic (0.42 *keV*)

electrons was convolved with the low energy tail of the electron spectrum.

Auroral ionization in processes with major thermospheric components contributes the following ionization sources

$$N_2 + e^* \longrightarrow N_2^+ + e \qquad \text{(P6)}$$

$$O_2 + e^* \longrightarrow O_2^+ + e \qquad \text{(P7)}$$

$$O + e^* \longrightarrow O^+(^4S, ^2D, ^2P) + e \; . \qquad \text{(P8)}$$

Knowing the total auroral ionization rate $q_{cor}(z)$, the production of different species can be calculated by weighting the ionization rate by the ionization cross-sections and the relative abundance of the major thermospheric species O, O_2, N_2 [*Rees*, 1989]

$$q\_N_2(z) = q_{cor}(z) \; \frac{0.92\, n(N_2)}{0.92\, n(N_2) + n(O_2) + 0.56\, n(O)} \qquad (4.13)$$

$$q\_O_2(z) = q_{cor}(z) \; \frac{n(O_2)}{0.92\, n(N_2) + n(O_2) + 0.56\, n(O)} \qquad (4.14)$$

$$q\_O(z) = q_{cor}(z) \; \frac{0.56\, n(O)}{0.92\, n(N_2) + n(O_2) + 0.56\, n(O)} \; . \qquad (4.15)$$

The yield of $O^+(^2D)$ by electron impact was determined to be between 35% and 48% of the total ionization rate of atomic oxygen, while the $O^+(^2P)$ yield is around 20%, and about 40% remains for the ground state $O^+(^4S)$. *Burnett and Roundtree* [1979] suggested the 40% : 40% : 20% branching ratio between $O^+(^4S)$, $O^+(^2D)$, and $O^+(^2P)$ respectively, that was adopted in the model.

4.2. Photo-chemical sources and sinks

The following is a description of the photochemical scheme adopted in the model. The concentrations of major thermospheric components (O, O_2, and N_2), temperatures (of neutrals, T_n, ions, T_i, and electrons, T_e), and production rates by the solar EUV irradiance and by precipitating particles, are all inputs to the photochemical calculations. Photo-chemistry completely determines the sink term L in all continuity equations, and contributes greatly to the source term P. Concentrations of ions and minor neutrals are necessary for determination of chemical sinks and sources as well as the parameters listed above, but are unknown at a given time step in the model calculations. Therefore, the values determined by the previous time step, starting with the initial conditions, are adopted as input to advance the time step for the calculations of the chemical sinks and sources. This approach imposes some limitations on the model time step, which must be short enough to preserve the continuity, or an iterative process must be implemented for the fast evolving species.

The sinks and sources due to chemical reactions with known reaction constants can be evaluated if the concentrations of reacting components are specified. To estimate the chemical lifetime of the minor species X reacting with the major component Y

$$X + Y \longrightarrow Z + \textit{other products} \tag{4.16}$$

and assuming that there are no other sinks and sources for minor species X, then the equation for concentration of species X in time is

$$\frac{d[X]}{dt} = - k_{xy}[X][Y] \tag{4.17}$$

where concentrations of species is denoted as $[X]$ and $[Y]$ (in units of cm^{-3}) and the proportionality coefficient k_{xy} is a reaction constant in units of $cm^3 sec^{-1}$). Equation (4.17) states that the minor species concentration changes are proportional to the concentrations of reagents

and the reaction constant. Physically, the reaction constant is an effective reaction cross-section (cm^2) times the velocity-distribution averaged relative velocity of the reagents ($cm\ sec^{-1}$), e.g. it is an effective collision frequency per unit concentration. Assuming the concentration of the major component *Y* is unaffected by this chemical process, we obtain an exponential solution for the concentration *[X]* with a time constant independent of concentration *[X]* (in units of *sec*)

$$\tau = (k_{xy}[Y])^{-1} \tag{4.18}$$

This time constant is called the lifetime of component *[X]* regarding the process (4.16). During the time τ the concentration of species *X* reacting in the process will be depleted by one *e*-folding magnitude.

In reality often both concentrations of reagents are affected by the chemical process and/or other sinks and sources of reagents are present. However, the lifetime concept is a very useful measure to evaluate an effectiveness of a given reaction as a sink of specified component.

Other parameters derived from chemical kinetic considerations are The production rate of the product *Z* by reaction (4.16) (in units of $cm^{-3}sec^{-1}$) is

$$P_z = k_{xy}[X][Y] \tag{4.19}$$

and the loss rate of species *X* is (in units of sec^{-1})

$$\ell_{xy} = k_{xy}[Y] \ . \tag{4.20}$$

To obtain the sink (in units of $cm^{-3}sec^{-1}$), the loss rate is multiplied by the concentration *[X]*

$$L_{xy} = [X]\ \ell_{xy} = k_{XY}[Y][X] \ . \tag{4.21}$$

For the multiple species system in the terrestrial ionosphere, a summation over all reactions must be applied to obtain the total sink and source rates

$$P_z = \sum_{y,x} P_{xy} = \sum_{y,x} k_{xy}[X][Y] \tag{4.22}$$

$$L_x = \sum_{y} L_{xy} = [X] \sum_{y} \ell_{xy} = [X] \sum_{y} k_{xy}[Y] \ . \tag{4.23}$$

Finally, for the single component process, like the process of radiative deactivation

$$X^* \longrightarrow X + h\nu \tag{4.24}$$

the process rate is convenient to express in terms of the excited component lifetime τ_x (*sec*). Then sink of X^* is reciprocal of its lifetime (in sec^{-1}) and source of X is $[X^*]\tau_x^{-1}$ (in units of sec^{-1}).

4.2.1. Photo-chemical scheme for the odd nitrogen family

The odd nitrogen chemical cycle in the height range of interest consists of the neutral-neutral and ion-neutral reactions of *NO*, $N(^4S)$, and $N(^2D)$ with major and minor neutrals and ions. This chemical cycle plays a very important role in the lower thermosphere. The release of excess energy in the chemical reactions of the odd nitrogen cycle is the main source of heat for the neutrals in the thermosphere up to 250 *km* [*Torr et al*, 1980a; *Roble and Emery*, 1983]. On the other hand, the thermal radiation at 5.3 μm band of *NO* provides the main radiative cooling above 120 *km* [*Kockarts*, 1980; *Richards et al.*, 1982, *Roble et al.*, 1987]. The odd nitrogen family is also closely chemically coupled with ion production, transformation, and recombination in the *E* and *F1* regions and is an important agent for the ionization balance at these altitudes.

The list of reactions representing the odd nitrogen cycle adopted in the model, the rates (in units of $cm^3 sec^{-1}$ if not otherwise specifi-

ed), and the excess energies, are summarized in the Table 4.2, together with corresponding references.

In spite of numerous theoretical and experimental studies, a number of substantial uncertainties still remain in the odd nitrogen chemical scheme. The main uncertainty is the yield of $N(^2D)$ by the electron impact dissociative excitation of N_2 (reaction R1). Laboratory measurements by *Zipf and McLaughlin* [1978] and evaluations of aurora measurements [*Zipf et al.*, 1980] suggest a branching ratio of 50%; other studies of aurora by *Frederick and Rusch* [1977] and *Rusch and Gerard* [1980] suggested an enhanced yield of $N(^2D)$ up to 80%. Due to this fundamental uncertainty, the $N(^2D)$ yield is often considered as a variable parameter for the best data fitting.

Photo-dissociation of N_2 is also a noticeable source of $N(^2D)$ [*Zipf and McLaughlin*, 1978; *Richards et al.*, 1981], but the largest sources are reactions involving NO^+ and N_2^+, which will be considered later in this section (reactions R22, R24, R30).

A critical parameter for the *NO* production is the reaction rate of the $N(^2D)$ quenching into the ground state $N(^4S)$ by atomic oxygen, which is a dominating thermospheric component. To a great extent the balance between $N(^2D)$ and $N(^4S)$ determines the *NO* concentration, since the former produces *NO* in the process (R4) and the latter destroys *NO* in reaction (R5). Contradictory reports have been published about the reaction rate; measurements of 5200Å airglow suggest that the rate must be below 10^{-12} cm^3sec^{-1}, but the laboratory studies [*Davenport et al.*, 1976; *Iannuzzi and Kaufman*, 1980] established the rates to be near $2x10^{-12}$ cm^3sec^{-1}. The most recent measurements by *Jusinski et al.* [1988] showed an extremely high quenching rate, in excess of 10^{-11} cm^3sec^{-1}, but this is not consistent with the currently adopted aeronomic schemes.

Regardless of the actual magnitude of the quenching reaction rate, the competition between quenching of $N(^2D)$ by *O* (R6) and reaction of $N(^2D)$ with O_2 (R4) makes thermospheric *NO* sensitive to the O/O_2 ratio [*Siskind et al.*, 1989]. Therefore, the seasonal changes and geomagnetic disturbances of the O/O_2 ratio has an effect on *NO*.

Although the radiative lifetime of $N(^2D)$ is longer than *26* hours (reaction R9), it is a short-lived component due to quenching reactions (R6, R7). The photochemical equilibrium approach can be implemented to the calculations of $N(^2D)$ density. $N(^4S)$ and *NO* are long-lived components and their concentrations are strongly affected by the vertical diffusive transport and by advection in the neutral wind field.

Since the continuity equation for $N(^2S)$ and *NO* becomes a diffusive partial differential equation due to the transport term, boundary conditions must be specified. The diffusive equilibrium assumption with zero vertical flux is a good approximation at the upper boundary, where chemical sinks and sources are negligible. At the lower boundary the photochemical equilibrium for $N(^2S)$ is a realistic assumption.

By contrast, *NO* chemistry at the model lower boundary (80 *km*) is rather complicated and slow in terms of lifetime compared with transport processes. The photochemical equilibrium condition is not applicable for *NO* at this height. The concentration of *NO* or its vertical flux must be specified at the lower boundary; both parameters are highly variable and poorly known. This is a severe limitation on the solution validity, since the lower boundary at *80 km* would affect the lowest thermospheric regions that are primarily of interest concerning *NO* density distribution. Because of that, alternative approaches to the lower boundary condition must be explored. One of these possibilities is a morphologically justified condition — that *NO* profile has a minimum at these heights and relation $d[NO]/dz = 0$ holds true.

Table 4.2 Chemical scheme for the odd nitrogen adopted in the model.

(R1) $N_2 + e \longrightarrow 2\,N(^2D, ^4S) + e$		(h)
(R2) $N_2 + h\nu(\lambda \leq 1270\text{Å}) \longrightarrow 2\,N(^2D, ^4S)$		(g)
(R3) $N(^4S) + O_2 \longrightarrow NO + O + 1.4\ eV$	$4.4\times10^{-12}exp(-3220/T_n)$	(a)
(R4) $N(^2D) + O_2 \longrightarrow NO + O(^1D) + 1.84\ eV$	5.0×10^{-12}	(b)
(R5) $N(^4S) + NO \longrightarrow N_2 + O + 2.68\ eV$	3.4×10^{-11}	(a)
(R6) $N(^2D) + O \longrightarrow N(^4S) + O + 2.38\ eV$	4.5×10^{-13}	(b, j)
(R7) $N(^2D) + e \longrightarrow N(^4S) + e + 2.38\ eV$	$6.0\times10^{-10}(Te/300)^{1/2}$	(b)
(R8) $N(^2D) + NO \longrightarrow N_2 + O + 5.63\ eV$	7.0×10^{-11}	(d)
(R9) $N(^2D) \longrightarrow N(^4S) + h\nu$	$1.06\times10^{-5}\ s^{-1}$	(c)
(R10) $NO + h\nu(\lambda \leq 1910\text{Å}) \longrightarrow N(^4S) + O$	ρ_{10}	(e)
(R11) $NO + h\nu(H\text{-}Ly\text{-}\alpha,\ \lambda=1216\ \text{Å}) \longrightarrow \begin{cases} NO^+ + e \\ N(^4S) + O \end{cases}$	ρ_{11}	(f)

(a) *JPL* [1981]; (b) *Frederick and Rusch* [1977]; (c) *Garstang* [1956];
(d) *Black et al.* [1969]; (j) *Rusch and Sharp* [1981];
(e) parameterization by *Nicolet* [1979], the dissociation rate at the optically thick regions is (in units of sec^{-1})

$$\rho_{10}(z) = 4.5\times10^{-6}exp(-10^{-8}[O_2(z)]^{0.38})\ exp(-5.0\times10^{-19}[O_3(z)])\ .$$

More recent studies by *Nicolet and Cielslik* [1980] suggest an increased rate of photo-dissociation in optically thin regions

$$\rho_{10}^{\infty} = 5.7\times10^{-6},\quad sec^{-1}\ .$$

The strong rate dependence upon the level of solar activity should be taken into account.

4.2.2. Photo-chemical scheme for O^+ ions in different excited states

The concentration of O^+ ions is governed by the equation of continuity with transport terms due to ambipolar diffusion, convective ExB-drift, and neutral wind drag. Boundary conditions are defined by the photo-chemical equilibrium at the bottom and the incoming or outgoing flux at the top. The simplifying assumption that molecular ions NO^+, O_2^+, N_2^+, and ion N^+ are in photochemical equilibrium with O^+ [*Torr et al.*, 1979], is adopted in the model. The determination of the respective ion concentrations can be made from an algebraic equation (equating of sinks and sources) once the concentration of O^+ is known. This simplification is based on the lifetime comparisons. While the lifetime of O^+ is hours, the lifetime of molecular ions is determined by fast processes of dissociative recombination on the order of $10^{-7} cm^{-3} sec^{-1}$ (reactions R33, R34 will be introduced later in this chapter). For high electron concentrations on the order of $10^6 cm^3$, the lifetime is just *10* seconds, for moderate electron concentration 10^5 cm^3 it is about one minute, and starting only from low electron concentrations 10^4 cm^3 it becomes compatible with the O^+ lifetime.

(f) except the lowest part [*Maurits and Shirochkov*, 1984], the thermosphere is optically thin for the *H-Lyman-α* radiation and the following holds

$$\rho_{11} = F_{Ly\text{-}\alpha} \cdot \sigma^{NO}_{Ly\text{-}\alpha}, \quad sec^{-1}$$

where $F_{Ly\text{-}\alpha}$ is the radiation intensity in the *H-Lyman-α* line and $\sigma^{NO}_{Ly\text{-}\alpha}$ is the absorption cross section of *NO* measured by *Watanabe* [1967] with the ionization quantum yield (80%) account.

(g) the dissociation rate was evaluated by *Richards et al.* [1981]

(h) the excitational cross-sections of singlet predissociation states should be lumped together to obtain an effective total dissociation cross-section [*Zipf and McLaughlin*, 1978, *Strickland and Meier*, 1982]. See text for the discussion of branching ratio values.

Due to the overall importance of the major ion O^+ in the *F* region ionosphere, its metastable electronic states $O^+(^2D)$ and $O^+(^2P)$ must be considered. This consideration is included in the model's photochemical scheme through processes R12-R21, summarized in Table 4.3.

The photoionization wavelength thresholds of different electron states are *911Å, 733Å,* and *666Å,* or, in terms of energy, *13.6 eV, 16.9 eV,* and *18.6 eV,* respectively [*Kirby-Docken et al.*, 1979]. The overall photoionization branching between the ground state $O^+(^4S)$ and the metastable $O^+(^2D)$, $O^+(^2P)$ states, integrated over all EUV spectrum, is roughly 43%, 29%, and 28% respectively [*Torr and Torr*, 1982]. In other words, almost 60% of O^+ ions formed by EUV ionization are initially in excited states. Since the long-living ion $O^+(^2D)$ has different ionic reactions rates compared to the ground state $O^+(^4S)$, the consideration of these states separately is important for the ionospheric chemistry and, thus, electron density.

The yield of $O^+(^2D)$ due to auroral electron impact was determined to be between 35% and 48% of the total oxygen ionization rate [*Oppenheimer et al.*, 1977]. The $O^+(^2P)$ yield is around 20%, and about 40% remains for the ground state $O^+(^4S)$. *Burnett and Roundtree* [1979] suggested the branching ratio between production of $O^+(^4S)$, $O^+(^2D)$, and $O^+(^2P)$ by the electron impact as 40%, 40%, and 20% respectively.

The $O^+(^2P)$ ion has a relatively short radiative lifetime of *4.57 sec.* The radiative decay branching ratio between the transition into $O^+(^4S)$ state (with the emission in the multiplet at *7320* Å) and the transition into $O^+(^2D)$-state (emission at *2470* Å) is *0.781* to *0.219,* according to the theoretical consideration of transition probabilities [*Seaton and Ostenbrock*, 1957].

Note that the quenching reaction rates (processes R19,20) obtained by *Rusch et al.* [1977] should be increased by 15-30% since the photoelectron source of $O^+(^2P)$ was not taken into account in the model [*Torr and Torr*, 1982].

Table 4.3. Photo-chemical reactions with $O^+(^4S)$, $O^+(^2P)$, $O^+(^2D)$ ions

(R12) $O + h\nu$ (see text) $\longrightarrow O^+(^4S, ^2D, ^2P) + e$		p_{12}
(R13) $O + e^*(E \geq 13.6, 16.9, 18.6eV) \longrightarrow O^+(^4S, ^2D, ^2P) + 2e$		p_{13}
(R14) $O^+(^2P) \longrightarrow \begin{cases} h\nu\ (\lambda=7320Å) + O^+(^2D), & f(^2D)=0.781 \\ h\nu\ (\lambda=2470Å) + O^+(^4S), & f(^4S)=0.219 \end{cases}$	,	$\tau=4.57sec$
(R15) $O^+(^2D) + N_2 \longrightarrow N_2^+ + O + 1.4eV,$	8×10^{-10}, $cm^3 sec^{-1}$	(a)
(R16) $O^+(^2D) + O \longrightarrow O^+(^4S) + O + 3.3eV,$	$<3\times10^{-11}$, $cm^3 sec^{-1}$	(b)
(R17) $O^+(^2D) + O_2 \longrightarrow O_2^+ + O + 4.8eV,$	1×10^{-9}, $cm^3 sec^{-1}$	(b)
(R18) $O^+(^2D) + e \longrightarrow O^+(^4S) + e + 3.31eV,$	$7.8 \times 10^{-8} F(Te)$	(c,d)
(R19) $O^+(^2P) + N_2 \longrightarrow N_2^+ + O + 3.0eV,$	$4.8\pm1.4\times10^{-10}$	(e,f)
(R20) $O^+(^2P) + O \longrightarrow O^+(^4S) + O + 5.0eV,$	$5.2\pm2.5\times10^{-11}$	(e,f)
(R21) $O^+(^2P) + e \longrightarrow \begin{cases} O^+(^4S) + e + 5.0eV, \\ O^+(^2D) + e + 3.3e \end{cases}$	$4.7\times10^{-8}F(Te)$, $1.5\times10^{-7}F(Te)$,	(c)

where $F(Te) = (300/T_e)^{1/2}$

(a) Rowe et al. [1980]; Johnsen and Biondi [1980]

(b) Torr and Torr [1979]

(c) Henry et al. [1969]; (d) Torr et al. [1980c]

(e) Rusch et al. [1977] (f) Torr and Torr [1982]

4.2.3. Photo-chemical scheme for molecular ions

The chemical reactions involving the molecular ionized components O_2^+, N_2^+, and NO^+ are discussed in the following. Primary ionization and dissociative ionization of major thermospheric components by solar EUV and by auroral electron impact is given by processes P1-P8 introduced previously in this chapter.

Ionization thresholds of O_2 and N_2 are *12.10 eV* and *15.58 eV*, respectively, or in terms of wavelengths are *1026* Å and *796* Å. The

ionization cross sections and dissociative ionization yields are compiled by *Kirby-Docken et al.* [1979]. Dissociative ionization thresholds are *700* Å and *510* Å, respectively. About 12% of total ionization of N_2 and 13% of total ionization of O_2 are directed into the dissociative ionization process [*Torr et al.*, 1979]. Atomic neutral and ionized products of the ionization and dissociative ionization are assumed to be in the electron ground states, since the radiative lifetime of excited products is short. For ionization and dissociative ionization by electron impact we adopt the same dissociative ionization yield as in the case of photoionization.

$$N_2^+ + O \longrightarrow NO^+ + N(^2D) + 0.70\ eV \qquad \text{(R22)}$$

The reaction rate of $1.4\times10^{-10}(T_R/300)^{-0.44}\ cm^3 sec^{-1}$ was initially established by McFarland *et al.* [1974] and was reconsidered for the higher temperature range ($T_R \geq 1500K$) by *Torr et al.* [1977] and *Schunk and Raitt* [1980] as $5.2\times10^{-11}(T_R/300)^{0.2}\ cm^3 sec^{-1}$, where $T_R = (T_i + T_n)/2$.

$$N_2^+ + O_2 \longrightarrow O_2^+ + N_2 + 3.53eV \qquad \text{(R23)}$$

The reaction rate of the process (R23) is taken from *Lindinger et al.* [1974] as $5.1\times10^{-11}(T_R/300)^{-0.8}$. The contribution of this reaction compared to the reaction (R26) is dominant in the lower part of the thermosphere (90-120 *km*) but insignificant at the higher altitudes above about 150 *km*.

$$N_2^+ + e \longrightarrow \begin{cases} N(^2D) + N(^4S) + 3.44eV, & f(^2D) = 0.9 \\ N(^4S) + N(^4S) + 5.82eV, & f(^4S) = 1.1 \end{cases} \qquad \text{(R24)}$$

The rate of dissociative recombination of N_2^+ (reaction R24) was determined by *Mehr and Biondi* [1969] as $1.8\times10^{-7}(T_e/300)^{-0.39}\ cm^3 sec^{-1}$

and the branching ratio, f, between the creation of $N(^2D)$ and $N(^4S)$ was adopted in the NCAR TIGCM model [*Roble et al.*, 1987] as 90% and 10%, respectively.

The charge exchange processes (R25) and (R26) are the major sinks for the O^+ ion, the dominant ion in the ionospheric F region. These processes determine the O^+ ion lifetime and, consequently, the lifetime of the F region ionization. The reaction rates are adopted after *Albritton et al.* [1977]; *St.-Maurice and Torr* [1978], and *Schunk and Raitt* [1980].

$$O^+(^4S) + O_2 \longrightarrow O_2^+ + O + 1.56eV \qquad \text{(R25)}$$

$$k_{25} = \left[28200 - 7740t + 1073t^2 - 51.7t^3 + 0.965t^4\right] \times 10^{-15},\ cm^3 sec^{-1}$$

where $t = (0.667T_i + 0.333T_n)/300$.

$$O^+(^4S) + N_2 \longrightarrow NO^+ + N(^4S) + 1.09eV \qquad \text{(R26)}$$

$$k_{26} = \begin{cases} \left[153.3 - 59.2t + 8.6t^2\right] \times 10^{-14}, & 300 \leq T2 < 1700\ K \\ \left[27.3 - 11.55t + 1.483t^2\right] \times 10^{-13}, & 1700 \leq T2 < 6000\ K \end{cases}$$

where $t = (0.6363T_i + 0.3637T_n)/300$ and $T2$ is $T2 = (T_i + T_e)/2$.

The rate of reaction (R27) of charge exchange of the O_2^+ ion with NO is $4.4 \times 10^{-10} cm^3 sec^{-1}$ according to *Lindinger et al.* [1974] and to *Huntress and Anicicoh* [1976].

$$O_2^+ + NO \longrightarrow NO^+ + O_2 + 2.81eV \qquad \text{(R27)}$$

Another NO^+ ion source is due to charge exchange of the O_2^+ ion reaction with $N(^4S)$ (R28). The reaction rate was determined by *Torr et*

al. [1976] as 1.8×10^{-10} $cm^3 sec^{-1}$ and by *Fehsenfeld* [1977], who obtained the similar value of 1.2×10^{-10} $cm^3 sec^{-1}$.

$$O_2^+ + N(^4S) \longrightarrow \begin{cases} NO^+ + O(^3P) + 4.21eV \\ NO^+ + O(^1D) + 2.25eV \\ NO^+ + O(^1S) + 0.04eV \end{cases} \qquad \text{(R28)}$$

A fast process of dissociative recombination of O_2^+ results in partial excitation of atomic oxygen into the $O(^1D)$ electronic state with quantum yield of 85% [*Roble et al.*, 1987]. The reaction rate is determined by *Mehr and Biondi*, 1969; *Walls and Dunn*, 1974; *and Torr et al.*,1979 for different temperature ranges.

$$O_2^+ + e \longrightarrow \begin{cases} O(^3P) + O(^3P) + 6.95eV, \\ O(^1D) + O(^3P) + 4.98eV, \quad f(^1D) = 0.85 \end{cases} \qquad \text{(R29)}$$

$$k_{29} = \begin{cases} 1.6\times10^{-7}(300/T_e)^{0.55}, & T_e \geq 1200K \\ 2.7\times10^{-7}(300/T_e)^{0.7}, & T_e < 1200K \end{cases}$$

The reaction rate of dissociative recombination of NO^+ ion was determined by *Walls and Dunn* [1974] as $4.2\times10^{-7}(300/T_e)^{0.85}$ $cm^3 sec^{-1}$. The branching ratio of $N(^2D)$ is not known decisively and is often used as a fitting parameter. A ratio *0.8* was adopted in the NCAR TIGCM model [*Roble et al.*, 1987]. The value of *0.75* was suggested in a review by *Torr and Torr* [1982].

$$NO^+ + e \longrightarrow \begin{cases} N(^4S) + O + 2.75eV, \quad f(^4S) = 0.2 \\ N(^2D) + O + 0.38eV, \quad f(^2D) = 0.8 \end{cases} \qquad \text{(R30)}$$

Several reactions with the N^+ ion are important for the odd nitrogen chemistry and for the energy balance. The charge exchange rate

with atomic oxygen (R31) is 10^{-12} $cm^3 sec^{-1}$ [*Torr*, 1985].

$$N^+ + O \longrightarrow O^+ + N + 0.93eV \qquad \text{(R31)}$$

The charge exchange reaction of N^+ with molecular oxygen is two orders of magnitude faster. As a sink of N^+, it makes this reaction comparable to the charge exchange process with the atomic oxygen (R31), regardless of a relatively lesser density of the molecular oxygen in the thermosphere. The rate of reaction (R32) and its branching ratio were determined by *Lindinger et al.* [1974] and *Huntress and Anicicoh* [1976].

$$N^+ + O_2 \longrightarrow \begin{cases} NO^+ + O + 6.699eV, & 2.0\times10^{-10}\ cm^3 sec^{-1} \\ O_2^+ + N(^4S) + 2.486eV, & 4.0\times10^{-10}\ cm^3 sec^{-1} \\ O_2^+ + N(^2D) + 0.1eV, & 2.0\times10^{-10}\ cm^3 sec^{-1} \\ O^+ + NO + 2.31eV, & 3.0\times10^{-11}\ cm^3 sec^{-1} \end{cases} \qquad \text{(R32)}$$

CHAPTER 5

NUMERICAL SOLUTION

This chapter is devoted to the numerical handling of the system of the governing equations. First, it will be shown how the transition to the Cartesian system affects the solution accuracy. Next, the numerical solution (relaxation method) of the equation of electron energy balance, which was reduced to the 1-D ordinary differential equation, will be described. Methods for the numerical solution of the 1-D diffusive parabolic PDE are also described together with the specification of the lower and upper boundary conditions and discussion of the initial condition and the solution convergence. The final section is devoted to the solution of the mixed diffusive-advective PDE in the corotating system.

5.1. The system of governing equations in Cartesian coordinates

The coordinate frame of the model was introduced in Chapter 2. A spherical coordinate system is more natural for spherical geometry, but has a significant disadvantage with a singularity near the geographic pole where the distances corresponding to the fixed latitudinal increments $\Delta\lambda$ decrease to zero. Therefore in the model a transition has been made to a convenient Cartesian system which has no singularity anywhere in the covered area. In Chapter 2 we described the applicability of the Cartesian system by noting that the curvature is negligible in the limited polar region for the height range which is much less when compared to the Earth radius. In this section this will be demonstrated by rigorous mathematical evaluation.

5.1.1. Azimuthal Equidistant Projection (AEP)

The method known as the Azimuthal Equidistant Projection (AEP) has been chosen to create the Cartesian coordinates. This method maps a spherical region of interest into the rectangular box with the base

parallel to the plane, which is tangential to the Earth at the pole. The base is 80 *km* above the Earth's surface at the height of the height of the lower boundary, the *X*-axis of this system is parallel to the Greenwich meridian, the *Y*-axis is parallel to meridian of 90°E, and the *Z*-axis is directed upward.

A location with the spherical coordinates (r, ϕ, λ) is projected into this AEP Cartesian system in accordance with the following expressions

$$\begin{aligned} x &= R_o \, \alpha \, cos\lambda \\ y &= R_o \, \alpha \, sin\lambda \\ z &= r - R_E \end{aligned} \qquad (5.1)$$

where α is co-latitude in radians, λ is longitude, r is the radial distance in the spherical system, and $R_o = R_E + z_o$ is the radial distance to the lower boundary at the altitude z_o. Thus, in this system a meridional displacement is equivalent to motion in the radial direction from the system center, and latitudinal circles are projected to equidistant concentric circles in the system plane. Radial motion in the spherical system is equivalent to the vertical motion along the z-axis in the Cartesian system. It is evident that the meridional distances correspond to the radial distances from the origin of AEP at the *x,y*-plane. Meridional distances are preserved under this projection, while the circumferences of the latitudinal circles are magnified by factor $\alpha/sin\alpha$, where α is the co-latitude. In the spherical system the meridional and zonal elements of distance depend on the radial coordinate, while in the chosen AEP system all *x,y*-coordinates are referenced to the spherical radial distance R_o (at altitude of 80 *km*) and all distance elements are independent on the vertical coordinate.

5.1.2. Metric coefficients of the AEP Cartesian system

Expressing the differentials of the AEP coordinates (x, y, z) in terms of the co-latitude, longitude, and radial distance,

$$dx = R_o [\cos\lambda \; d\alpha - \alpha \sin\lambda \; d\lambda]$$

$$dy = R_o [\sin\lambda \; d\alpha + \alpha \cos\lambda \; d\lambda] \qquad (5.2)$$

$$dz = dr \; ,$$

and taking into account that the "true" elements of distance $\{dx_s, dy_s, dz_s\}$ in the spherical coordinates are $dx_s = r \cos\phi \; d\lambda = r \sin\alpha \; d\lambda$, $dy_s = r \; d\phi = -r \; d\alpha$, $dz_s = dr$, one can obtain the following expression, combining the "true" elements of distance and the elements of distance in the AEP system $\{dx, dy, dz\}$ $(\alpha > 0)$:

$$dx = \frac{R_o}{r} \left[-\frac{\alpha}{\sin\alpha} \sin\lambda \; dx_s - \cos\lambda \; dy_s \right]$$

$$dy = \frac{R_o}{r} \left[\frac{\alpha}{\sin\alpha} \cos\lambda \; dx_s - \sin\lambda \; dy_s \right] \qquad (5.3)$$

$$dz = dz_s \; .$$

Or, omitting the trivial vertical direction, the relation between the distance elements dx, dy and dx_s , dy_s in the matrix form is $(\alpha > 0)$

$$\begin{pmatrix} dx \\ dy \end{pmatrix} = \frac{R_o}{r} \begin{pmatrix} -\sin\lambda & -\cos\lambda \\ \cos\lambda & -\sin\lambda \end{pmatrix} \begin{pmatrix} \frac{\alpha}{\sin\alpha} dx_s \\ dy_s \end{pmatrix} . \qquad (5.4)$$

In equation (5.4) the 2x2 matrix corresponds to a rotation of the spherical coordinates by angle $270-\lambda$, while the whole expression establishes a connection between the elements of "true" spherical distances dx_s, dy_s and the Cartesian increments of the introduced AEP coordinates dx, dy. The metric coefficients h_x, h_y, h_z of the AEP coordinate system can be established using the relations $dx = h_x dx_s$; $dy = h_y dy_s$; and $dz = h_z dz_s$. Hence, the metric coefficients of the AEP system are

$$h_x = \frac{R_o}{r}\frac{\alpha}{\sin\alpha}; \qquad h_y = \frac{R_o}{r}; \qquad h_z = 1 . \tag{5.5}$$

Using equations similar to (5.4), we can establish a relation of the velocities in the AEP system ("map" velocities) $\dot{x} \equiv dx/dt$, $\dot{y} \equiv dy/dt$; spherical curvilinear velocities $u \equiv dx_s/dt$, $v \equiv dy_s/dt$; and the velocity components relative to the Earth in the directions of the AEP system $\vartheta_x = h_x\dot{x}$, $\vartheta_y = h_y\dot{y}$

$$\begin{pmatrix} \dot{x} \\ \dot{y} \end{pmatrix} = \frac{R_o}{r}\begin{pmatrix} -\sin\lambda & -\cos\lambda \\ \cos\lambda & -\sin\lambda \end{pmatrix}\begin{pmatrix} \frac{\alpha}{\sin\alpha}u \\ v \end{pmatrix} \tag{5.6}$$

$$\begin{pmatrix} \vartheta_x \\ \vartheta_y \end{pmatrix} = \begin{pmatrix} -\sin\lambda & -\cos\lambda \\ \cos\lambda & -\sin\lambda \end{pmatrix}\begin{pmatrix} u \\ v \end{pmatrix} . \tag{5.7}$$

A relation similar to (5.7) is applicable to the transition of components of a force in the AEP system if the zonal and meridional components are known. Thus, this 2×2 operator from expressions (5.6) and (5.7) is applicable to the transformation of zonal and meridional components of the equation of motion (i.e. the equation of the force balance). Transformation of the vertical component is trivial, since the vertical metric coefficient is unity. In the next section the transformation of the governing equations to the AEP system will be performed.

The explicit relations of the velocity components relative to the Earth ϑ_x, ϑ_y and the velocities in the AEP coordinate system $\dot{x}$, $\dot{y}$ are

$$\begin{aligned} \vartheta_x &= h_x\dot{x} = \frac{R_o}{r}\frac{\alpha}{\sin\alpha}\dot{x} \\ \vartheta_y &= h_y\dot{y} = \frac{R_o}{r}\dot{y} \end{aligned} \tag{5.8}$$

The factor of R_o/r varies in the interval [0.95,1.00] for the model height range 80-500 *km* and represents the deceleration due to variability of circumference of the spherical surface at different spherical radial distances. A parcel with meridional and/or zonal velocities $v(r)$, $u(r)$ travels a longer path if $r > R_o$. Since the path at the AEP system is the same for any r, the correction coefficient R_o/r accounts for this effective path shortening by decreasing the corresponding velocities. This decreasing ratio, R_o/r, is height-dependent, while the same correction factor is applied on a horizontal AEP system plane for a fixed height.

The next factor, $\alpha/sin\alpha$, is an effective acceleration factor applicable to long latitudinal circles in the AEP system. This is a consequence of preserving the meridional distances in the AEP system and magnification of latitudinal circles by the same factor $\alpha/sin\alpha$. Acceleration effectively preserves the travel time for a given distance in the latitudinal direction. The factor is location-dependent and varies from zero at the pole to 0.900 at 45° degrees of latitude (see table 2.1 on page 32 of this thesis for the latitudinal dependence of this factor).

Both metric correction factors are within the range of a few percent and, taking into account all other sources of errors and uncertainties, are negligible. However, it is instructive to derive the model governing equations in the AEP system having in mind its possible expansion to the higher altitudes heights or to mid-latitudes, where corrections could become important.

5.1.3. Derivation of the governing equations in the AEP system

After derivation of the metric coefficient of the AEP system we are in position to modify the governing equations of the model for application in the AEP Cartesian system. Equations of continuity have a divergence term of the density flux $n\mathbf{v}$, which can be expressed in the general 3-D curvilinear coordinate system with the metrics coefficients h_1, h_2, and h_3 as follows

$$\mathbf{div}\cdot(n\mathbf{v}) = \frac{1}{h_1 h_2 h_3}\left[\frac{\partial}{\partial x_1}\left(h_2 h_3\ n\dot{x}_1\right) + \frac{\partial}{\partial x_2}\left(h_1 h_3\ n\dot{x}_2\right) + \frac{\partial}{\partial x_3}\left(h_1 h_2\ n\dot{x}_3\right)\right] . \qquad (5.9)$$

Substituting h_x, h_y, h_z from (5.5) into (5.9), the corrected equation of continuity in terms of "map" velocities $\dot{x}$, $\dot{y}$, $\dot{z}$ is

$$\frac{\partial n}{\partial t} + \frac{r^2 \sin\alpha}{R_o^2}\frac{}{\alpha}\left[\frac{\partial}{\partial x}\left(\frac{R_o}{r} n\dot{x}\right) + \frac{\partial}{\partial y}\left(\frac{R_o}{r}\frac{\alpha}{\sin\alpha} n\dot{y}\right)\right] + \frac{\partial}{\partial z}\left(n\dot{z}\right) = P - L \qquad (5.10)$$

Here we neglect a small term $(-n\dot{z} / r)$ that compensates for the absence of the spherical expansion in the Cartesian geometry of the AEP system.

Transition to the velocities in the directions of the AEP system $\vartheta_x, \vartheta_y, \vartheta_z$ that are relative to the Earth can be done in accordance with equation (5.8)

$$\frac{\partial n}{\partial t} + \frac{r^2 \sin\alpha}{R_o^2}\frac{}{\alpha}\left[\frac{\partial}{\partial x}\left(\frac{\sin\alpha}{\alpha} n\vartheta_x\right) + \frac{\partial}{\partial y}\left(\frac{\alpha}{\sin\alpha} n\vartheta_y\right)\right] + \frac{\partial}{\partial z}\left(n\vartheta_z\right) = P - L \qquad (5.11)$$

Equation (5.11) is the final form of the corrected equation of continuity in the AEP system. In this form it can be applied not only in the limited sub-polar region but for the entire hemisphere, where the use of AEP is still reasonable, i.e. up to the equator. Limitations on the height coverage are also eliminated by using the correction coefficient.

The equation of the energy balance for T_i and T_e was reduced in the ionospheric applications to a 1-D vertical equation. Since the vertical metric coefficient h_z is unity, there are no transformations for this equation.

The last governing equation is the equation of motion, or the force balance equation. In its simplified form, which is adopted in this model version, only the vertical derivatives are preserved. As we

noted before, transformation in the vertical direction is trivial, since the metrics are the same in both spherical and AEP systems. In the horizontal direction the motion is governed by the Lorentz force and by neutral drag. Both forces depend on the ion velocity; as long as we know the involved magnetic and electric fields, the equation of motion is solvable for the horizontal ion velocity components regardless of the system of reference. Thus, the transformation of the horizontal components of the ion velocities is a matter of choice of reference system. Both options are valid; either the zonal and meridional components of B and E-fields are first transformed into AEP system, then the resulting ion velocity components are specified in this system, or the meridional and zonal components of the B and E-fields are used to find the meridional and zonal components of ion velocities, which must then be transformed in the AEP system.

An important parameter for our consideration, the inclination of magnetic field or dip angle I, is derived from the reference geomagnetic field model IGRF80 and is transformed to the AEP system by point-by-point transformation for a given geographic location. It is a monotonic function of latitude and longitude and the AEP transformation does not cause an effect of the field lines crossing.

5.1.4. Other projections of the spherical system to the Cartesian frame

In conclusion, it must be pointed out that the AEP is not the only possible projection transforming the spherical segment to the Cartesian box. For instance, a widely used stereographic projection transforms both meridional and zonal metrics by

$$x = 2R_o \frac{\cos\phi \cos\lambda}{1 + \sin\phi}; \quad y = 2R_o \frac{\cos\phi \sin\lambda}{1 + \sin\phi}; \quad z = r - R_E \qquad (5.12)$$

Stereographic projection provides minimal distortions in mid-latitudes and is convenient for the coverage of the entire hemisphere.

Orthographic projection, in contrast to AEP, preserves the length

of the latitudinal circles and makes the meridional distances variable:

$$x = R_o \cos\alpha \cos\lambda \; ; \quad y = R_o \cos\alpha \sin\lambda \; ; \quad z = r - R_E \; . \tag{5.13}$$

As in the AEP, the orthographic projection has minimal distortion near the pole. However, because of variable meridional distances, it lacks the visual geometric simplicity of the AEP system.

5.2. Numerical treatment of the equations of energy balance for electrons and ions

In Chapter 3 it was shown that the equation of the electron and ion temperatures over the model height range can be reduced to a 1-D ordinary differential equation for T_e, and to an algebraic relation in case of T_i. Equation (3.18) for T_e

$$\sin^2 I \; \frac{\partial}{\partial z} \left(\lambda_e \; \frac{\partial T_e}{\partial z} \right) + Q_e - L_e = 0 \tag{3.15}$$

is solved at each model time-step by the standard relaxation method from the Fortran package *NUMERICAL RECIPES* by *Press et al.* [1992]. Adaptation of the method to thermospheric applications and the corresponding codes were developed by *Min* [1993]. Parameterizations of the heating sources and cooling sinks used in the calculations are described in section 3.2.2. The lower boundary condition is $T_e = T_n$, while the heat flux through the upper boundary is parameterized by *Roble et al.* [1988]

$$\Phi_e = \begin{cases} \Phi_{eD} & , \chi \le 80 \\ \Phi_{eD}\left[0.6 + 0.4 \cos\left(\pi \dfrac{\chi - 80}{20}\right)\right] & , 80 \le \chi \le 100 \\ \Phi_{eD} / 5 & , \chi \ge 100 \end{cases} \tag{5.14}$$

where χ is the solar zenith angle in degrees. The energy flux Φ_{eD} is dependent on the solar activity and on the geomagnetic latitude. In units of $erg\ cm^{-2} sec^{-1}$ it is

$$\Phi_{eD} = (A/2) \cdot 4.5 \times 10^{7} \cdot F_{10.7} \cdot 1.602 \times 10^{-12} \tag{5.14a}$$

and

$$A = \begin{cases} 1 & , \phi_{gm} \geq 60 \\ \frac{1}{2}\left(1 + \sin\left(\pi \frac{\phi_{gm} - 30}{60}\right)\right) & , \phi_{gm} < 60 \end{cases} \tag{5.14b}$$

where ϕ_{gm} is the geomagnetic latitude.

The ion temperature T_i is found from the algebraic relation for the ion energy balance (3.60) derived in Chapter 3:

$$T_i = T_n + \frac{m_n}{3k}\left[\left(\frac{E_{mer}}{B_z} - v_n^{zon}\right)^2 + \left(\frac{E_{zon}}{B_z} + v_n^{mer}\right)^2\right] . \tag{3.60}$$

This equation uses the meridional and zonal neutral wind velocity and electric field components, as well the vertical component of the magnetic field taken from IGRF80 model. Solution of this algebraic equation for T_i is performed at each time step of the model.

5.3. Numerical handling of the equation of continuity

In Chapter 3 two types of continuity equation were derived. First, a simplified consideration without account of horizontal advection of the odd nitrogen family NO, $N(^4S)$ resulted in a 1-D continuity equation in the vertical direction which mathematically represents a second order PDE of parabolic type. Second, the 3-D mixed diffusive-advective equation was derived for the major F-region ion $O^+(^4S)$.

In this section we will consider a fully implicit method for the numerical solution of the 1-D diffusive equation, discuss the boundary and initial conditions for different species, discuss the solution convergence and its numerical stability and accuracy. We then proceed to

a 3-D case to demonstrate how it can be reduced to the combination of of a purely advective 2-D equation that allows a simple and fast numerical solution in explicit form, and the 1-D diffusive equation, which is solvable by a fully implicit numerical scheme.

5.3.1. The 1-D equation of continuity

The equation of continuity for the 1-D case is reduced to the following form, provided the diffusion and advection processes are confined to the vertical direction:

$$\frac{\partial n}{\partial t} = A\frac{\partial^2 n}{\partial z^2} + B\frac{\partial n}{\partial z} + Cn + E \qquad (5.15)$$

where n is the density, and the height-dependent coefficients A, B, C, E were introduced in Chapter 3 for both the odd nitrogen family and for the $O^+(^4S)$ ion. Equation (5.15) is a second-order PDE of parabolic type. The explicit numerical schemes for its solution require prohibitively small time steps either as a stability condition or as an accuracy requirement (DuFort-Frankel scheme). There are several choices of numerically implicit, unconditionally stable schemes that solve the small time-step problem. The most common schemes are the fully implicit scheme, the Crank-Nicholson scheme, and the generalized three-level fully implicit scheme.

The fully implicit scheme is unconditionally stable and accurate to the second order in space and to the first order in time. Assuming that $\tilde{n}$ and n define the density at the current time step $\ell+1$ and at the previous time steps ℓ respectively and equation coefficients, when possible, are found at the intermediate time level $\ell+1/2$ or at the previous level ℓ (chemical losses can be calculated only with known densities from time level ℓ), the finite-difference representations of equation (5.15) at each of $k=2, \ldots, K-1$ height cells starting the indexing from bottom to top are:

$$\frac{\tilde{n}_k - n_k}{\Delta t} = A(k,\ell+1/2)\,\frac{\tilde{n}_{k+1} - 2\tilde{n}_k + \tilde{n}_{k-1}}{(\Delta z)^2} + B(k,\ell+1/2)\,\frac{\tilde{n}_{k+1} - \tilde{n}_{k-1}}{2\Delta z} + \\ + C(k,\ell)\tilde{n}_k + E(k,\ell+1/2)\ . \tag{5.16}$$

After collection of terms, this finite-difference representation gives rise to a tridiagonal system of $(K-2)$ linear algebraic equations for K variables $\tilde{n}_k$ $(k=1,\ldots,K)$

$$a_k\tilde{n}_{k+1} + b_k\tilde{n}_k + c_k\tilde{n}_{k-1} = d_k \tag{5.17}$$

where the constant coefficients a_k, b_k, c_k, d_k are functions of the temporal (Δt) and spatial (Δz) steps and the equation (5.15) coefficients A, B, C, D at the given height cell

$$\begin{aligned} a_k &= \Delta t\left(2A(k,\ell+1/2) + \Delta z\cdot B(k,\ell+1/2) \right) \\ b_k &= 2(\Delta z)^2\left(\Delta t\ C(k,\ell) - 1 - \frac{2\Delta t\cdot A(k,\ell+1/2)}{(\Delta z)^2} \right) \\ c_k &= \Delta t\left(2A(k,\ell+1/2) - \Delta z B(k,\ell+1/2) \right) \\ d_k &= 2(\Delta z)^2\left(n_k - \Delta t E(k,\ell+1/2) \right) \end{aligned} \tag{5.18}$$

Two boundary conditions for determination of $\tilde{n}_1$ and $\tilde{n}_K$ close the tridiagonal system and then allow the application the standard sweeping algorithm for its solution, known as the Thomas algorithm, that solves the system in $5(K-2) - 4$ multiplication and division operations.

The numbers $x_{k-1}, y_{k-1}, x_k, y_k$ can be found to satisfy the following expressions

$$\tilde{n}_k = x_{k-1}\tilde{n}_{k-1} + y_{k-1} \tag{5.19}$$

$$\tilde{n}_{k+1} = x_k\tilde{n}_k + y_k \tag{5.19a}$$

Substitution of the latter expression for $\tilde{n}_{k+1}$ into equation (5.17) gives the formal solution for $\tilde{n}_k$

$$\tilde{n}_k = \frac{-y_k}{a_k x_k + b_k}\tilde{n}_{k-1} + \frac{d_k - a_k y_k}{a_k x_k + b_k} \qquad (5.20)$$

Comparison with the relation (5.19) yields gives the recurrent expressions for x_{k-1} and y_{k-1}

$$x_{k-1} = \frac{-y_k}{a_k x_k + b_k} \qquad y^{k-1} = \frac{d_k - a_k y_k}{a_k x_k + b_k} \qquad (5.21)$$

Thus, if we know y_K, and x_K at $k = K$ (the upper boundary cell) we can sweep down to get the entire set of the coefficients x_k, y_k up to $k=1$ (lower boundary). Coefficients y_K, x_K can be found from the upper boundary condition. It is physically advantageous to represent the upper boundary condition as a condition on the vertical flux Φ. This flux is zero if diffusive equilibrium is achieved, positive if outflow takes place, or negative in the case of influx of species.

Considering the upper boundary condition for the odd nitrogen family, one can rewrite the vertical flux expression (3.104) near the upper boundary where the diffusion is purely molecular and the neutral temperature is practically constant ($D_m \ll K$, $\partial T/\partial z = 0$)

$$\Phi = -D_m\left(\frac{\partial \tilde{n}}{\partial z} + \frac{\tilde{n}}{H}\right) \cong -D_m\left(\frac{\tilde{n}_{K+1} - \tilde{n}_K}{\Delta z} + \frac{\tilde{n}_K}{H}\right) . \qquad (5.22)$$

From expression (5.22) one can derive the following relation

$$\tilde{n}_{K+1} = (1 + \frac{\Delta z}{H})\tilde{n}_K - \frac{\Phi \Delta z}{D_m} . \qquad (5.23)$$

Expression (5.23) after comparison with expressions (5.19),

yields coefficients y^K, x^K

$$y_K = - \frac{\Phi \Delta z}{D_m} \; ; \qquad x^K = 1 + \frac{\Delta z}{H} \; . \tag{5.24}$$

Note that the coefficient y_K is zero if diffusive equilibrium is assumed ($\Phi = 0$), or is defined by the specified flux Φ through the upper boundary. Starting from the upper cell $k = K$ down and using the recurrent expressions (5.21), we can now obtain the entire set of x_k, y_k coefficients.

The next step is a calculation of the corresponding densities $\tilde{n}_k$ using relation (5.19). To proceed in the direction of index increasing ($k = 2,\ldots,K$) using expression (5.19), we need to find the density $\tilde{n}_1$ at the bottom cell, which is subject to determination from the lower boundary condition. Photochemical equilibrium is chosen for $O^+(^4S)$ and $N(^4S)$ as the lower boundary condition, which are short-living species at these altitudes

$$\tilde{P}_1 + \tilde{n}_1 \tilde{L}_1 = 0 \tag{5.25}$$

where all parameters $\tilde{P}$, $\tilde{L}$, $\tilde{n}$ are calculated at the current time step. Note that the photochemical sinks and sources terms P and/or L can depend on the densities yet to be established for the current time step. In this case the densities from the previous time step are used to calculate P and/or L. This is a practical limitation for the time step in this unconditionally stable method. This limitation can be overcome either by iterations (one or two is usually enough to achieve a convergence at a reasonable level of several percent) or by choosing the time step when the density of species of interest does not dramatically change. A good practical compromise for most ionospheric applications is the choice of a time step that does not exceed ten minutes.

In case of NO, the photochemical equilibrium assumption is not applicable, as it is a long-lived component. A choice of fixed density as a boundary condition is not feasible for 3-D time-dependent model

since there is no adequate data about the *NO* distribution at 80 *km* for the variety of geophysical conditions. On the other hand, use of an inappropriate density value can distort the *NO* vertical profile for several height cells near the lower boundary. A well-established morphological feature of the *NO* vertical profile is the local minimum at heights of 75-85 *km*. The mathematical condition of this minimum *(d[NO]/dz = 0)* can be used as a more flexible lower boundary condition for *NO*, compared to the fixed density choice. The minimum condition in the finite-difference representation $(n_2 - n_1 = 0)$ and expression (5.19) written for cell $k = 2$ comprises a system for determination of n_1

$$\begin{aligned} n_2 - n_1 &= 0 \\ n_2 - x_1 n_1 &= y_1 \end{aligned} \qquad (5.26)$$

that yields for the *NO* lower boundary densities $n_1 = n_2 = y_1 / (1 - x_1)$.

As was noted previously, the upper boundary condition for the odd nitrogen family $(N(^4S), NO)$ is a diffusive equilibrium or zero flux through the upper boundary at 500 *km*. For $O^+(^4S)$ ions the upper boundary is open, allowing non-zero vertical non-diffusive flux $\Phi = n_K w_K$. Omitting the diffusive term in expression (3.92), the vertical flux near the upper boundary is as follows,

$$\Phi = n_K \left[w_K \sin^2 I + (v_K \cos D + u_K \sin D) \cos I \sin I + \frac{c}{B^2} |E \times B|_z \right] \qquad (5.27)$$

where the index K corresponds to the upper cell in the vertical mesh, w_K, v_K, u_K are vertical, meridional, and zonal velocity, respectively, I is the inclination, and D is the deviation of the magnetic field. The first term represents the neutral drag in the vertical direction, the second term is the vertical projection of the field-aligned component of the horizontal neutral drag, and the last term is the vertical ExB-drift component (see expression (3.92) for its explicit form). The relative contributions of these terms varies, and the vertical flux is

sign-varying, depending on location, local time, E-field, magnitudes of the neutral wind velocities, and numerous other factors. The flux has a magnitude of the order of $10^8 cm^{-2} sec^{-1}$ [*Min and Watkins,* 1995]

Numerical experiments have demonstrated that the $O^+(^4S)$ vertical profile is rather sensitive to the upper boundary flux value, especially in the night-side ionosphere, where the dynamics is a dominating factor compared to the weak ionization. The electron density profile is roughly equal to the $O^+(^4S)$ ion density at these heights. In figure 5.1 the typical dependence of the profiles on the fluxes is shown for both night-side (winter, midnight, low ionization density) and day-side (summer, noon, high ionization density) conditions at a typical polar location. It is evident that the effects on the night-side are more pronounced than on the day-side and the profiles are affected below the main ionospheric maximum, to about 150 *km* of altitude. The day-side effects are not so drastic since this dynamic source is masked by the abundant solar ionization. Another noticeable feature is a non-symmetric density response to negative (influx) and positive (outflow) fluxes. The profiles are more sensitive to outflow for both day-side and night-side conditions. The reason is that the upward directed diffusion cancels a downward flux and enhance an upward flux, thus decreasing the net effect on the density.

A peculiarity of the process is the existence of the critical outflow ($\Phi_o > 0$) level that corresponds to the regime of free expansion in a gravitational field. Outflow cannot exceed this value. It corresponds to the hypothetical situation when particles are removed by outflow through the upper boundary faster than they are supplied by the diffusion. In reality there is a dynamic equilibrium for this regime with a negative feedback that rapidly decreases the flux when the density decreases. To simulate this self-maintaining mechanism, an external condition that required the ion density to be non-negative is necessary for the code stability; otherwise calculations will yield the negative density values if outflow exceed critical value. By contrast, the influx is not limited by these factors and the scheme is stable for any magnitude of the negative flux through the upper boundary.

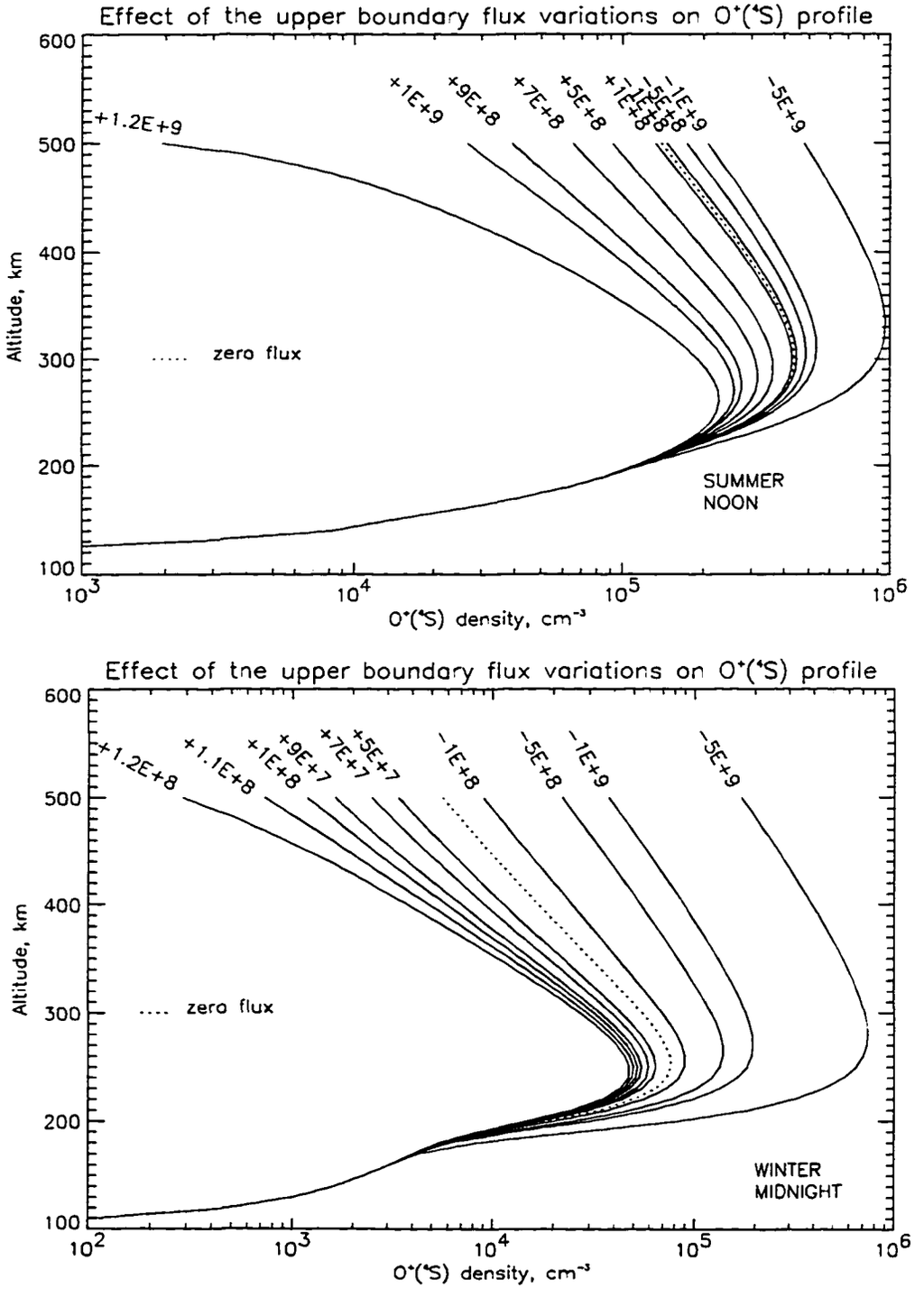

Figure 5.1. Dependence of the vertical profiles of $O^+(^4S)$ concentration on the flux through the upper boundary at 500 *km* for summer (noon) and winter (midnight) conditions. The curves are labeled with the assumed fluxes (in $cm^{-2}sec^{-1}$), with positive values indicating upward flux.

Another factor influencing the profile of $O^+(^4S)$ ion is the vertical ion advection. The effect of this is shown in figure 5.2. Negative (downward) drift velocities result in a downward displacement of the peak of ion concentration, while positive (upward) velocities cause an upward peak displacement. The peak magnitude is also affected. Downward displacement moves the bulk of ions into the denser thermospheric levels, where more effective recombination reduces the ion density. Upward motion results in two competing effects, depending on the drift velocity magnitude. Weak upward motion causes a small density increase due to reduced recombination, while the faster (100-150 *m/sec*) velocities start the ion density re-distribution, decreasing the peak magnitude and at the same time increasing the ion densities above the peak, making the profile slope steeper in its upper part.

These extreme effects are very rare, since the total velocity of the vertical drift rarely exceeds 100 *m/sec*. Magnitudes of a few tens of *m/sec* are more typical. However, for a realistic velocity range of ±50 *m/sec*, the peak height shifts by about 100 *km*. Contribution of the neutral thermospheric wind, which has a prominent diurnal periodicity, explains the diurnal variation of the height of the ionospheric peak, which varies up to 100 *km* during the course of the day.

After the boundary conditions are specified, the solution is found at each time-step, using the 3-D fields of all parameters of interest from the previous time step. The initial condition for the first time step of the 3-D system is inevitably just a rough approximation. In theory even an arbitrary initial condition of physically non-negative values (mass, density, temperatures) is sufficient for convergence. Faster convergence is achievable by selecting a realistic initial condition.

The diurnal periodicity of the solution under the influence of the diurnally periodical forcing is an important criteria of the solution convergence. In practice, the diurnal periodicity of the solution for a system like the terrestrial ionosphere — with poorly known initial conditions and the external sources of mass, momentum, and energy — is the only remaining criterion whether the solution has converged

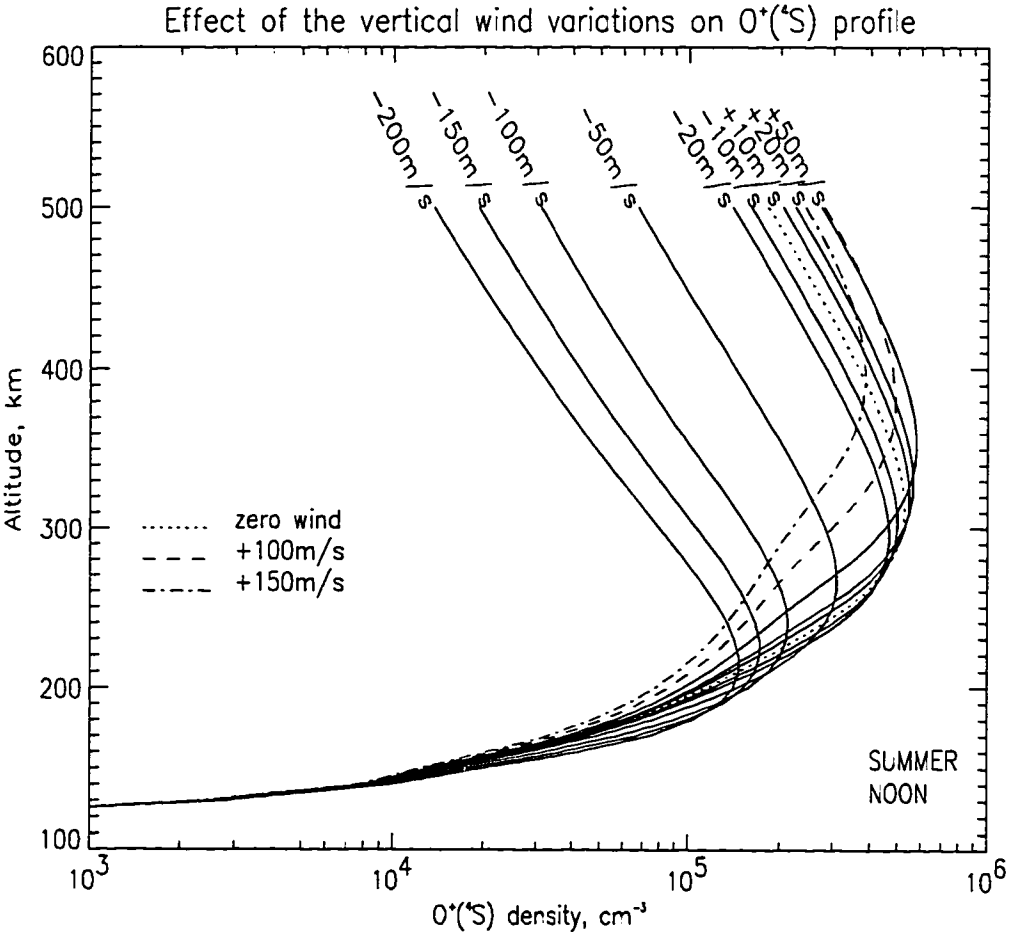

Figure 5.2. Effect of the vertical drift velocity on the $O^+(^4S)$ profile for the summer (noon) conditions. Negative velocities are directed downward, while the upward direction is positive. The wind variations in the realistic range ±50 *m/sec* cause shifts of 100 *km* in the main ionospheric peak height.

to the physically meaning values.

The 3-D fields of densities, winds, and drifts generated by the VSH model are also used as the initial conditions. The initial condition for *NO* density is a parameterization in terms of the major thermospheric components and temperature derived by *Mitra* [1968]. The convergence to the diurnally periodic solution can usually be achieved within several model hours for O^+ ions and within a few model days for the odd nitrogen group, comparable to periods that are reported in the literature for other models.

5.3.2. Equation of continuity in the 3-D case

The mixed advection-diffusion equation for the $O^+(^4S)$ ion density after substitution of the expression for the vertical flux (3.92) into equation (5.11) is

$$\frac{\partial n}{\partial t} = A\frac{\partial^2 n}{\partial z^2} + B\frac{\partial n}{\partial z} + \frac{r^2 \sin\alpha}{R_o^2}\frac{}{\alpha}\left[\frac{\partial}{\partial x}\left(\frac{\sin\alpha}{\alpha} n\vartheta_x\right) + \frac{\partial}{\partial y}\left(\frac{\alpha}{\sin\alpha} n\vartheta_y\right)\right] + Cn + E \qquad (5.28)$$

where the coefficients *A, B, C, E* were introduced in Chapter 3 and other parameters were explained previously in conjunction with derivation of equation (5.11).

Equation (5.28) belongs to a class of multi-dimensional partial differential equations (PDE). Several feasible numerical methods for solutions are well-known [e.g., *Potter*, 1977; *Fletcher*, 1991; *Ozisik*, 1994]. The method we use is a modification of a general multidimensional splitting approach. The splitting technique can be understood by an example of the Alternating Direction Implicit (ADI) method.

The ADI method is based on some useful properties of the matrices that arise from finite-difference representations in the general 3-D case. The general 3-D diffusion equation is:

$$\frac{\partial n}{\partial t} = D_x \frac{\partial^2 n}{\partial x^2} + D_y \frac{\partial^2 n}{\partial y^2} + D_z \frac{\partial^2 n}{\partial z^2} . \qquad (5.29)$$

The equivalent finite-difference expression gives rise to a linear system with a $N^3 \times N^3$ matrix, which is much more complex than the tridiagonal $N \times N$ matrix of the 1-D case (5.17). For the general case of n-dimensions the matrix size is $N^n \times N^n$, where N is the number of cells (assumed to be the same in each dimension), and n is the number of dimensions. Although these matrices are still sparse, their inversion is not a simple computational task. However, properties of the tridiagonal matrices can still be usefully employed in multi-dimensional problems by recognizing that the general matrix may be represented as a sum of certain tridiagonal matrices. To preserve this tridiagonal simplicity of the system matrix, intermediate time sub-steps with corresponding intermediate solutions are introduced. Applying this method to equation (5.29) represents it as three consecutive finite-difference equations to be solved on each time step

$$\frac{2}{\Delta t}(n^* - n) = \Delta_x^2 n^* + \Delta_y^2 n + \Delta_z^2 n \qquad (5.30a)$$

$$\frac{2}{\Delta t}(n^{**} - n^*) = \Delta_x^2 n^* + \Delta_y^2 n^{**} + \Delta_z^2 n \qquad (5.30b)$$

$$\frac{2}{\Delta t}(\tilde{n} - n^{**}) = \Delta_x^2 n^* + \Delta_y^2 n^{**} + \Delta_z^2 \tilde{n} \qquad (5.30c)$$

where $n = n_\ell$ is the known density at the previous time step ℓ, $\tilde{n} = \tilde{n}_{\ell+1}$ is the unknown density at the current time step $\ell+1$, n^* and n^{**} are the densities at the first and the second intermediate time sub-steps, respectively, and the finite-differential operators are introduced

$$\Delta^2_{x,y,z} n \equiv \frac{D_{x,y,z}}{(\Delta x, \Delta y, \Delta z)^2} (n_{k+1} - 2n_k + n_{k-1})$$

where the k-index is related to the corresponding variable x, y, or z.

Equations (5.30a)-(5.30c) are finite-difference representations that are implicit in only one direction. They are thus solvable sequentially one at a time by a standard 1-D implicit method involving tridiagonal matrix inversion. No time subscript is given to the two intermediate density values, as they are computed only as parameters for the final computation of the density $\tilde{n}(t_{\ell+1})$ at the current time step $\ell+1$. The values n^*, n^{**} are not representative of the actual densities at time $t_{\ell+1/3}$ or $t_{\ell+2/3}$ and should not be used as such.

The ADI method is formulated for the purely diffusive parabolic 3-D PDE and is not directly applicable to equation (5.28) since the latter is a mixed diffusive-advective equation with diffusive terms in the vertical direction and advective terms at the horizontal plane. This is a situation when the "parabolic" diffusion (diffusion is described by a PDE of a parabolic type) and the "hyperbolic" advection are separated and act predominantly in different directions. It is reasonable to distinguish between these processes and apply the basic ideas of multidimensional splitting methods, namely a separation of the dimensions in time and an introduction of the intermediate solutions for densities inside a given time step.

Let us distinguish between the vertical and the horizontal directions. The former is dominated by the diffusion processes, while the latter is influenced by advection. The lifetime of $O^+(^4S)$ ions (several hours) is long enough compared to the model time step (5-10 minutes) to neglect the processes of production and loss during an advection time step and consider the horizontal motion as a transfer of a passive substance by the external flow. Further, there is no need to separate between the two horizontal directions since the corresponding equation of advection can be solved in two dimensions simultaneously by an explicit scheme. Let us introduce the intermediate density n^* that results exclusively from the advective re-distribution during the current time step $\ell+1$ of the initial $O^+(^4S)$ density from the previous time step ℓ. Denoting all parameters calculated at the current time step $\ell+1$ a tilde, we can represent diffusive-advective equation (5.28) for $O^+(^4S)$ as two subsequent finite-difference equations

$$\frac{n^{*}_{ijk} - n_{ijk}}{\Delta t} = - R^{2}_{k} m_{ij} \left[\Delta_x (m_{ij} v_x n_{ijk}) + \Delta_y (m^{-1}_{ij} v_y n_{ijk}) \right] \qquad (5.31)$$

$$\frac{\tilde{n}_{ijk} - n^{*}_{ijk}}{\Delta t} = A_{ijk} \Delta^{2}_{z} \tilde{n}_{ijk} + B_{ijk} \Delta_{2z} \tilde{n}_{ijk} + C_{ijk} \tilde{n}_{ijk} + E_{ijk} \qquad (5.32)$$

where the ijk-indices correspond to the cell with coordinates $\{x_i, y_j, z_k\}$; Δt, Δx, Δy, Δz, v_x, v_y are the time- and spatial-steps, and the advective velocity in x, y, and z-direction, respectively; R_k is the curvature coefficient $R_k \equiv (R_E + z_1)(R_E + z_k)^{-1}$; $m_{ij} = \sin\alpha/\alpha$ is a "map coefficient" or the latitudinal distortion coefficient in the Azimuthal Equidistant Projection, with co-latitude, α, of the ij-column of cells. Note that the curvature and mapping distortions are neglected for current model runs in the limited high-latitude region and both R_k and m_{ij} coefficients are set to unity in the entire calculations domain.

The following finite-difference operators represent the upwind differencing scheme in the horizontal plane. The central differences for first and second derivatives in the vertical direction were introduced in equations (5.31) and (5.32)

$$\Delta_x n \equiv (\Delta x)^{-1} \begin{cases} (n v_x)^{jk}_{i+1} - (n v_x)^{jk}_{i}, & v_x < 0 \\ (n v_x)^{jk}_{i} - (n v_x)^{jk}_{i-1}, & v_x \geq 0 \end{cases}$$

$$\Delta_y n \equiv (\Delta y)^{-1} \begin{cases} (n v_y)^{jk}_{i+1} - (n v_y)^{jk}_{i}, & v_y < 0 \\ (n v_y)^{jk}_{i} - (n v_y)^{jk}_{i-1}, & v_y \geq 0 \end{cases}$$

$$\Delta^{2}_{z} n \equiv (\Delta z)^{-2} \left\{ n^{ij}_{k+1} - 2n^{ij}_{k} + n^{ij}_{k-1} \right\}$$

$$\Delta_{2z} n \equiv (2\Delta z)^{-1} \left\{ n^{ij}_{k+1} - n^{ij}_{k-1} \right\}$$

Adding equations (5.31) and (5.32) to each other gives the exact three-level, fully implicit, finite-difference representation of equation (5.28), since the terms with n^* vanish. The explicit equation (5.31) can be solved for n^* on the entire mesh given that the boundary conditions for $O^+(^4S)$ density are specified on the sides of the domain, and the initial distribution $\{n_{ijk}\}$ is known. The final stage of this algorithm is the solution of equation (5.32) for the ion density at the current time step using the above described method for inversion of the resulting tridiagonal matrix. This stage includes vertical diffusion account and the calculation of production and loss terms.

Thus, the only remaining unknowns for this scheme are the boundary conditions on the domain sides and the initial conditions. The solution advancing from the initial condition was considered in the 1-D case, and the same approach is applicable for 3-D consideration. Convergence of the solution to diurnally periodicity is the criteria that the initial condition influence is eliminated. The boundary conditions on the domain sides is a specific 3-D requirement.

The model domain is designed to avoid the boundary-related complications as much as possible. It is expanded to at least 50 degrees of geomagnetic latitude and, in the most locations, even beyond this circle of latitude (figure 2.3). This 50-degree circle is the approximate boundary of predominantly corotating plasma [*Sojka at al.*, 1983]. Thus, in the corotating frame the advective motion near the boundary is negligible. This is illustrated in figure 2.4, which shows the pattern of displacements of plasma parcels from their respective initial locations in the course of several days. The depicted displacements of plasma that was initially situated at low magnetic latitudes near 50 degrees is very small and completely unnoticeable for locations at 45 and 40 degrees regardless of the extended period of simulations (three days). This demonstrates the predominantly corotational nature of plasma motion at low geomagnetic latitudes.

This observation is valid for the quiet, moderate, and the moderately disturbed geomagnetic conditions. The magnetospheric electric field protrudes much further equatorward from its usual polar locations

only during severe disturbances, which shift the corotation boundary. The model boundary conditions must describe this situation realistically.

The model boundary conditions are an "open" boundary , i.e. a boundary through which the fluxes propagate undisturbed. This is based on the fact that the plasma flux through the boundary at 50 degrees geomagnetic latitude is predominantly a small outflow, if any, for up to the severely geomagnetic conditions. Knowing the incoming flux into a boundary cell from the domain, one can equate it to the outgoing flux through that particular cell, allowing only local processes of production and loss to change the plasma density. Mathematically, this assumption means that the wind and density behind the boundary is assumed the same as at the boundary cell.

For the opposite situation, when plasma flows into the domain through the boundary, a realistic assumption is the linear extrapolation for the density beyond the boundary and calculation of the flux difference to and from the cell. In any case, the major plasma flows are located well inside the domain, and the influence of the boundary is limited to a few neighboring cells. For severely disturbed geophysical situations, the domain boundary can be shifted equatorward until the corotation regime is approached. In this extended geometry the distortion of Cartesian projection is not negligible anymore and the appropriate metric coefficients must be taken into account.

Since explicit methods are applied to solve equation (5.31), the numerical stability requirement is 2-D Courant-Lewy-Friedrichs condition

$$\Delta t_s \leq \frac{min(\Delta x, \Delta y)}{max \sqrt{2(v_x^2 + v_y^2)}} \quad . \tag{5.33}$$

In the worst case scenario (high horizontal spatial resolution and large convection velocities of 1 *km/sec* and up) this limit is of the order of a few tens of seconds. For a horizontal resolution of

100x100 *km* and typical wind velocities, it is about one minute. In any case, it is out of the range of the desired model time steps, which are 5 to 10 minutes. To resolve this problem, the time sub-steps inside the model's basic time-steps are introduced and the subsequent calculation of several intermediate densities n^{*}, n^{**}, n^{***}, ... are performed according to the explicit formula (5.31). These intermediate densities can be thought of as the different stages of the advective density redistribution in time.

The code determines the duration of the time sub-steps to be not longer than the 90% of a Courant-Lewy-Friedrichs global limit. For instance, if the basic time step is 5 minutes and the mesh resolution is chosen as 100x100 *km*, this results in 4-5 sub-steps for the higher convection velocities corresponding to geomagnetically disturbed periods, 2-3 sub-steps for moderate conditions, and 1-2 sub-steps for quiet periods.

Higher horizontal resolution would result in even more sub-steps. However, the explicit methods of the advection calculations (5.31) are very fast compared to the inversion of the tridiagonal system (5.32). Even repetitive calculations of the advective redistribution of density do not significantly degrade the code performance, since the matrix inversion for the solution of the diffusion equation is still performed only once during the model time step. This is one of the main reasons for the computational effectiveness of an adopted algorithm.

Thus, the consecutive solutions of expression (5.31) several times during one model time step and one application of expression (5.32) generates the numerical solution for the 3-D equation (5.28). The development of the solution in time starts from 3-D initial conditions, which is the $O^{+}(^{4}S)$ density field generated by the VSH model for the corresponding geophysical situation. This choice significantly accelerates convergence of the solution. In practice, six model hours of simulation is sufficient to achieve convergence and to eliminate artifacts from the initial condition.

In conclusion, it must be noted that the adopted numerical scheme can be improved. The upwind explicit solution for the horizontal di-

rections is the simplest algorithm that has demonstrated the applicability of the direction-splitting method. This choice was also made with considerations of absence of numerical dispersion in the upwind scheme and the non-oscillating character of solutions it generates. However, the upwind method introduces significant numerical diffusion that can smooth out the horizontal plasma structures. It can be shown that the upwind non centered finite-difference scheme instead of initial advection equation approximates an equation with diffusivity

$$\frac{\partial n}{\partial t} + u\frac{\partial n}{\partial x} - \alpha'\frac{\partial^2 n}{\partial x^2} = 0 \qquad (5.34)$$

This artificial diffusion coefficient for the one-dimensional case is $\alpha' = (1-C)u\Delta x/2$, where Δx is the spatial step, u is the advection velocity, $C = u\Delta t/\Delta x$ is the Courant number, and Δt is the time step [*Fletcher*, 1991]. To evaluate the lifetime for this artificial numerical diffusion process a scaling can be done as

$$\tau = \frac{(\Delta x)^2}{\alpha'} = 2\Delta x u^{-1}(1-C)^{-1} \qquad (5.35)$$

In one-dimensional case with typical velocity and the grid size used in the model one can obtain the evaluation of the numerical diffusion lifetime as $\tau = (1-C)^{-1}10^3$ *[sec]*. The lifetime depends on the $(1-C)^{-1}$ factor (in the model C varies from *0* to *0.9*). However it is of the same order of magnitude as the chemical lifetime of the O^+ ion in the polar cap (1-2 hours). Thus, the artificial numerical diffusion concurs with the chemical removal of the long-lived $O^+(^4S)$ ion. Numerical experiments with varying chemical lifetimes of the $O^+(^4S)$ ion have demonstrated that the chemical removal is still faster, when compared to the numerical diffusion. However, transition to a finer grid will increase the numeric diffusivity and may introduce a non acceptable numerical diffusion in the upwind scheme. Adoption of a less diffusive scheme, such as the flux-corrected method or the generalized higher-order upwind scheme, can solve this problem.

CHAPTER 6

APPLICATIONS OF THE IONOSPHERIC MODEL

6.1. Model output and operational modes

The model output that was described in Chapter 2 is the time-dependent 3-D distribution of densities of electrons, seven ion species ($O^+(^4S)$, $O^+(^2D)$, $O^+(^2P)$, NO^+, O_2^+, N_2^+, N^+), isotropic ion and electron temperatures, and the ion drift velocity in the altitude range 80-500 *km*. The results are valid inside the circle of 50 degrees geographic latitude, although the calculations are performed in a broader domain. The densities of the minor neutral species *NO* and $N(^4S)$, $N(^2D)$, which are important for the ionization balance in the lower ionosphere, are also self-consistently calculated in the model.

Depending on the choice of inputs and their temporal variability, the model is capable of several simulation modes. First, the climatology-scale simulations utilize statistical inputs for electric fields and auroral precipitation. This type of model study is designed to investigate the average large-scale behavior of the ionosphere and to distinguish ionospheric responses to particular static or slowly varying geophysical conditions to establish their relative importance.

A different approach is seen in specific case studies when realistic reconstructions of the time-history of all model inputs are used. This reconstruction can for example be achieved either by introduction of measurements (e.g., precipitation characteristics from auroral imagers), or by input of pre-calculated values (AMIE-reconstruction of electric fields), or just by varying the outputs of the indices-driven statistical models in accordance to the time-history of the corresponding geophysical indices. This approach allows evaluation of how close the model response approximates reality by comparison of simulations with available data.

6.2. Climatology studies with the model

This type of simulation is designed to investigate the predominant behavior of the ionospheric parameters in response to the particular geophysical situations. There are three major cycles that determine the ionospheric parameters, while the current level of geomagnetic activity and Interplanetary Magnetic Field (IMF) orientation can be considered as the poorly predictable disturbing factors. The major cycle is the 11-year solar activity cycle, which governs the intensity of EUV radiation and total level of ionization. The second cycle is the yearly orbit of the Earth, which changes the terminator position and the balance between sunlit and night-side areas. Additionally, the seasonal changes in temperature and composition of the neutral thermosphere cause ionospheric responses. Finally, the diurnal rotation of the Earth includes effects due to displacement of the geomagnetic and geographic poles, and the varying position of electromagnetic drift pattern with respect to the sunlit and night-side regions. The highly variable geomagnetic activity changes are superimposed on these background seasonal and diurnal variations.

The variety of factors is so abundant that for climatological studies many variables must be kept fixed to simplify the picture and to trace the effects of a limited number of agents in the simulations. Figure 6.1 demonstrates the polar ionospheric structures simulated without the advection effects by ExB-drift. Gray scale contours of electron density represent the horizontal slice of calculated values at 350 *km* of altitude. Four panels on figure 6.1 correspond to different instants of UT (06.00, 12.00, 18.00, 00.00). The simulation was performed for winter solstice conditions and moderate levels of solar and geomagnetic activity. For this simulation the horizontal resolution of 200x200 *km* is used. The demonstrated results are obtained after 36 model hours of simulations. An initial 12 model hours are necessary for the solution to converge to the diurnal periodicity regime and to eliminate the influence of the initial conditions (electron density distribution derived from VSH model). This procedure is outlined in section 5.3 in more detail and it is a standard approach for all simu-

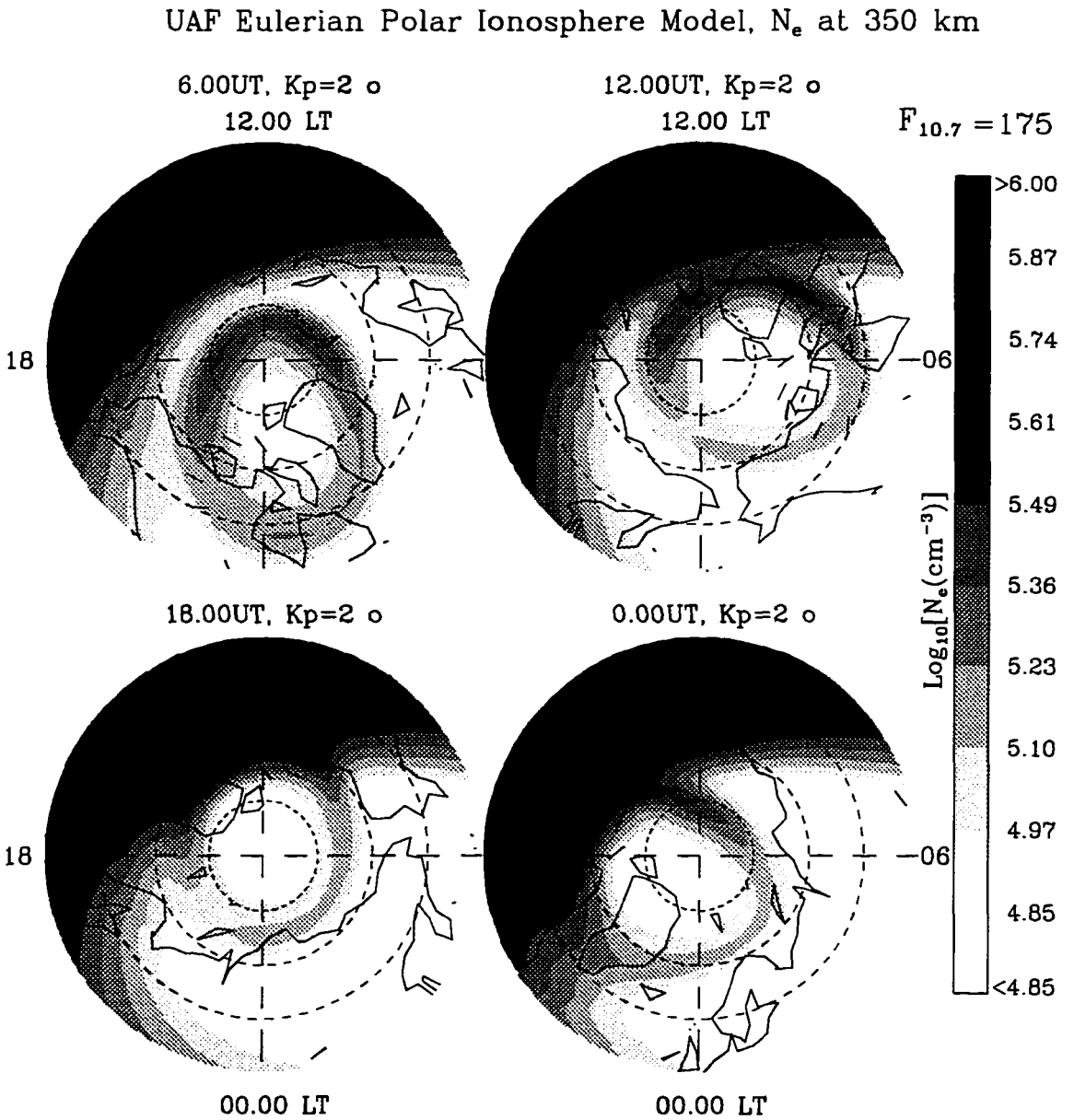

Figure 6.1 Distribution of electron density at 350 *km* in the winter ionosphere for four UT instants in the absence of advective motion by ExB-drift. The frame is geographic latitude and local time. See text for discussion.

lations described later.

The frame in figure 6.1 is geographic latitude from the pole down to 50 degrees and local time, with local noon at the top of each panel. The midnight-noon meridian defines the direction to the sun and the direction of the Earth's rotation is counter-clockwise. The terminator is fixed in this frame in the upper third of each panel. Its most poleward location for the winter solstice is the polar circle at 67 degrees latitude. Contours of electron density are roughly parallel to the terminator in the morning sector. However, corotation of the long-living species at these altitudes destroys this symmetry after crossing the noon meridian. This corotation creates an elongated ionization tail in the evening sector that reaches far into the night sector.

The next distinguishable feature in figure 6.1 is the auroral oval. The auroral oval is created at these altitudes by the soft component of precipitating spectrum. It has a maximum of ionization on its noon-side, in contrast to the *E* region oval, which has a night-side maximum. The oval is centered around the geomagnetic pole and in this geographic frame it rotates about the geographic pole, changing its location as displayed on different UT panels (UT-effect). Particle precipitation affects the neutral and ion temperatures and, consequently, the chemical reaction rates. The displaced auroral oval passage through the evening sector during approximately 20.00-03.00 UT intensifies the recombination process in the corotating plasma, shortening its lifetime. It is noticeable in figure 6.1 as the corotating ionization tail extension into night sector in three panels: First at 6.00 UT, immediately after the oval passed through the evening sector; second at 12.00 UT; and third at 18.00 UT. At 18.00 UT the corotating plasma lifetime is about three hours longer, which corresponds to further extension into night sector.

This simulation demonstrates the distribution of ionization sources and sinks in the ionospheric *F* region before introducing horizontal dynamics, which considerably affects the resulting features.

The figures 6.2-6.3a,b demonstrate the results of a more realistic two-day simulation which was performed for winter conditions, aver-

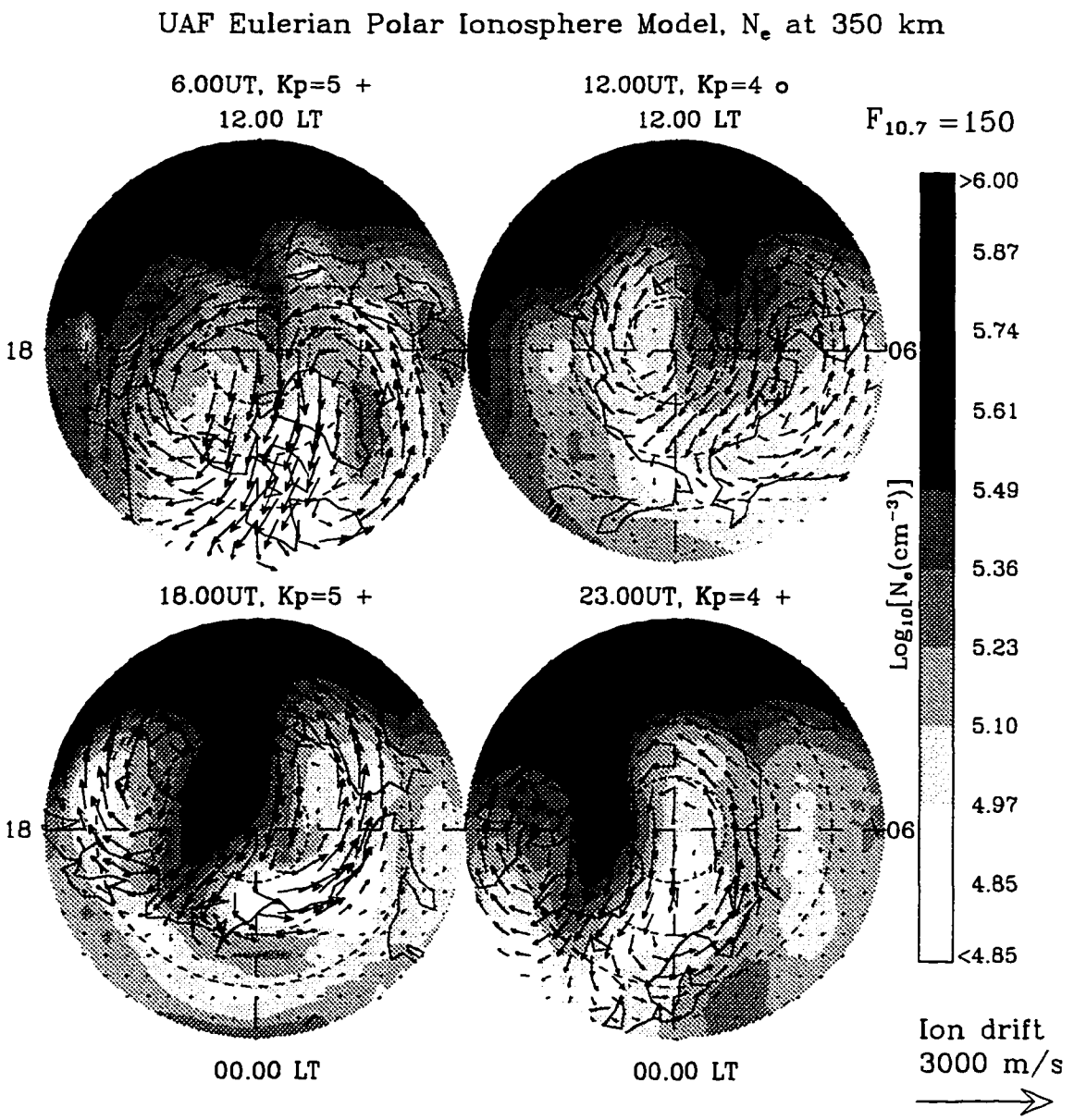

Figure 6.2. Position of convection system at different instants of UT and the corresponding ionospheric response at 350 *km* of altitude (ionospheric *F* region). Winter conditions, average level of solar activity ($F_{10.7}$ = *150*), and moderately disturbed geomagnetic conditions (*Kp = 4o + 5+*) are represented. UT instants and the corresponding geomagnetic activity are specified for each panel.

age solar activity ($F_{10.7}$ = 150), and moderately-disturbed magnetic activity (Kp = 4o - 5+) during the first model day with a subsequent transition to moderate activity (Kp = 2o - 3o) during the second day of the simulation. IMF orientation was adopted as B_y = 0 and B_z << 0 for the first model day, with transition to B_y = 0, B_z < 0 during the second simulation day to represent the adopted levels of geomagnetic activity.

Four panels in figure 6.2, each for a different instant of UT, represent the effects of rotation of the geomagnetic pole and convection system about the geographic pole. The vortex-like, two-cell, convection system rotates together with the geomagnetic pole preserving its orientation parallel to the noon-midnight meridian.

The flow of high density plasma over the polar cap from the sunlit region driven in the anti-sunward direction form a feature known as the "Tongue of Ionization" (ToI). Its relative development depends on the ionization abundance trapped by the converging flows at the upper part of two-cell convection system. Depending on the position of these flows with respect to the terminator, the ToI development varies during the course of a day. In this case the "throat" of the convection pattern, initially distant from the terminator (6.00 UT), approaches it in the dawn sector (12.00 UT), reaches the most inside position in the sunlit region (18.00 UT), and crosses the terminator again (23.00 UT) on the way out to the dark side in the dusk sector. Consequently, the ToI is not well pronounced at 6.00 UT, starts to appear by 12.00 UT, is most developed by 18.00 UT, and begins to fade at 23.00 UT. The ionization structures are not symmetric at 12.00 UT and 23.00 UT even though the convection system is at about the same distance from the terminator. The region of abundant day-side ionization is tilted toward the dusk sector due to co-rotation of the long-living O^+ ions. This supply of enhanced plasma to maintain the anti-sunward flow lasts well after the terminator is crossed by the convection system "throat."

The appearance of ionospheric troughs, or regions of depleted plasma density as low as 10^4 cm^{-3}, also follows the convection pattern displacements on figure 6.2. The troughs are situated in the regions

of convection reversal. The biggest shift of the equatorial edge of the main trough to the night-side takes place at 6.00 UT, when the convection system is shifted toward the night-side itself. Later, at 12.00 UT, the trough shapes up to a more regular oval-like structure and moves up in the general day-side direction. By 18.00 UT the strong plasma flow from the day-side separates the trough into three isolated features, dawn and dusk day-side troughs and the main night-side trough. The 18.00 UT panel shows the region of depleted ionization appears is divided by the ToI. This feature is known also as the polar hole. By 23.00 UT all three troughs merge together and move toward the night-side.

The next two figures, 6.3a and 6.3b, demonstrate the development of ionospheric structures during the same time period but with better time resolution (2 hour intervals). The plots cover a period of about 40 hours of model time and enable the reader to compare the situation for two consecutive days when, in accordance with the chosen scenario at the same instant of UT the geomagnetic activity is different. Comparison of panels for UT of 17.00, 19.00, 21.00 in figures 6.3a and 6.3b demonstrates the differences in the ionospheric response for $Kp = 5o - 5+$ (figure 6.3a) and at $Kp = 2o$ (figure 6.3b) related to the less intensive convection under the moderate geomagnetic activity.

Both dynamics-driven features, ToI and ionospheric troughs, are less pronounced. On the other hand, the sunlit ionization density is evidently higher for moderate geomagnetic conditions. This effect is related to the higher thermospheric temperatures under disturbed geomagnetic conditions. Higher temperatures cause an increased relative abundance of the heaver molecular major thermospheric component O_2 and N_2 at ionospheric F region heights, and a correspondingly higher ratio of molecular ions, which have much higher recombination rates compared to $O^+(^4S)$ ions. The chain of these events results in decreased electron density in the geomagnetically disturbed ionospheric F region. A similar effect is noted for the higher summer neutral thermosphere temperatures; decreases are found in the summer electron densities compared to the winter-time values.

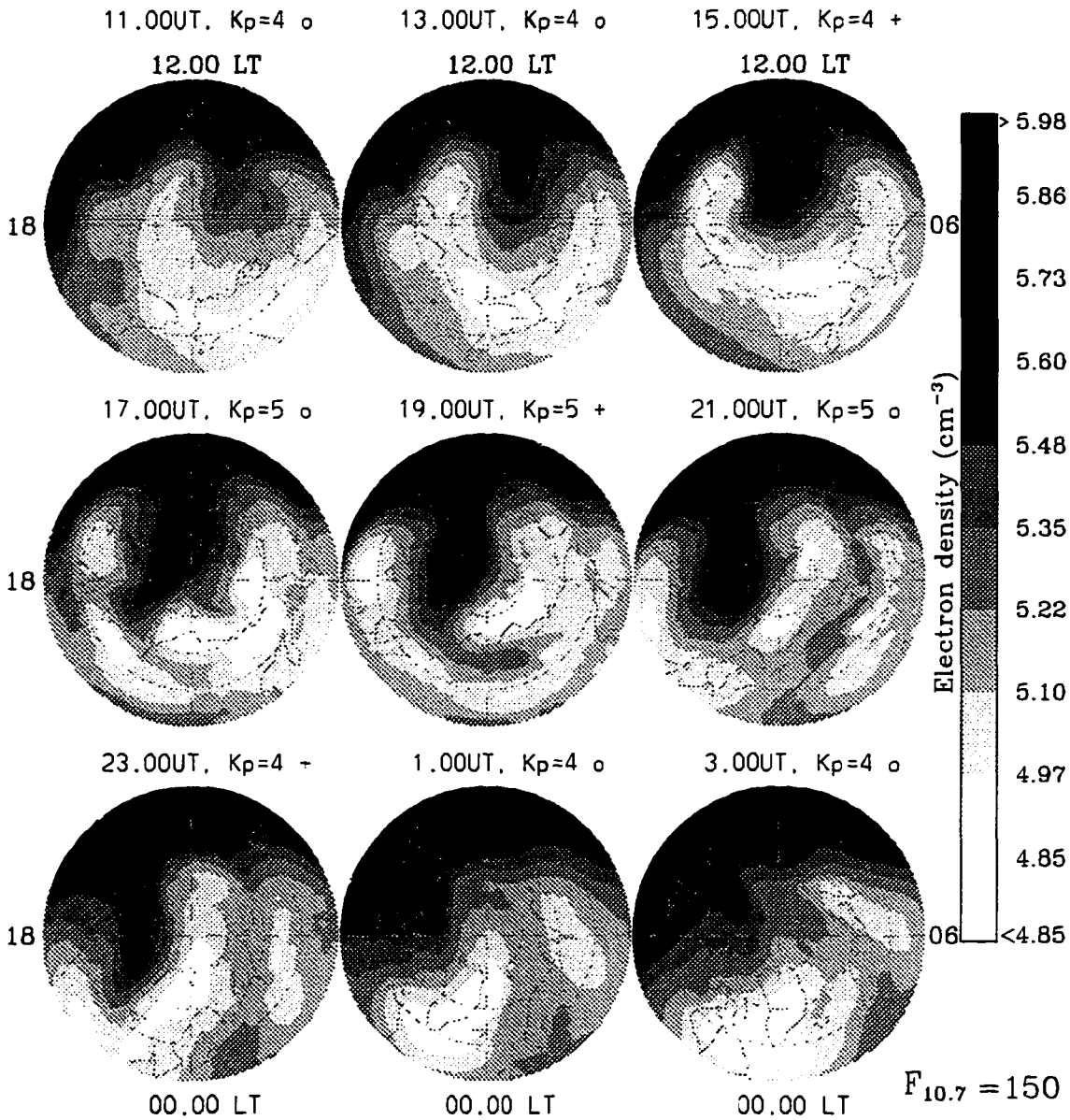

Figure 6.3a. Snapshots of contours of plasma density at 350 *km* taken every 2 hours in winter, during a moderately disturbed geomagnetic conditions. The frame is the same as in figure 6.2.

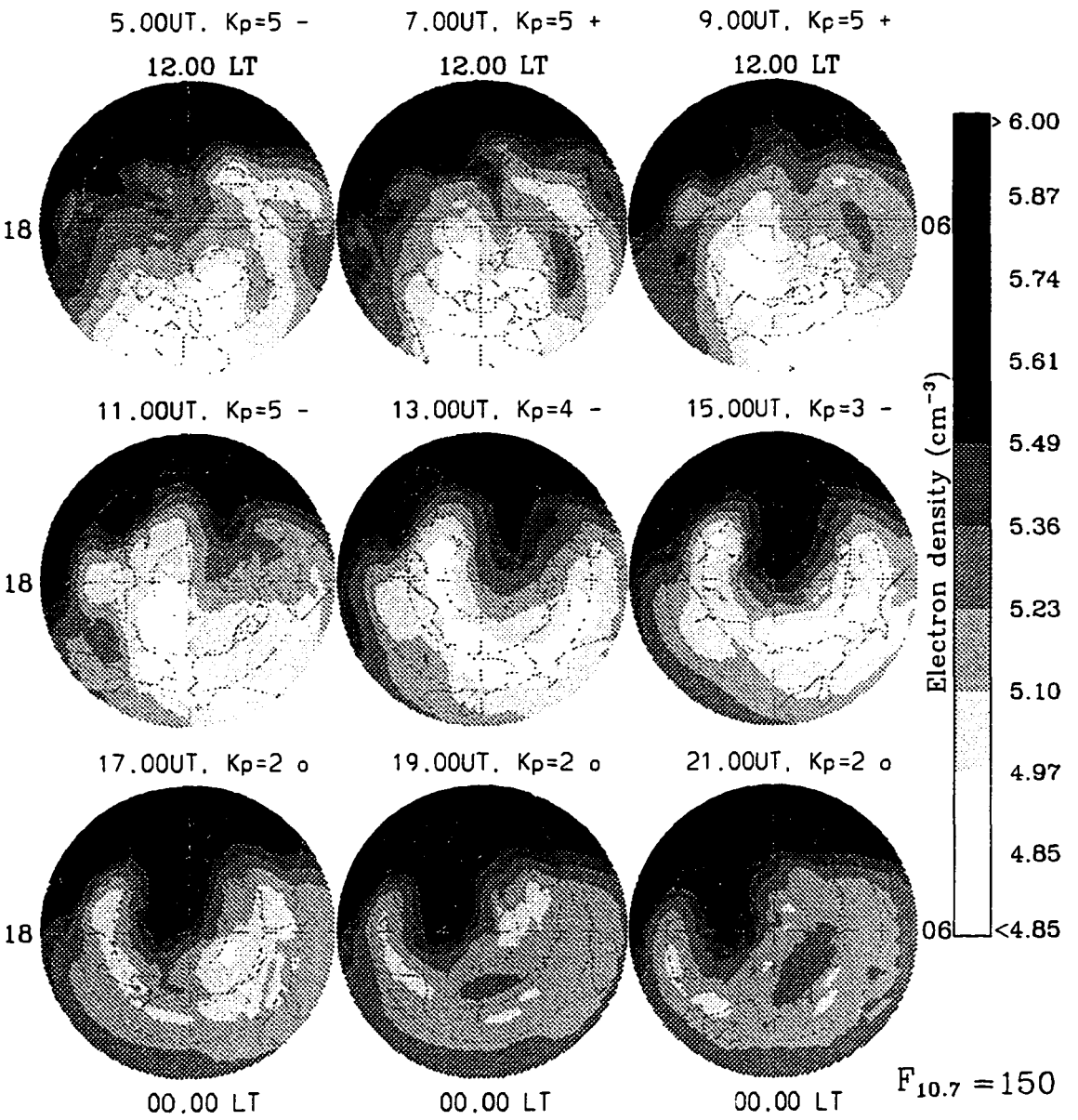

Figure 6.3b. Continuation of series of ionospheric snapshots from figure 6.3a. Note the transition to the quieter geomagnetic conditions starting from 15.00 UT. Comparisons with the same instants of UT but higher geomagnetic activity at previous day demonstrates the difference in ionospheric response (see text for the detailed discussion).

The next figure, 6.4a,b, shows the vertical cross-sections of the ionosphere at selected locations along the noon-midnight meridian at 5.00 UT (105°*E* - 75°*W* geographic meridian) when the geomagnetic pole and, correspondingly, convection system and auroral oval are maximally distanced from the dayside. The simulation was performed for the moderate solar ($F_{10.7}$ = *150)* and geomagnetic (K_p = *2+*) activity levels at winter solstice. The scenario of the weak convection was chosen and the IMF northward orientation was specified. These conditions correspond rather closely to the simulation demonstrated in figure 6.1 at the instant of 06.00 UT and that plot will be used in this discussion as an example to illustrate the horizontal configuration of the ionospheric *F*-region structures.

In figure 6.4a,b, the vertical ionospheric profiles are plotted every four degrees of geographic latitude. Each panel shows the electron density profile and contribution of each ion species, O^+, NO^+, O_2^+, N^+, and N_2^+, starting from the dayside and proceeding into the nightside direction. The common feature of the profiles is the different contribution of the molecular ions NO^+ and O_2^+ at different altitudes compared to the contribution of atomic oxygen ion O^+. In the upper ionosphere the O^+ ion is dominant, while in the ionospheric *E* region the molecular ions contribute the most. This determines different behavior of upper and lower ionosphere regions, since the lifetimes of these ions are different. Charge exchange processes with the major thermospheric neutral components O_2 and N_2 govern the chemical removal of the O^+ ion in contrast with the molecular ions, which are removed mostly by fast dissociative recombination. The lifetime of O^+ is a few hours with some variations due to the temperature dependency. The lifetime of the molecular ions is variable in a much wider range from 10 *sec* to a few hours, depending on the electron density. In the regions where molecular ions are dominant, this lifetime depends on their own concentration due to the plasma electrical neutrality. Because of these lifetime differences, the altitude of transition from one ion type to another is of considerable interest for ionospheric studies.

The first five plots of figure 6.4a show the dayside ionospheric

profiles corresponding to the different solar zenith angle, from 73.5° (50°*N*) to 89.5° (66°*N*). The next plot (70°*N*) is on the night-side from the terminator (66.7°*N*). Comparing these plots, a steady decrease of electron density takes place ($NmF2$ decreases from 1.6×10^{6} cm^{-3} to 7×10^{5} cm^{-3}), which accelerates after the terminator crossing (4×10^{5} cm^{-3}). The upper dayside ionosphere consists of predominantly the O^{+} ion with a few percent contribution from the N^{+} ion. Transition level from molecular ions to O^{+} is situated around 200 *km*. A noticeable feature of the profiles in the low *E* region near 90-80 *km* is ionization of *NO* by the strong solar H-Lyman-α line (1216 Å), which takes place during the daytime and disappears in the 70°*N* panel after the terminator crossing.

Two following plots, 74°*N* and 78°*N*, show continuing decreases of *F*-region electron density to values as low as 3×10^{4} cm^{-3}. Conversely, *E*-region values grow from 1.5×10^{4} cm^{-3} (70°*N*) to 6×10^{4} cm^{-3} (78°*N*). As is evident from the corresponding panel (UT=6.00) on figure 6.1, this growth is caused by crossing the auroral oval. Note that the spatial size of the oval is wider at the *E*-region altitudes compared to the *F*-region oval on figure 6.1, which is caused by the softer precipitating particles. Enhanced auroral ionization results in redistribution of the ion concentrations and increases of the $[NO^{+}]+[O_2^{+}]\ /[O^{+}]$ ratio. The transition height to the dominance of molecular ions increases to 250 *km*.

The next group of profiles, at 105°*E* meridian at latitudes 82°*N*, 86°*N*, 90°*N*, and at 86°*N* 75°*W*, represents the situation when the wider *E*-region oval is already crossed, but the crossing of the *F*-region oval is taking place. In these plots the *E* region is greatly depleted, while the ionization increases at the *F*-region heights. This increase maximizes at 86°*N* 105°*E*, exactly where the dayside maximum of ionization is situated in figure 6.1.

Inside the polar cap, starting from 82°*N* 75°*W*, precipitation at the *E* region altitudes become noticeable again and the ionization is increased to 1×10^{4} cm^{-3} level. In the *F* region there are no significant changes even though this is a region of minimum of the soft component of the precipitation, as figure 6.1 (UT=6.00) indicates. An ex-

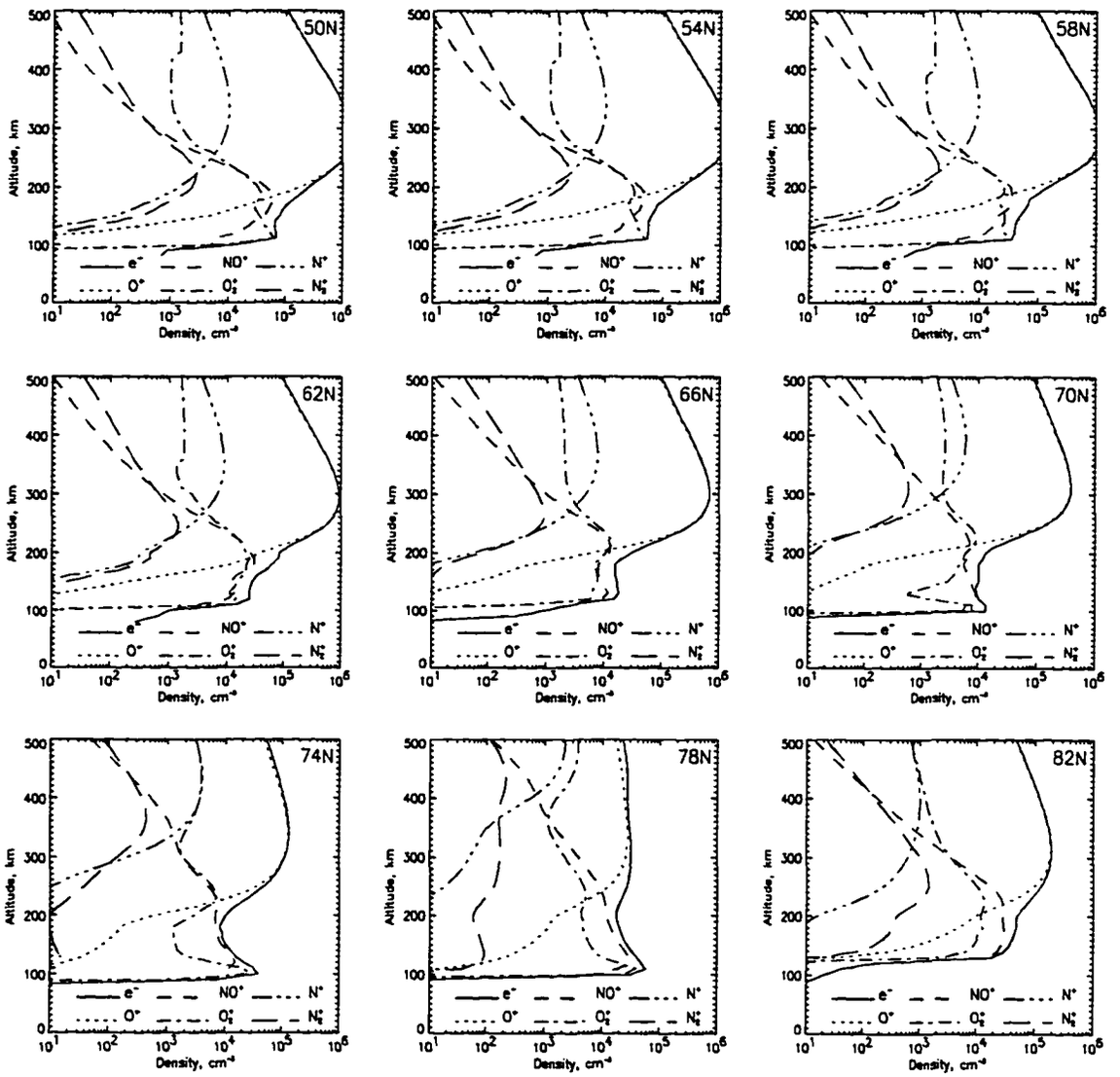

Figure 6.4a. Meridional ionospheric cross-section along the noon-midnight meridian at 5.00 UT (meridian 105°E - 75°W) for winter solstice and moderate solar and geomagnetic activity levels ($F_{10.7}$ = 150; Kp = 2o). The cross-section is comprised of the vertical profiles of electron density and different ions species which are represented by the different line types (see the legend). The direction of crossing is from noon (50°N 105°E) to midnight (50°N 75°W) across the geographic pole. Each panel location is specified in the upper right corner by the geographic latitude.

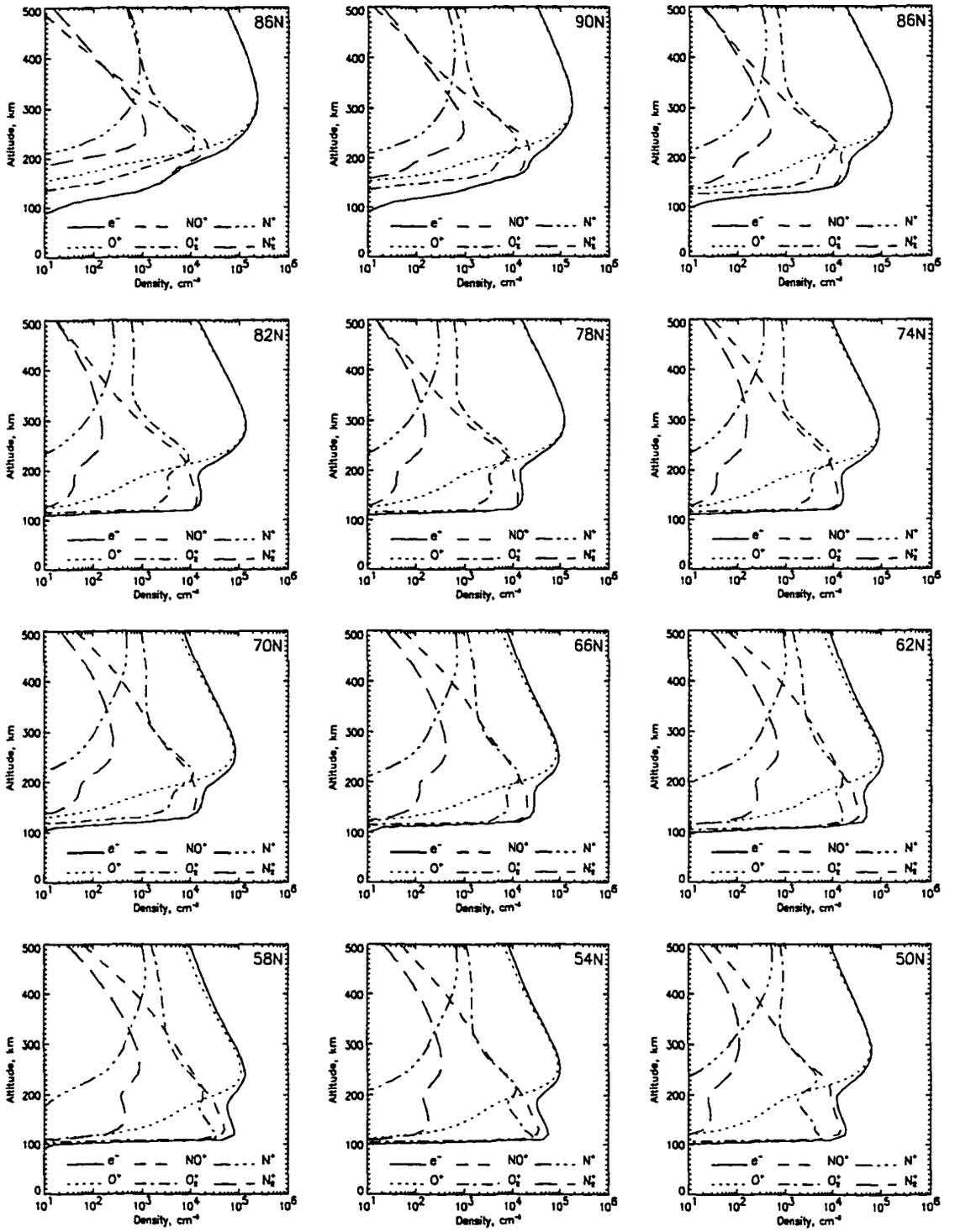

Figure 6.4b. Continuation of the meridional ionospheric cross-section

planation of this inertial behavior of the *F* region is the long lifetime of the dominant O^+ ion and the convection in anti-sunward direction, causing a mixing effect. These two factors maintain ionization on about the same level throughout the polar cap up to $70^\circ N$ $75^\circ W$.

By contrast, an absence of convective motion allowed a deep minimum in *F* region densities to develop at $78^\circ N$ $105^\circ E$ location, just 10° in latitude from the dayside after the terminator crossing. This is because the convection does not significantly affect the locations along the $105^\circ E$ meridian, which are symmetric in the geographic frame to the polar cap locations, but in the geomagnetic coordinates are situated considerably more equatorward.

Inside the polar cap, weak precipitation maintains the *E*-region ionization on a level exceeding 10^4 cm^{-3}. The O^+ ion dominates the *F*-region ion composition up to $70^\circ N$ when the second crossing of the night-side auroral oval starts. From this location the *E*-region density increases up to 8×10^4 cm^{-3} at $58^\circ N$ $75^\circ W$, exceeding the aurorally produced maximum at the dayside (6×10^4 cm^{-3} at $78^\circ N$ $105^\circ E$). As well was at the dayside oval, the ion composition changes are evident in the molecular ion profiles. However, the transition height to the O^+ ion domination is still the same, around 200 *km*, since the *F*-region densities are much higher compared to the minimum at $78^\circ N$ $105^\circ E$.

The analysis of this meridional cross section for the particular UT demonstrates the very complicated polar ionosphere behavior caused by a significant inhomogeneity in the ionization pattern and the dynamical influence in the *F* region. There are scenarios when the dynamics will be a major governing factor for the upper ionosphere when the convection pattern is situated in the vicinity of the abundant dayside plasma and the convection is sufficiently strong to transport it large distances across the polar cap. These periods are likely to create highly structured ionospheric features. The next section is devoted to simulations of these structures.

6.3. Mesoscale simulations with the model

The model has a scaleable horizontal resolution that varies in

range up to 100×100 *km* for a work-station version of the code. This current model version is therefore capable of simulations of the meso-scale phenomena. This section is devoted to the high-resolution simulations performed with the model.

The model was used to investigate the origin and evolution of plasma structures and patches that result from various changes in the IMF, including fast reversals of orientation of the IMF components. In the simulation that follows the real time-history of IMF variations for the period of February 19, 1990, was used. During this period observational data from Thule/Qaanaaq and Sondrestrom are available for comparison with the model. The last sub-section describes simulations for a period with prolonged negative orientation of B_z and suppressed convection with subsequent abrupt reversal of B_z sign and development of an intensive convection system.

6.3.1. Polar cap patches of ionization - introduction and background

Drifting islands of enhanced plasma have been observed in the polar cap. They have a characteristic size of several hundred kilometers and are known in the literature as ionospheric "patches." They range in size from 100 *km* to more than 1000 *km*, while a patch density is enhanced several times above the ambient background, up to an order of magnitude in extreme cases. The morphology is rather complicated and results from the dynamic origin of the patches, rather than the localized particles precipitation. It is well established that the plasma patches are produced by solar radiation in the sunlit ionosphere [*Buchau and Reinisch*, 1991 and references therein], and are then transported across the polar cap by the large-scale electric fields in anti-sunward direction. The patchy structure can be the result of rapid changes in the polar cap size, or configuration of the convection pattern (both IMF-controlled occurrences), or localized disturbances in the electric field [*Valladares at al.*, 1994] related to localized reconnection in the magnetosphere [*Todd et al.*, 1986], or, most likely, by a combination of these factors.

A strong UT-dependence of the patch occurrences is observed

[*Buchau and Reinisch*, 1991; *Scali et al.*, 1995]. In winter-time the UT window for patch formation is between 12 and 24 hours, a period when the convection system is close enough to the sunlit region to trap the enhanced plasma and transport it across the polar cap. In summer-time the sunlit region expands across the polar cap and the convection system always has a supply of high-density plasma. As a result, although summer-time patches exist, they have much weaker density modulation, usually not exceeding a factor of 1.5-2.

On ground-based ionosonde recordings the passage of a patch registers as a sharp local peak on the time series of the ionospheric f_0F2 parameter. Figure 6.5 shows an example of the ionosonde measurements of the critical frequency of ionospheric *F2* region in Thule (CGL 86 degrees). The measurements took place in winter (December 1983) for solar minimum conditions [*Buchau and Reinisch*, 1991]. Durations of patch-related peaks as short as ten minutes and as long as two hours are observed, with a median duration of about one hour. Analysis of the upper ionosphere parameters such as the critical frequency of *F2* region f_0F2, the height of the main ionospheric maximum h_mF2 and their comparison with characteristics from the lower ionospheric heights (critical frequency of *F1* and *E* regions and the layers heights) demonstrates that the patches are essentially an upper ionosphere *F* region phenomena. The patch-related fluctuations in *F2* region (250-400 *km*) are significantly attenuated in the *F1* region (160-200 *km*) and practically unnoticeable in the lowest *E* region (100-130 *km*).

Experimental studies of the polar-cap plasma patches with ionosonde and incoherent scatter radar (ISR) techniques by *Buchau and Reinisch* [1991] and *Scali et al.* [1995] have demonstrated the dominance of the height-independent E×B-drift in the patch motion and a strong dependence of the patch occurrence on the IMF orientation, particularly on the B_z-component. It was experimentally shown that extended periods of positive B_z, characterized by weak suppressed convection, are unlikely to produce patches of big magnitude.

Sojka et al. [1993, 1994] undertook a high-resolution simulation to investigate the polar-cap ionosphere response to the instant transi-

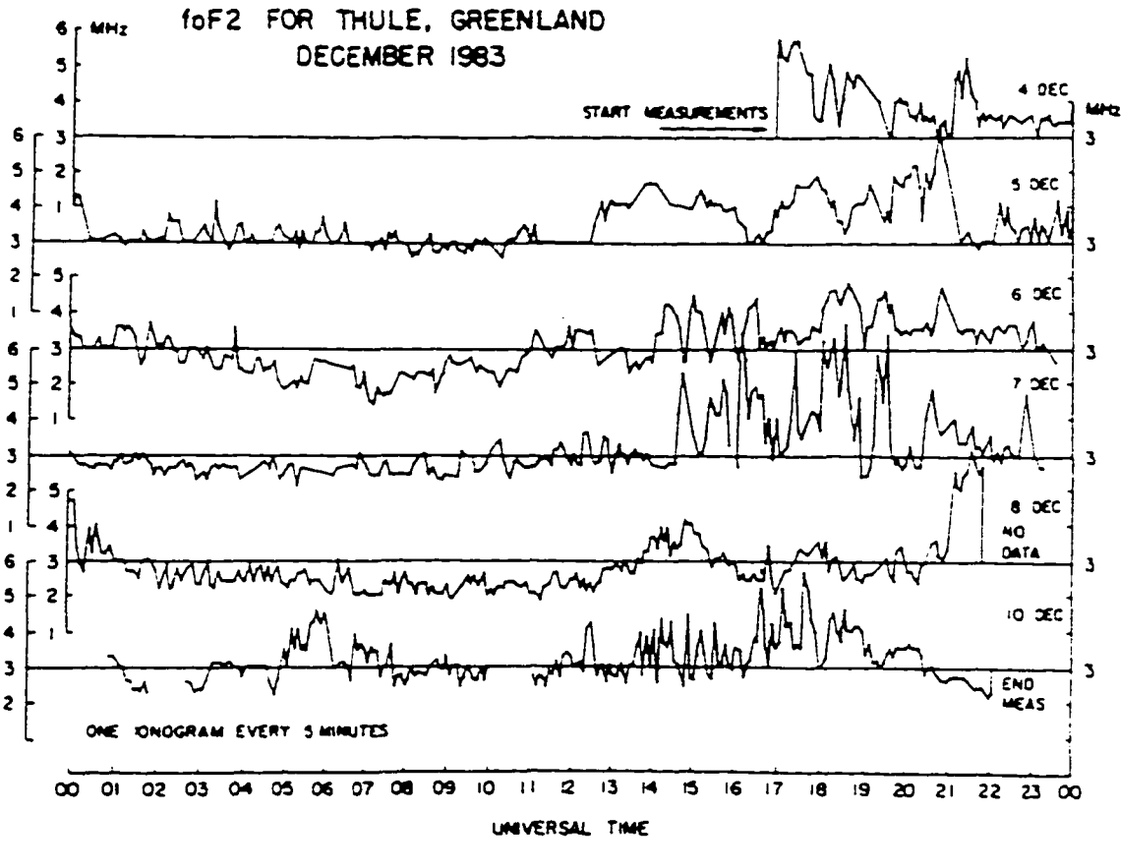

Figure 6.5. Digisonde 5-minutes measurements of the critical frequency of the ionospheric *F2* region at Thule, Greenland (86° Corrected Geomagnetic Latitude, CGL) in December, 1983 in solar minimum epoch (from *Buchau and Reinisch* [1991]).

tions from the convection patterns that correspond to IMF orientation with strong negative B_y ($B_z < 0$, $B_y << 0$) and to weak negative B_y ($B_z < 0$, $B_y < 0$) [*Heppner and Maynard*, 1987]. The winter, summer, and equinox conditions were reproduced in the simulations with a simplified time scenario of convection variability; instant transitions between two types of convection pattern every half hour. The simulation achieved a good reproduction of seasonal and UT dependencies of patch formation. The simulated patch size varied from several hundred kilometers to 2000 *km*, and the patch-to-background density ratio was established in a range from 2.5-3.5 for winter to 1.2-1.3 for summer.

6.3.2. Polar cap patches of ionization - simulations in response to IMF reversals

Compared to previous electric field models, the new electric field model by *Weimer* [1995] can simulate the IMF-driven variability in a much more flexible way. It includes situations of northward ($B_z > 0$) orientation of IMF that allow the user to specify an arbitrary IMF orientation and magnitude. Thus, it permits an ionospheric simulation that investigates the effects of rapid sign reversals of IMF both in B_y and in B_z component. This is a mechanism that is discussed in the literature as one of possible reasons of destruction of continuous ionospheric structures and patch formation.

Two simulations were performed with rapid sign reversals of, first, B_y and, second, the B_z IMF components. In both simulations the non-varying component was kept zero. Simulations were performed for winter conditions, with moderate solar and moderately disturbed geomagnetic activity levels. The results of these simulations are represented in figure 6.6. Using the simulated electron density profiles, the critical frequency *foF2* [*MHz*] was calculated for the location of Sondrestrom (74°CGL) in the polar cap

$$foF2\ [MHz] = \sqrt{1.114\times10^{-4}\ N_e\ [cm^{-3}]} \qquad (6.1)$$

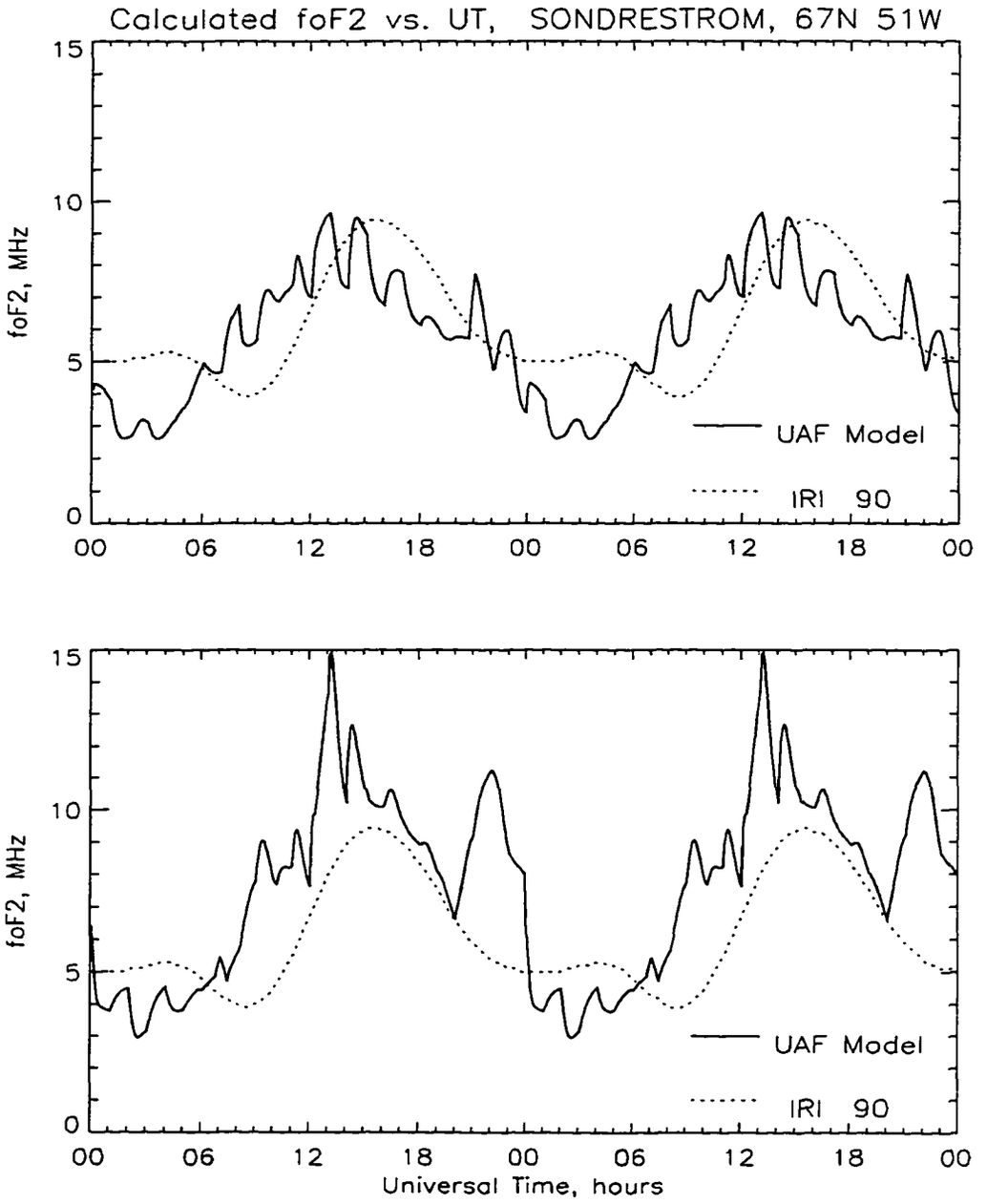

Figure 6.6. Calculated critical frequency f_oF2 [*MHz*] for the polar cap location (Sondrestrom) with a simple scenario of IMF variability for winter, moderately disturbed (K_p = 5o) geomagnetic conditions and moderate solar activity ($F_{10.7}$ = 150). The upper panel represents the sign reversals of B_y from -8γ to +8γ every hour, while B_z was kept zero. The lower panel represents the ionospheric response to the variations of B_z in the same limits while B_y was kept zero. International Reference Ionosphere values derived for similar conditions are shown for reference.

The upper panel in figure 6.6 represents the ionospheric effects of the the sign reversals of B_y from -8 γ to +8 γ at every model hour, while the B_z-component was kept constant ($B_z = 0$) for two model days. The lower panel demonstrates the results for a second run that was performed with the opposite arrangement, the B_y-component was kept constant ($B_y = 0$), while B_z-component has been changing from -8 γ to +8 γ every hour.

The oscillations on the resulting graph on figure 6.6 resemble the measured f_0F2 parameters in the polar cap. Having reasonable agreement in terms of mean values with the critical frequencies derived from the International Reference Ionosphere (IRI) model at the same location and similar geophysical conditions, the calculated f_0F2 is deeply modulated by variations in the IMF B_y and B_z components. As is evident from the graph, the peaks have 1-hour duration. The modulation is much larger in response to variations in B_z (lower panel) compared to the sign reversals of B_y. This difference is understandable from comparison of the corresponding convection patterns from the *Weimer* [1995] model (figure 2.2d) for opposite orientations of B_z and B_y, respectively, provided the second IMF component is kept zero. B_y reversal changes just tilt the orientation of generally anti-sunward convection toward dawn ($B_y >> 0$) or dusk ($B_y << 0$), mostly preserving the pattern and the convection intensity. B_z reversals dramatically change the convection pattern, from the most intensive convective regime ($B_z << 0$) to suppressed convection without clear orientation of the resulting flow ($B_z >> 0$).

The mechanism of formation of such a modulation is evident from a series of ionospheric snapshots over the course of one model hour for the simulation with variable B_y (figure 6.7). At 18.00 UT B_y was -8 γ and the tongue of anti-sunward flow inside the polar cap was directed with some tilt toward the dusk. B_y was changed rapidly to +8 γ and the new flow direction became tilted toward dawn by 18.05 UT. Development of a new configuration of the tongue of ionization started, while the existing structures continued their motion in a new convection pattern decaying into separated patches. A presence of one such patch above Greenland and the Sondrestrom location (67°N 51°W, west Greenland

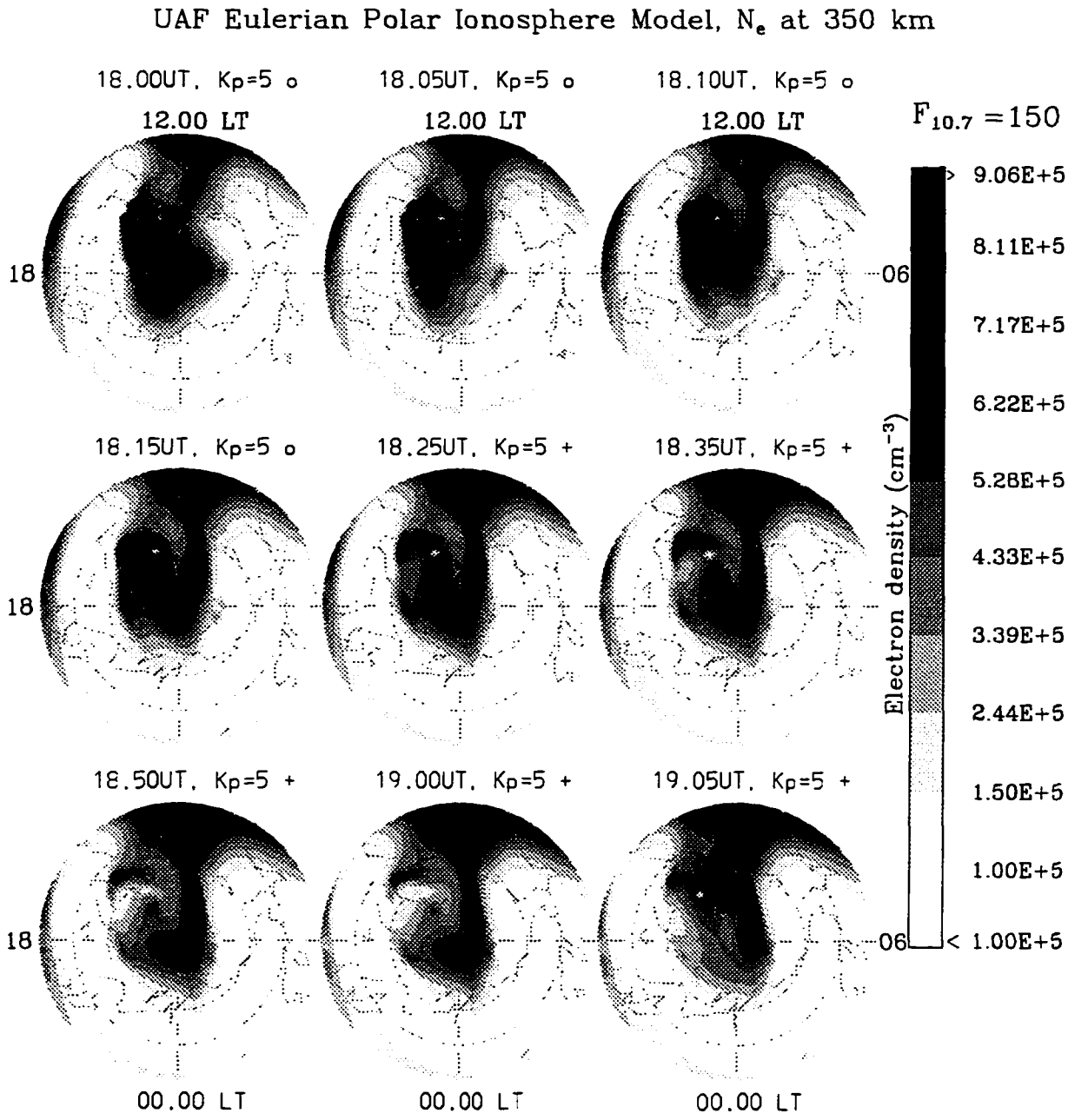

Figure 6.7. A series of contours of electron density corresponding to the winter conditions and the moderate solar and moderately disturbed geomagnetic activity over the course of one model hour (18.00 UT to 19.05 UT) after the sign reversal of the IMF *By* component. It was changed from -8γ at 18.00 UT to +8γ at 18.05 UT and was reversed back to -8γ at 19.05 UT. Development of new ToI corresponding to the current convection pattern is evident, while the previously existed ionospheric structures decayed into separated patches.

coast) is evident on the plot. By 18.35 UT the new ToI was fully developed. The patch above Sondrestrom persisted until about 19.00 UT. By 19.05 UT the B_y component was again reversed to -8 γ and the tongue of ionization started its reorientation again (this time in the dusk direction), generating a new cycle of patches.

These simulations with simplistic scenarios demonstrate that the IMF variability is responsible for considerable ionospheric variations in the polar cap. Such abrupt sign reversals are a common feature of real IMF variations. In the next subsection the time variations of the IMF corresponding to realistic data period will be considered.

6.3.3. Polar cap patches of ionization - simulations of realistic period

So far we have performed several simulations with exact specifications of B_y-, B_z-history prior to the period of interest for at least several hours to eliminate the influence of initial conditions. The electric field model by *Weimer* [1995] is applicable for arbitrary orientation of IMF components and therefore may be used to simulate time-varying convection patterns resulting from a realistic time-series of the IMF, provided B_y, B_z magnitudes are within certain limits. The tangential IMF component must satisfy $B_T \leq 13\ \gamma$ for *Wiemar's* [1995] model, that is not restrictive up to severely disturbed geomagnetic activity level.

The period studied is February 19, 1990. That was chosen because it is a period of continuous Sondrestrom Incoherent Scatter Radar (ISR) measurements as well as ionosonde measurements at Thule/Qaanaaq and Sondrestrom. Modeling efforts of other researchers have also been devoted to this period [*Valladares et al.*, 1994; *Decker et al.*, 1994].

Our simulation was started 12 hours prior to 00.00 UT February 19, 1990 with dynamically IMF-driven electric field input. IMF data were generally available for this time with the exception of the four hour period 22.20 UT February 18 till 02.10 UT February 19 when interpolated IMF values were substituted. After 02.15 UT, 5-minute interval IMF data were available for most of the period of interest with two

small gaps that were filled with interpolated values. The IMF data are plotted in the upper panels of figure 6.8.

Gaps in IMF data up to several hours are unfortunately a common occurrence. To investigate how the information loss affects the solution a series of numerical experiments were performed when the known IMF data were substituted by interpolated values in both B_y and B_z for a limited period of several hours. Comparison of an "exact" solution with valid IMF variability with the solution obtained from interpolated IMF data allows us to establish the recovery time when the "interpolated" solution merges the "exact" solution after switching to the valid IMF data in both simulations. The results demonstrate that the convergence took place within several model hours, in most cases from two to four. As one can expect, this time is comparable with the lifetime of $O^+(^4S)$ ion in the polar cap at F region altitudes.

Returning to the simulation of February 19, 1990, the ionospheric results in terms of critical frequencies calculated in accordance with expression (6.1) for Thule/Qaanaaq and for Sondrestrom locations are represented in the bottom panels of figure 6.8 together with ionosonde measurements and the time-history of IMF variations. After the IMF gap around midnight of February 19 within several model hours a remarkably close convergence of simulated values and real data took place. The only model fitting parameter, which can vary the output base within approximately the ±1 *MHz* range, is the soft electron background precipitation in the polar cap with characteristic energy 50 *eV*, and energy flux in the range of $0.01\text{-}0.1\ erg\ cm^{-2}sec^{-1}$. The best fit was established for the flux level of $0.02\ erg\ cm^{-2}sec^{-1}$, which was maintained constant throughout the calculations.

There is a discrepancy of about 2 *MHz* in f_oF2 values between the data and the model results that begins at about 14.00 UT at Sondrestrom and about half an hour later at Thule. This discrepancy can be explained as follows. The Sondrestrom ISR measurements [*Valladares et al.*, 1994] demonstrate that the localized plasma jet with a velocity exceeding 2 *km/sec* emerged near Sondrestrom at approximately the same time. This jet moved in the direction of anti-sunward convection with

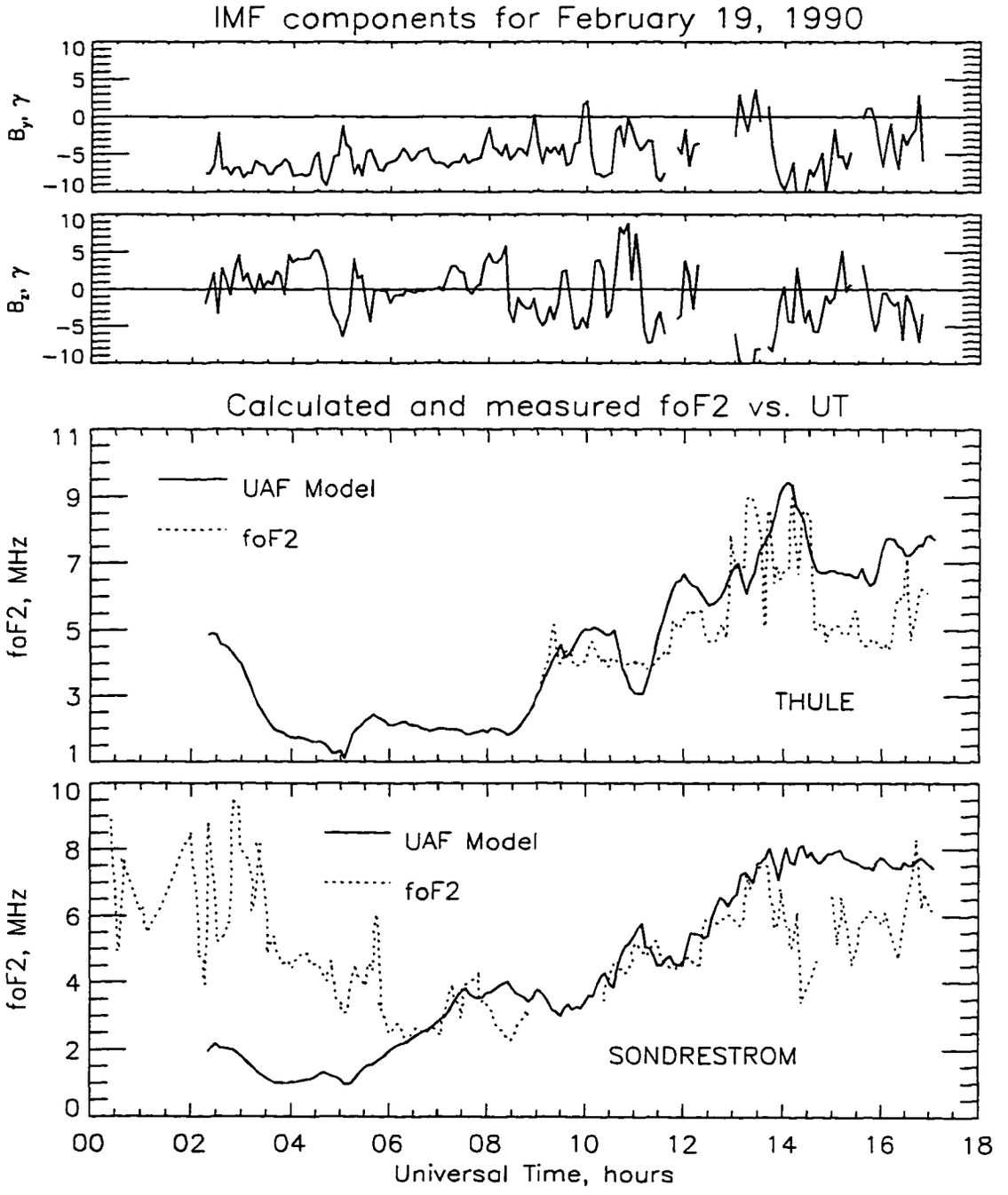

Figure 6.8. Comparison of simulated critical frequencies with ionosonde measurements at Thule/Qaanaaq and Sondrestrom for period of February 19, 1990. Corresponding IMF variations are represented on the upper panels.

a velocity of about 600 *m/sec*. At this location and UT the poleward direction coincides with the anti-sunward direction and the jet had reached Thule about half an hour later. Thus, the observed local depletions of the plasma density are explained by the enhanced recombination of the Joule-heated plasma.

This localized jet-related E-field disturbance, which exceeded 100 *mV/m*, is certainly not represented in the statistical E-field and, consequently, was not accounted for in the ionospheric model input. Therefore, a discrepancy of model and data at this time is not unreasonable.

Another departure of simulated values from data takes place during 02.00-06.00 UT, the local night hours at Sondrestrom, when a precipitation occurs. It can only partially be explained by the IMF gap preceding 02.00 UT and a time delay for the model to converge to realistic conditions. The model ionization rate is obviously low to match the density values caused by the night-time precipitation. The statistical model by *Hardy at al*. [1987] was used in the simulation to specify the precipitation pattern. This model assumes a constant number and energy flux in the polar cap. During the period in question the B_z IMF component was positive from 2.00 UT to 5.00 UT, while the IMF data for previous hours are absent. A positive orientation of B_z creates favorable conditions for the polar cap precipitation that may have occurred on February 19, 1990 and was not accounted for by the ionospheric model inputs.

6.3.4 Dynamic regime for periods of northward orientation of IMF

The second period we modeled for December 20, 1988. It is a period of high solar ($F_{10.7}$ = 240) and moderate geomagnetic activity (K_p = 1o - 2o). The distinct feature of this day is a strong northward (positive) orientation of B_z from 7.00 UT to 14.45 UT (figure 6.9), then a fast reversal took place and B_z orientation changed to the southward direction (negative). The first regime corresponds to a period of weak convection, while the second regime generates intensive convective motion in the polar cap. An abrupt transition from one convective regime

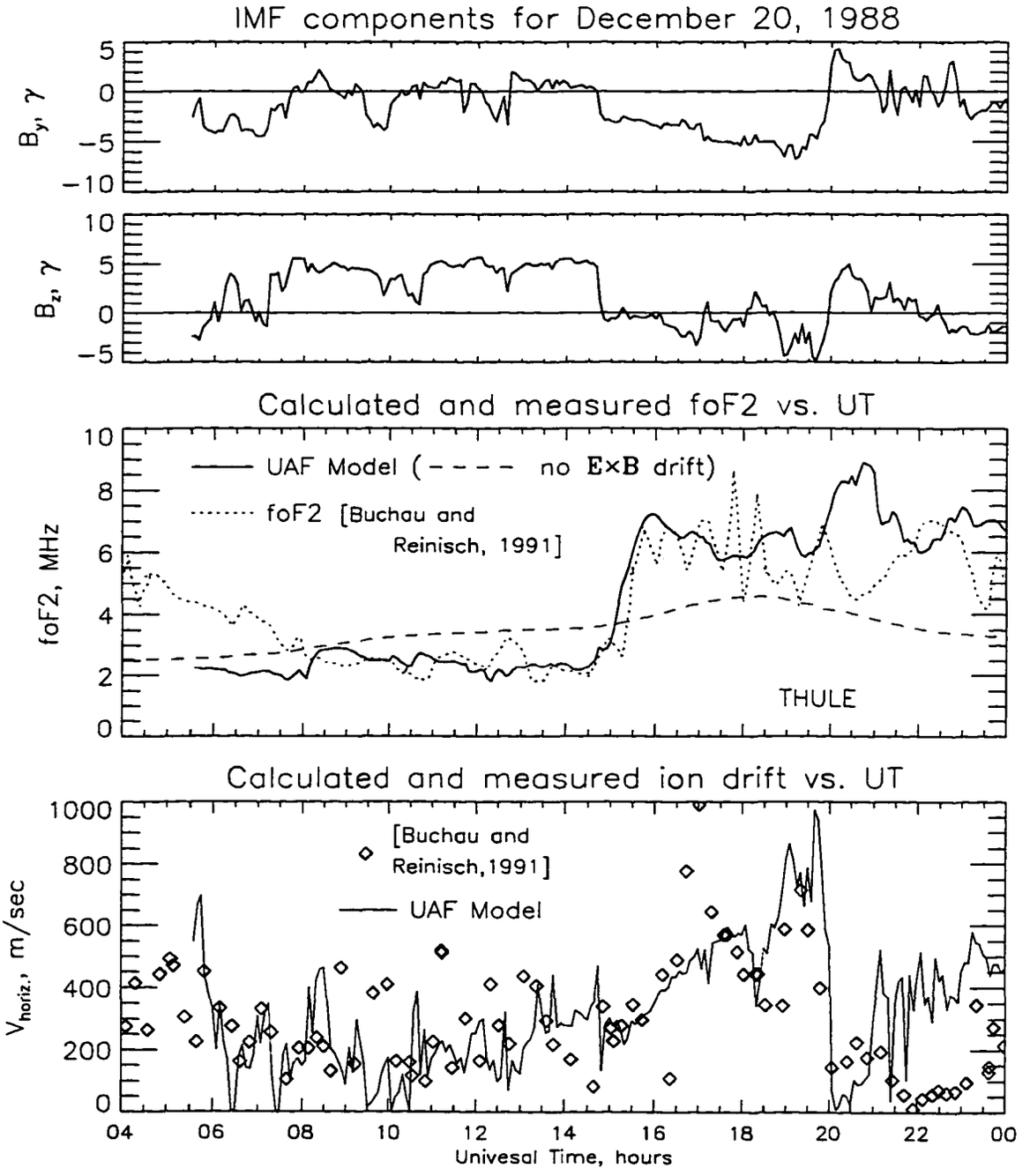

Figure 6.9. Comparison of simulated critical frequencies and the drift velocities with digisonde measurements at Thule/Qaanaaq for period of December 20, 1988. Corresponding IMF variations are represented on the upper panels.

to another is evident from the ionosonde measurements for this period by *Buchau and Reinisch* [1991], which are plotted in figure 6.9 as a dotted curve for *foF2* (middle panel) and as diamonds for the drift velocity (bottom panel).

This period was modeled using the technique described above, i.e. the simulation started 12 hours prior of the period of interest, and IMF data were used to derive the dynamically varying convection pattern. A few gaps in IMF information were filled by interpolation; unfortunately, a three-hour (2.30-5.30 UT) gap occurred just before the modeled period. It took about two hours of model time for the solution (solid curve in figure 6.9) to converge closer to measured values after this IMF data gap.

A second simulation was performed for this period, where the model was run without account for the horizontal transport (dashed curve in figure 6.9), i.e. the plasma density depended only on local production and loss including only transport by vertical diffusion.

Including simulation results that were performed without the advective transport demonstrates how small the influence of convective motion is under conditions of northward orientation of B_z. Smooth variations of measured critical ionospheric frequency foF2 near the ambient ionization level of non-dynamical origin can be modeled well without accounting for the horizontal plasma motion. However, an abrupt transition to negative B_z and to the related strong convection, results in significant fluctuations in the critical frequency curve. These fluctuations correspond to the horizontal transport of the patch-like plasma structures over the measurement site (Thule).

As one may expect, the model run without accounting for horizontal dynamics failed to simulate this behavior. On the other hand, the ionospheric response simulated with the full model version with E×B drift follows this data trend rather closely, demonstrating a remarkably good overall agreement for the transitional time and the magnitude of foF2 changes.

Comparison of the measured and calculated drift velocities (bottom panel in figure 6.9) is also favorable for the simulations, al-

though the variability of the measured velocities is significantly higher than the smoother curve from the model simulation. Many surges in the velocity data correspond to peaks on the measured f_0F2 curve. The simulated values generally follow the trends in the measured drifts, not the individual measurements.

The transition of the IMF B_z component at 14.45 UT to southward orientation and at 20.00 UT back to northward direction should result in prominent variations in the measured drift velocities. These trends were well approximated by the simulated velocities. However, the model failed to achieve an agreement with the drift measurements as low as 50-100 *m/sec* after about 22.00 UT. Agreement between model and observations improved again at 23.30 UT. This period corresponds to the worst disagreement in f_0F2 comparisons as well.

Figure 6.10 shows four panels plotted for different UT instants, representative of different stages of the large scale dynamics in this simulation. The Thule location on these plots can be found on the very northwest of Greenland near the coast. Stable positive orientation of B_z occurred after about 7.00 UT. The first panel shows ionospheric conditions at 9.00 UT, two hours after a weak convection established. The morning cell of convection pattern is almost completely suppressed, while the evening cell still exists with greatly decreased drift velocities. This convection pattern corresponds to the upper central panel in figures 2.2b representing the electric field model by *Weimer* [1995]. The drift vectors represent the motion of 200-400 *m/sec*, which is slow compared to about 1 *km/sec* typical for strong convection patterns of negative B_z orientation.

Distribution of the plasma density in this panel demonstrates the remnants of structures developed under previous conditions of strong convection several hours before 9.00 UT. On the next panel corresponding to 11.30 UT these structures are weaker, while the convection type is mostly the same. On this plot the contours of soft auroral precipitation become apparent. This is one more manifestation of weak convection; a strong convection system usually destroys these contours. These tendencies strengthen during the course of this positive B_z pe-

riod. The situation for 13.00 UT, six hours after establishing of positive B_z, to some extent resembles the corresponding panel from figure 6.1 calculated with zero drifts. In figure 6.9 this period corresponds to close agreement of the simulation performed with zero drift with data.

This resemblance is completely destroyed in the 15.00 UT panel, 15 minutes after B_z reversal to negative direction took place. The convection system in this panel is much stronger with the presence of a two-cell structure. Anti-sunward flow was strong enough to create a prominent tongue of ionization that covers the Thule location. This is reflected in figure 6.9 by the abrupt enhancement of f_0F2 values by about 5 *MHz*, or in terms of electron density by an order of magnitude, from about 4×10^4 to 4×10^5 cm^{-3}. This increase had a completely dynamic reason and, consequently, is not reproduced by the "zero drift" simulation. As was mentioned above, an account of the appropriate plasma drifts resulted in very close agreement of simulated values with data.

6.4. AMIE-reconstruction of electric field and simulations of the intensive magnetic storm of March 20-21, 1990

Assimilative Mapping of Ionospheric Electrodynamics (AMIE) is a powerful technique for reconstruction of an actual realization of the electric field in the ionosphere [*Richmond and Kamide*, 1988] by recreation of an equivalent current system using magnetometer data and ionospheric conductivities. It is capable of high-resolution output both in time and space. However, it is a very time consuming technique and the coverage of available reconstructions is limited to a total of 15-20 days. Data for three periods covering 2 days each are available in the CEDAR database. A recent reconstruction, which has a better resolution compared to earlier AMIE sets (5 minutes in temporal resolution, 1.67° in geomagnetic latitude, and 10° in geomagnetic longitude), covers two days of intensive magnetic storm March 20-21, 1990 [*Knipp et al.*, 1994].

IMF data is available for a significant part of this period. Although there are two gaps of 4 and 12 hours, the choice of AMIE periods

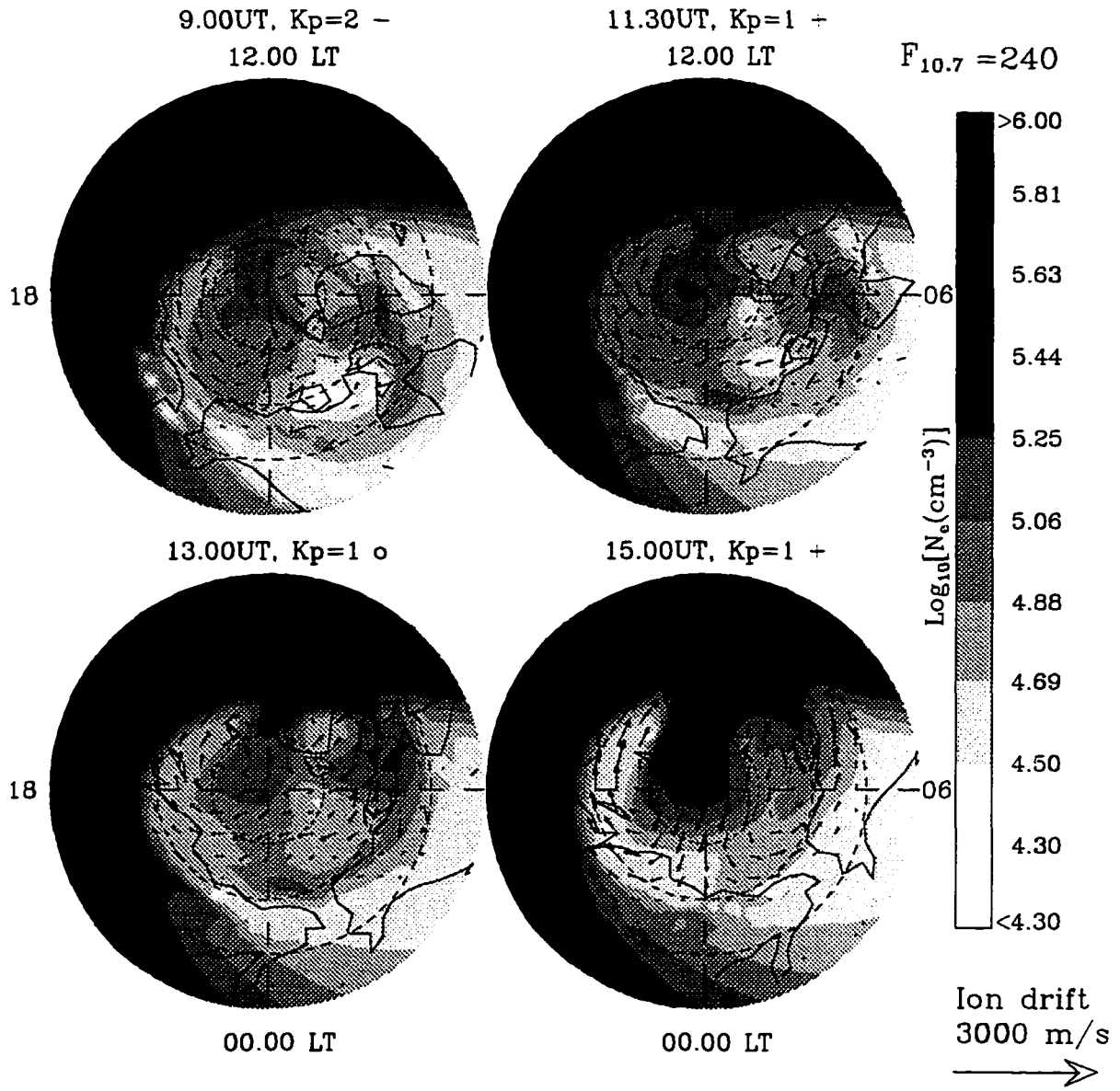

Figure 6.10. Distribution of electron density at 350 *km* corresponding to four instants of UT December 20, 1988 with a stable northward orientation of the IMF (9.00, 11.30, 13.00 UT) and 15 minutes after abrupt transition to negative B_z (15.00 UT). See text for discussion.

is rather scarce and this is one of the best available coverage.

A presence of IMF data for this period enables us to compare the results of ionospheric simulations with the statistical electric field model dynamically adjusted for IMF time series, and the AMIE-reconstruction of particular realization of electric field for this period. In is also favorable for this comparison that the period is long enough to cover different geomagnetic conditions, from moderate (Kp = 3o - 3+, March 20) to severely disturbed (Kp = 7o - 7+, March 21).

Results of these simulations are reproduced in figure 6.11. The upper panels show the Kp index and IMF B_y and B_z components for this period, leaving the blank space for IMF data gaps. The middle panel shows the UT dependency of the tangential component, B_T, of the IMF - the magnitude of the vector sum of B_z and B_y - and by dashed line the upper limit value the statistical model is applicable (B_T = 13 γ). The lower panel reproduces the simulated critical frequency f_oF2, that was calculated for the Sondrestrom location and was obtained with three different runs of the ionospheric model. The dashed line represents the results obtained without accounting for horizontal dynamics, the solid line represents the results with the electric field input using the Weimer [1995] model with linear interpolation of B_y, B_z-components inside the IMF data gaps, and the dashed-dotted line corresponds to the results obtained with the AMIE-reconstruction of electric field as an input to ionospheric model. The dotted line represents the Sondrestrom ISR data. The initial electron density profiles were available every 2-minutes and for representation purposes were averaged within a sliding 20-minute interval.

All three runs were started five model hours prior to 00.00 UT of March 20, 1990 to eliminate the influence of the initial condition and to achieve convergence of the solution to the current conditions. During these initial five model hours the statistical electric field model was used in all three runs and at 00.00 UT March 20 the electric field input was replaced in two runs, respectively, to zero field to describe the situation of absence of horizontal drifts, and to the AMIE-reconstructed electric field. The third simulation continued to use

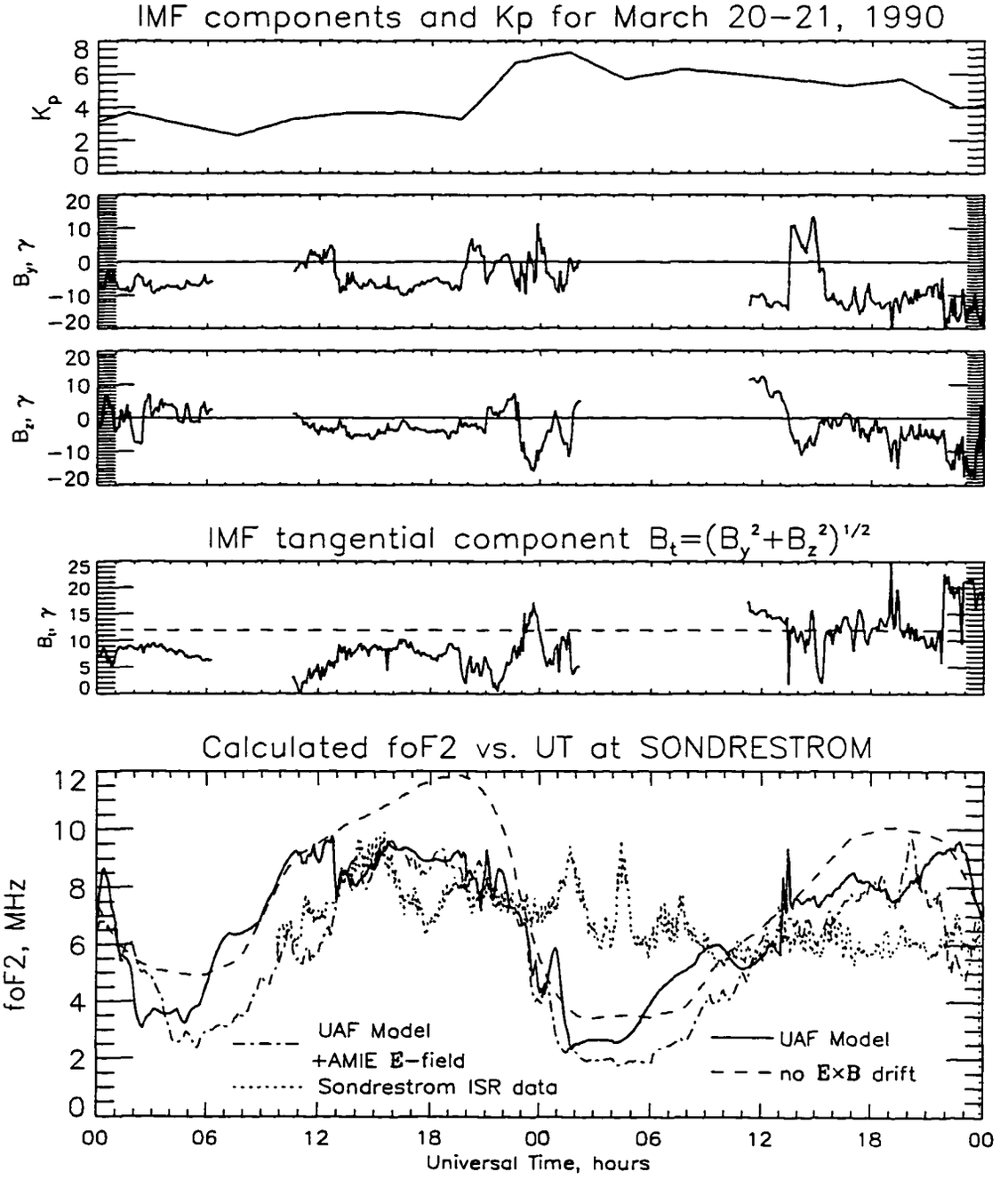

Figure 6.11 Geophysical indices and calculated critical frequency foF2 vs. UT for period of intensive magnetic storm of March 20-21, 1990.

the Weimer electric field model input throughout the entire run.

Tracing all three curves together, it is evident that the "zero-drift" run is rather distant from the other solutions and at best just approaches them, normally in the situations when dynamics is less important compared to the ionization processes and chemistry, usually during the local night. Sondrestrom is situated at $66^{\circ}59'N$ $50^{\circ}57'W$ and the interval 00.00-09.00 UT approximately corresponds to 21.30-5.30 LT at the site. The convection system is located on the night-side and the ToI is not sufficiently developed to transport the day-side plasma in any noticeable amounts. Figures 6.2 and 6.3a,b are instructive in this context to visualize the corresponding configuration for UT periods of interest.

There is a period from 06.00 to 12.00 UT, March 20 when "zero-drift" and "Weimer E-field" solutions almost coincide. An explanation lies with the lack of IMF data, that was substituted by interpolation in positive B_z range for a rather long period of time that resulted in severely suppressed convection. Transition to valid IMF data destroyed this coincidence within two hours (11.00-13.00 UT).

Comparing the "AMIE-field" and the "Weimer-field" runs, it is evident from the plot that agreement is very good in the situations when IMF data is available and the statistical electric field model has a valid input. Gaps in IMF data eventually result in the formation of discrepancies that are eliminated later within 2-3 hours after IMF data is available again. This tendency is violated only once throughout the two days' run starting from about 20.00 UT, March 21 due to anomalously large values of both B_z and B_y (up to -20γ) during this particular period. The statistical model is derived within the range of 13-14 γ for tangential IMF component B_T, the range that covers 90-95% of all realizations. However, only an extrapolation of the model, with all uncertainties and distortions that an extrapolation on the long range can not avoid, can be applied to disturbances of such unique scale as the magnetic storm with K_p up to 7+.

The above considerations are generally applicable to the ionospheric model and its comparison with the storm data. An agreement is

very good for the moderate geomagnetic conditions of March 20, but it is mostly out of range when the intense storm started at 23.00 UT March 20. Discrepancies started during the night and morning period 00.00-12.00 UT. As it was pointed out above, the statistical auroral model input does not provide an adequate description of the precipitation pattern in the polar cap, especially for disturbances of such intensity.

For the next period, 12.00 to 17.00 UT, the data agreement of the "AMIE-field" run is rather good, while the "Weimer-field" run, being at this time period on an edge of the statistical model applicability, gives higher values of f_0F2 by 1-1.5 *MHz* (25-40% higher in terms of electron density N_e [cm^{-3}]). However, both runs failed to describe an anomalously low after-storm noon maximum, giving about a 2 *MHz* higher (50% in N_e) prediction, a situation which is also common with the after-storm predictions for mid-latitude models [*Richards et al.*, 1994]. Apparently, it is caused by a poor response of the thermospheric model during the storm-time and after-storm conditions for neutral thermospheric temperatures and composition [*Richards et al.*, 1994], and possibly by unaccounted ionization sinks by the vibrationally exited nitrogen, which can be important during the negative phase of significant storms [*Pavlov*, 1994].

6.5 Preliminary conclusions

As a general conclusion to this chapter, it is necessary to point out that results of ionospheric models are critically dependent on their E-field and precipitation inputs. For experimental periods when the real E-field structures are well represented by the statistical representation which we use as the ionospheric model input, the modeled electron density is a close representation of real data. However, when localized E-field structures result in significant departures from the statistical model, the modeled ionospheric data do not accurately reflect reality.

Precipitation input specified by the statistical auroral model is not sufficient for description of individual periods, especially in the

auroral cap. High auroral variability necessitates an implementation of alternative approaches for the input description.

Ionospheric simulation with the exact specifications of the previous history of dynamics is a promising approach. Due to the long lifetime of ionization in the upper ionosphere, its present state depends on the prior time-sequence of input parameters. An ability to trace the influence of critical ionospheric inputs such as convective electric field and the auroral precipitation is necessary to reproduce particular ionospheric behavior. Implementation of the new generation electric field input by *Weimer* [1995] has significantly improved the simulation vs. data agreement. Comparison of model runs with AMIE-reconstructions of the electric field for particular periods and with statistical electric field model have demonstrated a good applicability of the statistical approach for the description of electric field input.

CHAPTER 7

SUMMARY, CONCLUSIONS, AND FUTURE WORK

7.1. Summary and conclusions

This thesis describes the development of a high-latitude ionospheric model in the corotating reference frame. The model can successfully simulate large-scale features of the polar ionosphere, such as the sunlit region of abundant ionization, ionization tail of the long-living corotating plasma in the dawn sector, the polar cap tongue of ionization due to dynamic anti-sunward flow of the day-side plasma to the dark region, several regions of different locations of the low plasma density known as ionospheric troughs, auroral oval, the polar hole, and other morphological features.

In addition to morphological or "climate"-scale simulations, the model was applied to high-resolution simulations of some "space weather" effects. These runs have reproduced such mesoscale short-term features as destruction of polar cap plasma into separate patches of ionization that form under the influence of rapidly changing IMF. It was confirmed that the effect takes place for variations of the IMF B_y-component [*Sojka et al.*, 1993, 1994] and established that variations of B_z-component also produce the similar effects.

Adoption of the new IMF-driven electric field model by *Weimer* [1995] allowed us to simulate periods with northward (positive) orientation of the IMF B_z-component. Moreover, it is possible to specify a dynamically varying B_y, B_z time-series to reproduce specific geophysical periods of time. Such reconstructions of real events were performed and the calculated results demonstrate a high level of agreement with ionospheric data including the temporal variability. Among the simulated events are periods with extended positive B_z-orientation, followed by rapid reversals to negative values, reflected in the convection regime changes. The model predictions of ionospheric behavior coincide very closely in time and magnitude with the ionosonde polar

cap data and the Sondrestrom incoherent radar measurements.

This approach was also applied to the intensive storm period of March 20-21, 1990. A comparison of several model runs with different electric field inputs, including an independently developed AMIE-reconstruction, have demonstrated that for undisturbed geomagnetic conditions the ionospheric model with statistical IMF-driven electric field input is capable of reproducing the ionospheric response with a high level of accuracy. During the severe magnetic storm the simulation vs. data agreement was partially lost, but the runs with different electric field inputs gave similar results. This suggests that other factors, not the electric field, are not adequately represented for the storm period; apparently the neutral thermosphere and the precipitation parameters are inadequate.

The general agreement of the ionospheric model simulations with real data is an important result of this work. However, it is necessary to point out that this agreement is dependent on the validity of the statistical E-field and precipitation models that are used as inputs to the ionospheric model. Discrepancies from the statistically averaged model inputs result in discrepancies in the simulated ionospheric responses. Poor representation of the polar cap precipitation with the statistical auroral model often causes discrepancies of the night-time simulations from data. The storm simulations demonstrate the limits of applicability of the statistical electric field model.

Among other conclusions concerning the model ionospheric results, it is necessary to mention that the model development has demonstrated the computational strength of the corotating frame approach for high-resolution applications. The regular grid coverage and fast numerical algorithm resulted in very efficient use of computing resources; this will enhance the value of future high-resolution space-weather applications of this model when used on supercomputers, including massively parallel architectures. Regularity of the 3-D computational domain, which arises in the corotating frame approach, and the local representation of the finite-difference scheme are especially important for transition to parallel architecture. These factors facilitate the code

partition among the neighboring processors and minimize the inter-processors' overhead.

7.2. Future work

Future work will focus on the development of the model in a higher resolution format on a parallel computing platform, improvements in the chemistry and dynamics of the *E* region portion of the model, and modification to the electro-dynamic input. Examples of possible future tasks and model applications are

- creation of multi-grid versions with fine coverage over important local regions (e.g. ISR and ionosonde stations) combined with coarser coverage of the entire domain
- further refining of the model in the *E*-region, inclusion of full transport of molecular ions, and account of the sheared advection of the odd nitrogen family of the minor neutrals
- studies of *E*-region fine structure in the ionization using time sequence of auroral images as a high-resolution particle precipitation input
- self-consistent electro-dynamics combined with the ionospheric model to establish an instantaneous distribution of conductivities and polarization fields induced by the perpendicular ion motion in the *E* region that, in turn, distorts the electric field of magnetospheric origin at the *F* region heights and modifies the convection pattern
- further participation in the CEDAR Storm Study program performing simulations of the ionospheric storm-time response in the high-latitudes. Further expansion of the model frame into mid-latitudes to trace the mid-latitude effects of the polar disturbances

REFERENCES

Ajello, J.M., Dissociative excitation of O_2 in the vacuum ultraviolet by electron impact, *J.Chem.Phys.*, **55**, 3156, 1971.

Albritton, D.L., I. Dotan, W. Lindinger, M. McFarland, J. Tellinghuisen, and F.C. Fehsenfeld, Effects of ion speed distributions in flow drift tube studies on ion-neutral reactions, *J.Chem.Phys.*, **66**, 410, 1977.

Anderson, D.N., and Rusch D.W., Composition of the nighttime ionospheric *F1* region near magnetic equator, *J.Geophys.Res.*, 85, 569, 1980.

Baker K.B., S. Wing, A new magnetic coordinate system for conjugate studies at high latitude, *J.Geophys.Res.*, **94**, No.A7, 9139-9143, 1989.

Banks, P.M., Collision frequencies and energy transfer: Electrons, *Planet. Space Sci.*, **14**, 1085-1104, 1966a.

Banks, P.M., Collision frequencies and energy transfer: Ions, *Planet. Space Sci.*, **14**, 1105-1122, 1966b.

Banks, P.M., Electron thermal conductivity in the atmosphere, *Earth Planet. Sci. Lett.*, **1**, 151-154, 1966c.

Banks, P.M., Ion temperature in the upper atmosphere, *J.Geophys. Res.*, **72**, 3365-3385, 1967.

Banks, P.M., and G. Kockarts, *Aeronomy*, Academic Press, N.Y., Part A pp.430, Part B pp.355, 1973.

Banks P.M., C.R. Chappel, and A.F. Nagy, A new model for the interaction of auroral electrons with the atmosphere: Spectral degradation, backscatter, optical emission, and ionization, *J.Geophys.Res.*, **79**, 1459, 1974.

Barret, J.L, and P.B. Hays, Spacial distribution of energy deposited in nitrogen by electrons, *J.Chem.Phys.*, **64**, 743, 1976.

Black, G., T.G. Slanger, G.A. St.John, and R.A. Young, Vacuum ultraviolet photolysis of N_2O. IV. Deactivation of $N(^2D)$, *J. Chem. Phys.*, **51**, 116, 1969.

Borst, W.L., and E.C. Zipf, Cross section for electron impact excita-

tion of the (0,0) First Negative Band of N_2^+ from threshold to 3 keV, *Phys. Rev., Sect. A*, 1, 834, 1970.

Buchau J. and B.Reinisch, Electron density structures in the polar F region, *Adv.Space Res.*, 11, (10)29, 1991.

Burnett, T., and S.P. Roundtree, Differential and total cross sections for electron-impact ionization of atomic oxygen., *Phys. Rev., Sect. A*, 20, 1468, 1979.

Cartwright, D.C., Vibrational populations of the excited states of N_2 under auroral conditions, *J.Geophys.Res.*, 83, 517-531, 1978.

Cartwright, D.C., S. Trajmar, A. Chutjian, and W. Williams, Electron impact excitation of the electronic states of N_2. II.Integral cross section at incident energies from 10 to 50 eV, *Phys.Rev., Sect. A*, 16, 1041-1051, 1977.

CEDAR data base catalogue, ed. B.A.Emery and R.M. Barnes, NCAR, Boulder, CO, pp.142, 1995.

Crowley, G., B.A. Emery, R.G. Roble, H.C. Carson, Jr., and D.J. Knipp, Thermospheric dynamics during September 18-19, 1984. 1. Model simulations, *J.Geophys.Res.*, 94, 16,925-16,944, 1989.

Dalgarno, A., Inelastic collisions at low energies, *Can.J.Chem.*, 47, 1723-1731, 1969.

Davenport, J.T., T.G. Slander, and G.Black, The quenching of $N(^2D)$ by $O(^3P)$, *J.Geophys.Res.*, 81, 12, 1976.

Decker, D.T., C.E. Valladares, R. Sheehan, Su.Basu, D.N. Anderson, R.A. Heelis, Convection of polar cap patches observed at Qaanaaq, Greenland during the winter of 1989-1990, *Radio Sci.*, 29, No.1, 249, 1994.

Desloge, E.A., Exchange of energy between gases at different temperatures, *Phys.Fluids*, 5, 1223-1225, 1962.

Dickinson, R.E., E.C. Ridley, and R.G. Roble, A three dimensional general circulation model of the thermosphere, *J.Geophys.Res.*, 86, 1499, 1981.

Dickinson, R.E., E.C. Ridley, and R.G. Roble, General circulation with coupled dynamic and composition , *J.Atmos.Sci.*, 41, 205, 1984.

Dreyer, J.W., and D. Perner, Deactivation of $N_2(A^3\Sigma_u, \nu = 0\text{-}7)$ by ground

state nitrogen, ethane and ethylene measured by kinetic absorption spectroscopy, *J.Chem.Phys.*, 58, 1195, 1973.

Dreyer, J.W., D. Perner, and C.R.Roy, Rate constants for the quenching of $N_2(A^3\Sigma_u, v_a = 0\text{-}8)$ by CO, CO_2, NH_3, NO and O_2, *J.Chem. Phys.*, 61, 3164, 1974.

Evans, W.F.J., and A. Vallance Jones, Some observations of type-B red aurora with a multichannel photometer, *Can.J.Phys.*, 43, No.4, 697, 1965.

Fehsenfeld, F.C., The reaction of O_2^+ with atomic nitrogen and $NO^+ \cdot H_2O$ and NO_2^+ with atomic oxygen, *Planet.Space Sci.*, 28, 105, 1980.

Felder, W., R.A. Young, Quenching of $O(^1S)$ by $O(^3P)$, *J.Chem.Phys.*, 56, No.12, 6028-6030, 1972a.

Felder, W., R.A. Young, Is $O(^1D)$ produced in the reaction of N with NO, *J.Chem.Phys.*, 57, No.1, 572-573, 1972b.

Fesen, C.G., R.E. Dickinson, and R.G. Roble, Simulations of thermospheric tides at equinox with the NCAR thermospheric general circulation model, *J.Geophys.Res.*, 91, 4471-4489, 1986.

Fletcher, C.A.J. , *Computational Techniques for Fluid Dynamics*, vol I , pp. 401, Springer-Verlag, 1991

Frederick, J.E. and D.W. Rusch, On the chemistry of metastable atomic nitrogen in the F region deduced from simultaneous satellite measurements of the 5200-Å airglow and atmospheric composition, *J. Geophys. Res.*, 82, 3509, 1977.

Frederick, J.E., D.W. Rusch, G.A. Victor, W.E. Sharp, P.B. Hays, and H.C. Brinton, The OI(λ5577Å) airglow: Observations and excitation mechanisms, *J.Geophys.Res.*, 81, 3923, 1976.

Fuller-Rowell T. J., D. S. Evans, Height integrated Pedersen and Hall conductivity patterns inferred from TIROS-NOAA satellite data, *J. Geophys. Res.*, 92, A8, 7606-7618, 1987.

Garstang, R.H., Transition probabilities in auroral lines, in *The Airglow and Aurora*, edited by E.B. Armstrong and A. Dalgarno, pp.324, Pergamon, New York, 1956.

Green, A.E.S., and R.S. Stolarski, Analytic models of electron impact excitation cross sections, *J.Atm.Terr.Phys.*, 34, 1703, 1972.

Hardy, D.A., M.S. Gussenhoven, and E. Holeman, A statistical model of the auroral electron precipitation, *J.Geophys.Res.*, 90, 4229-4248, 1985.

Hardy, D.A., M.S. Gussenhoven, R. Raistrick, and W.J. McNeil, Statistical and functional representations of the pattern of auroral energy flux, number flux and conductivity, *J.Geophys. Res.*, 92, 12,275-12294, 1987.

Hedin A.E., MSIS-86 thermospheric model, *J.Geophys.Res.*, 92, 4649, 1987.

Hedin, A.E., Extension of the MSIS thermosphere model into the middle and lower atmosphere, *J.Geophys.Res.*, 96, A2, 1159-1172, 1991a.

Hedin, A.E., M.A. Biondi, R.G. Burnside, G. Hernandes, R.M. Johnson, T.L. Kileen, C.Mazaudier, J.W.Meritwether, J.E. Salah, R.J. Sica, R.W. Smith, N.W. Spencer, V.B.Wickwar, and T.S. Virdi, Revised global model of thermospheric winds using satellite and ground-based observations, *J.Geophys. Res.*, 96, A5, 7657-7688, 1991b.

Heelis, R.A., J.K. Lowel, and R.W. Spiro, A model of the high-latitude convection pattern, *J.Geoph.Res.*, 87, 6339, 1982

Heelis, R.A., The effect of interplanetary magnetic field orientation on dayside high-latitude ionospheric convection, *J.Geoph.Res.*, 89, 2873-2880, 1984.

Heelis, R.A., W.R. Coley, M. Loranc, M.R. Hairston, Three-dimensional ionospheric plasma circulation, *J.Geoph.Res.*, 97, A9, 13,903-13,910, 1992.

Heidner, R.E., and D. Hussain, Quenching of $O(2^1D^d2)$ by atomic gases, *Nature*, 241, 10, 1973.

Henry, R.J.W., and M.B. McElroy, Photoelectrons in planetary atmospheres, in *The Atmospheres of Venus and Mars*, edited by J.C. Brandt and M.B. McElroy, pp.251-285, Gordon and Breach, New York, 1968.

Henry, R.J.W., and R.E. Williams, Collision strength and photoionization cross section for nitrogen, oxygen, and neon, *Publ. Astron. Soc.Pac.*, 80, 669-679, 1968.

Henry, R.J.W., P.G. Burke, and A.L. Sinfailam, Scattering of electrons by C, N, O, N^+, O^+, and O^{++}, *Phys. Rev.*, 178, 218, 1969.

Heppner, J.R., and N.C. Maynard, Empirical high-latitude electric field

model, *J.Geophys.Res.*, 92, 4467-4489, 1987.

Hoegy, W.R., New fine structure cooling rate, *Geophys.Res.Lett*, 3, 541-544, 1976.

Hoegy, W.R., Ambient electron heating rate, *IAGA/IAMAP symposium*, AGU, Seattle, August 1977.

Huntress, W.T., Jr., and V.G. Anicicoh, On the reaction of N^+ ions with O_2, *Geophys.Res.Lett.*, 3, 317, 1976.

Iannuzzi, M.P., and F. Kaufman, Rates of some reactions of $N(^2D$ and $^2P)$ near 300 K, *J.Chem.Phys.*, 73, 4701, 1980.

Itikawa, Y., Effective collision frequency of electrons in atmospheric gases, *Planet.Space Sci.*, 19, 993-1007, 1971.

Itikawa, Y., Momentum transfer cross sections for electron collisions on atoms and molecules and their application to effective collision frequencies, *Rep.ANL-7939*, pp. 1-32, Argonne Nat. Lab., Argonne, Ill., 1973.

Jet Propulsion Laboratory (JPL), *Chemical Kinetic and Photochemical Data for Use in Stratospheric Modeling, JPL* 81-3, p. 124, NASA Panel for Data Evaluation, Jet Propulsion Laboratory, Pasadena, CA, 1981.

Johnsen, R., and M.A. Biondi, Laboratory measurements of the $O^+(^2D)$ + N_2 and $O^+(^2D)$ + O_2 reactions rate coefficients and their ionospheric implications, *Geophys.Res.Lett.*, 7, 401, 1980.

Jusinski, L.E., G.Black, and T.G. Slander, Resonance-enhanced multiphoton ionization measurements of $N(^2D)$ quenching by $O(^3P)$, *J.Phys. Chem.*, 92, 5977, 1988.

Killeen, T.L., R.G. Roble, and N.W. Spencer, A computer model of global thermospheric winds and temperatures, *Adv.Space.Res.*, 7, 207-215, 1987.

Kirby-Docken, K., E.R. Constantinides, S. Babeu, M. Oppenheimer, Photoionization of He, O, N_2, and O_2 for aeronomic calculations, *Atomic Data Nucl.Data Tables*, 23, 63, 1979.

Knipp, D., B.A. Emery, A.D. Richmond, and W.F. Roberts, Current, Conductance and Convection Patterns for the Geomagnetic Storm of 20-21 March, 1990, Abstracts of AGU Fall 1994 Meeting, p.498, 1994.

Knipp, D., B.A. Emery, and W.F. Roberts, Mapped ionospheric current response to the initial phase of the 3 November Geomagnetic Storm, Abstracts of AGU Fall 1995 Meeting, p.F434, 1995.

Kockarts G., Nitric oxide cooling in the terrestrial thermosphere, *Geophys.Res.Lett*, 7, 137, 1980.

Kopp, J.P., J.E. Frederick, D.W. Rusch, and G.A. Victor, Morning and evening behavior of the *F* region green line emission: evidence concerning the sources of $O(^1S)$, *J.Geophys. Res.*, 82, 4715, 1977.

Langford, A.O., V.M. Bierbaum, and S.R. Leone, Branching ratios for electronically excited oxygen atoms formed in the reaction of N^+ with O_2 at 300K, *J.Chem.Phys.*, 84, No.4, 2158, 1986.

Lawton, S.A., and A.V. Phelps, Excitation of the $b^1\Sigma_u^+$ state of O_2 by low energy electrons, *J.Chem.Phys.*, 69, No.3, 1055-1068, 1978.

Lilensten J., W. Kofman, J. Wisemberg, E.S. Oran, and C.R. Devore, Ionization efficiency due to primary and secondary photoelectrons: A numerical model, *Ann. Geoph.*, 7, 83-90, 1989.

Lindinger, W., F.C. Fehsenfeld, A.L. Schmeltekopf, and E.E. Ferguson, Temperature dependence of some ionospheric ion-neutral reactions from 300-900 K°, *J.Geophys.Res.*, 79, 4753, 1974.

Link, R., J.C. McConnell, and G.C. Shepherd, A self-consistent evaluation of the rate constants for the production of the OI 6300Å airglow, *Planet.Space Sci.*, 29, 589, 1981

London, G., R. Gilpin, H.I. Schiff, K.H. Welge, Collisional deactivation of $O(^1S)$ by O_3 at room temperature, *J.Chem.Phys.*, 54, No.10, 4512, 1971.

Lummerzheim D., M.H. Rees, J.D. Craven, and L.A. Frank, Ionospheric conductances derived from DE-1 auroral images, *J.Atmos.Terr.Phys.*, 53, 3-4, 281-292, 1991.

Lummerzheim D., Comparison of energy dissipation functions for high energy auroral electron and ion precipitation, Geophysical Institute Report, UAG-R-318, 1992.

Märk, T.D., Cross section for single and double ionization of N_2 and O_2 molecules by electron impact from threshold up to 170 eV, *J. Chem.Phys.*, 63, 3731, 1975.

Maurits S. A., and A.V. Shirochkov, The effect of seasonal variations of the optical depth of the mesosphere on the ionization rate of the lower ionosphere by radiation in the Lyman-α (1216Å), *Geomag. Aeron.*, 14, 421-423 (English edition), 1984.

Maurits S. A., and G. S. Ivanov-Kholodny, Ionospheric structure and modeling, *Review of Radio Science*, 1990-1992, pp.491-522, Ed. by W. R. Stone, Oxford University Press, N.Y., 1993

McEwan, M.J., and L.F. Phillips, *Chemistry of the atmosphere*, New York, Wiley, pp.301, 1975.

McFarland, M., D.L. Albritton, F.C. Fehsenfeld, E.E. Ferguson, and A.L. Schmeltekopf, Energy dependence and branching ratio of the $N_2^+ + O$ reaction, *J.Geophys.Res.*, 79, 2925, 1974.

Mehr, F.J., and M. Biondi, Electron temperature dependence of recombination of O_2^+ and N_2^+ ions with electrons, *Phys.Rev.*, 181, 264, 1969.

Mentzoni, M.H., and R.V.Rao, Rotational excitation of electron relaxation in nitrogen, *Phys. Rev.*, 130, 2312-2316, 1963.

Min, Q.-L., *A Self-Consistent Time Varying Auroral Model*, pp. 120, PhD thesis, University of Alaska Fairbanks, 1994

Min, Q.-L., Watkins B.J., Determination of auroral heat fluxes and thermal ion out-flows using a numerical ionospheric model and incoherent-scatter radar, *J.Geophys.Res.*, 100, 251, 1995.

Mitra, A.P., A review of D-region processes in non-polar latitudes, *J.Atm.Terr.Phys.*, 30, 1065-1114, 1968

Nicholls, R.W., Aeronomically important transition probability data, *Can.J. Chem.*, 47, 1847, 1969.

Nicolet, M., Photodissociation of nitric oxide in the mesosphere and stratosphere: Simplified numerical relations for atmosphere model calculations, *Geophys.Res.Lett.*, 6, 866, 1979.

Nicolet, M., Aeronomical aspects of mesospheric photodissociation: Processes resulting from the solar H Lyman-alpha line, *Planet. Space Sci.*, 33, 69, 1985.

Nicolet, M., and S. Cielslik, The photoionization of nitric oxide in the mesosphere and stratosphere, *Planet.Space Sci.*, 28, 105, 1980.

Oppenheimer, M., E.R. Constantininides, K. Kirby-Docken, G.A. Victor,

and A. Dalgarno, Ion photochemistry of the thermosphere from Atmospheric Explorer C measurements, *J. Geophys. Res.*, 82, No.35,5485, 1977.

Ozisik, M.N., *Finite Difference Methods in Heat Transport*, pp. 412, CRC Press, 1994.

Pavlov, A,V., Determination of the molecular nitrogen vibrational tem perature in the auroral region using intensity measurements of the N_2^+ ion first negative band system, *Geomagn.Aeronomy*, 34, No.3, 306-310, 1994.

Perkins, F.W., and R.G. Roble, Ionospheric heating by radio waves: Predictions for Arecibo and the satellite power station, *J.Geophys. Res.*, 83, 1611-1624, 1978.

Piper, L.G., The excitation of $O(^1S)$ in the reaction between $N_2(A^3\Sigma_u^+)$ and $O(^3P)$, *J.Chem.Phys.*, 77(5), 2373-2377, 1982.

Piper, L.G., G.E. Caledonia, J.P. Kennealy, Rate constants for deactivation of $N_2(A^3\Sigma_u^+, v'=0,1)$ by O, *J.Chem.Phys.*, 75(6), 2847 - 2852, 1981.

Pitchford, L.C., and A.V. Phelps, Comparative calculations of electron-swarm properties in N_2 at moderate E/N values, *Phys. Rev., Sect.A*, 25, 540, 1982.

Potter, D., *Computational Physics*, pp. 304, John Wiley & Sons, 1977.

Prasad, S.S., and D..Furman, Electron cooling by molecular oxygen, *J. Geophys. Res.*, 78, 6701-6707, 1973.

Press, W.H., S.A. Teukolsky, W.T. Vetterling, B.P. Flannery, *Numerical Recipes in Fortran, The Art of Scientific Computing*, Cambrige University Press, pp. 963, 1992

Rapp, D., and P. Englander-Golden, Total cross sections for ionization and attachment in gases by electron impact. I. Positive ionization, *J.Chem. Phys.*, 43, 1464, 1965.

Rees D., and T. J. Fuller-Rowell, Modelling the response of the thermosphere/ionosphere system to time dependent forcing, *Adv.Space Res.*, 12, No. 6, 69-86, 1992.

Rees, M.H., Auroral ionization and exitation by incident energetic electrons, *Planet. Space Sci.*, 11, 1209, 1963.

Rees, M.H., *Physics and chemistry of the upper atmosphere*, pp.289, Cambridge Univesity Press, Cambridge, 1989.

Rees M.H., Auroral energy deposition rate, *Planet.Space Sci.*, 40, No. 2/3, 299-313, 1992.

Rees, M.H., and J.C.G. Walker, Ion and electron heating by auroral electric fields, *Ann.Geophys.*, 24, 193-199, 1968

Rees, M.H., and R.G. Roble, Excitation of $O(^1D)$ atoms in aurorae and emission of the [OI] 6300-Å line, *Can.J.Phys.*, 64, 1608-1613, 1986.

Rees, M.H., R.A. Jones, J.C.G. Walker, The influence of field-aligned currents on auroral electron temperatures, *Planet. Space Sci.*, 19, 313-325, 1971.

Rees, M.H., D. Lummerzheim, R.G. Roble, J.D.Winningham, J.D. Craven, and L.A. Frank, Auroral energy deposition rate, characteristic electron energy, and ionospheric parameters derived from Dynamics Explorer 1 images, *J.Geophys.Res.*, 93, 12,841-12,860, 1988.

Rees, M.H., D. Lummerzheim, and R.G. Roble, Modeling of the Atmosphere-magnetosphere-ionosphere system MAMI, *Space Sci. Rev.*, 71, 691-703, 1995.

Richards, P.G., D.G.Torr, and M.R.Torr, Photodissociation of N_2: A significant source of the thermospheric atomic nitrogen, *J. Geophys. Res.*, 86, 1495, 1981.

Richards, P.G, M.R. Torr, and D.G. Torr, The seasonal effect of nitric oxide cooling on the thermospheric U.V. heat budget, *Planet.Space Sci.*, 30, 515, 1982.

Richards, P.G., D.G. Torr, M.J. Buonsanto, and D.. Sipler, Ionospheric effects of the March 1990 magnetic storm: Comparison of theory and measurement, *J.Geophys.Res.*, 99, A12, 23,359-23,365, 1994.

Richmond, A.D., and Y. Kamide, Mapping electrodynamic features of the high-latitude ionosphere from localized observations: technique. *J.Geophys.Res.*, 93, A6, 5741-5759, 1988.

Roble R.G., The polar lower thermosphere, *Planet.Space Sci.*, v.40, No.2/3, pp. 217-297, 1992.

Roble, R.G., and R.E.Dickinson, Time-dependent behavior of a stable auroral red arc excited by an electric field, *Planet. Space Sci.*,

20, 591-605, 1972.

Roble, R.G. and B.A. Emery, On the global mean temperature of the thermosphere, *Planet.Space Sci.*, 31, 597, 1983.

Roble, R.G., and M.H. Rees, Time-dependent studies of the aurora: effects of particle precipitation on the dynamic morphology of ionospheric and atmospheric properties, *Planet.Space Sci.*, 25, 991-1010, 1977.

Roble R.G., and E.C. Ridley, An auroral model for the NCAR thermospheric general circulation model (TGCM), *Ann. Geophys, ser. A*, 5, No. 6, 369-382, 1987.

Roble, R.G., R.E. Dickinson, and E.C. Ridley, Global circulation and temperature structure of the thermosphere with high-latitude plasma convection, *J.Geophys.Res.*, 87, 1599, 1982.

Roble, R.G., E.C. Ridley, and R.E. Dickinson, On the global mean structure of the thermosphere, *J.Geophys.Res.*, 92, 8745-8758, 1987.

Rohrbaugh, R.P., W.E.Swartz, R.Simonaitis, and J.S.Nisbet, Effect of exited states of atomic oxygen ions on the reaction rates and thermal balance in the *F*-region, *Planet.Space Sci.*, 21, 159-163, 1973.

Rostoker, G., A Quantative Relationship between AE and Kp, *J.Geophys. Res.*, 96, No.A4, 5853-5857, 1991.

Rowe, B.R., D.W. Fahey, F.C. Fehsenfeld, and D.L.Albritton, Rate constants for the reactions of metastable O^{++} ions with N_2 and O_2 at collision energies 0.04 to 0.2 eV and the mobilities of these ions at 300 K, *J.Chem.Phys.*, 73, 194, 1980.

Ruohoniemi, M. and R.Greenwald, A New Statistical model of high-latitude convection, *The CEDAR Post*, No.26, p.15, 1995.

Rusch, D.W., and J.C. Gerard, Satellite studies of $N(^2D)$ emission and ion chemistry in aurorae, *J.Geophys.Res.*, 85, 1285, 1980.

Rusch, D.W., and W.E. Sharp, Nitric oxide band emission in the earth's atmosphere: Comparison of a measurement and a theory, *J. Geophys. Res.*, 86, 10,111, 1981.

Rusch, D.W., D.G. Torr, P.B. Hays, and J.C.G. Walker, The OII (7319-7330 Å) dayglow, *J.Geophys.Res.*, 82, 719, 1977.

Rusch, D.W, J.C. Gerard, and W.E. Sharp, Te reaction of $N(^2D)$ with O_2

as a source of O(^{1}D) atoms in aurorae, *Geophys.Res.Lett.*, 5, 1043, 1978.

Scali, J.L., B.W. Reinisch, C.J. Heinselman, T.W. Bullet, Coordinated digisonde and incoherent scatter radar *F* region drift measurements at Sondre Stromfjord, *Radio Sci.*, 30, No.5, 1481-1498, 1995.

Schiff, H.I., Neutral atmospheric chemistry -introduction and review, in *"Physics and Chemistry of the Atmosphere"* (ed. by B.M. McCormac, D. Reidel Publishing Co., Dordrecht-Holland), 1973.

Schunk, R.W., Transport equation for aeronomy, *Planet.Space Sci.*, 23, 437-485, 1975.

Schunk, R.W., and A.F.Nagy, Electron temperatures in the *F* region of the ionosphere: Theory and observations, *Rev.Geophys. Space Phys.*, 16, 355-399, 1978.

Schunk, R.W., and W.J. Raitt, Atomic nitrogen and oxygen ions in the daytime high-latitud F region, *J.Geophys.Res.*, 85, 1255, 1980.

Seaton, M.J., and D.E. Ostenbrock, Relative OII intensities in gaseous nebulae, *Astrophys.J.*, 125, 66, 1957.

Shirochkov, A.V., L.N. Makarova, S.A. Maurits, A numerical model of polar ionosphere and the possibilities of its application, *Ionospheric Research*, Moscow, Nauka, pp.26-33, 1993 (in Russian).

Shyn, T.W., and W.E. Sharp, Differential excitation cross section of atomic oxygen by electron impact: (^{3}P - ^{1}D transition), *J.Geophys. Res.*, 91, 1691, 1986.

Shyn, T.W., S.Y. Cho, and W.E. Sharp, Differential excitation cross section of atomic oxygen by electron impact: (^{3}P-^{1}S transition), *J. Geophys.Res.*, 91, 13,751 , 1986.

Siskind, D.E., The response of thermospheric nitric oxide to an auroral storm, PhD Thesis, pp.176, University of Colorado, Boulder, CO, 1988.

Siskind, D.E., C.A. Barth, D.S. Evans, R.G.Roble, The response of thermospheric nitric oxide to an auroral storm. 1. Low and middle latitudes, *J.Geophys.Res.*, 94, 16,885-16,898, 1989a.

Siskind, D.E., C.A. Barth, D.S. Evans, R.G.Roble, The response of thermospheric nitric oxide to an auroral storm. 2. Auroral latitudes,

J.Geophys. Res., 94, 16,899-16,911, 1989b.

Slanger, T.G., and G. Black, O(^{1}S) quenching profile between 75 and 115 km, *Planet. Space Sci.*, 21, No.10, 1757-1761, 1973.

Slanger, T.G., and G. Black, Quenching of O(^{1}S) by $O_2(a^1\Delta_g)$, *Geophys. Res.Lett.*, 8, 535, 1981.

Smith III F.L., Smith G., Numerical evaluation of Chapman's grazing incidence integral ch(X,χ), *J.Geophys.Res.*, 77, No.19, 3592-3597, 1972.

Sojka, J.J., W.J. Raitt, and R.W. Schunk, Effect of displaced geomagnetic and geographic poles on high-latitude plasma convection and ionospheric depletions, *J.Geophys.Res.*, 84, 5943, 1979.

Sojka, J.J., Global scale, physical models of the F-region, *Rev. of Geophys*, 27, No. 3, 371-403, 1989.

Sojka, J.J, Latest developments in the display of large-scale ionospheric and thermospheric data sets, *Adv.Space Res.*, 12, No.6, (6)51-(6)58, 1992.

Sojka, J.J., R.W.Schunk, J.V. Evans, J.M. Holt, and R.H. Wand, Comparison of model high-latitude electron densities with Millstone Hill Observations, *J.Geoph.Res*, 88, A10, 7783-7793, 1983.

Sojka J.J., R.W. Schunk, D. Rees, T.J. Fuller-Rowell, R.J. Moffett, and S. Quegan, Comparision of the USU ionospheric model with the UCL-Sheffield coupled thermospheric-ionospheric model, *Adv. Space Res.*, 12, No.6, 89-92, 1992.

Sojka, J.J, M.D. Bowline, R.W. Shunk, D.T. Decker, C.E. Valladares, R. Sheehan, D.N. Anderson, and R.A. Heelis, Modeling polar cap *F*-region patches using time varying convection, *Geophys.Res.Lett.*, 20, No.17, 1783-1786, 1993.

Sojka, J.J, M.D. Bowline, and R.W. Shunk, Patches in the polar ionosphere: UT and seasonal dependence, *J.Geoph.Res*, 99, A8, 14,959-14,970, 1994.

Solheim, B.H., and E.J. Llewellin, An indirect mechanism for the production of O(^{1}S) in the aurora, *Planet. Space Sci.*, 27, 473-479, 1979.

Spitzer, L., *Physics of fully ionized Gases*, pp.105, Interscience, New

York, 1956.

Spiro, R.W., P.F. Reiff, L.J. Maher, Precipitating electron energy flux and auroral zone conductances - an empirical model, *J.Geophys.Res.*, 87, 8215-8227, 1982.

Stamnes, K., and M.H. Rees, Heating of thermal ionospheric electrons by suprathermal electrons, *Geophys.Res.Lett.*, 10, 309-312, 1983a.

Stamnes, K., and M.H. Rees, Inelastic scattering effects on photoelectron spectra and ionospheric electron temperature, *J.Geophys.Res.*, 88, 6301, 1983b.

St.-Maurice, J.P., and D.G. Torr, Nonthermal rate coefficients in the ionosphere: The reactions of O^+ with N_2, O_2, and NO, *J.Geophys. Res.*, 83, 969, 1978.

Stone, E.J., and E.C. Zipf, Electron-Impact exitation of the $^3S^0$ and $^5S^0$ states of atomic oxygen, *J.Chem.Phys.*, 60, 4237, 1974.

Streit, G.E., C.L. Schemeltekopf, A.L. Davidson, H.I. Schiff, Temperature dependence of $O(^1D)$ rate constants for reactions with O_2, N_2, CO_2, O_3, and H_2O, *J.Chem.Phys.*, 65, No.11, 4761-4764, 1976.

Strickland, D.G, and R.R. Meier, A photoelectron model for the rapid computation of atmospheric excitation rates, *NRL Memo. Rep.*, 5004, 1-40, 1982.

Strobel D.F., T.R. Young, R.R Meier, T.P. Coffey, A.W. Ali, The night-time ionospfere: *E* region and lower *F* region, *J.Geophys.Res.*, 79, No.22, 3171-3185, 1974.

Strobel D.F., C.B. Opal, and R.R. Meier, Photoionization rates in the night-time *E*- and *F*-region ionosphere, *Planet.Space Sci.*, 28, 1027-1033, 1980.

Stubbe, P., and W.S. Varnum, Electron energy transfer rates in the ionosphere, *Planet. Space Sci.*, 20, 1121-1126, 1972.

Swartz, W.E., J.S. Nisbet, and A.E.S. Green, Analytic expression for the energy transfer rate from photoelectrons to thermal electrons, *J.Geophys.Res.*, 76, 8425, 1971.

Tobiska, W.K., C.A. Barth, A solar EUV flux model, *J.Geophys.Res.*, 95, A6, 8243-8251, 1990.

Todd, H., B.J.I. Bromage, S.W.H. Cowley, M. Lockwook, A.P. van Eiken,

and D.M. Willis, EISCAT obsevations of bursts of rapid flow in the high latitude dayside ionosphere, *Geophys.Res.Letters*, 13, No.9, 910-912, 1986.

Torr, D.G., The photochemistry of the upper atmosphere, in *The Photochemistry of the Atmospheres*, pp.165-286, Academic, Orlando, FL, 1985.

Torr, D.G., and M.R. Torr, Chemistry of the thermosphere and ionosphere, *J.Atmos.Terr.Phys.*, 41, 797, 1979.

Torr, D.G., M.R. Torr, J.C.G. Walker, and A.O. Nier, Recombination of O_2^+ in the ionosphere, *J.Geophys.Res.*, 81, 5578, 1976.

Torr, D.G., N. Orsini, M.T. Torr, W.B. Hanson, J.H.Hoffman, and J.C.G. Walker, Determination of the rate for the N_2^+ + O reaction in the ionosphere, *J.Geophys.Res.*, 82, 1631, 1977.

Torr, D.G., M.R. Torr, H.C. Brinton, L.H. Brace, N.W. Spencer, A.E. Hedin, W.B. Hanson, J.H. Hoffman, A.O. Nier, J.C.G. Walker, and D.W. Rusch, An experimental and theoretical study of the main diurnal variation of O^+, NO^+, O_2^+, and N_2^+ ions in the midlatitude F_1 layer of the ionosphere, *J.Geophys. Res.*, 84, 3360, 1979.

Torr, M.R., and D.G. Torr, The dissociative recombination of O_2^+ in the ionosphere, *Planet.Space Sci.*, 29, 999, 1981.

Torr, M.R., and D.G. Torr, The role of metastable species in the thermosphere, *Rev.Geophys.*, 20, 91, 1982.

Torr, M.R., P.G. Richards, and D.G.Torr, A new determination of the ultraviolet heating efficiency of the thermosphere, *J.Geophys.Res.*, 85, 6819, 1980a.

Torr, M.R., D.G. Torr, and H.E. Hinterregger, Solar flux variability in the Schummann-Runge continuum as a function of solar cycle 21, *J. Geophys.Res.*, 85, 6063, 1980b.

Torr, M.R., D.G. Torr, and P.Richards, Quenching of $O^+(^2D)$ by electrons in the thermosphere, *Planet.Space Sci.*, 28, 581, 1980c.

Valladares, C.E., S. Basu, J. Buchau, E. Friis-Christensen, Experimental evidence for the formation and entry of patches into the polar cap, *Radio Sci.*, 29, No.1, 167, 1994.

Vallance Jones, A., *Aurora*, pp.301, D. Reidel Publishing Co., Dordrecht

- Holland, 1974 .

Walker, J.C.G., and M.H. Rees, Ionospheric electron densities and temperatures in aurora, *Planetary Space Sci.*, 16, 459, 1968

Watanabe, K., F.M. Matsunaga, and H.Sakai, Absorption coefficient and photoionization yield of *NO* in the region 580-1350 Å, *Appl.Opt.*, 6, No.3, 391-396, 1967.

Weimer, D.R., Models of high-latitude electric potential derived with a least-error fit of spherical harmonic coefficients, *J. Geophys. Res.*, 100, 19,595, 1995.

Zipf, E.C., The collisional deactivation of metastable atoms and molecules in the upper atmosphere, *Can.J.Chem.*, 47, No.10, 1863-1870, 1969.

Zipf, E.C., and P.W Erdman, Electron impact excitation of atmospheric oxygen: Revised cross sections values, *EOS*, 66, 321, 1985.

Zipf, E.C., P.J. Espy, and C.F. Boyle, The excitation and collisional deactivation of metastable $N(^2P)$ atoms in auroras, *J.Geophys.Res.*, 85, 687, 1980.

Zipf, E.C., and R.W. McLaughlin, On the dissociation of nitrogen by electron impact and by EUV photo-absorption, *Planet.Space Sci.*, 26, 449, 1978.